Reduced order finite element models for the nonlinear dynamic analysis of reinforced concrete structures under seismic excitations

Naim Ayoub

To cite this version:

Naim Ayoub. Reduced order finite element models for the nonlinear dynamic analysis of reinforced concrete structures under seismic excitations. Mécanique [physics]. HESAM Université, 2021. Français. NNT : 2021HESAC053 . tel-03999367

HAL Id: tel-03999367
https://theses.hal.science/tel-03999367v1

Submitted on 21 Feb 2023

HESAM UNIVERSITÉ

le cnam

ÉCOLE DOCTORALE Sciences des Métiers de l'Ingénieur
Laboratoire de Mécanique des Structures et des Systèmes Couplés

THÈSE

présentée par : **Naim AYOUB**

soutenue le : 15 décembre 2021

pour obtenir le grade de : **Docteur d'HESAM Université**

préparée au : **Conservatoire national des arts et métiers**

Discipline : **Mécanique, génie mécanique, génie civil**

Spécialité : **Mécanique**

Reduced order finite element models for the nonlinear dynamic analysis of reinforced concrete structures under seismic excitations

Modèles d'éléments finis d'ordre réduit pour l'analyse dynamique non linéaire de structures en béton armé soumises à des excitations sismiques

THÈSE dirigée par :
M. Walid LARBI Professeur des Universités, Cnam Paris
M. Jean-François DEÜ Professeur des Universités, Cnam Paris

et co-encadrée par :
Mme Lucie ROULEAU Maître de Conférences, Cnam Paris

Jury

M. Luc DAVENNE, Professeur des Universités, Université Paris Nanterre	Président
M. Fabrice GATUINGT, Professeur des Universités, ENS Paris-Saclay	Rapporteur
M. Marwan SADEK, Professeur de l'Université Libanaise, Liban	Rapporteur
M. Marc OUDJENE, Professeur de l'Université Laval, Canada	Examinateur
M. Walid LARBI, Professeur des Universités, Cnam Paris	Directeur de thèse
M. Jean-François DEÜ, Professeur des Universités, Cnam Paris	Co-directeur de thèse
Mme. Lucie ROULEAU, Maître de Conférences, Cnam Paris	Co-encadrante de thèse
M. Francis GUILLEMARD, Founder & President of Board, GRAITEC GROUP	Invité
M. Joseph PAIS, Chief Product Officer, GRAITEC GROUP	Invité

THÈSE

Affidavit

Je soussigné, Naim AYOUB, déclare par la présente que le travail présenté dans ce manuscrit est mon propre travail, réalisé sous la direction scientifique de Walid LARBI et de Jean-François DEÜ, dans le respect des principes d'honnêteté, d'intégrité et de responsabilité inhérents à la mission de recherche. Les travaux de recherche et la rédaction de ce manuscrit ont été réalisés dans le respect de la charte nationale de déontologie des métiers de la recherche. Ce travail n'a pas été précédemment soumis en France ou à l'étranger dans une version identique ou similaire à un organisme examinateur.

Fait à Paris, le 15 décembre 2021

Naim AYOUB

Affidavit

I, undersigned, Naim AYOUB, hereby declare that the work presented in this manuscript is my own work, carried out under the scientific direction of Walid LARBI and of Jean-François DEÜ, in accordance with the principles of honesty, integrity and responsibility inherent to the research mission. The research work and the writing of this manuscript have been carried out in compliance with the French charter for Research Integrity.
This work has not been submitted previously either in France or abroad in the same or in a similar version to any other examination body.

Paris, December the 15th 2021

Naim AYOUB

Remerciements

Cette thèse a été effectuée au Laboratoire de Mécanique des Structures et des Systèmes Couplés (LMSSC) du Conservatoire national des arts et métiers (Cnam) de Paris, dans le cadre d'un contrat Cifre avec la société GRAITEC INNOVATION.

Je souhaite remercier toutes les personnes qui ont contribué à l'élaboration de ce travail et surtout :

- Mes encadrants au LMSSC : Walid LARBI, Jean-François DEÜ et Lucie ROULEAU pour leurs idées, direction et support.
- Mes encadrants à GRAITEC INNOVATION : Francis GUILLEMARD et Joseph PAIS pour leurs conseils, orientations et soutiens.
- Les professeurs : Fabrice GATUINGT, Luc DAVENNE, Marc OUDJENE et Marwan SADEK pour avoir accepté de participer à mon jury de thèse.
- La société GRAITEC INNOVATION et l'Association Nationale de la Recherche et Technologie (ANRT) pour avoir financé mes travaux de recherche.
- Mes collègues au LMSSC et GRAITEC INNOVATION pour leurs encouragements, assistances et le temps agréable qu'on a passé ensemble.
- Ma famille, mes amis et mes proches : votre amour et support continus est la fondation de tout mon succès.

Résumé

Cette thèse concerne le développement de modèles d'ordre réduit pour l'analyse dynamique des structures en béton armé avec des non-linéarités matérielles et soumises à des excitations sismiques. La réduction du modèle est réalisée en étendant l'application de la décomposition orthogonale aux valeurs propres (POD) aux modèles dynamiques de structures en béton armé avec des non-linéarités matérielles dues à la plasticité des armatures en acier et à l'endommagement du béton. Cette technique de réduction est d'abord testée sur une structure de type portique à plusieurs étages où la non-linéarité des matériaux est modélisée par l'approche de la section multifibre. Dans le cas d'un seul séisme, une analyse dynamique non-linéaire du modèle complet est menée sur une partie de l'excitation sismique. Ensuite, les modes POD sont extraits et utilisés pour réduire l'analyse dynamique de la partie restante de l'excitation, réduisant ainsi le coût de calcul. Pour les scénarios de séismes multiples, une analyse dynamique non-linéaire du modèle complet est menée sur une partie d'une excitation sismique sélectionnée. Ensuite, les modes POD sont extraits et utilisés pour réduire l'analyse dynamique des autres excitations permettant ainsi d'économiser une grande partie du coût de calcul. Des essais similaires sont effectués sur un voile de contreventement à plusieurs étages en béton armé avec des non-linéarités matérielles introduites par une approche de membrane multicouche. Pour évaluer l'efficacité et la précision de cette technique de réduction, une comparaison est faite entre les modèles d'ordre réduit et les modèles complets. Cette comparaison porte sur le coût de calcul, le déplacement de la structure en fonction du temps et le comportement hystérétique des matériaux en acier et en béton.

Mots clés: Structures en béton armé, Non-linéarités matérielles, Modèle dynamique d'ordre réduit, Décomposition orthogonale aux valeurs propres, Poutre multifibre, Membrane multicouche, Excitations sismiques.

Abstract

This thesis concerns the development of reduced order models for dynamic analysis of reinforced concrete structures with material nonlinearities and subjected to seismic excitations. Model reduction is achieved by extending the application of the Proper Orthogonal Decomposition (POD) to dynamic models of reinforced concrete structures with material nonlinearities originating from steel reinforcement plasticity and concrete damaging. This reduction technique is tested first on a reinforced concrete multistory frame structure where material nonlinearity is modeled by the multifiber section approach. In the case of a single earthquake, a full model nonlinear time-history analysis is conducted on a portion of the seismic base excitation. Then, proper orthogonal decomposition modes are extracted and used to reduce the dynamic analysis of the remaining excitation portion, thus reducing the computational cost. For multiple earthquake scenarios, a full model nonlinear time-history analysis is conducted on a portion of only one selected seismic base excitation. Then, proper orthogonal decomposition modes are extracted and used to reduce the dynamic analysis of the other base excitations while saving a large part of the computational cost. Similar testing is made on a multistory planar reinforced concrete shear wall with material nonlinearities introduced via the layered membrane approach. To evaluate the efficiency and accuracy of this reduction technique, a comparison is made between the reduced order models and the full order ones. This comparison covers the computational cost, the structural displacement in function of time and the hysteretic behavior of steel and concrete materials.

Keywords: Reinforced concrete structures, Material nonlinearities, Reduced order dynamic model, Proper orthogonal decomposition, Multifiber beam, Layered membrane, Seismic excitations.

Contents

List of Tables

List of Figures

Introduction

Motivations and context

Since the dawn of mankind, humans are constantly upgrading their habitats for better protection against nature's elements. The constant development of sciences during the past thousands of years, made it possible for us to move from caves to skyscrapers. Humanity is always developing sciences to improve our way of living.

Earthquakes are one of the major natural disasters that threaten human life. Without any warning, strong ground shakings transform structures from a place once full of life into debris. Roads and infrastructures get severely damaged (no electricity, no communications, no clean water, gas explosions …).

Facing this catastrophic scenario, researchers have developed techniques for designing new structures or retrofitting existing ones in order to improve their earthquake resistance and lower human causalities.

Generally, structures experience nonlinear behavior when subjected to earthquake inertial loadings. Three types of structural nonlinearities exist: contact, geometrical and material nonlinearities.

Contact nonlinearities are generally the case where forces between structural elements are generated only when physical contact is established between these elements. The foundation uplift is a good example of this nonlinearity. In fact, when the foundation is pushing down on the supporting soil, the soil exerts a vertical reaction back. However, when foundation uplift occurs (foundation tries to move up due to high wind or earthquake…) the soil do not exert any force on the foundation.

Geometric nonlinearities are due to large displacements in the structure causing a modification in the structural geometry and thus changing the application point of the loads carried by the structure.

Material nonlinearities occur when stress in structural elements surpasses the linear elastic limit of materials, the stress-strain relation of the materials becomes nonlinear. Materials nonlinear behavior is a very large subject and is by far the most complicated type of structural nonlinearities. In fact, numerous interacting complex physical phenomena like plastic flow, damaging, fracturing, bond slip … are at the origin of this nonlinearity.

Since the classical common engineering practice is founded on elastic linear behavior, material nonlinearities in the linear seismic analyses that were initially developed are considered by a global reduction factor applied on inertial loads. However, summarizing all the complex physical phenomena behind material nonlinearities by a simple load reduction factor is a very rough estimation. In addition, linear seismic models do not provide additional knowledge on the location and extent of nonlinear deformations in the structures during earthquakes which are essential information to avoid the development of soft stories in the structures.

By now, it is clear that linear seismic analyses alone are not sufficient and more complex models incorporating nonlinearities are required. As will be furtherly detailed in chapter 1, two types of nonlinear seismic analysis are commonly used: the pushover and the nonlinear direct integration time history analysis. The pushover analysis is limited to regular structures and provides only the maximum seismic structural response. So, even though it incorporates material nonlinearities, the pushover analysis is still insufficient. On the other hand, the nonlinear direct integration time history analysis is applicable to all types of structures and provide a time-dependent response of the structure during earthquake. But this comes at a heavy price: the time cost for nonlinear direct integration time history analysis is enormous with respect to other seismic analysis techniques. In fact, even with today’s computing technologies, some models require weeks of analysis time. To make things even worse, this costly analysis should be carried for multiple base excitations occurring in different directions to cover all possible earthquake scenarios.

Objectives and outline

Facing the dilemma between the pushover analysis limitations and the huge time cost of the nonlinear direct integration time history analysis, this thesis proposes the reduction of the dynamic model by extending, for the first time, the application of the Proper Orthogonal Decomposition (POD) technique to Reinforced Concrete (RC) structures with material nonlinearities originating simultaneously from steel reinforcements, confined and unconfined concrete. The Reduced Order Model (ROM) is then used in nonlinear direct integration time history analysis to reduce the time cost while maintaining an acceptable level of accuracy. For this purpose, the POD time saving techniques in seismic analysis introduced by (Bamer and Bucher, 2012; Bamer, Amiri and Bucher, 2017) were adopted and extended to RC structures with material nonlinearities. This approach was tested on a multistory RC frame structure and on a RC shear wall. Results were compared with the time costly Full Model (FM) nonlinear direct integration time history analysis to test the accuracy and efficiency in time saving of the ROM.

This thesis was conducted in an industrial partnership (known as French “CIFRE” thesis) with GRAITEC INNOVATION an international engineering softwares developer, provider and consultant. This cooperation was essential in the mutual experience exchange between research and industrial fields and proved to be vital in the orientation of the work.

In Chapter 1, a literature review is made on the most commonly used types of seismic analysis. Linear and nonlinear analyses are presented and separated between techniques giving only the maximum structural response and others providing time-dependent responses.

In Chapter 2, the 1D and 2D structural element models that consider material nonlinearity are presented. Justifications are made for using in this thesis the multifiber approach for 1D elements (beams and columns) and the layered membrane for 2D elements (shear walls). Then nonlinear uniaxial and biaxial material models available for unconfined and confined concrete and steel reinforcing bars are presented in addition to nonlinear behavior of materials under cyclic loading. Explanations are provided for adopting a simplified version of the Mander uniaxial concrete model and the Darwin Pecknold biaxial concrete orthotropic model.

In Chapter 3, the finite element models of multifiber beams and layered membranes are developed. Then, these nonlinear numerical models are validated by a comparison with experimental results.

In Chapter 4, nonlinear reduction techniques are presented. Then, detailed explanation on the Proper Orthogonal Decomposition (POD) and its applications for reducing nonlinear dynamic analysis’ time cost is made. In addition, numerical algorithms for full and POD reduced order models (POD-ROM) are developed for both multistory Reinforced Concrete (RC) frame structures and shear walls with material nonlinearities.

In Chapter 5, a numerical comparison between Full Models (FM) and POD-ROM for the RC multistory frame and shear wall is made (in MATLAB). The results are then analyzed to evaluate the efficiency in time saving and accuracy of the POD-ROM on RC structural elements with material nonlinearities.

Chapter 1

1. Literature review on structural seismic analysis

Abstract: *This chapter presents a literature review on linear and nonlinear structural seismic analysis techniques while showing the advantages and limitations for each one of them. As a consequence, the motivation of this thesis work to make the time integration nonlinear dynamic analysis less computationally demanding is highlighted.*

Chapter content

1.1. Introduction

Since ancient times, people tried constructing earthquake resistant structures. According to (Carpani, 2017), primitive forms of seismic base isolators consisting of loosening the connection between the structure and the foundation soil date back to 3000 years ago.

Modern seismic analysis techniques and codes started appearing in the late 19th century and are currently divided into two major categories: linear and nonlinear analysis. In addition, there are seismic analysis methods that solely provide the maximum structural response to earthquakes while other techniques offer a time-dependent response (refer to Figure 1.1).

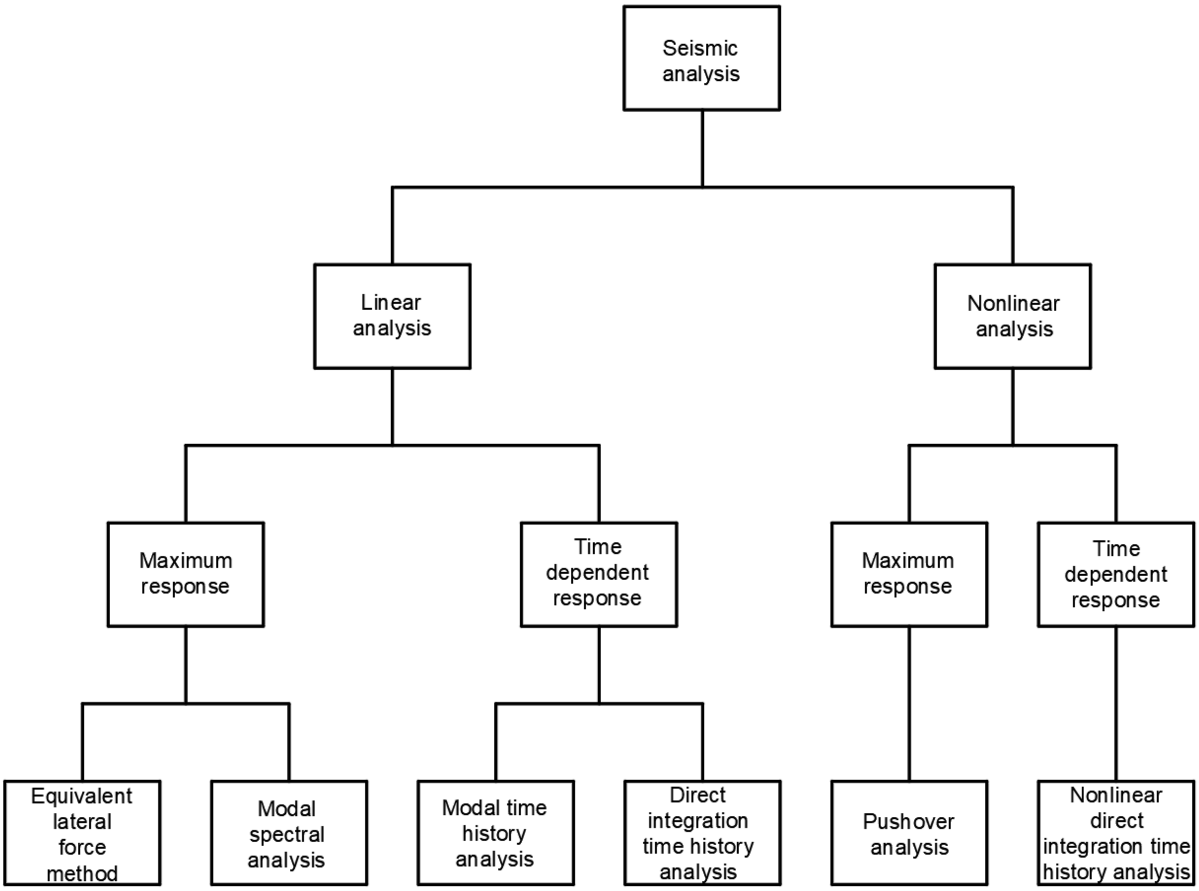

Figure 1.1: Seismic analysis techniques.

Generally, the structural response to earthquakes exceeds the materials elastic limits. However, structural engineers are more used to linear calculations. In order to facilitate seismic analysis, linear calculations are proposed with the application of a reduction factor (ductility coefficient) on seismic loads to take into account the materials ductile deformations and hysteresis energy dissipation. This procedure is derived from the equivalent displacement rule set up by (Muto *et al.*, 1960; Veletsos and Newmark, 1960) which was the first step in accounting for material nonlinearity.

To demonstrate the equivalent displacement rule, a force is considered to be applied on a structure with a bilinear elastic perfectly plastic behavior. F_{el} is the elastic force limit to which corresponds an elastic displacement d_{el}. In reality, the applied force on the structure cannot exceed F_{el} and once this force is reached the structure will start yielding until reaching a certain total plastic displacement d_{pl} (refer to Figure 1.2). If linear analysis was used, for a displacement d_{pl} the applied force on the structure F_{pl} would be:

$$F_{pl} = K_{el} d_{pl} \tag{1.1}$$

where K_{el} is the linear elastic stiffness of the structure. But since F_{el} can not be exceeded, the applied load should be divided by a reduction factor R as expressed in the equal displacement rule.

$$R = \frac{F_{pl}}{F_{el}} = \frac{d_{pl}}{d_{el}} \tag{1.2}$$

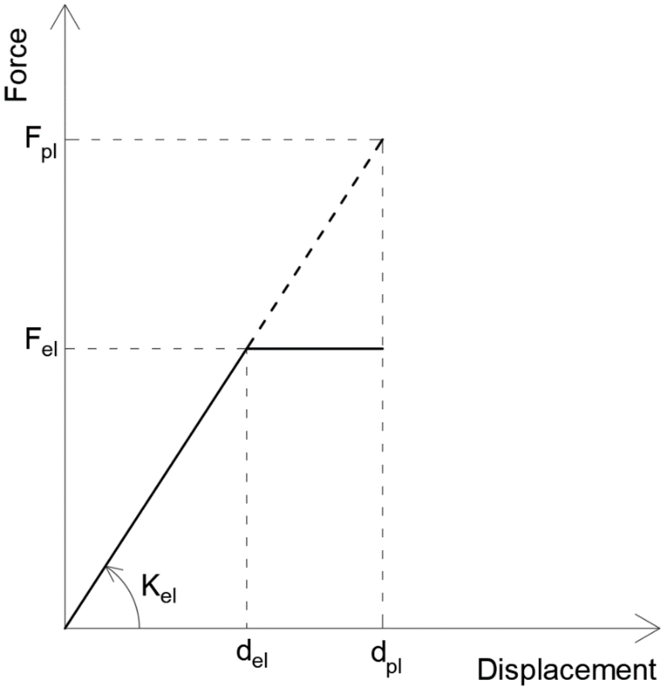

Figure 1.2: Equivalent displacement rule.

Linear seismic analysis belongs to strength-based designs in which structural elements are dimensioned according to their strength (resistance) while accounting for the reduction factor R. Whereas nonlinear seismic analysis is a performance-based design in which the dimensioning criteria is not the element strength but the scale of the plastic deformation and its effect on the structure’s use and performance. In the following, a detailed technical presentation of each seismic analysis technique is made.

1.2. Equivalent lateral force method

The equivalent lateral force method is limited to buildings where the dynamic response is governed by the fundamental translational mode shape in the considered horizontal direction of analysis. In addition, buildings should respect the horizontal and vertical regularity criteria specified in the seismic codes as well as the structural height limitation.

The origin of the equivalent lateral force method dates from the Messina-Reggio earthquake that occurred on December 28, 1908, in Sicily Italy. Following the high number of casualties (more than 75000 deaths) a scientific committee was formed and it proposed the first form of the equivalent lateral force method (Reitherman, 2006). The first formal code for seismic design was due to the Japanese Building Ordinance, after the 1923 Great Kanto earthquake. “The regulations stipulated that buildings should be designed to resist a force equivalent to 10% (response coefficient $C = 10\%$) of their weight applied horizontally” (Elnashai, 2002). With time and after multiple earthquake disasters, many seismic codes adopting the equivalent lateral method were developed and the response coefficient C was continuously updated to take into consideration the seismic zone, fundamental period of the structure, soil conditions (Mitchell *et al.*, 2010; Bourahla, 2014).

The equivalent lateral force method is a linear static approach in which horizontal loads representing the earthquake effect are distributed laterally on the structure and in both directions. The resulting base shear of these lateral forces V is equal to the gravity loads participating in the earthquake W multiplied by a response coefficient C $(V = CW)$. Generally, the response coefficient C is determined by seismic codes (UBC, 1997; EC8-1, 2004; FEMA P-750, 2009; ASCE/SEI 7-16, 2017) in function of the quake’s response spectrum, fundamental period of the structure, site and soil conditions, importance of the structure and type of the lateral resisting system. Since linear calculation is used, a reduction factor is introduced to account for the hysteretic damping occurring in the structure. This factor reduces the seismic loads applied on the linear structural model and is generally specified by seismic codes in function of the lateral resisting system used. The structure is assumed to respond solely according to its fundamental lateral vibration mode shape for each of the considered directions. Lateral static forces representing earthquake loads are distributed on the floors proportionally to the fundamental lateral vibration mode shape under consideration.

Improvements on this seismic analysis method are constantly being developed. (Hajirasouliha and Moghaddam, 2009) proposed improvements on the lateral seismic loads distribution pattern. (Kim and LaFave, 2017) proposed adjustments for the equivalent lateral force method in order to use it for low-rise reinforced concrete wall-frame mixed building systems. (Roy and Mahato, 2013) studied the applicability of the equivalent lateral force method on buildings with setback. (Mohammadi and EL Naggar, 2004) proposed adjustments for the reduction factor that accounts for the nonlinear behavior.

1.3. Modal spectral analysis

The modal analysis of a continuous system appeared during the 19th century with (Strutt and Rayleigh, 1877). The basic concept of modal analysis is to breakdown the dynamic behavior of a structure into a set of vibration modes. Each mode has its unique natural vibration frequency and damping ratio in addition to a mode shape vector representing the displacement pattern that the structure will undergo when vibrating according to this mode. The total dynamic response of the system is obtained by the summation of vibrations along every mode in the structure.

The modal parameters (natural frequency, damping and mode shape vectors) can be determined by experimental, analytical or numerical means. Experimental approaches are generally based on monitoring the structural response due to an impact or shaking by using accelerometers, velocimeters and piezoelectric force transducers attached to the structure. Measurements made by these sensors as a function of time are then transformed to the frequency domain using the Fast Fourier Transform (FFT). By analyzing the collected data, modal parameters of the tested structure can be determined. For further information on modal testing refer to (Ewins, 2000; Rainieri and Fabbrocino, 2014). In addition to determining modal parameters, modal testing is used for damage detection in structures. For more information regarding damage detection by modal analysis refer to (Hearn and Testa, 1991; Sampaio, Maia and Silva, 1999; Cha and Buyukozturk, 2015).

1.3. Modal spectral analysis

Analytical modal analysis of continuous systems require solving complicated differential equations and is generally limited to relatively simple small structures for further details on this topic refer to (Rao, 2007).

On the other hand, numerical modal analysis using the Finite Element (FE) discretization is much simpler to use and easier to implement in computer calculation.

Let's consider a structure discretized by FE with n Degrees Of Freedom (DOF). The dynamic equation of the undamped free vibrating linear elastic discretized system becomes:

$$[M]\{\ddot{U}(t)\} + [K]\{U(t)\} = \{0\} \tag{1.3}$$

where $[M]$ is the mass matrix (dimensions $n \times n$), $[K]$ is the stiffness matrix (dimensions $n \times n$) and $\{U(t)\}$ is the displacement vector (dimensions $n \times 1$) varying with time t and relative to the base reference. It should be noted that in this entire thesis a matrix is indicated by [ ] and a vector by { }. The general solution of this differential equation is a harmonic response with space and time separation.

$$\{U(t)\} = \{\emptyset\}a\sin(\omega t + \theta) \tag{1.4}$$

where $\{\emptyset\}$ is a mode shape (displacement pattern) vector (dimensions $n \times 1$), ω is the corresponding angular frequency (pulsation), a is the vibration amplitude and θ is the phase angle. Solving equation (1.5) will result in n specific eigenvalue ω^2 (specific angular frequency ω for each mode of vibration). Then, an eigenvector $\{\emptyset\}$ (mode shape vector) can be deducted for each eigenvalue.

$$\det([K] - \omega^2[M]) = 0 \tag{1.5}$$

The displacement vector along the ith vibration mode will be:

$$\{U_i(t)\} = \{\emptyset_i\}a_i\sin(\omega_i t + \theta_i) = \{\emptyset_i\}q_i(t) \tag{1.6}$$

with

$$q_i(t) = a_i\sin(\omega_i t + \theta_i) \tag{1.7}$$

where $q_i(t)$ is the modal coordinate of the ith vibration mode. The total dynamic response of the system will become:

$$\{U(t)\} = \sum_{i=1}^{n}\{\emptyset_i\}q_i(t) \tag{1.8}$$

amplitudes a_i and phase angles θ_i are determined by the system's initial conditions.

The most appealing aspect of modal analysis in structural dynamics is the orthogonality of mode shape vectors with respect to the mass and stiffness matrices.

$$\{\emptyset_i\}^T[K]\{\emptyset_j\} = 0 \; for \; i \neq j \tag{1.9}$$

$$\{\emptyset_i\}^T[M]\{\emptyset_j\} = 0 \; for \; i \neq j \tag{1.10}$$

Replacing $\{U(t)\}$ in equation (1.3) by its equivalent in equation (1.8) and left multiplying both sides of the equation with $\{\emptyset_j\}^T$ we get:

$$\{\emptyset_j\}^T[M]\sum_{i=1}^{n}\{\emptyset_i\}\ddot{q}_i(t) + \{\emptyset_j\}^T[K]\sum_{i=1}^{n}\{\emptyset_i\}q_i(t) = \{0\} \tag{1.11}$$

Since mode shape vectors are orthogonal with respect to the mass and stiffness matrices, we can decouple the dynamic differential equation of the MDOF structural system equation and get n independent differential equations of a Single Degree Of Freedom (SDOF) structural system.

$$\{\emptyset_j\}^T[M]\{\emptyset_j\}\ddot{q}_j(t) + \{\emptyset_j\}^T[K]\{\emptyset_j\}q_j(t) = 0 \tag{1.12}$$

For a MDOF structural system subjected to any excitation at its base the corresponding dynamic equation is:

$$[M]\{\ddot{U}(t)\} + [C]\{\dot{U}(t)\} + [K]\{U(t)\} = -[M]\{I\}\ddot{u}_g(t) \tag{1.13}$$

where $[C]$ is the damping matrix (dimensions $n \times n$), $\ddot{u}_g(t)$ is the time-dependent acceleration of the excitation applied at the base of the structure, $\{I\}$ is the influence vector specifying the degrees of freedom affected by the base excitation. Since base excitation is applied in a specific direction, the influence vector specifies which masses on which DOF are affected by the base excitation.

In order to keep the decoupling advantage of modal analysis, the mode shape vectors need to be orthogonal with respect to the damping matrix. This can be achieved by considering Rayleigh damping which produces the damping matrix by a factored combination of the mass and stiffness matrices.

Decoupling equation (1.13) will give:

$$\begin{aligned}\{\emptyset_i\}^T[M]\{\emptyset_i\}\ddot{q}_i(t) + \{\emptyset_i\}^T[C]\{\emptyset_i\}\dot{q}_i(t) + \{\emptyset_i\}^T[K]\{\emptyset_i\}q_i(t) \\ = -\{\emptyset_i\}^T[M]\{I\}\ddot{u}_g(t)\end{aligned} \tag{1.14}$$

which can be expressed as:

$$M_i\ddot{q}_i(t) + C_i\dot{q}_i(t) + K_i q_i(t) = -L_i\ddot{u}_g(t) \tag{1.15}$$

where M_i, C_i, K_i and $-L_i\ddot{u}_g(t)$ are respectively the generalized mass, damping, stiffness and loading of the i$^{\text{th}}$ vibration mode.

Dividing both sides of equation (1.15) by the generalized mass M_i we get:

$$\ddot{q}_i(t) + \frac{C_i}{M_i}\dot{q}_i(t) + \frac{K_i}{M_i}q_i(t) = -\frac{L_i}{M_i}\ddot{u}_g(t) \tag{1.16}$$

which can be written as:

$$\ddot{q}_i(t) + 2\zeta_i\omega_i\dot{q}_i(t) + {\omega_i}^2 q_i(t) = -\Gamma_i\ddot{u}_g(t) \tag{1.17}$$

where ζ_i and Γ_i are respectively the damping ratio and modal participation factor of the i$^{\text{th}}$ vibration mode. Let $d_i(t)$ be the modal displacement of the i$^{\text{th}}$ vibration mode and is expressed as:

$$q_i(t) = \Gamma_i d_i(t) \tag{1.18}$$

Replacing $q_i(t)$ in equation (1.17) by its equivalent in equation (1.18) we get the modal displacement dynamic equation.

$$\ddot{d}_i(t) + 2\zeta_i\omega_i\dot{d}_i(t) + {\omega_i}^2 d_i(t) = -\ddot{u}_g(t) \tag{1.19}$$

The effective modal mass of the i$^{\text{th}}$ vibration mode M_i^* is given by:

$$M_i^* = \Gamma_i L_i = \frac{(\{\emptyset_i\}^T[M]\{I\})^2}{\{\emptyset_i\}^T[M]\{\emptyset_i\}} \tag{1.20}$$

Later on, the effective modal mass is used in modal truncation (the classic requirement of 90% effective modal mass participating in the direction of vibration).

Modal analysis allows the determination of the displacement field but in some cases only the maximum dynamic displacement is needed. For such scenarios, modal spectral analysis is adopted. This technique consists in determining the maximum dynamic response of an elastic linear structure based on the pseudo-acceleration response spectrums. Let us explain how to obtain the pseudo-acceleration spectrum for a damped linear elastic SDOF system subjected to a base excitation having the following dynamic equation:

$$m\ddot{u}(t) + c\dot{u}(t) + ku(t) = -m\ddot{u}_g(t) \tag{1.21}$$

which gives:

$$\ddot{u}(t) + 2\zeta\omega\dot{u}(t) + \omega^2 u(t) = -\ddot{u}_g(t) \tag{1.22}$$

The return force also known as internal force $f(t)$ is given by:

$$f(t) = ku(t) \tag{1.23}$$

Replacing k by $m\omega^2$ in equation (1.23) we get:

$$f(t) = m\omega^2 u(t) \tag{1.24}$$

$\omega^2 u(t)$ is called the pseudo-acceleration.

Equation (1.22) can be expressed as:

$$2\zeta\omega\dot{u}(t) + \omega^2 u(t) = -\left(\ddot{u}_g(t) + \ddot{u}(t)\right) \tag{1.25}$$

$\ddot{u}_g(t) + \ddot{u}(t)$ is the absolute acceleration of the system and is different from the pseudo-acceleration due to the presence of damping. The maximum return force f_{max} applied on this system is:

$$f_{max} = ku_{max} = m\omega^2 u_{max} \tag{1.26}$$

Considering the same base vibration and repeating this calculation for many SDOF systems having the same damping ratio but different vibration periods we get the displacement and pseudo-acceleration response spectrums:

$$S_d(T,\zeta) = max|u(t,T,\zeta)| \tag{1.27}$$

$$S_a(T,\zeta) = max|\omega^2 u(t,T,\zeta)| = \omega^2 S_d(T,\zeta) \tag{1.28}$$

where $S_d(T,\zeta)$ and $S_a(T,\zeta)$ are respectively the spectral displacement and pseudo-acceleration of a system having a period T and a damping ratio ζ.

If the purpose of the dynamic analysis is only to find maximum displacements and return forces applied on the system, displacement or pseudo-acceleration response spectrums are enough and there is no need for having the applied base acceleration as a function of time (base excitation accelerogram) $\ddot{u}_g(t)$.

In general, the structure, a MDOF system, is decoupled into vibration modes and each mode is analyzed separately to find the maximum modal response (base shear, support reactions, story drifts, internal forces and stresses). For the i^{th} vibration mode of the structure, the maximum displacement vector produced in the structure by this mode is given by:

$$\{U_{i\,max}\} = \{\emptyset_i\}q_{i\,max} = \{\emptyset_i\}\Gamma_i d_{i\,max} \tag{1.29}$$

The maximum modal displacement $d_{i\,max}$ is in fact the spectral displacement corresponding to the ith vibration mode $S_d(T_i, \zeta_i)$ so we get:

$$\{U_{i\,max}\} = \{\emptyset_i\}\Gamma_i S_d(T_i, \zeta_i) \tag{1.30}$$

The maximum acceleration vector of the structure by this mode $\{\ddot{U}_{i\,max}\}$ is given by:

$$\{\ddot{U}_{i\,max}\} = \{\emptyset_i\}\ddot{q}_{i\,max} = \{\emptyset_i\}\Gamma_i \ddot{d}_{i\,max} \tag{1.31}$$

The maximum return force applied on the structure by this mode is given by:

$$\{F_{i\,max}\} = [K]\{U_{i\,max}\} = [K]\{\emptyset_i\}\Gamma_i S_d(T_i, \zeta_i) \tag{1.32}$$

or also by:

$$\begin{aligned}\{F_{i\,max}\} &= [M]{\omega_i}^2\{U_{i\,max}\} = [M]\{\emptyset_i\}\Gamma_i {\omega_i}^2 S_d(T_i, \zeta_i) \\ &= [M]\{\emptyset_i\}\Gamma_i S_a(T_i, \zeta_i)\end{aligned} \tag{1.33}$$

The base shear V_{bi} of the structure resulting from $\{F_{i\,max}\}$ is given by:

$$V_{bi} = M_i^* S_a(T_i, \zeta_i) \tag{1.34}$$

Knowing the maximum return force applied on the structure$\{F_{i\,max}\}$ and the corresponding base shear V_{bi}, we can calculate the support reactions, story drifts, internal forces and stresses corresponding to the ith vibration mode.

In seismic codes, the pseudo-acceleration response spectrums are defined according to site characteristics (seismic zone, soil type …) and are not based on a single specific accelerogram. In fact, these pseudo-acceleration response spectrums are the envelope spectrums of many real potential base excitation accelerograms and are constructed by a statistical analysis carried on these probable base excitations. Generally, the pseudo-acceleration response spectrums defined in seismic codes feature the same overall shape (refer to Figure 1.3). Firstly, for low periods we have a linear variation of the spectral acceleration. Then a constant maximum spectral acceleration branch is considered. After that, the spectral acceleration starts decreasing proportionally to $1/T$ and this decrease becomes proportional to $1/T^2$ in the final branch (which is equivalent to a constant spectral displacement branch).

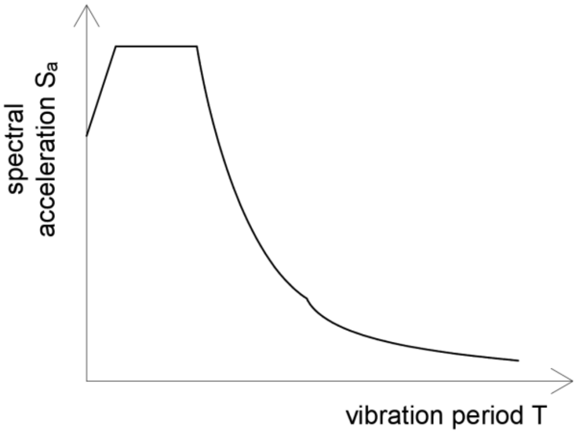

Figure 1.3: Typical pseudo-acceleration response spectrum.

Generally, only important modes are considered, usually these are the first vibration modes, to reach a total effective modal mass equal to 90% of the total structural mass in the direction of vibration. It should be noted that maximum responses of vibration modes do not occur simultaneously. Therefore, to obtain the maximum response of the full structure, special modal combinations are used to add the maximum modal response obtained at each important vibration mode. Many modal combination techniques are available, the most famous being the Square Root Sum of the Squares (SRSS) and the Complete Quadratic Combination (CQC). For further information on modal combinations refer to (Chopra, 2017, 2021).

1.4. Linear time history analysis

Time history analysis is used to determine the structural dynamic response in function of time. Therefore, response spectrums are useless for this type of analysis since they only provide maximum responses. Instead, the structure should be subjected to a base excitation with a well-defined record of acceleration as a function of time (accelerogram). The main concern in using the time history analysis is its high computational cost, especially when applied in structural seismic analysis as the structure is then subjected to dynamic excitations at its base. These excitations are generally based on the accelerograms of previously recorded quakes in the region. In order to cover all probable scenarios, the structure should be subjected to multiple accelerograms vibrating in all different directions which greatly increases the time cost of this analysis technique. Multiple time history analysis techniques are available and will be briefly presented hereafter.

1.4.1. Modal time history analysis

As its name indicates, the modal time history analysis consists in decoupling the MDOF elastic linear structure into SDOF vibration modes. Then the dynamic equation of each vibration mode is solved separately and thus the dynamic response in function of time of the corresponding vibration mode is obtained. Only important vibration modes can be considered (satisfying the 90% effective modal mass criteria) and the total dynamic response of the system corresponds to the summation of the dynamic responses of each important vibration mode.

1.4.2. Direct time integration analysis

In this approach, temporal discretization is considered and the direct time-integration is conducted over time steps using implicit methods like Newmark-β (Newmark, 1959), Wilson θ (Wilson, 1968), Houbolt (Houbolt, 1950), HHT-α (Hilber, Hughes and Taylor, 1977), WBZ- α (Wood, Bossak and Zienkiewicz, 1980), CH- α (Chung and Hulbert, 1993) and HP-θ_1 (Hoff and Pahl, 1988a, 1988b) or explicit methods like central difference and Runge-Kutta. To determine the dynamic response of a given system at time t_i, implicit time-integration techniques use the dynamic equation at time t_i whereas explicit techniques are based on the dynamic equation at a different time.

1.4.2.1. Implicit analysis

The Newmark-β method (Newmark, 1959) is one of the most famous and widely used implicit direct integration time history analysis in structural dynamics. It consists in assuming a variation pattern for the acceleration vector between time t_i and t_{i+1}. This allows to establish the following relations between the dynamic responses at time t_i and t_{i+1}:

$$\{\dot{U}(t_{i+1})\} = \{\dot{U}(t_i)\} + (1-\gamma)\Delta t\{\ddot{U}(t_i)\} + \gamma\Delta t\{\ddot{U}(t_{i+1})\} \tag{1.35}$$

$$\begin{aligned}\{U(t_{i+1})\} = \{U(t_i)\} + \Delta t\{\dot{U}(t_i)\} + (0.5-\beta)\Delta t^2\{\ddot{U}(t_i)\} \\ + \beta\Delta t^2\{\ddot{U}(t_{i+1})\}\end{aligned} \tag{1.36}$$

where Δt is the calculation time step, γ and β are parameters corresponding to the assumed acceleration variation pattern ($\gamma = 1/2$ & $\beta = 1/4$ for constant average acceleration pattern and $\gamma = 1/2$ & $\beta = 1/6$ for linear variation of acceleration).

Using relations (1.35) and (1.36), it can be shown that the dynamic equation at time t_{i+1}:

$$[M]\{\ddot{U}(t_{i+1})\} + [C]\{\dot{U}(t_{i+1})\} + [K]\{U(t_{i+1})\} = \{F(t_{i+1})\} \tag{1.37}$$

is equivalent to:

$$\{\hat{F}(t_{i+1})\} = [\hat{K}]\{U(t_{i+1})\} \tag{1.38}$$

where

$$[\hat{K}] = [K] + \frac{\gamma}{\beta\Delta t}[C] + \frac{1}{\beta\Delta t^2}[M] \tag{1.39}$$

and

$$\begin{aligned}\{\hat{F}(t_{i+1})\} = \{F(t_{i+1})\} &+ \left(\frac{1}{\beta\Delta t^2}[M] + \frac{\gamma}{\beta\Delta t}[C]\right)\{U(t_i)\} \\ &+ \left(\frac{1}{\beta\Delta t}[M] + \left(\frac{\gamma}{\beta} - 1\right)[C]\right)\{\dot{U}(t_i)\} \\ &+ \left(\left(\frac{1}{2\beta} - 1\right)[M] + \left(\frac{\gamma}{2\beta} - 1\right)\Delta t[C]\right)\{\ddot{U}(t_i)\}\end{aligned} \tag{1.40}$$

Knowing the dynamic response at time t_i, $[\hat{K}]$ and $\{\hat{F}(t_{i+1})\}$ are determined respectively by equations (1.39) and (1.40) Then, solving equation (1.38) will give $\{U(t_{i+1})\}$ and by recurring to equations (1.35) and (1.36) $\{\dot{U}(t_{i+1})\}$ and $\{\ddot{U}(t_{i+1})\}$ are determined respectively. As a result, the dynamic response is obtained at time t_{i+1} and now can be used for calculations at time t_{i+2} and so on.

It should be noted that Newmark-β method is unconditionally stable only when a constant average acceleration pattern is considered ($\gamma = 1/2$ & $\beta = 1/4$). For all other cases, the following stability condition should be respected:

$$\Delta t < \frac{T_{min}\sqrt{2}}{2\pi\sqrt{\gamma - 2\beta}} \tag{1.41}$$

where T_{min} is the smallest natural period of vibration for the system under consideration.

1.4.2.2. Explicit analysis

The central difference method is one of the most commonly used explicit direct integration time history analysis in structural dynamics. It is based on the finite difference approximation in the calculation of the velocity and acceleration vectors, i.e. at a given time t_i.

$$\{\dot{U}(t_i)\} = \frac{1}{2\Delta t}(\{U(t_{i+1})\} - \{U(t_{i-1})\}) \tag{1.42}$$

$$\{\ddot{U}(t_i)\} = \frac{1}{\Delta t^2}(\{U(t_{i+1})\} - 2\{U(t_i)\} + \{U(t_{i-1})\}) \tag{1.43}$$

Using equations (1.42) and (1.43), the dynamic equation at time t_i:

$$[M]\{\ddot{U}(t_i)\} + [C]\{\dot{U}(t_i)\} + [K]\{U(t_i)\} = \{F(t_i)\} \tag{1.44}$$

can be rearranged to get the following form:

$$\{\hat{F}(t_i)\} = [\hat{K}]\{U(t_{i+1})\} \tag{1.45}$$

where

$$[\hat{K}] = \frac{1}{\Delta t^2}[M] + \frac{1}{2\Delta t}[C] \tag{1.46}$$

and

$$\begin{aligned}\{\hat{F}(t_i)\} = \{F(t_i)\} - \left(\frac{1}{\Delta t^2}[M] - \frac{1}{2\Delta t}[C]\right)\{U(t_{i-1})\} \\ - \left([K] - \frac{2}{\Delta t^2}[M]\right)\{U(t_i)\}\end{aligned} \tag{1.47}$$

Knowing $\{U(t_{i-1})\}$ and $\{U(t_i)\}$, $[\hat{K}]$ and $\{\hat{F}(t_i)\}$ are determined respectively by equations (1.46) and (1.47). Then, solving equation (1.45) will give $\{U(t_{i+1})\}$. Now $\{U(t_i)\}$ and $\{U(t_{i+1})\}$ can be used for calculating $\{U(t_{i+2})\}$ and so on. For determining velocity and accelerations vectors, equations (1.42) and (1.43) can be used respectively.

The central difference approach is conditionally stable and the following stability condition should always be respected:

$$\Delta t < \frac{T_{min}}{\pi} \tag{1.48}$$

Due to this conditional stability, the central difference method generally requires a smaller time step than the constant average acceleration Newmark-β method.

1.5. Pushover analysis

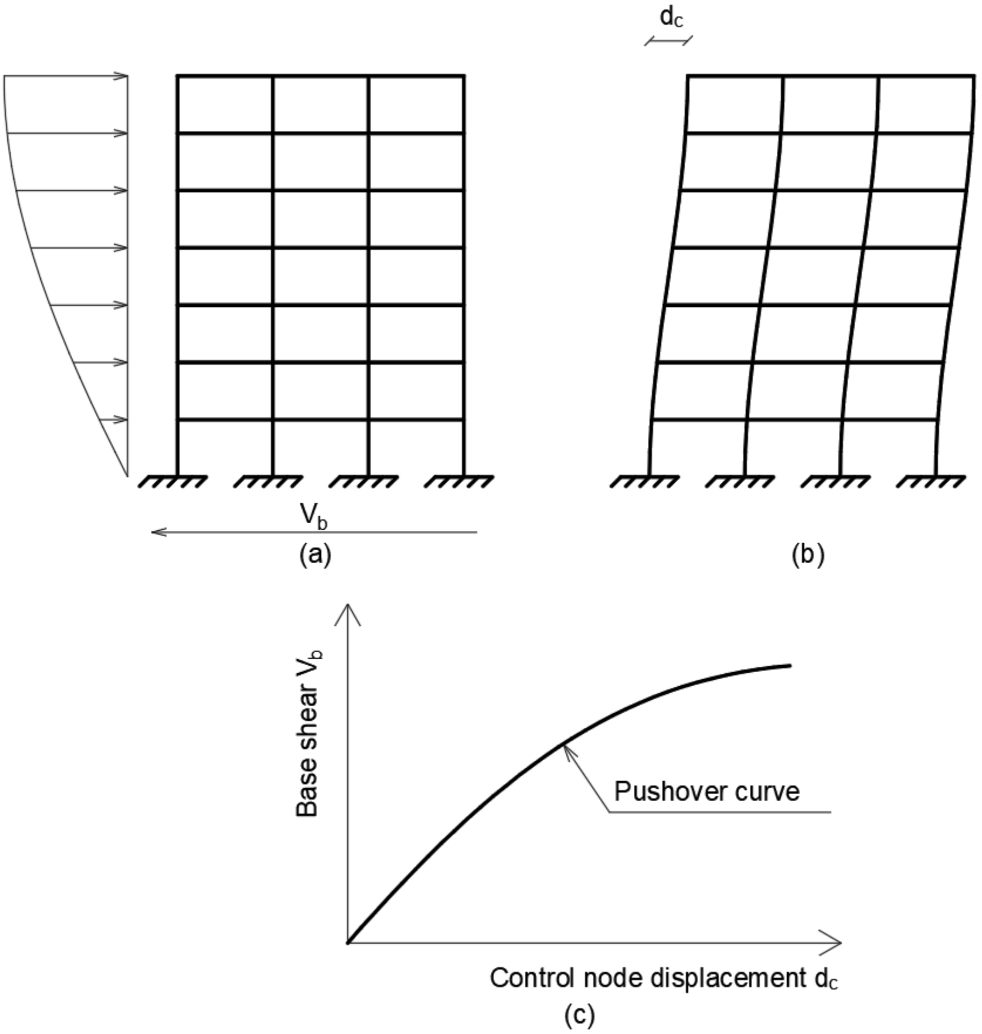

Figure 1.4: Pushover analysis: (a) Lateral load on the structure; (b) Control node displacement; (c) Pushover curve.

Pushover is a static nonlinear analysis consisting of progressively increasing lateral loads on a structure according to a predefined load pattern distribution while considering material and geometrical nonlinearities. At each calculation step, the base shear is calculated and plotted versus the displacement of a “control node” (generally it is a point on the top of the structure adopted for monitoring horizontal displacement). The resulting curve is called the pushover curve (refer to Figure 1.4) and is used in conjunction with an adequate seismic response spectrum to determine the maximum structural response under earthquake loading.

1.5.1. Calculation of the pushover curve

The first step in the pushover curve calculation is to define the load pattern according to which the horizontal load will be progressively increased. Many options, regulated by seismic codes such as (FEMA 356, 2000; EC8-1, 2004; FEMA 440, 2005), are available:

- Distribution proportional to the structural mass (included in seismic analysis) and the fundamental translational mode shape in the considered horizontal direction of the analysis
- Distribution according to the following formula:

$$F_i = V_b \frac{M_i h_i^k}{\sum_{j=1}^{n} M_j h_j^k} \tag{1.49}$$

where V_b is the base shear (total lateral force) that should be distributed on the stories, F_i is the lateral force applied on the ith story, M_i and h_i are respectively the mass and height (measured from ground level) of the ith story. k is the shape parameter, for $k = 1$ or 2 or 3 the load pattern is respectively uniform or linear or parabolic (refer to Figure 1.5).

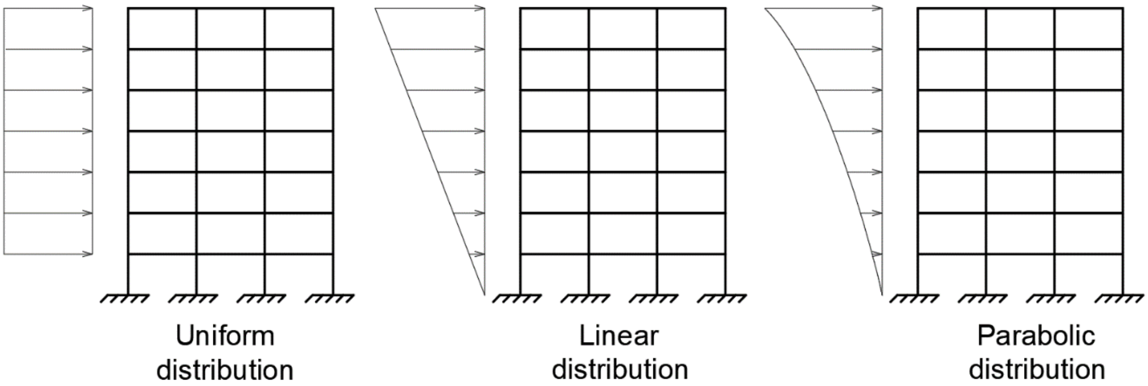

Figure 1.5: Pushover load patterns.

As for any nonlinear seismic analysis, the location and behavior of material nonlinearity should be defined. In fact, giving all structural elements the potential to undergo nonlinear material deformations is very time-consuming during analysis. For this reason, in nonlinear seismic analysis, material nonlinearity is supposed to occur only at predefined locations. Generally, these locations are the most stressed parts in the structure during an earthquake: beams and columns ends at lower stories for frame resisting structures and wall elements at lower stories for wall resisting structures. The most commonly used nonlinear model in pushover analysis is the concentrated plastic hinge and will be illustrated in chapter 2. Geometrical nonlinearities such as the $p-\Delta$ effect and large displacements can also be considered in the pushover analysis.

The model is then pushed progressively while conducting nonlinear calculations until reaching either base shear force limit, a displacement limit or structural collapse. Nonlinear solving techniques such as Newton-Raphson and displacement control can be used for that purpose (for further information on nonlinear calculations, refer to Appendix A). The pushover curve is obtained by plotting the base shear as a function of the control node's displacement. It is also called capacity curve since it represents the structural capacity to resist lateral loads.

1.5.2. Determination of the performance point

After calculating the structural capacity, the seismic demand should be determined. This demand is represented by the pseudo-acceleration response spectrum generally defined by seismic codes in function of zone seismicity and soil type. In order to determine the maximum response of the structure due to seismic loads, a search for a balance point called "performance point" is conducted. This point balances between the structural capacity (pushover curve) and the seismic demand (pseudo-acceleration response spectrum). However, the pushover curve is expressed as a force versus displacement curve and the pseudo-acceleration response spectrum is in the form of pseudo-acceleration versus vibration period. To overcome this issue, a common reference called Acceleration Displacement Response Spectrum (ADRS) is used. This reference has spectral displacement and spectral acceleration respectively on its abscissa and ordinate axis (refer to Figure 1.6). To convert the capacity spectrum to ADRS form, the structure is assumed to respond quasi-totally along its fundamental vibration mode. Then, the spectral acceleration corresponding to the base shear is calculated via equation (1.34) and the spectral displacement corresponding to the control node displacement is obtained via equation (1.30). To convert the demand spectrum into ADRS form, equation (1.28) is used for calculating the equivalent spectral displacement.

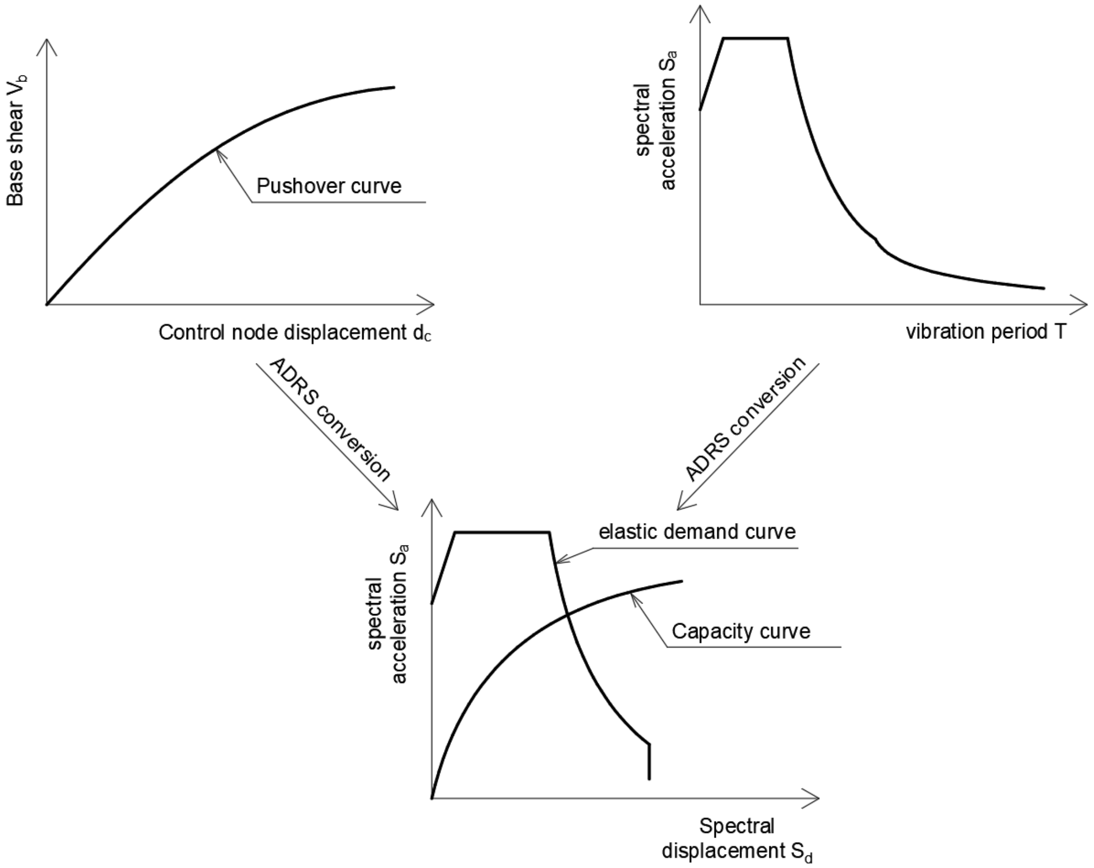

Figure 1.6: ADRS conversion

It should be noted that the demand curve represents the seismic demand for a linear elastic structure with 5% viscous damping ratio for reinforced concrete structures. However, when the structure undergoes nonlinear deformation the overall damping in the structure increases due to hysteretic energy dissipation. Therefore, the elastic 5% damped demand curve does not apply anymore on the plasticized structure (refer to Figure 1.7).

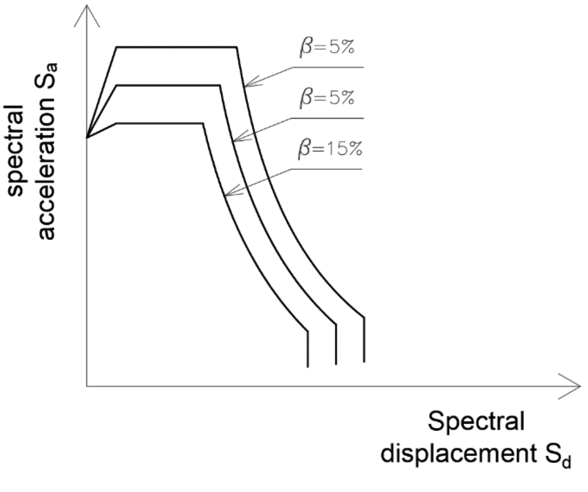

Figure 1.7: Effect of damping on demand curve.

In fact, a reduced demand curve taking into account the damping increase represents now the current seismic demand on the plasticized structure. For a specific point on the capacity curve, the reduced demand curve corresponding to the plastic state at this point is calculated. If this reduced demand curve intersects the capacity curve at this specific point, then this point is the sought performance point that balances between the structural capacity and seismic demand.

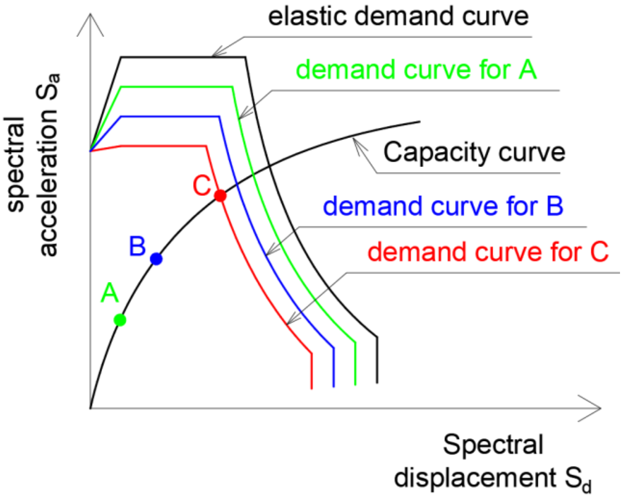

Figure 1.8: Identification of the performance point.

By referring to Figure 1.8, the demand curve corresponding to the plastic state of point A does not intersect the capacity curve at this point so it is not the performance point and same for point B. However, the demand curve corresponding to the plastic state of point C intersects the capacity curve at point C so it is the sought performance point. The search for the performance point is done by trial and error and it should be noted that for the case when the structure cannot meet the demand of the earthquake a performance point cannot be found, in other words the seismic loads cause structural collapse. Based on this search concept, seismic codes present many techniques for calculating the performance point. The most common are the N2 method used in (EC8-1, 2004) and the Capacity Spectrum Method (CSM) presented in (ATC 40, 1996).

Once the performance point is found, its spectral displacement is converted to real displacement via equation (1.30). This is the maximum displacement of the control node that will occur during earthquake, so the structure is pushed and studied until this level of displacement. The pushover analysis provides, in a step-by-step manner, the location and degree of plasticization in structural elements which is essential for a performance-based design, in addition to giving information on the progressive collapse of structures in extreme cases. Furthermore, this analysis can provide the exact reduction factor R of equation (1.2) for each structural element or the entire structure.

The pushover analysis is a modal spectral nonlinear analysis conducted only for the fundamental vibration mode while considering the hysteretic damping effect on the seismic response spectrum. It is criticized for using elastic linear modes in nonlinear analysis and for considering only the fundamental mode of vibration which limits its application to regular structures. In addition, the load pattern is considered to remain identical throughout the whole analysis which is not the case when material nonlinear deformations occur. Researchers tried overcoming some of these limitations, (Bracci, Kunnath and Reinhorn, 1997; Atik, Sadek and Shahrour, 2013) worked on the adaptive pushover analysis which consists in modifying the load pattern at each step by taking into account the nonlinear deformations occurring in the structure. (Chopra and Goel, 2002) tried solving the single mode limitation by introducing the Modal Pushover Analysis (MPA) in which separate pushover analyses are conducted for each important vibration mode and the total result is obtained by modal combination.

1.6. Nonlinear direct time integration analysis

Nonlinear time history analysis is more complicated than the linear one due to the fact that the system’s stiffness matrix is no longer constant over time. In fact, material and geometrical nonlinearities are continuously changing the system’s stiffness matrix. As a consequence, the term tangent stiffness matrix is introduced $[K_T(\{U(t)\})]$ which represents the stiffness matrix at displacement $\{U(t)\}$. The time history analysis was already computationally expensive for linear systems, now with the changing stiffness matrix and nonlinear calculations this analysis becomes a lot more time consuming, especially when multiple base excitations in different directions are considered. The classical modal analysis is no longer applicable since it requires a constant stiffness matrix for modal calculations. The only available approach is the nonlinear direct integration time history analysis. Similarly to the linear analysis, temporal discretization is considered and the direct time-integration is conducted on time steps using implicit or explicit methods. The difference here is that the stiffness matrix is no longer constant and a nonlinear calculation is conducted at each time step.

1.6.1. Implicit nonlinear analysis

The famous implicit Newmark-β method (Newmark, 1959) is applicable for nonlinear analysis. Due to material and/or geometrical nonlinearities, the nonlinear internal force of the system also known as return force $\{F_{NL}(t_{i+1})\}$ at time t_{i+1} is a nonlinear function of the displacement vector $\{F_{NL}(\{U(t_{i+1})\})\}$ and the dynamic equation of the system becomes:

$$[M]\{\ddot{U}(t_{i+1})\} + [C]\{\dot{U}(t_{i+1})\} + \{F_{NL}(\{U(t_{i+1})\})\} = \{F(t_{i+1})\} \tag{1.50}$$

This nonlinear dynamic equation is generally solved at each time step by the Newton-Raphson method, which consists in an iteratively look for an approximation of the solution (for further details, refer to Appendix A).

1.6.2. Explicit nonlinear analysis

The explicit central difference method is applicable for nonlinear analysis and is simpler to use than implicit approaches. In fact, determining the state of the system at time t_{i+1} is based on the dynamic equation at time t_i.

$$[M]\{\ddot{U}(t_i)\} + [C]\{\dot{U}(t_i)\} + \{F_{NL}(\{U(t_i)\})\} = \{F(t_i)\} \tag{1.51}$$

The only required nonlinear calculation is the return force $\{F_{NL}(\{U(t_i)\})\}$ and since $\{U(t_i)\}$ is known, it can be calculated directly without the need for an iterative procedure. By applying the central difference approach, equation (1.51) becomes:

$$\{\hat{F}(t_i)\} = [\hat{K}]\{U(t_{i+1})\} \tag{1.52}$$

where

$$\begin{aligned}\{\hat{F}(t_i)\} = \{F(t_i)\} - \left(\frac{1}{\Delta t^2}[M] - \frac{1}{2\Delta t}[C]\right)\{U(t_{i-1})\} \\ + \left(\frac{2}{\Delta t^2}[M]\right)\{U(t_i)\} - \{F_{NL}(\{U(t_i)\})\}\end{aligned} \tag{1.53}$$

and

$$[\hat{K}] = \frac{1}{\Delta t^2}[M] + \frac{1}{2\Delta t}[C] \tag{1.54}$$

Equation (1.52) is solved linearly and $\{U(t_{i+1})\}$ can be used for calculating $\{U(t_{i+2})\}$ and so on. To evaluate the velocity and accelerations vectors, equations (1.42) and (1.43) can be used respectively. Despite being simpler than implicit methods, the main issue for the central difference approach remains its conditional stability.

1.7. Conclusions

In this chapter, a large variety of seismic analysis techniques in structural engineering were presented. In linear approaches, the equivalent lateral force method is the simplest to use but is only applicable to regular structures and limited to maximum response. The modal spectral analysis provides the maximum structural response for any type of structures. Model time history analysis and linear direct integration time history analysis are capable of calculating the time-dependent dynamic response of the structure but at a higher computational cost. It is obvious that linear analyses (especially for the techniques providing only maximum responses) are much less time consuming than nonlinear analyses. However, representing the materials ductility of the entire structure with a single reduction factor applied on all seismic loads is a very rough estimation.

On the other hand, nonlinear analyses provide information regarding the location and values of nonlinear deformations in the structure. In addition, loads redistribution in the structure due to nonlinear deformations is computed and geometrical nonlinearities can be considered. The pushover analysis provides only the maximum response and is solely applicable to regular structures. Due to these limitations, the technique remains a complementary tool that is used after the linear seismic design to check for nonlinear deformation locations and degree of plasticization. On the other hand, the nonlinear direct integration time history analysis is applicable to all structures and provides a time-dependent response but at an extremely high computational cost (refer to Figure 1.9).

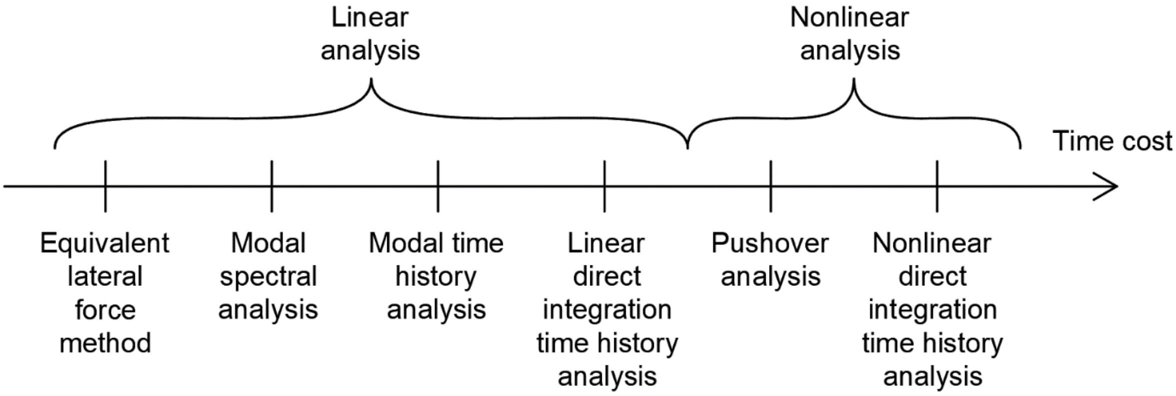

Figure 1.9: Time cost scale for seismic analysis techniques.

The contribution of this thesis is to propose a reduced dynamic model that maintains the advantages of the nonlinear direct integration time history analysis while reducing the time cost.

Chapter 2

2. Structural models with material nonlinearities

Abstract: *The prediction of the nonlinear dynamic response of reinforced concrete structures under seismic excitations requires a structural Finite Element (FE) model with material nonlinearities adapted to seismic analysis. In structural engineering, the most common elements are unidimensional (beams, columns ...) and superficial (walls, slabs ...). So, this chapter presents the classically used 1D and 2D structural models capable of incorporating material nonlinearities during seismic analysis. Arguments were provided for choosing multifiber section for line elements and layered membrane for surface elements. In addition, this chapter discusses the available nonlinear material constitutive models for concrete and reinforcing steel bars. Finally, simplified nonlinear material models were adopted since this thesis is more focused on the efficiency and accuracy of nonlinear model reduction techniques rather than material constitutive relations.*

Chapter content

2.1. Introduction

Generally, the most common structural elements (columns, beams, slabs, walls …) are discretized in 1D and 2D FE. For this reason, we are interested in 1D structural elements incorporating 1D nonlinear material behavior for beams and columns and 2D elements with biaxial nonlinearities for surface elements. The 1D nonlinear structural models are relatively simple, easy to implement in structural analysis softwares and computationally efficient. Consequently, they can be used for the analysis of large-scale structures. In this thesis, 1D nonlinear structural elements are used for modelling a multistory multispan reinforced concrete planar 2D frame.

On the other hand, the 2D nonlinear structural models require multidimensional material constitutive laws to predict the behavior of the elements. They are a very powerful tool for predicting local phenomena inside the structural element. However, due to their complexity, they require more computational time than the 1D approach and are thus limited to relatively simple small-scale structures. for this work, 2D nonlinear structural elements are used for modeling a small multistory planar reinforced concrete shear wall with in-plane behavior. In the following, the most commonly used 1D and 2D nonlinear structural models are presented. In addition, uniaxial and biaxial nonlinear material behavior of reinforced concrete is discussed.

2.2. Structural models

2.2.1. 1D structural models

2.2.1.1. Concentrated lumped plasticity

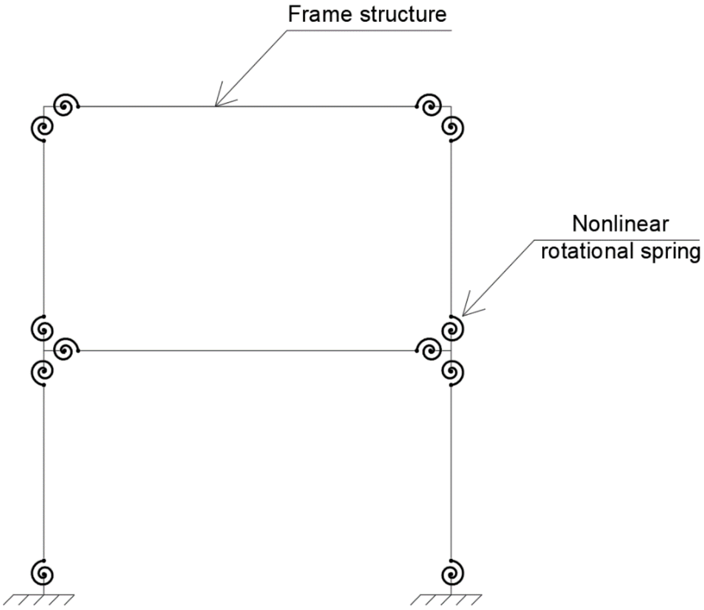

Figure 2.1: Concentrated plastic hinges in a frame structure.

In this approach, the plastic behavior of the structural member is represented by a concentrated zero length plastic hinge (nonlinear spring) (refer to Figure 2.1). The constitutive law of these springs is expressed in the form of moment-rotation curves for bending hinges and force-displacement curves for axial hinges. The concentrated plasticity approach is adopted in most seismic codes such as (FEMA 356, 2000; EC8-3, 2005) where the behavior curve of the hinges is determined in function of the structural element geometry, reinforcements, concrete confinement conditions and internal forces.

The first to introduce the concentrated plasticity modeling was (Clough and Johnston, 1966), his model was known as the parallel model and offered a bilinear moment rotation behavior curve. It was based on dividing the structural member into two parallel elements, one representing the yielding by an elastic perfectly plastic behavior and the other representing the strain hardening by a perfectly elastic behavior. (Giberson, 1967) proposed the series model in which the structural element was modeled as a linear behaving element with zero length nonlinear springs located at its ends. (Clough and Benuska, 1967; Takeda, Sozen and Nielsen, 1970) models included stiffness degradation in plastic hinges due to cyclic loading. (Powell and Chen, 1986) studied the interaction between bending moments and axial forces in hinges. (Banon, Irvine and Biggs, 1981; Ibarra, Medina and Krawinkler, 2005) presented the pinching effect in hysteresis loops. (Otani, 1974; Filippou and Issa, 1988) included the fixed end rotation due to bond slip effect of steel reinforcements. Additional improvements are constantly being added to the hinge modeling such as in (Fajfar *et al.*, 2006; Scott and Fenves, 2006; Dolsek, 2010).

The concentrated plasticity approach is highly computationally efficient and can be used for complex structures. Furthermore, it is relatively simple to apply and has a large database in seismic codes. Consequently, this method is very popular in nonlinear material modeling for seismic analysis. However, the lumped plasticity approach is based on the assumption that plastic behavior occurs only at specified concentrated points of the structural member (which is a major simplification). In addition, interaction between bending moments and varying axial forces in dynamic analysis is not taken into account (the springs are calibrated based on the initial axial force only). Moreover, the nonlinear spring behavior curves provided by the seismic codes are based on rough estimations and assumptions which reduce their accuracy.

2.2.1.2. Fiber element model

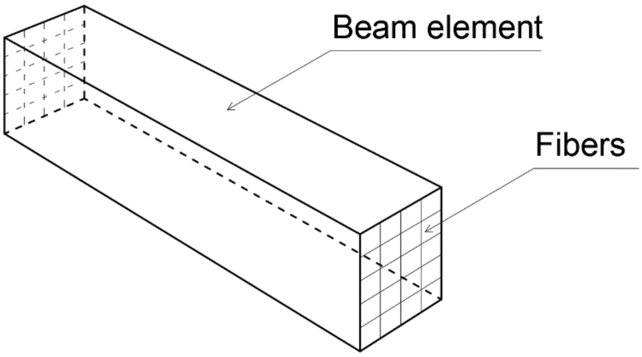

Figure 2.2: Multifiber beam element.

The fiber modeling also known as the multifiber approach consists in dividing the structural element cross section into a set of longitudinal fibers (refer to Figure 2.2). Each fiber is made up of a single material and has the potential of undergoing nonlinear inelastic longitudinal deformation according to the uniaxial stress-strain behavior of its corresponding material. The fiber element modeling is a distributed plasticity approach since material nonlinearity can occur anywhere along the fibers' length.

One of its earliest citing was by (Mark and Roesset, 1976; Owen and Hinton, 1980; Hellesland and Scordelis, 1981). Later on, it was presented in (Kaba and Mahin, 1984; Ciampi and Carlesimo, 1986) and numerically improved by (Zeris and Mahin, 1988). (Izzuddin, 1990) presented a comparison between lumped plasticity and fiber element modeling. (Taucer, Spacone and Filippou, 1991; Spacone, Filippou and Taucer, 1996) introduced an algorithm for fiber element modeling using flexibility based finite element formulation. (Neuenhofer and Filippou, 1997) made a comparison between force-based and displacement-based multifiber beam elements and proposed a bypass for the iterative calculation used for internal state determination in flexibility-based approach. (Kotronis and Mazars, 2005) adopted a continuous damage concrete model with multifiber beams based on Euler Bernoulli and Timoshenko formulations (stiffness based finite element). (Papaioannou, Fragiadakis and Papadrakakis, 2005) compared force-based and displacement-based multifiber beam elements and proposed multiple methods for the calculation of the stiffness matrix. To better calculate the interaction between axial force and bending moment, (Bitar, 2017) proposed a kinematic enrichment for a displacement-based enhanced multifiber element model while adopting the Timoshenko beam model.

Despite being more time consuming than the concentrated plasticity approach, the fiber element modeling is computationally efficient and can be used for modelling complex structures with non-typical cross sections. Moreover, the interaction between bending moments and varying axial loads is taken into account by this modelling approach. Some works addressed the bond slip effect on fiber modeling such as (Monti and Spacone, 2000) and shear flexure interactions like (Petrangeli, Pinto and Ciampi, 1999; Mazars *et al.*, 2006; Ceresa *et al.*, 2009; Jiang and Kurama, 2010; Feng *et al.*, 2017). However, in practical seismic analysis, fiber element model considers a perfect bond between fibers (plane sections remain plane) plus shear and flexure modes are decoupled with the nonlinear behavior solely considered along the fiber’s longitudinal direction (1D nonlinearity).

In this thesis, the multifiber elements are used for modeling material nonlinearity in beams and columns. In fact, this modeling technique is more accurate than the concentrated plastic hinges, has a wide range of applicability and comes at an acceptable computational cost.

2.2.2. 2D structural models

2.2.2.1. Multiple Vertical Line Element Model (MVLEM)

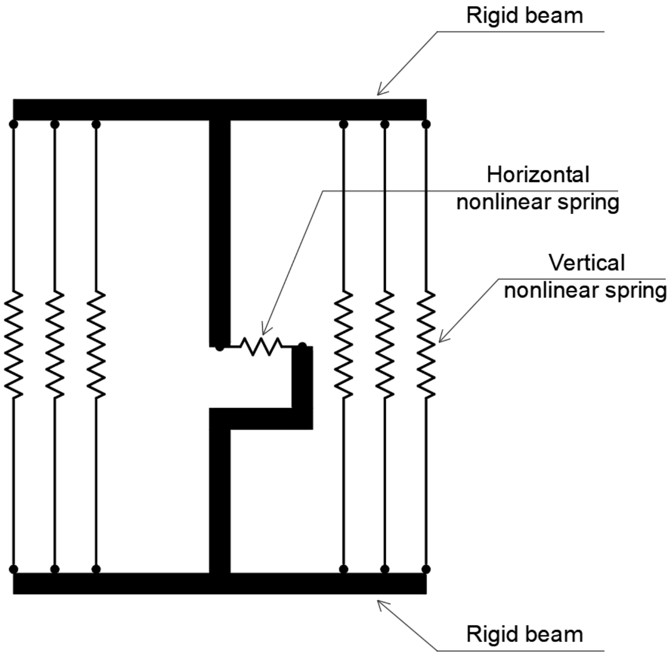

Figure 2.3: Multiple Vertical Line Element Model (MVLEM).

The MVLEM is used to model structural walls and was first proposed by (Vulcano, Bertero and Colotti, 1988). The flexural behavior of walls is represented by a set of vertical nonlinear springs connected to infinitely rigid beams at top and bottom levels whereas the shear behavior is represented by a horizontal nonlinear spring (refer to Figure 2.3). For the first proposed models, shear and flexure modes are uncoupled. (Fajfar and Fischinger, 1990) replaced single MVLEM with a stack of MVLEMs to increase the model's computability. (Fischinger, Isakovic and Kante, 2004) expanded the 2D MVLEM to a 3D bidirectional model suitable for T and H wall sections. (Fischinger, Rejec and Isaković, 2012; Kolozvari, Orakcal and Wallace, 2015) developed a fiber based MVLEM with nonlinear shear-flexure interaction. Despite the fact that extensive research has been conducted on MVLEM, this modeling technique is not widely spread in computer programs. Fiber based wall elements inspired from the MVLEM are more commonly used.

2.2.2.2. Layered membrane model

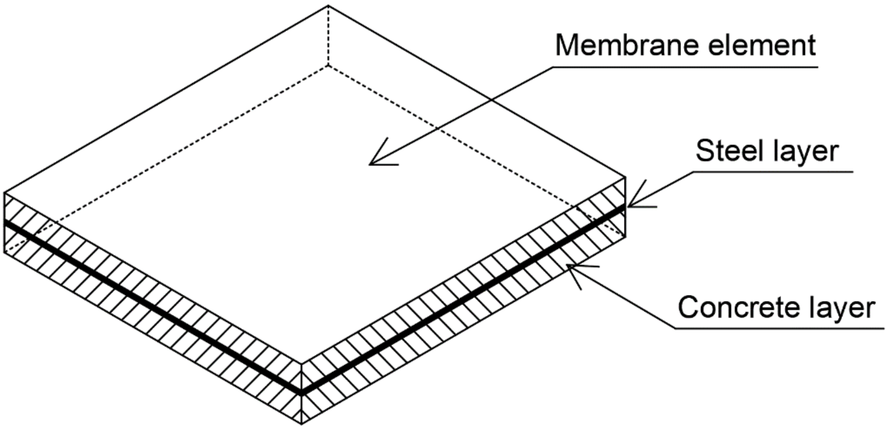

Figure 2.4: Layered membrane element.

In this approach, structural members are modeled as planar membrane elements with in-plane behavior. This membrane finite element is considered to have only 2 degrees of freedom per node corresponding to in plane translations. The structural element is divided into layers along its thickness. Each layer is made up of a single material, steel rebars are considered to be distributed homogeneously and are represented by an equivalent steel layer working uniaxially in the direction of reinforcements (refer to Figure 2.4). In practical seismic analysis models, layers are considered perfectly bonded together and no slipping is allowed. 2D nonlinear constitutive laws are considered for concrete layers and 1D laws for steel layers.

Early citations of the layered membrane approach were with (Cervenka, 1970; Cervenka and Gerstle, 1971, 1972). (Ibrahimbegović, 1993; Ibrahimbegović and Frey, 1993, 1995; Zouari, Hammadi and Ayad, 2016) worked on adding a rotational degree of freedom for RC membrane nodes while considering geometrical nonlinearity. (Rojas, 2012; Rebiai and Belounar, 2013; Rojas, Anderson and Massone, 2016) developed RC layered membrane elements with rotational degree of freedom at nodes while considering nonlinear material behavior. (Kaufmann and Marti, 1998; Sato and Fujii, 2002; Foster and Marti, 2003; Cerioni *et al.*, 2008; Huguet *et al.*, 2017) considered the bond slipping effect in RC membrane elements. In parallel, lot of research was conducted on reducing the computational cost of concrete 2D constitutive laws. In fact, (Darwin and Pecknold, 1974, 1977a, 1977b) introduced the equivalent uniaxial strains concept for concrete orthotropic models. This concept allowed the decoupling of the concrete 2D behavior into two uniaxial stress-strain curves (one for each principal direction) that account for the 2D interaction. Due to their balance between accuracy and time cost, the orthotropic concrete models based on the equivalent uniaxial strains concept are widely used for structural analysis. Some examples of such models can be found in (Ayoub and Filippou, 1998; Foster and Marti, 2003; Cerioni *et al.*, 2008) who worked on 2D orthotropic concrete models.

The layered membrane approach has the advantage of capturing the two-dimensional nonlinear behavior of composite membrane elements while considering the axial-shear coupling. However, the layered membrane model is computationally demanding, thus limiting its use to relatively small-scale structures.

2.2.2.3. Layered shell model

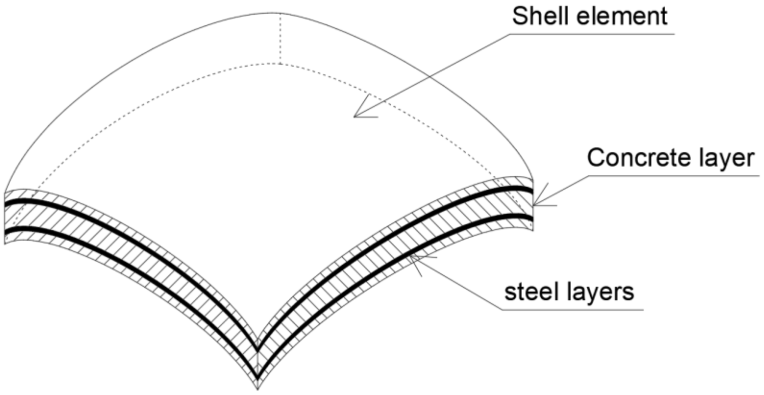

Figure 2.5: Layered shell element.

The layered shell approach is used for capturing both the in-plane and out of plane behavior of structural members. Similarly to the previous approach, the structural element is divided into layers along its thickness and material nonlinearity is expressed in the same way (refer to Figure 2.5). Early citings of the layered shell modelling were with (Hand, Pecknold and Schnobrich, 1972; Schnobrich, 1977). Later on, this topic was addressed by (Scordelis and Chan, 1987; Barzegar, 1988; Massicotte, MacGregor and Elwi, 1990; Hu and Schnobrich, 1991). (Polak and Vecchio, 1993) considered both material and geometrical nonlinearities for RC layered shell. (Polak, 1998) used the layered shell element to predict the failure of RC slabs by punching shear. (Zhang, Bradford and Gilbert, 2007) studied RC cylindrical shells and slabs using the layer approach while considering material and geometrical nonlinearities. (Gopinath *et al.*, 2012) examined the bond slip effect in RC layered shells. (Valoroso, Marmo and Sessa, 2014) considered the material nonlinearity while studying the coexistence of layered shell RC shear walls with frame elements present within the same structure. (Kim, Lee and Shin, 2002; Rojas, 2012; Rojas, Anderson and Massone, 2019) evaluated RC layered shell elements with drilling degrees of freedom while considering material nonlinearity.

The shell approach is the most complete 2D finite element model for capturing the shear walls' and slabs' behavior. However, this comes at a high computational cost. In fact, shell elements require more degrees of freedom than membrane elements. Also, in order to capture an accurate out of plane behavior, layered shell models require a discretization along their thickness finer than the one used for layered membrane. In other words, shell models require a larger number of layers than the membrane models do. In practical engineering, planar shear walls are considered to provide lateral resistance only along their strong direction, so a membrane finite element is sufficient. The shell element is only recommended for slabs and particular cases of shear walls with complex cross sections (T, C, L, I sections).

In this thesis, small planar shear walls with solely in plane behavior are studied while considering biaxial nonlinearity. Consequently, layered membranes are chosen for being the best fit for this work.

2.3. Reinforced concrete constitutive models

Determining the behavior of reinforced concrete elements requires a deep knowledge of their constitutive materials behavior. In fact, concrete and steel reinforcements are very different materials. Concrete is a brittle compressive material; under nonlinear deformations it dissipates energy by cracks formation and propagation. On the other hand, steel reinforcements are a ductile material that dissipates energy in nonlinear deformations by yielding. Luckily, these two materials have relatively close thermal expansion coefficients (in the order of $10^{-5}/°C$) which makes it possible to use them together as reinforced concrete and benefit from their qualities. In common engineering practices, concrete is used to resist compressive stresses while steel reinforcements resist tensile stresses and can also provide help for concrete in resisting compressive stresses. Large number of concrete and steel reinforcements constitutive models exist (Babu, Benipal and Singh, 2005; Abd El Fattah, 2012; Qi and Li, 2014).

Some researchers proposed to study homogenized Reinforced Concrete (RC) material with its constitutive model influenced by the steel and concrete present in it (Fan, 2012; Benakli *et al.*, 2020). In this work, since fibers and layers in the structural elements are made up each of unique material, RC homogenization will not be considered.

2.3.1. Concrete constitutive models

Modeling concrete behavior has always been an important research topic and lots of efforts are still being put in this subject today. The difficulty in this field is due to the complexity of the concrete material. Firstly, it is a nonsymmetrical material that behaves differently in compression and tension (tensile strength is generally around 10% of the compressive strength and is often neglected in engineering practices). Secondly, concrete cracking in tension redistributes the tensile stress previously carried by the concrete to the steel reinforcements. It should be noted that the concrete located between consecutive cracks continues to work partially in tension, this phenomenon is known as tension stiffening. In the case of cyclic loadings, when concrete cracks are closed by a reverse deformation, the previously cracked not working concrete is now capable of providing a compressive resistance. This difference in concrete behavior results in a continuous change, damaging and deterioration of the material stiffness under cyclic loading. Thirdly, triaxial effects should also be taken into account. They are evidenced by a reduction of concrete strength in one direction if the other perpendicular directions are subjected to tensile strains (this phenomenon is known as concrete softening) or by an increase in concrete strength and compressive failure strain due to concrete confinement by steel reinforcements (ex: stirrups, hoops…). In the following, the literature review is focused on uniaxial (1D) and biaxial (2D) concrete models adapted to the chosen structural elements.

2.3.1.1. Uniaxial concrete models

Due to triaxial stress effect, concrete strength and compressive failure strain increase as a result of the confinement provided by transversal steel reinforcements (ex: stirrups, hoops, spirals…). The improved characteristics of confined concrete are very appealing in seismic design (stronger and more ductile material) and for this reason most of seismic codes require additional confining reinforcements where structural nonlinear deformations are expected during earthquakes (i.e. extremities of beams and columns). (Richart, Brandtzaeg and Brown, 1928, 1929) were among the first to propose a concrete model that takes into account the confinement effect. (Roy and Sozen, 1965; Kent and Park, 1971) studied concrete confined by rectangular transverse ties. In their stress-strain models the confined concrete had an increased ductility but with no enhancement in maximum strength. (Sargin, 1971; Park, Priestley and Gill, 1982; Scott, Park and Priestley, 1982) considered the ductility increase in addition to the enhancement of maximum strength in their models. (Popovics, 1973) studied the effect of concrete age on the stress-strain model. (Mander, 1983; Mander, Priestley and Park, 1988) developed a general confined concrete stress-strain model applicable for circular or rectangular cross sections with any type of transversal confinement reinforcements and subjected to static or dynamic loadings. (Cusson and Paultre, 1995) noticed that in some cases confined concrete failure occurred prior to the yielding of confinement reinforcements so they studied the stress-strain model based on the actual effective stress in the transversal confinement reinforcements instead of yielding stress. (Razvi and Saatcioglu, 1999; Mendis, Pendyala and Setunge, 2000) worked on high strength concrete stress-strain models. (Torre-Casanova *et al.*, 2013) studied the confinement effect on the steel-concrete bond strength. In the last two decades research was more focused on the behavior of the Fiber Reinforced Polymer (FRP) confined concrete such as the work of (Harajli, 2006; Lam and Teng, 2009; Li *et al.*, 2018). For more details on concrete models, the thesis of (Abd El Fattah, 2012) provides a well-structured chronological detailed presentation of confined concrete stress-strain models.

When concrete is subjected to a relatively intense cyclic loading, material nonlinear behavior is triggered and a damaging phenomenon (stiffness degradation) is observed during the hysteresis cycles. In addition to a certain plasticity behavior is due to confinement steel effect (Refer to Figure 2.6).

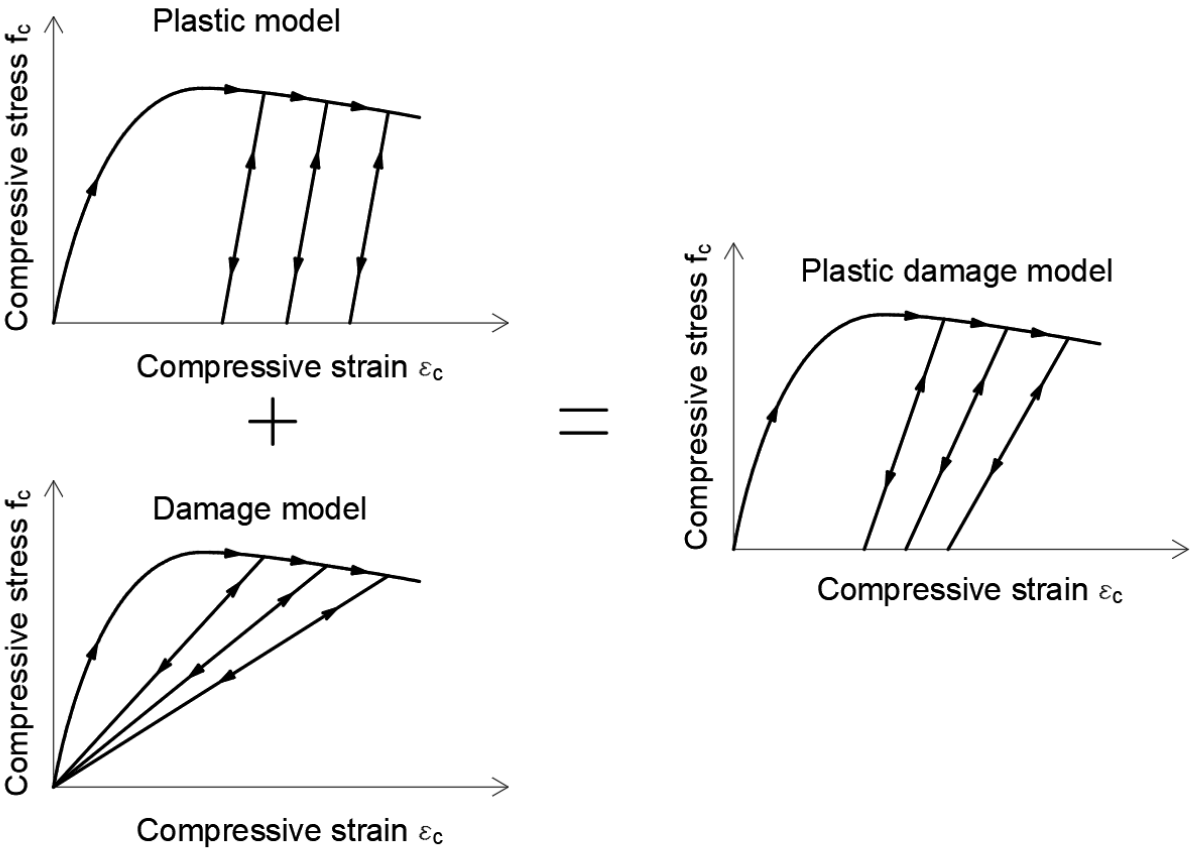

Figure 2.6: Concrete plastic damage model.

(Sinha, Gerstle and Tulin, 1964) were among the first to study the concrete damaging under cyclic loading. (Karsan and Jirsa, 1969) conducted several tests and concluded that the concrete response depends on the previous loading history and the number of loading cycles conducted. (Yankelevsky and Reinhardt, 1987) developed a concrete model for random cyclic loading. (Mander, Priestley and Park, 1988) introduced the confinement effect on concrete response to reversal loading. (Bahn and Hsu, 1998) proposed a general cyclic concrete model based on parametric studies and experimental investigations. (Sima, Roca and Molins, 2008) studied stiffness degradation of concrete for both compression and tensile cyclic loadings, their work has been modified by (Breccolotti *et al.*, 2015) to improve the damage accumulation strategy.

In this thesis, the (Mander, Priestley and Park, 1988) concrete stress-strain model was considered due to its applicability to most cross sections and under various loading and confinement conditions.

According to the (Mander, Priestley and Park, 1988) model, the uniaxial backbone stress–strain curve of confined concrete in compression is:

$$f_c = \frac{f'_{cc} x r}{r - 1 + x^r} \tag{2.1}$$

where f_c is the compressive stress of the confined concrete corresponding to a strain of ε_c, f'_{cc} is the compressive strength (maximum stress) of the confined concrete, r is defined as:

$$r = \frac{E_c}{E_c - E_{sec}} \tag{2.2}$$

and x as:

$$x = \frac{\varepsilon_c}{\varepsilon_{cc}} \tag{2.3}$$

with

$$\varepsilon_{cc} = \varepsilon_{co}\left[1 + 5\left(\frac{f'_{cc}}{f'_{co}} - 1\right)\right] \tag{2.4}$$

ε_{cc} is the confined concrete strain corresponding to the compressive strength f'_{cc}. Likewise, f'_{co} and ε_{co} are respectively the unconfined concrete compressive strength and its corresponding strain. E_c is the initial tangent modulus of elasticity of concrete (same value for confined and unconfined concrete) and is defined by:

$$E_c = 5000\sqrt{f'_{co}} \tag{2.5}$$

where E_c and f'_{co} are both expressed in MPa. $E_{sec}$is the secant modulus of elasticity corresponding to the maximum strength.

$$E_{sec} = \frac{f'_{cc}}{\varepsilon_{cc}} \tag{2.6}$$

The Mander concrete model can be used for unconfined concrete by simply considering $f'_{cc} = f'_{co}$ which results in $\varepsilon_{cc} = \varepsilon_{co}$ (refer to Figure 2.7). In addition, this concrete model takes into account the effect of strain rate on the backbone curve via a magnification factor. However, in this work the strain rate is not constant which makes it difficult to take into consideration, therefore its effect was neglected.

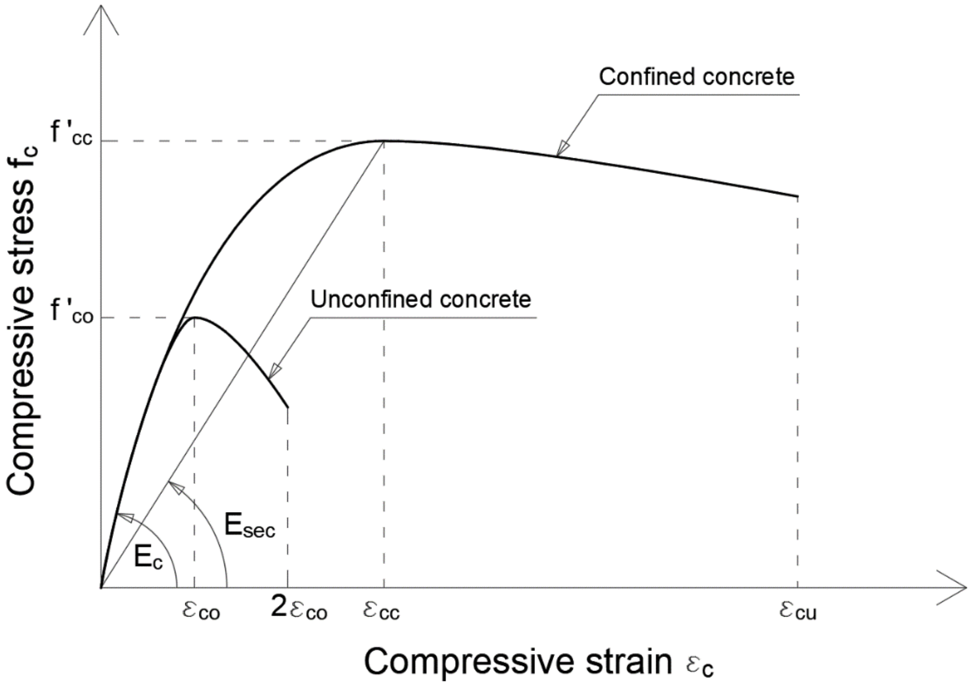

Figure 2.7: Uniaxial stress-strain backbone curves for confined and unconfined concrete according to Mander model.

f'_{cc} and consequently ε_{cc} are affected by the confining pressure created by the transversal steel reinforcements. For structural elements with circular cross section confined by circular hoops or spirals, the lateral pressure from the transverse reinforcements f_l is considered to be uniformly distributed all over the circumference of the confining steel. It can be demonstrated that:

$$f_l = \frac{1}{2}\rho_s f_{yh} \tag{2.7}$$

where f_{yh} is the yield strength of the transverse reinforcements and ρ_s is the ratio of transverse confining steel volume over the confined concrete volume.

$$\rho_s = \frac{A_{sp}\pi d_s}{\frac{\pi}{4}d_s^2 s} = \frac{4A_{sp}}{d_s s} \tag{2.8}$$

where A_{sp} is the area of the transverse reinforcement bar, s is the center to center spacing of circular hoops or the pitch of circular spiral and d_s is the diameter of circular hoops or spiral measured from bar center line (refer to Figure 2.8).

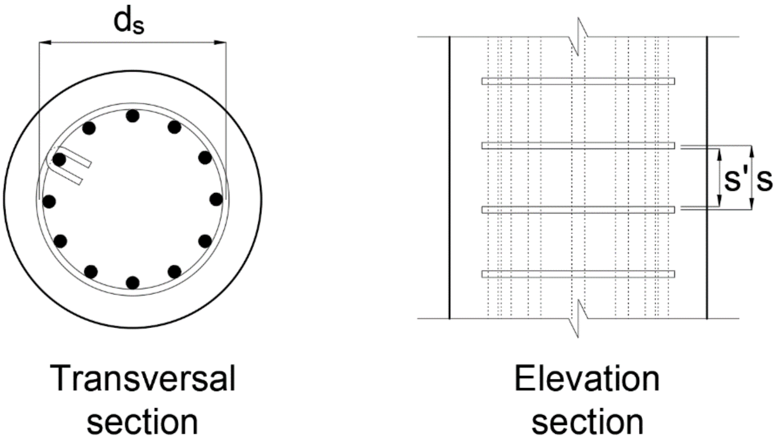

Figure 2.8: Confined concrete in a structural element with circular cross section.

Since transverse reinforcements are spaced apart in elevation, the confinement effect cannot be considered to be the same all along the elevation. In other words, the confinement at hoops level is not the same as the one at mid midway height between hoops. To take this in consideration, an effective lateral confining pressure f_l' is considered.

$$f_l' = k_e f_l = \frac{1}{2} k_e \rho_s f_{yh} \tag{2.9}$$

where k_e is the confinement effectiveness coefficient and is given by:

$$k_e = \begin{cases} \dfrac{\left(1 - \dfrac{s'}{2d_s}\right)^2}{1 - \rho_{cc}} \rightarrow \text{for circular hoops} \\ \dfrac{1 - \dfrac{s'}{2d_s}}{1 - \rho_{cc}} \rightarrow \text{for circular spirals} \end{cases} \tag{2.10}$$

where s' is the clear spacing between circular hoops or the clear pitch of the circular spiral (refer to Figure 2.8) and ρ_{cc} is the ratio of longitudinal steel area to the core of section area (area enclosed by the center line of circular hoops or spirals).

$$\rho_{cc} = \frac{A_l}{\frac{\pi}{4} d_s^2} \tag{2.11}$$

where A_l is the area of longitudinal steel reinforcements.

For elements with circular cross section confined by circular hoops or spirals, the confined concrete strength f'_{cc} is given by:

$$f'_{cc} = f'_{co}\left(-1.254 + 2.254\sqrt{1 + \frac{7.94f'_l}{f'_{co}}} - 2\frac{f'_l}{f'_{co}}\right) \tag{2.12}$$

For elements with rectangular cross sections confined by rectangular hoops and crossties, the lateral confinement is no longer uniformly distributed since the section is no longer axisymmetric with respect to its central longitudinal axis. Therefore, the effective lateral pressure should be calculated in both cross section directions x and y (refer to Figure 2.9).

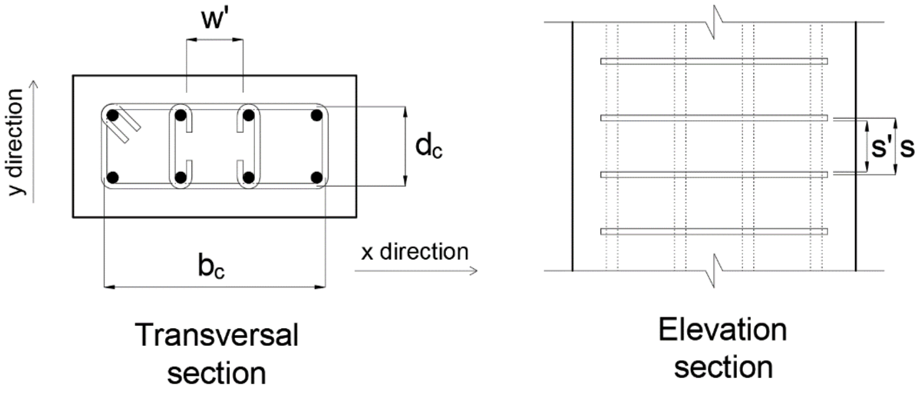

Figure 2.9: Confined concrete in a structural element with rectangular cross section.

f'_{lx} and f'_{ly} are respectively the effective lateral confining pressure in x and y directions and are given by:

$$f'_{lx} = k_e \rho_x f_{yh} \tag{2.13}$$

$$f'_{ly} = k_e \rho_y f_{yh} \tag{2.14}$$

where ρ_x and ρ_y are respectively the ratios of transverse confining steel in x and y directions.

$$\rho_x = \frac{A_{sx}}{sd_c} \tag{2.15}$$

$$\rho_y = \frac{A_{sy}}{sb_c} \tag{2.16}$$

and where A_{sx} and $A_{sy}$are the total area of transverse bars running respectively in the x and y directions. b_c and d_c are the dimensions of the peripheral rectangular hoop measured from the bar centerline respectively in the x and y directions (refer to Figure 2.9).

For rectangular cross sections, the confinement effectiveness coefficient k_e is given by:

$$k_e = \frac{\left(1 - \sum_{i=1}^{n} \frac{(w_i')^2}{6b_c d_c}\right)\left(1 - \frac{s'}{2b_c}\right)\left(1 - \frac{s'}{2d_c}\right)}{(1 - \rho_{cc})} \tag{2.17}$$

where w_i' is the i$^{\text{th}}$ clear distance between adjacent longitudinal bars (refer to Figure 2.9). For rectangular section, the ratio of longitudinal steel area to the core of section area ρ_{cc} is:

$$\rho_{cc} = \frac{A_l}{b_c d_c} \tag{2.18}$$

Once f_{lx}' and f_{ly}' are calculated, the smallest is referred to as f_{l2}' and the largest as f_{l1}'. The confined concrete strength f_{cc}' is then determined from the graphs in Figure 2.10.

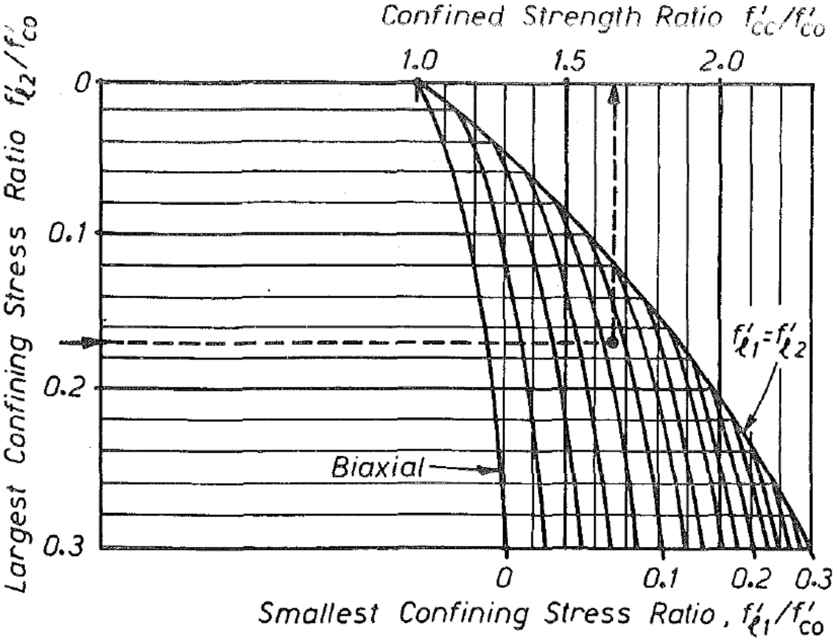

Figure 2.10: Graphs from (Mander, Pristley and Park, 1988) to determine the confined strength ratio.

Since the extra ductility of confined concrete is due to the energy dissipation in the confining reinforcements, (Mander, Priestley and Park, 1988) considered the ultimate compression strain for confined concrete ε_{cu} to correspond to the first rupture of the transverse confinement steel.

For monotonic tensile loading, the uniaxial stress-strain curve is considered linear until reaching the tensile strength f_t' (generally considered to be equal to 10% of the compressive strength) (refer to Figure 2.12).

$$f_c = E_c \varepsilon_c \quad for\ \varepsilon_c \leq \varepsilon_t \tag{2.19}$$

where ε_t is the strain corresponding to the tensile strength. For tensile strains higher than ε_t, concrete cracks and the tensile stress is considered zero.

The uniaxial stress-strain curve, obtained in response to a monotonically increasing strain, represents the material backbone curve and cyclic loadings occur within this envelop curve. At compression phase, concrete unloading starts from a point on the backbone curve until reaching the zero-stress axis (horizontal axis). Let $(\varepsilon_{un}, f_{un})$ be the coordinates of the unloading point on the backbone curve and $(\varepsilon_{pl}, 0)$ its corresponding zero stress point after unloading (refer to Figure 2.11).

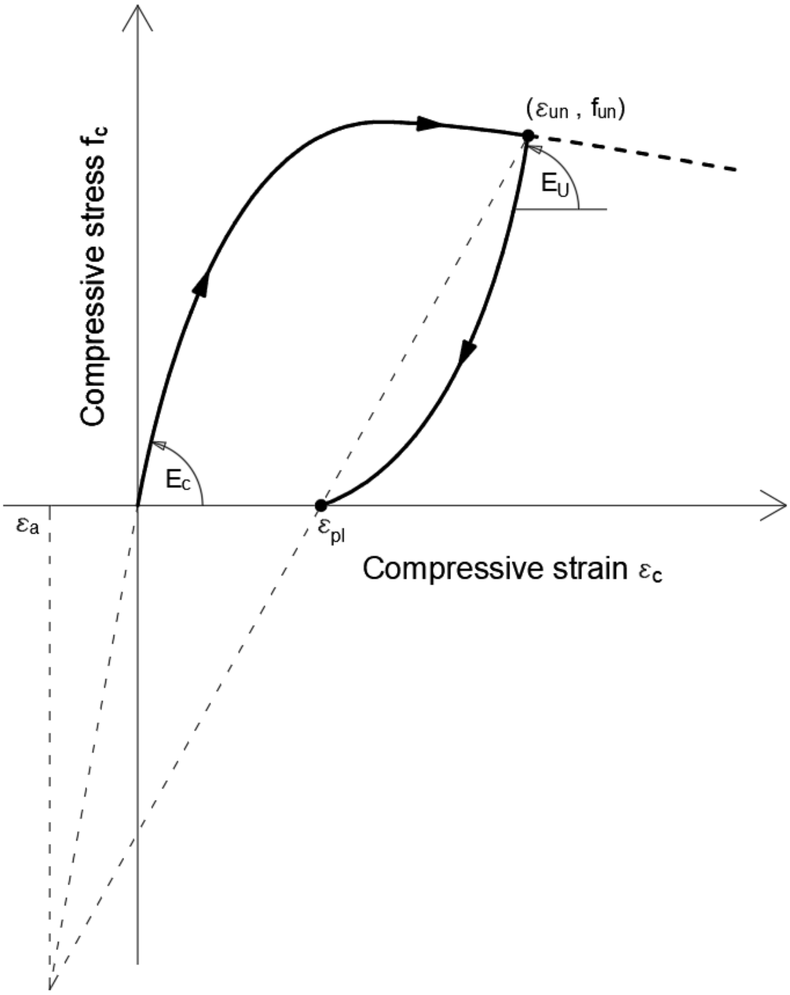

Figure 2.11: Unloading of Mander concrete model.

According to the Mander model, unloading occurs along a curve defined by:

$$f_c = f_{un} - \frac{f_{un} x r}{r - 1 + x^r} \tag{2.20}$$

where

$$r = \frac{E_u}{E_u - E_{sec}} \tag{2.21}$$

and

$$x = \frac{\varepsilon_c - \varepsilon_{un}}{\varepsilon_{pl} - \varepsilon_{un}} \tag{2.22}$$

E_u is the modulus of elasticity at the beginning of unloading and is given by:

$$E_u = bcE_{sec} \tag{2.23}$$

with

$$b = \frac{f_{un}}{f'_{co}} \geq 1 \tag{2.24}$$

and

$$c = \left(\frac{\varepsilon_{cc}}{\varepsilon_{un}}\right)^{0.5} \leq 1 \tag{2.25}$$

The plastic residual strain ε_{pl} is determined by:

$$\varepsilon_{pl} = \varepsilon_{un} - \frac{(\varepsilon_{un} + \varepsilon_a)f_{un}}{f_{un} + E_c\varepsilon_a} \tag{2.26}$$

with

$$\varepsilon_a = a\sqrt{\varepsilon_{un}\varepsilon_{cc}} \tag{2.27}$$

and

$$a = \max\left(\frac{\varepsilon_{cc}}{\varepsilon_{cc} + \varepsilon_{un}}; \frac{0.09\varepsilon_{un}}{\varepsilon_{cc}}\right) \tag{2.28}$$

After reaching the point$(\varepsilon_{pl}, 0)$, if the strain continues decreasing in absolute value, the material will start to reload in tension. According to Mander model, previous compression loading will result in tensile strength deterioration (refer to Figure 2.12) and the new tensile strength f_t becomes:

$$f_t = f'_t\left(1 - \frac{\varepsilon_{pl}}{\varepsilon_{cc}}\right) \tag{2.29}$$

For $|\varepsilon_{pl}| \geq |\varepsilon_{cc}|$, the material does not have any tensile strength.

Tensile loading and unloading are considered to occur on the same line.

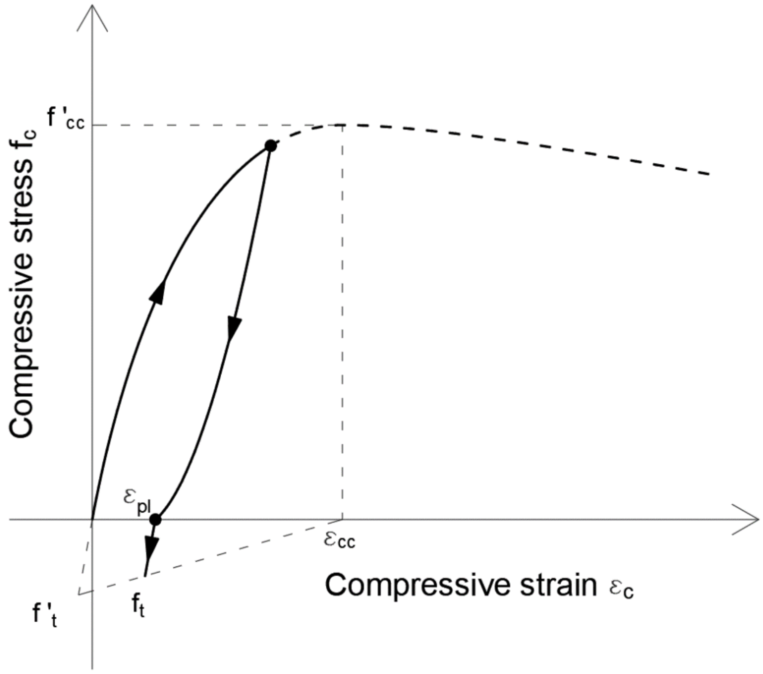

Figure 2.12: Reverse loading of Mander concrete model.

For compression reloading, let $(\varepsilon_{ro}, f_{ro})$ be the coordinates of the reloading point. A linear reloading is considered between points $(\varepsilon_{ro}, f_{ro})$ and $(\varepsilon_{un}, f_{new})$ and then a parabolic transition is made to rejoin the backbone curve at point $(\varepsilon_{re}, f_{re})$ (refer to Figure 2.13)

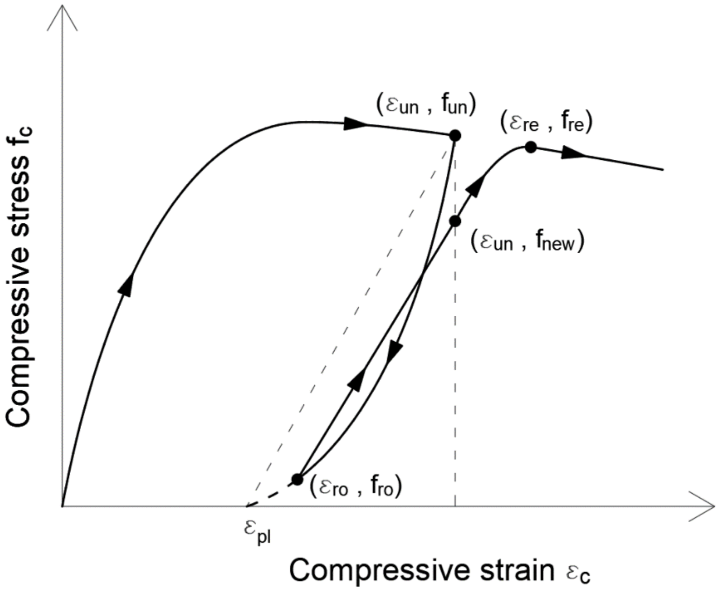

Figure 2.13: Unloading and reloading of Mander concrete model.

f_{new} is given by:

$$f_{new} = 0.92 f_{un} + 0.08 f_{ro} \tag{2.30}$$

and

$$\varepsilon_{re} = \varepsilon_{un} + \frac{f_{un} - f_{new}}{E_r\left(2 + \frac{f'_{cc}}{f'_{co}}\right)} \tag{2.31}$$

where E_r is the Young modulus of the linear reloading phase (slope of line between $(\varepsilon_{ro}, f_{ro})$ and $(\varepsilon_{un}, f_{new})$.

$$E_r = \frac{f_{ro} - f_{new}}{\varepsilon_{ro} - \varepsilon_{un}} \tag{2.32}$$

Since point $(\varepsilon_{re}, f_{re})$ exists on the backbone curve, f_{re} can be calculated using equation (2.1).

For simplicity purpose, in this work, the compression unloading and reloading will be considered to occur linearly between points $(\varepsilon_{un}, f_{un})$ and $(\varepsilon_{pl}, 0)$ (refer to Figure 2.14). This simplified version of (Mander, Priestley and Park, 1988) uniaxial concrete stress-strain model is adopted in this thesis for the multifiber elements (uniaxial concrete behavior).

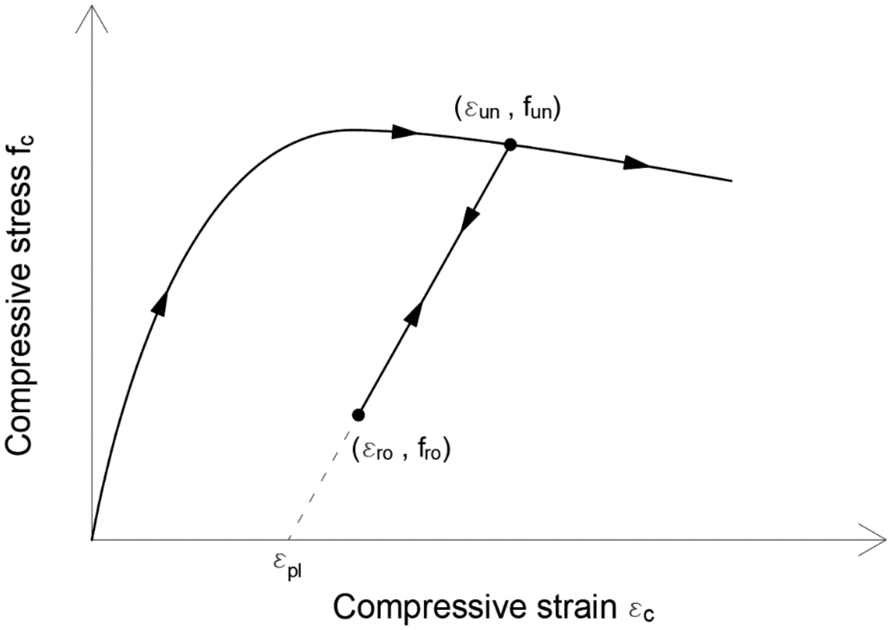

Figure 2.14: Simplified unloading and reloading used in this thesis for Mander concrete model.

2.3.1.2. Biaxial concrete models

Modeling concrete biaxial behavior starts by taking into account the cracking phenomena. Generally, concrete cracking is studied with two approaches: discrete crack and smeared crack. Discrete crack modeling started with (Clough, 1962; Ngo and Scordelis, 1967; Nilson, 1968). It consisted in including a geometrical discontinuity in the Finite element mesh of the structure by changing the nodal connectivity (previously connected nodes are spaced apart to make room for the crack). In addition, at each crack propagation stage, the nodal connectivity had to be modified in order to account for the crack growth (refer to Figure 2.15).

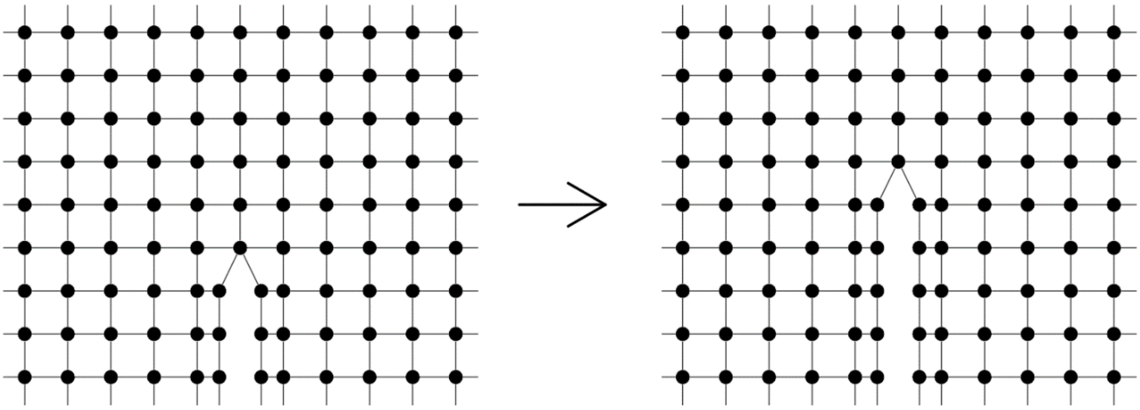

Figure 2.15: Crack propagation in early discrete crack models

The problem with this approach was that crack growth had to follow a predefined trajectory and modifying the nodal connectivity resulted in the increase of degrees of freedom (each node on the crack trajectory is divided to two nodes) which makes the analysis less effective. (Ingraffea and Saouma, 1985; Cervenka, 1994) worked on algorithms for automatic mesh generation at each cracking stage. (Gerstle and Xie, 1992) worked on aligning the FE mesh with the crack orientation in order to optimize the cracking propagation procedure. (Prasad and Krishnamoorthy, 2002; Contrafatto, Cuomo and Fazio, 2012) considered the bond slip effect on discrete concrete cracks. (Yang and Chen, 2005) modeled multiple discrete crack propagation in a reinforced concrete beam while considering the bond slip effect. (Patel *et al.*, 2021) simulated 3D crack propagation in high strength concrete.

In an attempt to overcome the drawbacks of early discrete crack models, (Rashid, 1968) was among the first to propose the smeared crack approach with concrete modeled as an orthotropic material after cracking. This technique considers the cracked concrete regions to be continuous but with orthotropic characteristics due to cracking. The smeared crack approach distributes the cracking effect over the entire zone while maintaining a continuous material model. In addition, it takes into account the densely distributed cracks (which is difficult to achieve with the discrete approach due to meshing limitations) while remaining computationally effective (Bazant, 1985). Due to its relative simplicity, smeared cracking is generally preferred when studying the overall behavior of the structural element. On the other hand, discrete crack models become interesting when special attention is needed to a specific crack in the structure. In this thesis, the global nonlinear behavior of elements is considered. Thus, the smeared crack approach is adopted.

Smeared crack models are generally classified into two subcategories: the fixed angle and the rotating angle approaches. The fixed angle smeared crack model considers the material orthotropic directions to coincide with the principal stresses axis until cracking, after that the orthotropic directions are fixed and they no longer change. The rotating angle smeared crack model always considers the material orthotropic directions to coincide with the principal stresses regardless of cracking phenomena.

Early smeared crack models corresponded to fixed angle approaches, such as (Rashid, 1968; Cervenka, 1970; Cervenka and Gerstle, 1971, 1972; Valliappan and Doolan, 1972) where the concrete was considered to carry stress only parallel to the crack. The problems with these models is that they had an abrupt switch between isotropic and orthotropic behavior and neglected all shear transmission through cracks in addition to axial stress normal to the crack. (Suidan and Schnobrich, 1973; Yuzugullu and Schnobrich, 1973) improved the fixed angle smeared crack model by considering shear stiffness at crack level as a percentage of the initial elastic shear stiffness. Similarly, (Bažant and Oh, 1983) considered axial stiffness normal to the crack as a percentage of the initial elastic axial stiffness.

The rotating angle smeared crack model started with (Cope *et al.*, 1980; Gupta and Akbar, 1984). (Vecchio and Collins, 1986; Vecchio, 1989) added the modified compression field theory to it. (Jirásek and Zimmermann, 1998) extended the rotating single crack concept to a multiple orthogonal cracks model. (Cervera, 2008; Cervera, Chiumenti and Codina, 2011; Burnett and Schreyer, 2019) proposed solutions for the mesh sensitivity issues of the smeared crack model.

The orthotropic material model is the most common approach for introducing concrete nonlinear biaxial behavior in finite element analysis. (Darwin and Pecknold, 1974) were the first to introduce the equivalent uniaxial stress-strain relationship for an orthotropic concrete constitutive model. This concept consisted of dividing the biaxial behavior of concrete into equivalent uniaxial behaviors along the directions of orthotropy. Generally, the equivalent uniaxial behavior is derived by multiplying the classical concrete uniaxial stress-strain curve by a biaxial coefficient that considers concrete softening due to orthogonal tensile strain or concrete strengthening due to biaxial compressive stress. Many researches have provided formulas for calculating this biaxial coefficient such as (Vecchio and Collins, 1986; Ayoub and Filippou, 1998; Foster and Marti, 2003). In this thesis, concrete softening was considered using a reduction factor β_s proposed by (Belarbi and Hsu, 1995).

$$\beta_s = \frac{k}{\sqrt{1 + k_\sigma \varepsilon_{tension}}} \tag{2.33}$$

where k_σ is a factor depending on the loading type (taken 250 in this work) and k initially proposed to be 0.9 by (Belarbi and Hsu, 1995). However, similarly to what was found by (Rojas, 2012), for $k = 1$ better convergence in the calculation model was noticed.

Due to problems with the fixed angle smeared crack model regarding the shear and axial stress transfer at crack level, the (Darwin and Pecknold, 1974) planar stress concrete orthotropic rotating angle smeared crack model will be considered in this work. The formulation will be presented in incremental form in order to be used in a nonlinear analysis. As previously indicated, the directions of orthotropy are considered to coincide with the principal stresses. In addition, the principal stresses and strains are assumed to have the same directions. The stress-strain relations in the principal directions are:

$$\Delta\varepsilon_1 = \frac{\Delta\sigma_1}{E_{T1}} - \nu_2 \frac{\Delta\sigma_2}{E_{T2}} \tag{2.34}$$

$$\Delta\varepsilon_2 = -\nu_1 \frac{\Delta\sigma_1}{E_{T1}} + \frac{\Delta\sigma_2}{E_{T2}} \tag{2.35}$$

where $\Delta\varepsilon_1, \Delta\sigma_1$, E_{T1} and ν_1 are respectively the axial strain increment, axial stress increment, tangent Young modulus and Poisson ratio along principal direction 1. Similarly, $\Delta\varepsilon_2$, $\Delta\sigma_2$, E_{T2} and ν_2 are along principal direction 2. Expressing equations (2.34) and (2.35) in matrix form gives:

$$\begin{Bmatrix} \Delta\sigma_1 \\ \Delta\sigma_2 \end{Bmatrix} = \frac{1}{1 - \nu_1\nu_2} \begin{bmatrix} E_{T1} & \nu_2 E_{T1} \\ \nu_1 E_{T2} & E_{T2} \end{bmatrix} \begin{Bmatrix} \Delta\varepsilon_1 \\ \Delta\varepsilon_2 \end{Bmatrix} \tag{2.36}$$

For energy considerations $\nu_1 E_{T2} = \nu_2 E_{T1}$ and an equivalent Poisson ration ν is considered where $\nu^2 = \nu_1 \nu_2$. Equation (2.36) becomes:

$$\begin{Bmatrix} \Delta\sigma_1 \\ \Delta\sigma_2 \end{Bmatrix} = \frac{1}{1-\nu^2} \begin{bmatrix} E_{T1} & \nu\sqrt{E_{T1}E_{T2}} \\ \nu\sqrt{E_{T1}E_{T2}} & E_{T2} \end{bmatrix} \begin{Bmatrix} \Delta\varepsilon_1 \\ \Delta\varepsilon_2 \end{Bmatrix} \tag{2.37}$$

Considering the shear stress results:

$$\begin{Bmatrix} \Delta\sigma_1 \\ \Delta\sigma_2 \\ \Delta\tau_{12} \end{Bmatrix} = \frac{1}{1-\nu^2} \begin{bmatrix} E_{T1} & \nu\sqrt{E_{T1}E_{T2}} & 0 \\ \nu\sqrt{E_{T1}E_{T2}} & E_{T2} & 0 \\ 0 & 0 & (1-\nu^2)G \end{bmatrix} \begin{Bmatrix} \Delta\varepsilon_1 \\ \Delta\varepsilon_2 \\ \Delta\gamma_{12} \end{Bmatrix} \tag{2.38}$$

where $\Delta\tau_{12}$, $\Delta\gamma_{12}$ and G are respectively the increment in shear stress, increment in shear strain and the shear modulus. For the shear modulus G to be independent of reference directions it can be proven that:

$$G = \frac{1}{4(1-\nu^2)}\left(E_{T1} + E_{T2} - 2\nu\sqrt{E_{T1}E_{T2}}\right) \tag{2.39}$$

The stress-strain relation in the material reference (principal directions reference) becomes:

$$\{\Delta\sigma\}_{1-2} = [D_T]_{1-2}\{\Delta\varepsilon\}_{1-2} \tag{2.40}$$

with

$$\{\Delta\sigma\}_{1-2} = \begin{Bmatrix} \Delta\sigma_1 \\ \Delta\sigma_2 \\ \Delta\tau_{12} \end{Bmatrix} \quad \{\Delta\varepsilon\}_{1-2} = \begin{Bmatrix} \Delta\varepsilon_1 \\ \Delta\varepsilon_2 \\ \Delta\gamma_{12} \end{Bmatrix} \tag{2.41}$$

and

$$\begin{aligned} &[D_T]_{1-2} \\ &= \frac{1}{1-\nu^2} \begin{bmatrix} E_{T1} & \nu\sqrt{E_{T1}E_{T2}} & 0 \\ \nu\sqrt{E_{T1}E_{T2}} & E_{T2} & 0 \\ 0 & 0 & \frac{1}{4}\left(E_{T1} + E_{T2} - 2\nu\sqrt{E_{T1}E_{T2}}\right) \end{bmatrix} \end{aligned} \tag{2.42}$$

To express the stress-strain relation in the finite element reference $(\vec{x}, \vec{y})$ a transformation matrix $[T(\theta)]$ is required where θ is the angle between the finite element reference and the material reference (refer to Figure 2.16):

$$[T(\theta)] = \begin{bmatrix} cos^2\theta & sin^2\theta & cos\theta sin\theta \\ sin^2\theta & cos^2\theta & -cos\theta sin\theta \\ -2cos\theta sin\theta & 2cos\theta sin\theta & cos^2\theta - sin^2\theta \end{bmatrix} \tag{2.43}$$

and

$$\theta = \frac{1}{2} arctan\left(\frac{\gamma_{xy}}{\varepsilon_x - \varepsilon_y}\right) \tag{2.44}$$

where ε_x, ε_y, and γ_{xy} are the axial and shear strains in the $(\vec{x},\vec{y})$ reference (finite element reference).

$$\{\Delta\varepsilon\}_{1-2} = [T(\theta)]\{\Delta\varepsilon\}_{x-y} \tag{2.45}$$

and

$$\{\Delta\sigma\}_{x-y} = [T(\theta)]^T\{\Delta\sigma\}_{1-2} \tag{2.46}$$

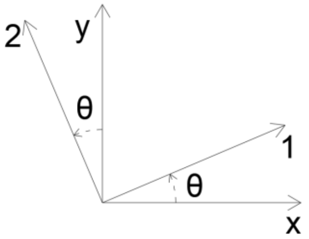

Figure 2.16: Principal directions with respect to the finite element reference $(\vec{x},\vec{y})$.

Using equations (2.40), (2.45) and (2.46) gives:

$$\{\Delta\sigma\}_{x-y} = [T(\theta)]^T[D_T]_{1-2}[T(\theta)]\{\Delta\varepsilon\}_{x-y} \tag{2.47}$$

with

$$[D_T]_{x-y} = [T(\theta)]^T[D_T]_{1-2}[T(\theta)] \tag{2.48}$$

Generally, the Poisson ratio is set to zero at cracking. However, for simplification purpose and as made by (Rojas, 2012) $[D_T]_{1-2}$ will be considered diagonal. In addition, the Poisson ratio will be set to zero in all the calculations for this thesis. As a result:

$$[D_T]_{1-2} = \begin{bmatrix} E_{T1} & 0 & 0 \\ 0 & E_{T2} & 0 \\ 0 & 0 & \frac{1}{4}(E_{T1}+E_{T2}) \end{bmatrix} \tag{2.49}$$

In this thesis, 2D concrete biaxial material model was used in layered membrane elements. The (Darwin and Pecknold, 1974) planar stress concrete orthotropic rotating angle smeared crack model was adopted while neglecting the Poisson coefficient (refer to equation (2.49)). Concrete softening was considered as proposed by (Belarbi and Hsu, 1995) with slight adjustments on k factor (refer to equation (2.33)). The 1D uniaxial concrete behavior considered at each orthotropy direction of the biaxial 2D model is identical to the one used for multifiber elements.

2.3.2. Steel reinforcement constitutive models

Generally, in linear RC structural elements (beams and columns), steel rebars are considered to work solely along their longitudinal direction. For 2D RC structural elements (membranes, plates and shells), the steel layers work only in the rebars direction. In other words, rebars carry only longitudinal axial stress and their capacity for shear transmission is usually neglected in RC elements design. Steel is a ductile symmetrical material that behaves identically in tension and in compression (when there is no risk of compression buckling) and exhibits nonlinear material deformation in the form of plastic yielding with strain hardening. Generally, a kinematic or isotropic strain hardening is considered (for more information on strain hardening refer to (Houlsby and Puzrin, 2006; Hosford, 2013)). One of the first and most famous steel rebar constitutive models was proposed by (Giuffrè and Pinto, 1970; Menegotto and Pinto, 1973) and is known as the Giuffre-Menegotto-Pinto (GMP) model. By making modifications on the GMP model, (Chang and Mander, 1994) accounted for the steel damaging in the hysteresis behavior; (Gomes and Appleton, 1997; Dhakal and Maekawa, 2002) considered the buckling effect of the longitudinal rebars; (Hoehler and Stanton, 2006) presented a formulation capable of handling any arbitrary loading cycles; (Kunnath, Heo and Mohle, 2009) studied rebars buckling, low-cycle fatigue and cyclic damaging; (Mendes and Castro, 2014) considered ultra-low-cycle fatigue and (Vallejos, 2018) studied large diameter reinforcement subjected to large strain cyclic reversals.

2.3.2.1. Uniaxial steel models

In most proposed models, the monotonic uniaxial stress-strain curve for steel rebars is made up of 4 regions (refer to Figure 2.17):

- I: Linear region
- II: Yield plateau
- III: Strain hardening region
- IV: Steel softening due to necking failure

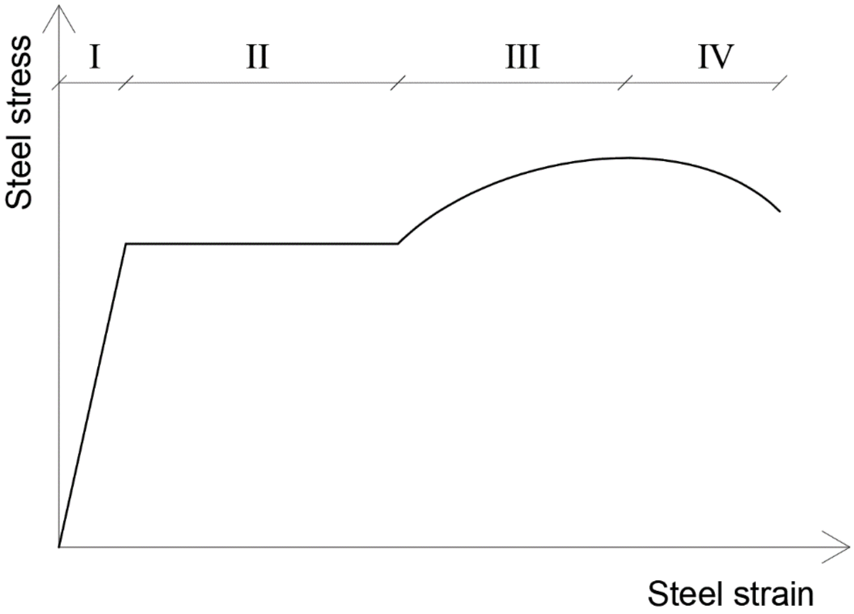

Figure 2.17: Typical uniaxial stress-strain backbone curve for steel reinforcements.

For cyclic loading, the general shape of the hysteresis loops is as indicated in Figure 2.18.

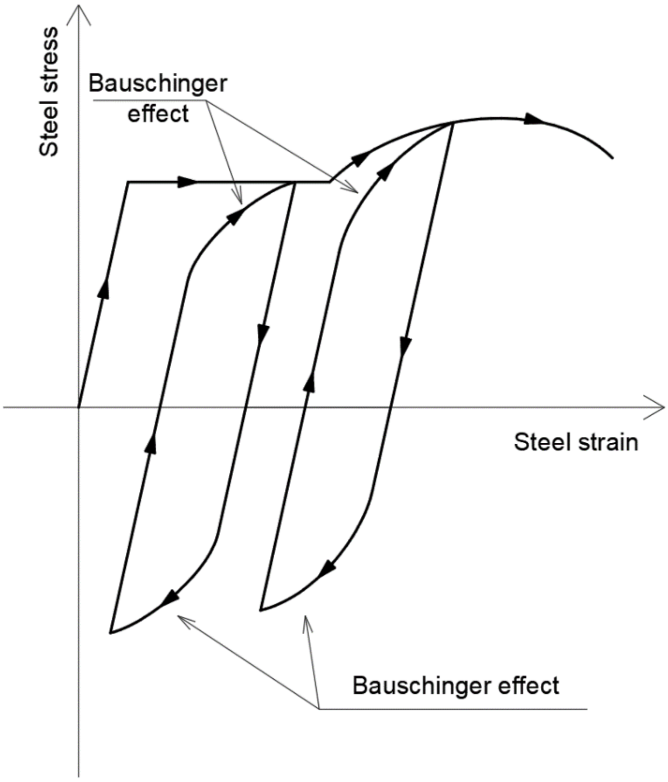

Figure 2.18: Hysteresis loops for steel reinforcements.

The Bauschinger effect in steel, demonstrated by (Bauschinger, 1886), occurs when the material reaches yielding and then loading is reversed. During the reverse loading phase and prior to reaching the reverse yielding stress, material softening is observed (refer to Figure 2.18).

For simplification purpose in this work, the monotonic uniaxial steel rebar stress-strain curve will be considered as a bilinear curve in this thesis (this is a very common approximation in structural engineering). The first line represents the linear elastic phase and the second represents the strain hardening phase (refer to Figure 2.19)

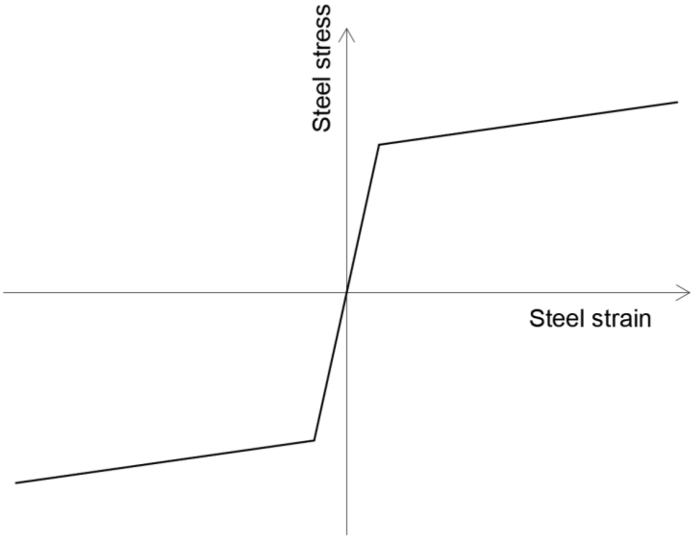

Figure 2.19: Bilinear uniaxial stress-strain backbone curve for steel reinforcements.

In addition, the Bauschinger effect will be neglected and hysteresis loops will be considered as perfect parallelograms (refer to Figure 2.20).

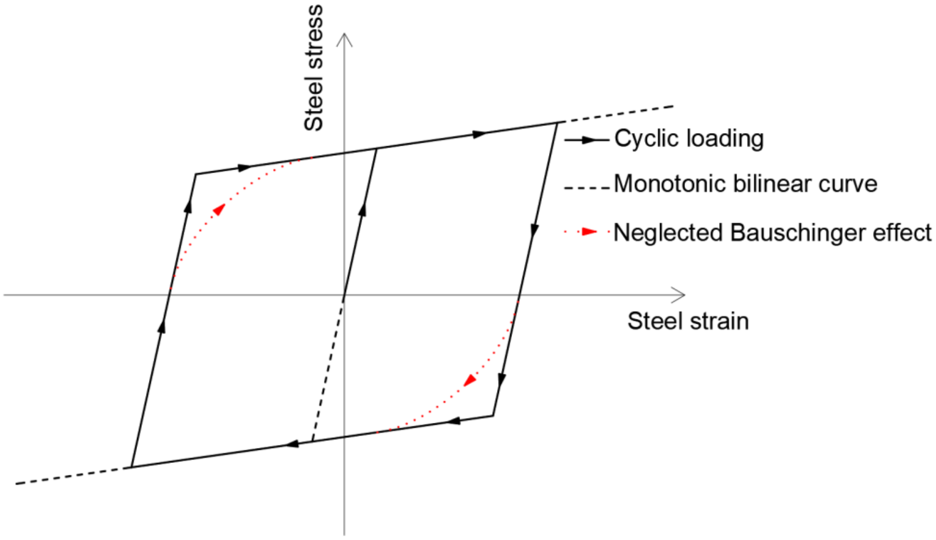

Figure 2.20: Hysteresis loops for steel reinforcements while neglecting the Bauschinger effect.

In this thesis, for multifiber element, steel reinforcements are considered to behave uniaxially (along the bars' direction) according to a bilinear elastic plastic stress-strain curve with kinematic strain hardening.

2.3.2.2. Biaxial steel models

In 2D analysis, steel layers are made up of reinforcement bars. As a result, a steel layer can only carry loads in the direction parallel to its bars. Let x' be the bar axis, $\overrightarrow{x'}$ and $\overrightarrow{y'}$ are the steel layer principal directions.

$$\begin{Bmatrix} \Delta\sigma_{x'} \\ \Delta\sigma_{y'} \\ \Delta\tau_{x'y'} \end{Bmatrix} = \begin{bmatrix} E_T & 0 & 0 \\ 0 & 0 & 0 \\ 0 & 0 & 0 \end{bmatrix} \begin{Bmatrix} \Delta\varepsilon_{x'} \\ \Delta\varepsilon_{y'} \\ \Delta\gamma_{x'y'} \end{Bmatrix} \tag{2.50}$$

and

$$[D_T]_{x'-y'} = \begin{bmatrix} E_T & 0 & 0 \\ 0 & 0 & 0 \\ 0 & 0 & 0 \end{bmatrix} \tag{2.51}$$

Using equation (2.48), for the case where the bars direction (axis x') coincide with axis x ($\theta = 0$):

$$[D_T]_{x-y} = [T(0°)]^T [D_T]_{x'-y'} [T(0°)] = \begin{bmatrix} E_T & 0 & 0 \\ 0 & 0 & 0 \\ 0 & 0 & 0 \end{bmatrix} \tag{2.52}$$

Also, for the case where the bars direction (axis x') coincide with axis y ($\theta = 90°$):

$$[D_T]_{x-y} = [T(90°)]^T [D_T]_{x'-y'} [T(90°)] = \begin{bmatrix} 0 & 0 & 0 \\ 0 & E_T & 0 \\ 0 & 0 & 0 \end{bmatrix} \tag{2.53}$$

In this thesis, for layered membrane, steel reinforcements layers are considered to behave unidirectionally (along the bars' direction) according to a bilinear elastic plastic stress-strain curve with kinematic strain hardening.

2.4. Conclusions

As seen in this chapter, a wide variety of models exist for incorporating material nonlinearities in structural elements. The more accurate and realistic a model is in representing the material nonlinear behavior, the more it is computationally demanding.

After considering the size of the structure, a compromise shall be made between high accuracy and time efficiency in choosing the most adequate nonlinear modeling approach.

In this thesis, for frame elements (beams and columns), the additional benefits of multifiber elements in providing a higher accuracy and a wide range applicability outweighed its increased time cost with respect to concentrated plastic nodes. Therefore, multifiber elements were considered for 1D structural elements.

For 2D elements (shear walls), since only in-plane behavior was considered, the optimum model to adopt is the 2D layered membrane element.

Both structural models rely on steel and concrete constitutive models. Modeling concrete behavior is not a straightforward task. In fact, concrete is made from a mixture of materials (cement paste, sand, aggregate …) and has an asymmetric brittle behavior with tensile cracking. Thus, concrete constitutive models are still being improved nowadays especially for the multidimensional behavior. On the other hand, steel nonlinear modeling is relatively simpler due to the material homogeneity. In addition, steel reinforcement bars are generally considered to behave uniaxially in their longitudinal direction.

In this thesis, despite the importance of having reliable nonlinear materials model, it is not the essential purpose of this work. So, simplifications on the non-linear behavior of materials were made while maintaining a satisfactory level of reliability. For confined and unconfined concrete, uniaxial behavior was defined according to (Mander, Priestley and Park, 1988) and a simplification was made in cyclic loading by merging the unloading and reloading paths. For biaxial nonlinear behavior, the (Darwin and Pecknold, 1974) planar stress concrete orthotropic rotating angle smeared crack model was used in layered membrane elements. For steel reinforcements, a simplified bilinear uniaxial model was considered with kinematic strain hardening for cyclic loading while neglecting the (Bauschinger, 1886) effect.

Chapter 3

3. Finite elements implementation and validation

Abstract: *This chapter presents the Finite Elements (FE) implementation of multifiber models for line elements (beams and columns) and layered membrane for surface elements (planar shear walls). In addition, these obtained FE models are validated by conducting a comparison with experimental results.*

Chapter content

3.1. Introduction

Classically, a displacement-based (also known as stiffness based) approach finite element analysis is used. It is founded on interpolation functions (shape functions) to calculate the internal displacement field of structural members in function of nodal degrees of freedom. This formulation is widely used because it is easy to implement in classical finite element calculation algorithms. The adopted shape (interpolation) functions are usually cubic or quadratic polynomials and are limited to structures with linear behavior. To reduce the error of using them in nonlinear analysis, structural members need to be subdivided into several elements (fine meshing around zones of nonlinearity is required if typical mesh size is relatively large). This increase in the number of finite elements and consequently the system’s degrees of freedom reduces the calculation efficiency of the model. This problem can be softened by lumping the nonlinear behavior in zero length concentrated hinges or using higher degree polynomial shape functions.

In this section, the finite element formulation for multifiber 1D elements (beams and columns) and layered membrane 2D elements (planar walls) is presented and a validation of the obtained models is made via comparison with experimental results.

3.2. Finite element formulation

3.2.1. Multifiber element

As previously mentioned, the multifiber element approach consists in dividing the structural elements (beams and columns) cross section into a set of longitudinal fibers with each fiber having the potential to undergo a nonlinear material behavior in its longitudinal direction. The multifiber element modeling is a 3-level analysis (fiber level, cross section level and finite element level). In this work, 2D planar behavior of structural elements is considered.

3.2.1.1. Fiber level

Fibers are the basic constitutive elements of a cross section. Each fiber is made up of only one single material. For reinforced concrete structures, the fibers can be made of steel reinforcements, confined concrete or unconfined concrete. A fiber behaves in its longitudinal direction according to the uniaxial stress-strain relationship of its constitutive material. The uniaxial constitutive models described in chapter 2 for concrete and steel are introduced at this level: the Mander model for confined and unconfined concrete, a simplified bilinear model for steel. By knowing the longitudinal strain occurring in a fiber ε_{fiber}, we can determine the corresponding axial stress σ_{fiber} and longitudinal tangent Young modulus $E_{T\ fiber}$.

$$\sigma_{fiber} = f(\varepsilon_{fiber}) \tag{3.1}$$

The longitudinal tangent Young modulus $E_{T\ fiber}$ is the derivative of the axial stress with respect to axial strain.

$$E_{T\ fiber} = \frac{d\sigma_{fiber}}{d\varepsilon_{fiber}} \tag{3.2}$$

This longitudinal tangent modulus will be used at the FE level during nonlinear increments.

3.2.1.2. Cross section level

As indicated earlier, each cross section is divided into a set of fibers. The Euler-Bernoulli hypothesis is considered which states that each planar cross section before deformation remains planar after deformation and orthogonal to the beam's centerline (perfect bond conditions between fibers). As a consequence, for a fiber having its centroid located at the coordinates (x, y, z) in the section reference, the axial longitudinal strain in the fiber $\varepsilon(x, y)$ can be determined in function of the section's uniform axial strain along $\vec{x}$ axis $\varepsilon_x(x)$ and the curvature along $\vec{z}$ axis $\phi_z(x)$ (bending along $\vec{y}$ axis is not accounted since 2D planar behavior is solely considered, refer to Figure 3.1).

$$\varepsilon(x, y) = \varepsilon_x(x) - y\phi_z(x) = \{1 \quad -y\}\begin{Bmatrix} \varepsilon_x(x) \\ \phi_z(x) \end{Bmatrix} \tag{3.3}$$

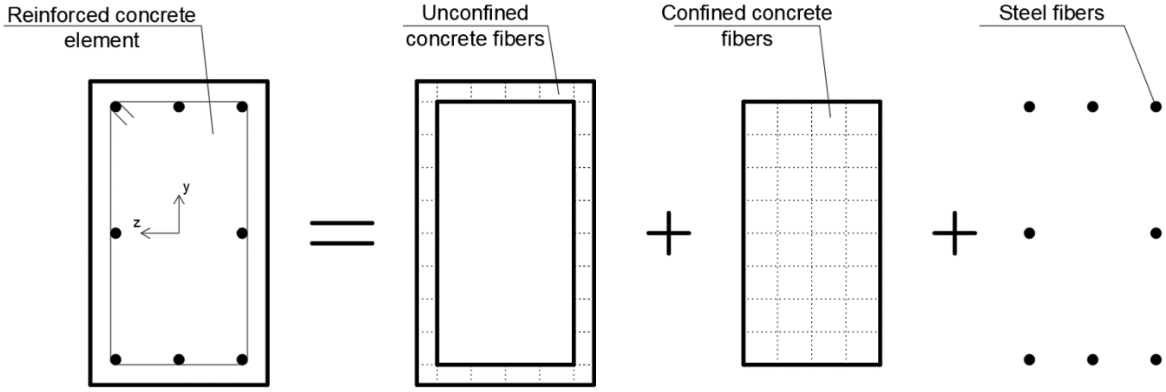

Figure 3.1: Multifiber reinforced concrete cross section.

Let $u(x)$ and $v(x)$ be respectively the displacement in $\vec{x}$ and $\vec{y}$ directions of a point located on the element centerline at abscissa x.

$$\varepsilon_x(x) = \frac{du(x)}{dx} \tag{3.4}$$

and

$$\phi_z(x) = \frac{d^2v(x)}{dx^2} \tag{3.5}$$

so

$$\varepsilon(x,y) = \{1 \quad -y\} \begin{bmatrix} \frac{d}{dx} & 0 \\ 0 & \frac{d^2}{dx^2} \end{bmatrix} \begin{Bmatrix} u(x) \\ v(x) \end{Bmatrix} \tag{3.6}$$

This definition of the fiber axial longitudinal strain will be used at the FE level to compute the stiffness matrix.

3.2.1.3. Finite element level

For the finite element modeling of beams in this work, a 1D element composed of 2 nodes with three degrees of freedom each is used (refer to Figure 3.2). Hermitian shape functions are considered for bending and linear interpolation is adopted for longitudinal translation.

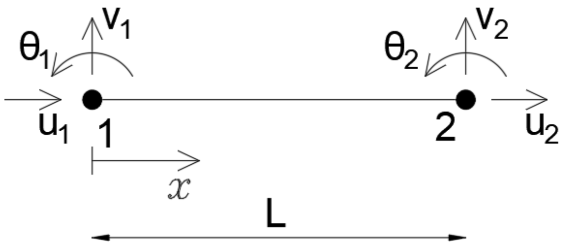

Figure 3.2: Beam/Column finite element.

The displacement vector of a point on the element centerline at abscissa x is given by:

$$\begin{Bmatrix} u(x) \\ v(x) \end{Bmatrix} = [N(x)]\{u_{nodes}\} \tag{3.7}$$

with

$$[N(x)] = \begin{bmatrix} N_1^t(x) & 0 & 0 & N_2^t(x) & 0 & 0 \\ 0 & N_1^b(x) & N_2^b(x) & 0 & N_3^b(x) & N_4^b(x) \end{bmatrix} \tag{3.8}$$

and

$$\{u_{nodes}\} = \begin{Bmatrix} u_1 \\ v_1 \\ \theta_1 \\ u_2 \\ v_2 \\ \theta_2 \end{Bmatrix} \tag{3.9}$$

where $\{u_{nodes}\}$ is the nodal displacement vector (refer to Figure 3.2). $N_1^t(x)$ and $N_2^t(x)$ are the translation shape functions while $N_1^b(x)$ to $N_4^b(x)$ are the bending shape functions (for further details on shape functions, refer to Appendix B).

Inserting equation (3.7) in (3.6) gives:

$$\varepsilon(x,y) = \{1 \quad -y\}[B(x)] \begin{Bmatrix} u_1 \\ v_1 \\ \theta_1 \\ u_2 \\ v_2 \\ \theta_2 \end{Bmatrix} \tag{3.10}$$

with

$$[B(x)] = \begin{bmatrix} \frac{dN_1^t(x)}{dx} & 0 & 0 & \frac{dN_2^t(x)}{dx} & 0 & 0 \\ 0 & \frac{d^2N_1^b(x)}{dx^2} & \frac{d^2N_2^b(x)}{dx^2} & 0 & \frac{d^2N_3^b(x)}{dx^2} & \frac{d^2N_4^b(x)}{dx^2} \end{bmatrix} \tag{3.11}$$

Let $\{\delta u_{nodes}\}$ be a virtual displacement occurring at the nodes of the beam element. To this displacement corresponds a virtual internal strain $\delta\varepsilon(x)$. The external system energy $w_{external}$ is expressed as:

$$w_{external} = \{\delta u_{nodes}\}^T \{F_{nodes}\} \tag{3.12}$$

where $\{F_{nodes}\}$ is the force vector applied at the element's nodes. By applying the virtual work principal, external virtual work should be equal to internal virtual work. Since the Euler-Bernoulli model is considered, the shear strain energy is neglected. The internal system energy is then given by the following integral over the structural element volume:

$$w_{internal} = \int_V \delta\varepsilon(x)^T \sigma(x,y)\, dV \tag{3.13}$$

Since

$$\delta\varepsilon(x) = \{1 \quad -y\}[B(x)]\{\delta u_{nodes}\} \tag{3.14}$$

equation (3.13) becomes:

$$w_{internal} = \int_V \{\delta u_{nodes}\}^T [B(x)]^T \begin{Bmatrix} 1 \\ -y \end{Bmatrix} \sigma(x,y)\, dV \tag{3.15}$$

By equating the internal and external virtual works:

$$\{\delta u_{nodes}\}^T \{F_{nodes}\} = \int_V \{\delta u_{nodes}\}^T [B(x)]^T \begin{Bmatrix} 1 \\ -y \end{Bmatrix} \sigma(x,y)\, dV \tag{3.16}$$

which results in:

$$\{F_{nodes}\} = \int_V [B(x)]^T \begin{Bmatrix} 1 \\ -y \end{Bmatrix} \sigma(x,y)\, dV \tag{3.17}$$

For linear systems, this corresponds to:

$$\{F_{nodes}\} = [K]\{u_{nodes}\} \tag{3.18}$$

where $[K]$ is the stiffness matrix of the beam element.

Since

$$\sigma(x,y) = E(x,y)\varepsilon(x,y) = E(x,y)\{1 \quad -y\}[B(x)]\{u_{nodes}\} \tag{3.19}$$

where $E(x,y)$ is the longitudinal Young modulus at point (x,y), inserting equations (3.18) and (3.19) in equation (3.17) gives:

$$[K]\{u_{nodes}\} = \int_V [B(x)]^T \begin{Bmatrix} 1 \\ -y \end{Bmatrix} E(x,y)\{1 \quad -y\}[B(x)]\{u_{nodes}\}\, dV \tag{3.20}$$

which results in:

$$[K] = \int_V [B(x)]^T \begin{Bmatrix} 1 \\ -y \end{Bmatrix} E(x,y)\{1 \quad -y\}[B(x)]\, dV \tag{3.21}$$

For nonlinear systems, equation (3.17) remains applicable. Since incremental calculation is used in nonlinear analysis, equation (3.21) becomes:

$$[K_T] = \int_V [B(x)]^T \begin{Bmatrix} 1 \\ -y \end{Bmatrix} E_T(x,y)\{1 \quad -y\}[B(x)]\, dV \tag{3.22}$$

with

$$\{\Delta f\} = [K_T]\{\Delta u\} \tag{3.23}$$

where $[K_T]$ is the tangent stiffness matrix of the beam element, $E_T(x, y)$ is the tangent longitudinal Young modulus at point (x, y), $\{\Delta f\}$ and $\{\Delta u\}$ are respectively the beam nodal force and displacement vectors increments.

The volumetric integral is decomposed into a surface integral over the transversal cross section and a linear integral over the element's length.

$$\{F_{nodes}\} = \int_0^L [B(x)]^T \left(\int_s \begin{Bmatrix} 1 \\ -y \end{Bmatrix} \sigma(x, y) ds \right) dx \tag{3.24}$$

and

$$[K_T] = \int_0^L [B(x)]^T \left(\int_s \begin{Bmatrix} 1 \\ -y \end{Bmatrix} E_T(x, y) \{1 \quad -y\} ds \right) [B(x)] dx \tag{3.25}$$

In order to apply Gauss point integration, a reference change is required from axis $(O, \vec{x})$ where the beam is located at $x \in [0; L]$ to axis $(O', \vec{\xi})$ where the beam is located at $\xi \in [-1; 1]$ (refer to Figure 3.3).

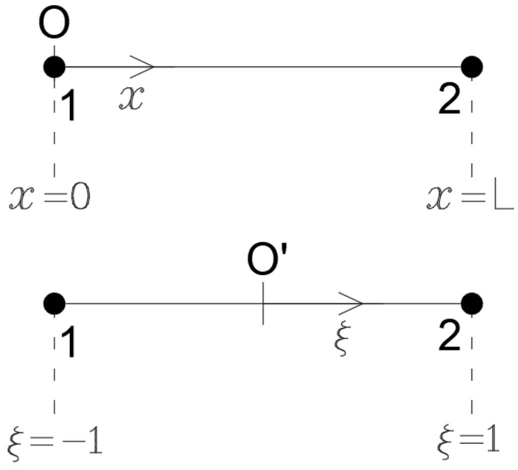

Figure 3.3: Reference change for beam/column finite element.

Once the variable x is changed to ξ and we get:

$$\{F_{nodes}\} = \int_{-1}^1 [B(\xi)]^T \left(\int_s \begin{Bmatrix} 1 \\ -y \end{Bmatrix} \sigma(\xi, y) ds \right) \frac{dx}{d\xi} d\xi \tag{3.26}$$

and

$$[K_T] = \int_{-1}^1 [B(\xi)]^T \left(\int_s \begin{Bmatrix} 1 \\ -y \end{Bmatrix} E_T(\xi, y) \{1 \quad -y\} ds \right) [B(\xi)] \frac{dx}{d\xi} d\xi \tag{3.27}$$

Since the beam is made up of fibers, the surface integral along the beam cross section can be replaced by a summation of fibers:

$$\int_s \begin{Bmatrix} 1 \\ -y \end{Bmatrix} \sigma(\xi, y) ds \cong \sum_{i=1}^{n_{fibers}} \begin{Bmatrix} 1 \\ -y_i \end{Bmatrix} \sigma_i(\xi) \, A_i \tag{3.28}$$

and

$$\int_s \begin{Bmatrix} 1 \\ -y \end{Bmatrix} E_T(\xi, y) \{1 \quad -y\} ds \cong \sum_{i=1}^{n_{fibers}} \begin{Bmatrix} 1 \\ -y_i \end{Bmatrix} E_{T\,i}(\xi) \{1 \quad -y_i\} \, A_i \tag{3.29}$$

where n_{fibers} is the number of beam fibers, A_i and y_i are respectively the cross-section area and centroid ordinate of fiber i. $\sigma_i(\xi)$ and $E_{T\,i}(\xi)$ are respectively the longitudinal axial stress and tangent Young modulus of fiber i at abscissa ξ. Inserting equation (3.28) in (3.26) gives:

$$\{F_{nodes}\} = \int_{-1}^{1} [B(\xi)]^T \left(\sum_{i=1}^{n_{fibers}} \begin{Bmatrix} 1 \\ -y_i \end{Bmatrix} \sigma_i(\xi) \, A_i \right) \frac{dx}{d\xi} d\xi \tag{3.30}$$

Inserting equation (3.29) in (3.27) gives:

$$[K_T] = \int_{-1}^{1} [B(\xi)]^T \left(\sum_{i=1}^{n_{fibers}} \begin{Bmatrix} 1 \\ -y_i \end{Bmatrix} E_{T\,i}(\xi) \{1 \quad -y_i\} \, A_i \right) [B(\xi)] \frac{dx}{d\xi} d\xi \tag{3.31}$$

The nodal force vector $\{F_{nodes}\}$ and the element tangent stiffness matrix $[K_T]$ can now be calculated by linear Gauss point integration. Let us define two functions:

$$f(\xi) = [B(\xi)]^T \left(\sum_{i=1}^{n_{fibers}} \begin{Bmatrix} 1 \\ -y_i \end{Bmatrix} \sigma_i(\xi) \, A_i \right) \frac{dx}{d\xi} \tag{3.32}$$

and

$$g(\xi) = [B(\xi)]^T \left(\sum_{i=1}^{n_{fibers}} \begin{Bmatrix} 1 \\ -y_i \end{Bmatrix} E_{T\,i}(\xi) \{1 \quad -y_i\} \, A_i \right) [B(\xi)] \frac{dx}{d\xi} \tag{3.33}$$

Considering a 3-point Gauss quadrature rule leads to:

$$\{F_{nodes}\} = \int_{-1}^{1} f(\xi)d\xi = \sum_{p=1}^{3} W_p f(\xi_p) \tag{3.34}$$

and

$$[K_T] = \int_{-1}^{1} g(\xi)d\xi = \sum_{p=1}^{3} W_p g(\xi_p) \tag{3.35}$$

where W_p and ξ_p are respectively the integration weight and abscissa of Gauss point p (for further details on Gauss points, refer to Appendix B).

It should be noted that the previous force vectors, displacement vectors and stiffness matrices were calculated in the element local reference $(\vec{x}, \vec{y})$. They can be expressed in the global reference $(\vec{X}, \vec{Y})$ via a transformation matrix $[T(\theta)]$ (refer to Figure 3.4).

$$[T(\theta)] = \begin{bmatrix} cos(\theta) & sin(\theta) & 0 & 0 & 0 & 0 \\ -sin(\theta) & cos(\theta) & 0 & 0 & 0 & 0 \\ 0 & 0 & 1 & 0 & 0 & 0 \\ 0 & 0 & 0 & cos(\theta) & sin(\theta) & 0 \\ 0 & 0 & 0 & -sin(\theta) & cos(\theta) & 0 \\ 0 & 0 & 0 & 0 & 0 & 1 \end{bmatrix} \tag{3.36}$$

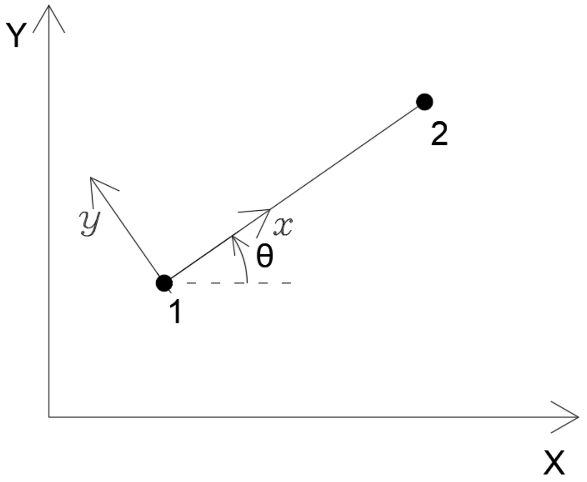

Figure 3.4: Finite element local reference $(\vec{x}, \vec{y})$ with respect to global reference $(\vec{X}, \vec{Y})$.

Using $[T(\theta)]$, the following relations can be established:

$$\{\Delta f\}_{global} = [T(\theta)]^T \{\Delta f\}_{local} \tag{3.37}$$

$$\{\Delta u\}_{global} = [T(\theta)]^T \{\Delta u\}_{local} \tag{3.38}$$

$$[K_T]_{global} = [T(\theta)]^T [K_T]_{local} [T(\theta)] \tag{3.39}$$

So for multifiber elements, the nodal force vector $\{F_{nodes}\}$ and tangent stiffness matrix $[K_T]$ are calculated in their local reference by equations (3.34) and (3.35) respectively. Then, expressed in global reference via the transformation matrix $[T(\theta)]$. Now that tangent stiffness matrix and nodal force vector are determined, they can be used in the nonlinear Newmark and central difference calculations (presented in chapter 1).

3.2.2. Layered membrane

The layered membrane approach consists in dividing the structural element into a set of layers along its thickness where each layer can undergo nonlinear material deformations. Similarly to the multifiber section model, the layered membrane approach is a 3-level analysis (layer level, thickness level and finite element level).

3.2.2.1. Layer level

Layers are the fundamental constitutive elements of the membrane thickness. Each layer is made up of only one single material. For reinforced concrete membranes, the layers can be made of steel reinforcements, confined or unconfined concrete. It should be noted that the concrete layers used in RC membranes present a biaxial planar stress behavior. In material nonlinearity, the simplified Darwin and Pecknold planar stress concrete orthotropic rotating angle smeared crack model presented in chapter 2 was adopted for confined and unconfined concrete layers. Steel layers were considered to work uniaxially in the bars' longitudinal direction according to a simplified bilinear model (refer to chapter 2). Let us consider a point located at (x, y) in a layer, the stress-strain relation is governed by:

$$\{\Delta\sigma_{layer}\}_{x-y} = [D_{T\ layer}]\{\Delta\varepsilon_{\ layer}\}_{x-y} \tag{3.40}$$

where $\{\Delta\sigma_{layer}\}_{x-y}$ and $\{\Delta\varepsilon_{\ layer}\}_{x-y}$ are respectively the stress and strain increment vectors at point (x, y) of the corresponding layer and expressed in reference $(\vec{x}, \vec{y})$.

$$\{\Delta\sigma_{layer}\}_{x-y} = \begin{Bmatrix} \Delta\sigma_{x\ layer} \\ \Delta\sigma_{y\ layer} \\ \Delta\tau_{xy\ layer} \end{Bmatrix} \tag{3.41}$$

$$\{\Delta\varepsilon_{layer}\}_{x-y} = \begin{Bmatrix} \Delta\varepsilon_{x\,layer} \\ \Delta\varepsilon_{y\,layer} \\ \Delta\gamma_{xy\,layer} \end{Bmatrix} \tag{3.42}$$

This definition of strain in layers will be used at the FE level to compute the stiffness matrix.

3.2.2.2. Thickness level

The structural membrane thickness is made of layers. A fundamental hypothesis is to consider perfect bond conditions between the different layers (no sliding between layers is allowed). Furthermore, since membranes are considered (no bending, no out of plane behavior), for any point on the membrane surface located at (x, y), strains and displacements are independent of z (strains and displacements do not vary with the depth z). In other words, for a point located on the membrane surface, displacements and strains in all layers beneath this point are equal.

3.2.2.3. Finite element level

For finite element modeling of membranes, the studied membranes are 2D planar elements, i.e. an 8-node quadrilateral element (Q8) is adopted (refer to Figure 3.5).

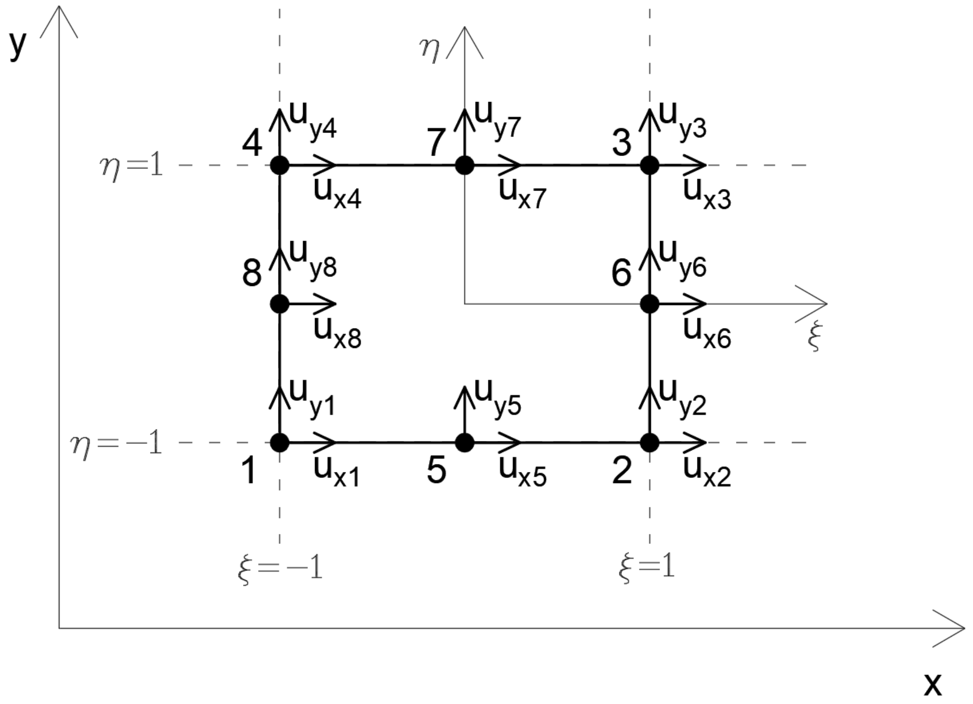

Figure 3.5: Q8 membrane finite element.

Considering a point on the membrane having coordinates (x, y) and a displacement vector

$$\{u\} = \begin{Bmatrix} u_x \\ u_y \end{Bmatrix} \tag{3.43}$$

The strains resulting from the displacement at point (x, y) are:

$$\varepsilon_x(x, y) = \frac{\partial u_x}{\partial x} \tag{3.44}$$

$$\varepsilon_y(x, y) = \frac{\partial u_y}{\partial y} \tag{3.45}$$

$$\gamma_{xy}(x, y) = \frac{\partial u_x}{\partial y} + \frac{\partial u_y}{\partial x} \tag{3.46}$$

Condensing these equations in a matrix form gives:

$$\{\varepsilon(x, y)\} = \begin{Bmatrix} \varepsilon_x(x, y) \\ \varepsilon_y(x, y) \\ \gamma_{xy}(x, y) \end{Bmatrix} = \begin{bmatrix} \frac{\partial}{\partial x} & 0 \\ 0 & \frac{\partial}{\partial y} \\ \frac{\partial}{\partial y} & \frac{\partial}{\partial x} \end{bmatrix} \begin{Bmatrix} u_x \\ u_y \end{Bmatrix} \tag{3.47}$$

To simplify shape functions formulas and later on Gauss point integration, a local reference $(\vec{\xi}, \vec{\eta})$ is considered at the center of the Q8 element which in turn covers the domain of $\xi \in [-1; 1]$ and $\eta \in [-1; 1]$ (refer to Figure 3.5). The previous point located at (x, y) in the global reference, has now local coordinates(ξ, η). The displacement vector $\{u\}$ is calculated in function of nodal displacements via the shape functions.

$$\{u\} = \begin{Bmatrix} u_x \\ u_y \end{Bmatrix} = [N(\xi, \eta)]\{u_{nodes}\} \tag{3.48}$$

with

$$[N(\xi, \eta)] = \begin{bmatrix} N_1(\xi, \eta) & 0 & N_2(\xi, \eta) & 0 & \cdots & N_8(\xi, \eta) & 0 \\ 0 & N_1(\xi, \eta) & 0 & N_2(\xi, \eta) & \cdots & 0 & N_8(\xi, \eta) \end{bmatrix} \tag{3.49}$$

and

$$\{u_{nodes}\} = \begin{Bmatrix} u_{x1} \\ u_{y1} \\ u_{x2} \\ \vdots \\ u_{y8} \end{Bmatrix} \tag{3.50}$$

where u_{x1} to u_{y8} are the displacements of the Q8 element nodes in the global reference $(\vec{x}, \vec{y})$ (refer to Figure 3.5). $N_1(\xi, \eta)$ to $N_8(\xi, \eta)$ are the shape functions for the Q8 finite element model (for further details on shape functions, refer to Appendix B).

$$\begin{Bmatrix} \varepsilon_x(x,y) \\ \varepsilon_x(x,y) \\ \gamma_{xy}(x,y) \end{Bmatrix} = [B(x,y)] \begin{Bmatrix} u_{x1} \\ u_{y1} \\ u_{x2} \\ \vdots \\ u_{y8} \end{Bmatrix} \tag{3.51}$$

with

$$[B(x,y)] = \begin{bmatrix} \frac{\partial N_1(x,y)}{\partial x} & 0 & \frac{\partial N_2(x,y)}{\partial x} & 0 & \cdots & \frac{\partial N_8(x,y)}{\partial x} & 0 \\ 0 & \frac{\partial N_1(x,y)}{\partial y} & 0 & \frac{\partial N_2(x,y)}{\partial y} & \cdots & 0 & \frac{\partial N_8(x,y)}{\partial y} \\ \frac{\partial N_1(x,y)}{\partial y} & \frac{\partial N_1(x,y)}{\partial x} & \frac{\partial N_2(x,y)}{\partial y} & \frac{\partial N_2(x,y)}{\partial x} & \cdots & \frac{\partial N_8(x,y)}{\partial y} & \frac{\partial N_8(x,y)}{\partial x} \end{bmatrix} \tag{3.52}$$

Let $\{\delta u_{nodes}\}$ be a virtual displacement occurring at the nodes of the membrane element. To this displacement corresponds virtual internal strains $\{\delta\varepsilon(x,y)\}$. By applying the virtual work principal, the external system energy $w_{external}$ should be equal to its internal one $w_{internal}$:

$$w_{external} = \{\delta u_{nodes}\}^T \{F_{nodes}\} \tag{3.53}$$

where $\{F_{nodes}\}$ is the force vector applied at the element's nodes.

$$w_{internal} = \int_V \{\delta\varepsilon(x,y)\}^T \{\sigma(x,y,z)\}\, dV \tag{3.54}$$

Since

$$\{\delta\varepsilon(x,y)\} = [B(x,y)]\{\delta u_{nodes}\} \tag{3.55}$$

equation (3.54) becomes:

$$w_{internal} = \int_V \{\delta u_{nodes}\}^T [B(x,y)]^T \{\sigma(x,y,z)\}\, dV \tag{3.56}$$

Since equations (3.53) and (3.56) are equal:

$$\{\delta u_{nodes}\}^T \{F_{nodes}\} = \int_V \{\delta u_{nodes}\}^T [B(x,y)]^T \{\sigma(x,y,z)\}\, dV \tag{3.57}$$

which results in:

$$\{F_{nodes}\} = \int_V [B(x,y)]^T \{\sigma(x,y,z)\}\, dV \tag{3.58}$$

For linear systems, this corresponds to:

$$\{F_{nodes}\} = [K]\{u_{nodes}\} \tag{3.59}$$

where $[K]$ is the stiffness matrix of the membrane element.

Since

$$\{\sigma(x,y,z)\} = [D(x,y,z)]\{\varepsilon(x,y)\} = [D(x,y,z)][B(x,y)]\{u_{nodes}\} \tag{3.60}$$

where $[D(x,y,z)]$ is the elasticity matrix at point (x,y,z), inserting equations (3.59) and (3.60) in equation (3.58) gives:

$$[K]\{u_{nodes}\} = \int_V [B(x,y)]^T [D(x,y,z)][B(x,y)]\{u_{nodes}\}\, dV \tag{3.61}$$

which results in:

$$[K] = \int_V [B(x,y)]^T [D(x,y,z)][B(x,y)]\, dV \tag{3.62}$$

For nonlinear systems, equation (3.58) remains applicable. Since incremental calculation is used in nonlinear calculation, equation (3.62) becomes:

$$[K_T] = \int_V [B(x,y)]^T [D_T(x,y,z)][B(x,y)]\, dV \tag{3.63}$$

with

$$\{\Delta f\} = [K_T]\{\Delta u\} \tag{3.64}$$

where $[K_T]$ is the tangent stiffness matrix of the membrane element, $[D_T(x,y,z)]$ is the tangent elasticity matrix at point (x,y,z) defined in chapter 2, $\{\Delta f\}$ and $\{\Delta u\}$ are respectively the membrane nodal force and displacement vectors increments.

The volumetric integral is decomposed into a linear integral over the membrane thickness and a surface integral over the membrane area.

$$\{F_{nodes}\} = \int_S \; [B(x,y)]^T \left(\int_{-\frac{h}{2}}^{\frac{h}{2}} \{\sigma(x,y,z)\} dz \right) ds \tag{3.65}$$

and

$$[K_T] = \int_S \; [B(x,y)]^T \left(\int_{-\frac{h}{2}}^{\frac{h}{2}} [D_T(x,y,z)] \, dz \right) [B(x,y)] \, ds \tag{3.66}$$

Changing from global variables (x,y) to local variables (ξ,η) gives:

$$\{F_{nodes}\} = \int_{-1}^{1} \int_{-1}^{1} [B(\xi,\eta)]^T \left(\int_{-\frac{h}{2}}^{\frac{h}{2}} \{\sigma(\xi,\eta,z)\} dz \right) det([J]) d\xi d\eta \tag{3.67}$$

and

$$[K_T] = \int_{-1}^{1} \int_{-1}^{1} [B(\xi,\eta)]^T \left(\int_{-\frac{h}{2}}^{\frac{h}{2}} [D_T(\xi,\eta,z)] \, dz \right) [B(\xi,\eta)] det([J]) \, d\xi d\eta \tag{3.68}$$

where $[J]$ is the Jacobian matrix used to transform global variables to local ones.

$$[J] = \begin{bmatrix} \dfrac{\partial x}{\partial \xi} & \dfrac{\partial x}{\partial \eta} \\ \dfrac{\partial y}{\partial \xi} & \dfrac{\partial y}{\partial \eta} \end{bmatrix} \tag{3.69}$$

Since the membrane is made up of layers, the integral along the membrane thickness (axis $\vec{z}$) can be replaced by a summation of layers.

$$\int_{-\frac{h}{2}}^{\frac{h}{2}} \{\sigma(\xi,\eta,z)\} dz = \sum_{i=1}^{n_{layers}} \{\sigma_i(\xi,\eta)\} \, t_i \tag{3.70}$$

and

$$\int_{-\frac{h}{2}}^{\frac{h}{2}} [D_T(\xi,\eta,z)]\,dz = \sum_{i=1}^{n_{layers}} [D_{T\,i}(\xi,\eta)]\,t_i \tag{3.71}$$

where n_{layers} is the number of membrane layers, t_i is the thickness of layer i, $\{\sigma_i(\xi,\eta)\}$ and $[D_{T\,i}(\xi,\eta)]$ are respectively the stress vector and the tangent elasticity matrix of layer i at point (ξ,η). Inserting equation (3.70) in (3.67) gives:

$$\{F_{nodes}\} = \int_{-1}^{1}\int_{-1}^{1} [B(\xi,\eta)]^T \left(\sum_{i=1}^{n_{layers}} \{\sigma_i(\xi,\eta)\}\,t_i \right) det([J]) d\xi d\eta \tag{3.72}$$

Inserting equation (3.71) in (3.68) gives:

$$[K_T] = \int_{-1}^{1}\int_{-1}^{1} [B(\xi,\eta)]^T \left(\sum_{i=1}^{n_{layers}} [D_{T\,i}(\xi,\eta)]\,t_i \right) [B(\xi,\eta)] det([J])\,d\xi d\eta \tag{3.73}$$

The force vector applied on membrane nodes $\{F_{nodes}\}$ and the membrane tangent stiffness matrix $[K_T]$ can now be calculated by surface Gauss point integration.

Let us define to functions f and g:

$$f(\xi,\eta) = [B(\xi,\eta)]^T \left(\sum_{i=1}^{n_{layers}} \{\sigma_i(\xi,\eta)\}\,t_i \right) det([J]) \tag{3.74}$$

and

$$g(\xi,\eta) = [B(\xi,\eta)]^T \left(\sum_{i=1}^{n_{layers}} [D_{T\,i}(\xi,\eta)]\,t_i \right) [B(\xi,\eta)] det([J]) \tag{3.75}$$

Considering a 4-point Gauss quadrature rule leads to:

$$\{F_{nodes}\} = \int_{-1}^{1}\int_{-1}^{1} f(\xi,\eta)\,d\xi d\eta \cong \sum_{p=1}^{4} W_p f(\xi_p,\eta_p) \tag{3.76}$$

and

$$[K_T] = \int_{-1}^{1}\int_{-1}^{1} g(\xi,\eta)\, d\xi d\eta \cong \sum_{p=1}^{4} W_p g\left(\xi_p,\eta_p\right) \tag{3.77}$$

Where W_p and $\left(\xi_p,\eta_p\right)$ are respectively the integration weight of Gauss point p and its local coordinates (for further details on Gauss points, refer to Appendix B).

3.3. Experimental validation in static

In order to validate the proposed Finite Element (FE) models, a comparison between experimental results and numerical simulation was made. The considered experiment is well detailed in (Thomsen and Wallace, 2004; Orakcal and Wallace, 2006). It consists of a reinforced concrete wall designated by “RW2” with a height of 3.66 m, width of 1.22 m and a thickness of 10.2 cm (refer to Figure 3.6).

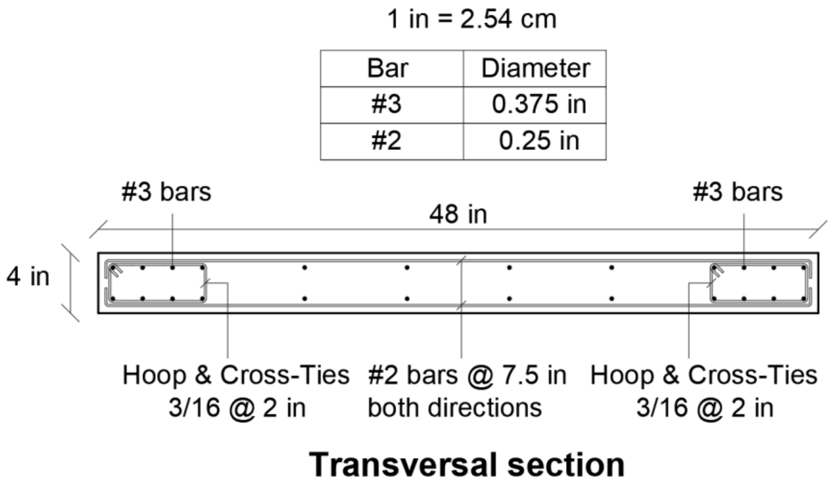
1 in = 2.54 cm

Bar	Diameter
#3	0.375 in
#2	0.25 in

Figure 3.6: Geometry and reinforcements of the experimental wall.

The wall is initially compressed by a post-tensioning mechanism that generates a uniform vertical compressive stress in the element equal to 7% of the concrete stress strength. Then, this experimental structure is subjected to a quasi-static cyclic imposed displacement on its top via a hydraulic actuator (refer to Figure 3.7 and Figure 3.8). Finally, the applied load on top is plotted versus the lateral displacement.

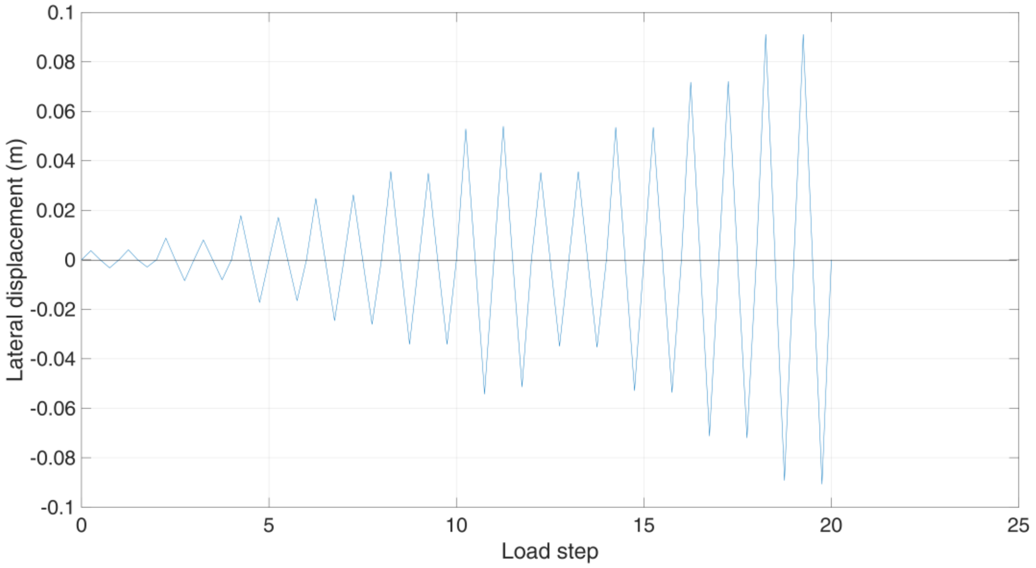

Figure 3.7: Imposed displacement at the top of the experimental wall.

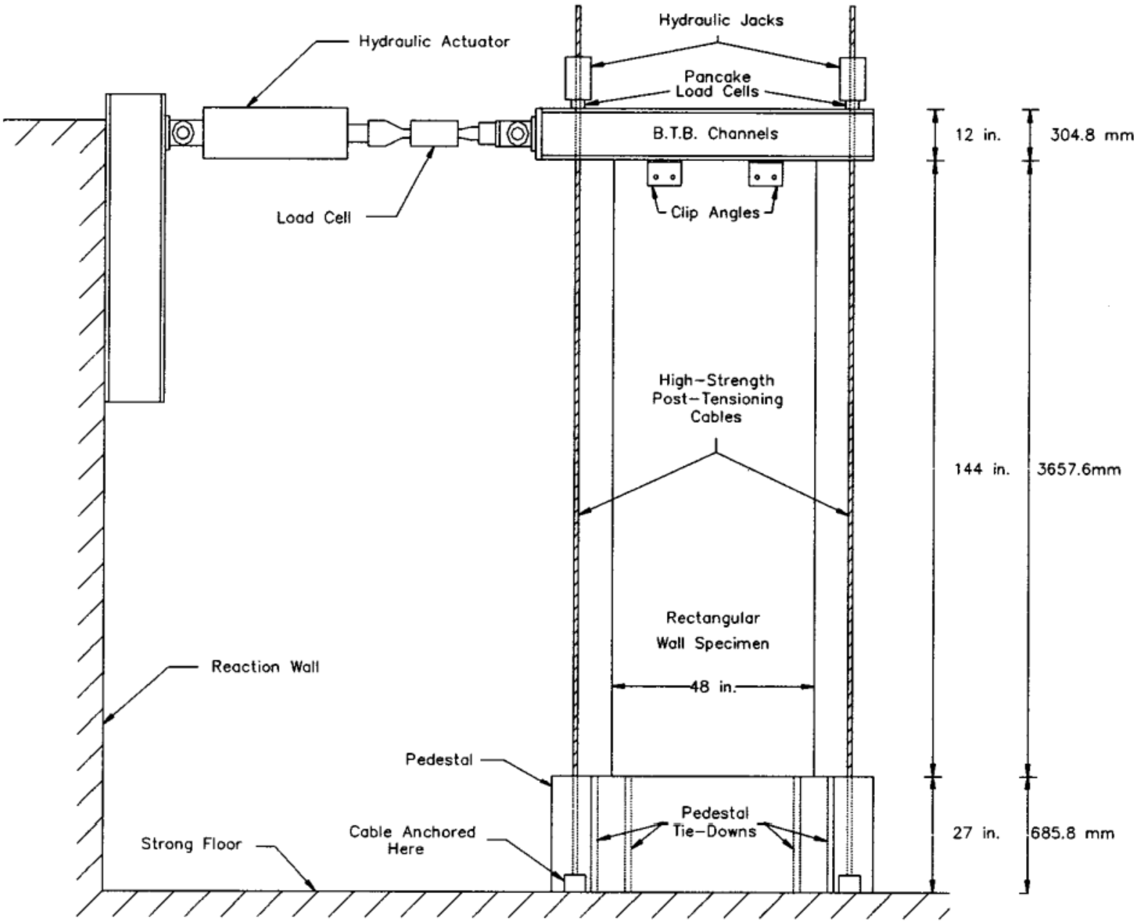

Figure 3.8: Experimental setup (Thomsen and Wallace, 2004).

We tried to recreate the same experimental conditions in the numerical model. Since the experiment is piloted by displacement, displacement control nonlinear solver was used (for further details on displacement control nonlinear calculation refer to Appendix A). The material backbone curves were taken as specified in (Thomsen and Wallace, 2004; Orakcal and Wallace, 2006) and hysteresis behavior was modeled according to the choice made in chapter 2. In the following, the multifiber beam and layered membrane wall are both tested numerically and their results compared with the experimental data. In a first approach, the wall is modeled as an equivalent column with multifiber section and divided into three FE (refer to Figure 3.9 and Figure 3.10).

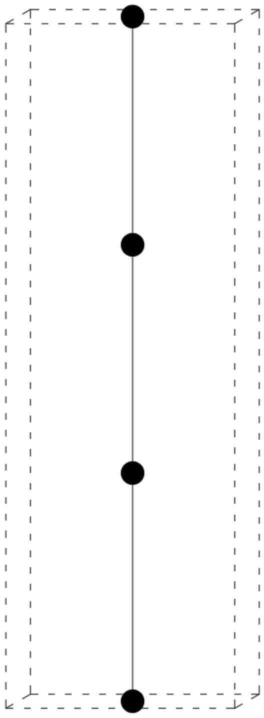

Figure 3.9: Equivalent column model meshing.

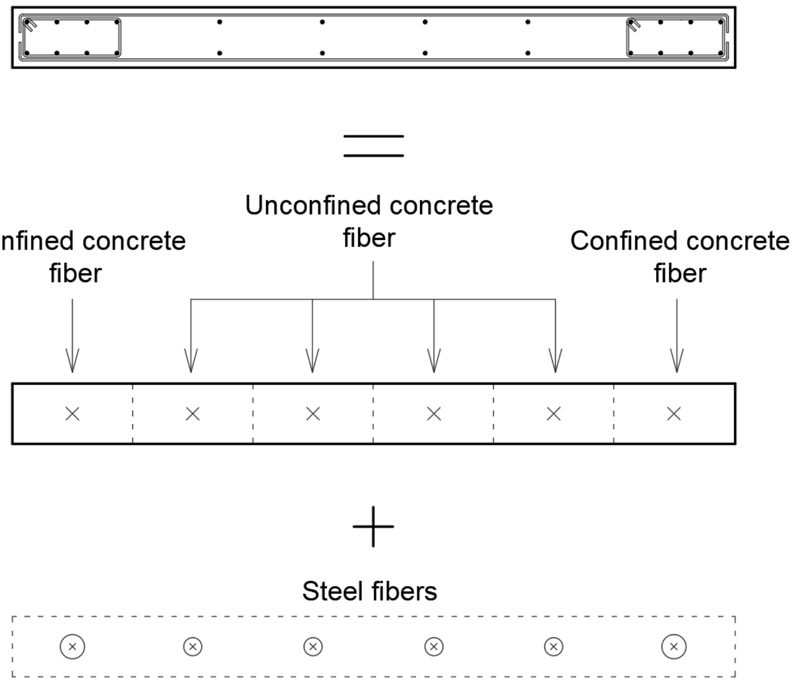

Figure 3.10: Multifiber section of equivalent column model.

The top force-displacement responses for numerical multifiber model and experiment are compared (refer to Figure 3.11).

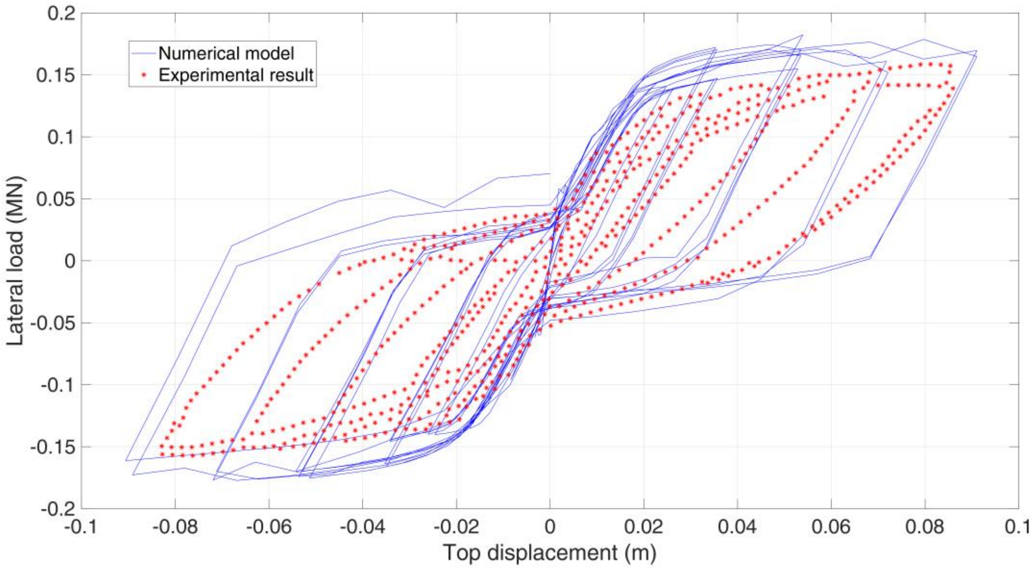

Figure 3.11: Column numerical model result Versus experiment.

It can be seen that the numerical model gave very close results to the experiment. However, the numerical hysteresis loops seem to have a slightly higher slope than the real behavior and this could be a consequence for neglecting the Bauschinger effect in the numerical steel model.

In a second approach, the wall is modeled using the layered membrane approach and divided into a mesh of 6 by 18 elements (refer to Figure 3.12 and Figure 3.13).

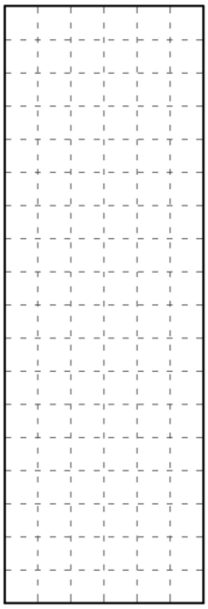

Figure 3.12: Wall mesh using the layered membrane approach.

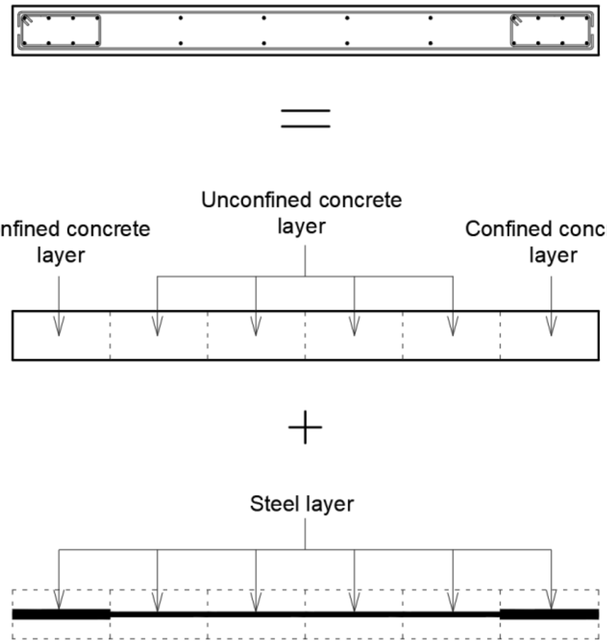

Figure 3.13: Layers of wall model.

The top force-displacement responses for numerical and experimental approaches are compared (refer to Figure 3.14).

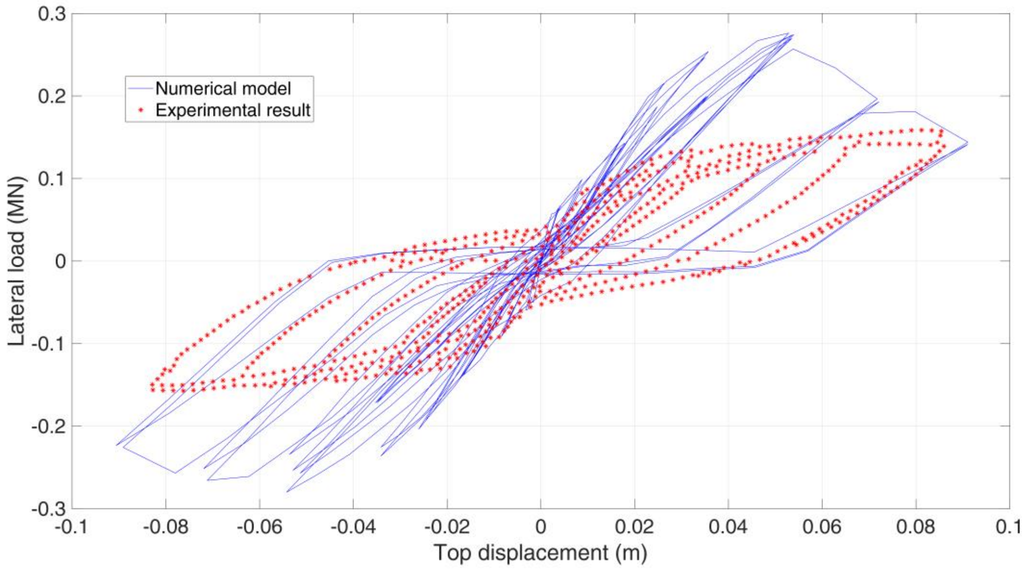

Figure 3.14: Wall numerical model result Versus experiment.

It is clear that there are some differences in force strength, but the overall shape of hysteresis loops is similar. Due to the complexity of concrete nonlinear biaxial behavior and the simplifying assumptions made in chapter 2, it is expected for the layered membrane model to be less accurate than the multifiber element model. However, this is not a major concern since the main objective of this thesis is to test the efficiency and accuracy of reduced dynamic models containing material nonlinearity with respect to the full numerical models.

3.4. Conclusions

The goal of this chapter is to describe the finite element implementation and validation of the two structural models with material nonlinearities adopted in chapter 2 (multifiber element and layered membrane). For both models, the implementation is based on a 3-level analysis: a fiber/layer level incorporating the nonlinear constitutive models of each constituent of reinforced concrete, a cross section/thickness level where kinematic assumptions are made, and a finite element level where the nodal force vector and the tangent stiffness matrix are calculated by a volumetric integral over the whole element. This volumetric integration is conducted in two steps: first a summation at the cross section/thickness level then followed by a 1D/2D Gauss point integration.

3.4. Conclusions

Both multifiber elements and layered membranes numerical models were compared with experimental results and thus will be considered as valid models for use in the following chapters. Also, it should be noted that for these models a displacement-based finite analysis was used. This means that shape functions corresponding to linear behavior were used for elements presenting material nonlinearity. To minimize the error resulting from this process, a fine meshing is required in zones of nonlinearities if typical mesh size was relatively large.

Chapter 4

4. POD model order reduction

Abstract: *This chapter presents the concept of the Proper Orthogonal Decomposition (POD) reduction technique in addition to its applications for computational time reduction for nonlinear dynamic structural analysis. Numerical algorithms are introduced for POD applications on multistorey frame Reinforced Concrete (RC) structure and RC planar shear wall.*

Chapter content

4.1. Introduction

As seen in chapter 1, for nonlinear seismic analysis, the pushover is sometimes not enough since it provides only maximum responses and is solely applicable to regular structures. On the other hand, the complete nonlinear time history analysis is very time consuming. Consequently, the purpose of this thesis is to reduce the time cost of the nonlinear time history analysis by using a reduced dynamic model.

Various techniques exist for dynamic model reduction of linear systems. The modal truncation is the most common. This approach consists in projecting the dynamic system on a reduced basis made up of the most important vibration modes. Vibration modes are independent of the applied loading while the Krylov subspace method constructs a reduction basis depending on the loads applied on the structure. Reduction techniques proposed by (Guyan, 1965; Craig and Bampton, 1968) are based on reducing the total number of degrees of freedom (DOF) in the structure by coupling the internal DOF with the external ones. Additional modal truncation techniques can be found in (Besselink *et al.*, 2013)

For nonlinear dynamic systems, reduction techniques get more difficult due to complicated nonlinear relations governing the return force of the system. For dynamic nonlinear models, the potentially useful reduction techniques highlighted in several works such as (Djukic and Saric, 2012; Mahdiabadi, 2019; Shen *et al.*, 2021) are :

- Model linearization approach: consists mainly in dividing the nonlinear model to a combination of linear models. Each of these linear models is capable of recreating the nonlinear behavior locally in a portion of the model (called expansion point). Then, these linear models are gathered via a weighted combination. The main issue with this approach is the choice of the number of expansion points and the weight coefficient for each one.
- Implicit Condensation (IC): in this approach, a set of statical loads corresponding to low frequency linear vibration modes are applied on the structure to construct a manifold used to reduce the nonlinear dynamics. The accuracy of this approach is dependent on the choice of static loading sets.
- Enforced Displacement (ED): in this approach, imposed displacements sets are applied on the structure to construct a manifold used to reduce the nonlinear dynamics. The accuracy of this approach is dependent on the choice of the imposed displacement sets.

- Proper Orthogonal Decomposition (POD): A reduction basis is deducted by analyzing snapshots taken of the full vibrating model. The disadvantages of this method are that a full model analysis is required to obtain the snapshots and that it is a load-dependent technique.

In this thesis, the Proper Orthogonal Decomposition (POD) is adopted for model reduction and adapted to reduce the impact of the required initial full model analysis. In the frame of seismic analysis, structures are subjected to base excitations. So, in theory, the inertial load pattern distribution on the structure is the same for all excitations which will help in limiting the load-dependency effect of the POD method.

4.2. Generalities on the POD approach

Classically, modal analysis is an exclusive tool for linear elastic structural systems since it requires having an invariant stiffness matrix. However, going back to its basic physical concept, this method is based on presenting the dynamic behavior of the structure as a function of the principal and most influential components of the structural vibration (modes of vibration).

Trying to find the principal components of vibration in a nonlinear system is not a straightforward task. In fact, direct computational approaches are very complicated (almost impossible) due to the nonlinearity in the system. However, if the nonlinear structure was previously exposed to a base excitation and vibration response data (displacement vectors) were recorded, the sought principal vibration components can be determined via a Proper Orthogonal Decomposition (POD) of the response data.

The POD dates back to the early twentieth century, (Hotelling, 1933) was among the first to introduce this technique which was later addressed by (Kosambi, 1943; Karhunen, 1946; Loève, 1948; Pugachev, 1953; Obukhov, 1954). It should be noted that POD is also called Karhunen-Loève decomposition. Today, the POD method is applied for model reduction of turbulent flow in fluid mechanics, model reduction of structural dynamics, damage detection, reduction of dynamic models for microelectromechanical systems and in lots of other domains.

A portion of the following is extracted from the author's conference paper (Ayoub *et al.*, 2021) with slight modifications. The POD is a data driven-method based on the statistical Principal Component Analysis (PCA) of observation dataset. Let us consider a data matrix $[X]$ containing n observation vectors $[X] = [\{X_1\} \quad \cdots \quad \{X_n\}]$ and each observation vector (displacement vector) a m-dimensional vector.

$$[X] = [\{X_1\} \quad \cdots \quad \{X_n\}] = \begin{bmatrix} x_{11} & \cdots & x_{1n} \\ \vdots & \ddots & \vdots \\ x_{m1} & \cdots & x_{mn} \end{bmatrix} \tag{4.1}$$

Each row i of matrix $[X]$ is denoted $\{S_i\} = \{x_{i1} \quad \cdots \quad x_{in}\}$ and represents all the data collected on dimension i. If data set $\{S_i\}$ $\forall$ i has a zero mean, the variance of $\{S_i\}$ becomes:

$$\begin{aligned} \sigma^2(\{S_i\}) &= \frac{1}{n-1} \times \sum_{k=1}^{n} \big(x_{ik} - mean(\{S_i\})\big)^2 = \frac{1}{n-1} \times \sum_{k=1}^{n} (x_{ik})^2 \\ &= \frac{1}{n-1} \{S_i\}\{S_i\}^T \end{aligned} \tag{4.2}$$

and the covariance of $\{S_i\}$ and $\{S_j\}$ becomes:

$$COV\big(\{S_i\}, \{S_j\}\big) = \frac{1}{n-1} \times \sum_{k=1}^{n} \big(x_{ik} - mean(\{S_i\})\big) \Big(x_{jk} - mean\big(\{S_j\}\big)\Big) \tag{4.3}$$

and can be expressed as:

$$COV\big(\{S_i\}, \{S_j\}\big) = \frac{1}{n-1} \times \sum_{k=1}^{n} (x_{ik})\big(x_{jk}\big) = \frac{1}{n-1} \{S_i\}\{S_j\}^T \tag{4.4}$$

High value of $\sigma^2(\{S_i\})$ indicates high action on dimension i and vice versa. High value of $COV\big(\{S_i\}, \{S_j\}\big)$ indicates high similarity between the actions on dimension i and dimension j. On the other hand, $COV\big(\{S_i\}, \{S_j\}\big) = 0$ indicates zero resemblance (total independence) between the actions on dimension i and dimension j. If the data set $\{S_i\}$ $\forall$ i has a zero mean, the covariance of matrix $[X]$ becomes:

$$COV([X]) = \frac{1}{n-1} [X][X]^T \tag{4.5}$$

such that:

$$\begin{aligned} &COV([X]) \\ &= \begin{bmatrix} \sigma^2(\{S_1\}) & COV(\{S_1\}, \{S_2\}) & \cdots & COV(\{S_1\}, \{S_n\}) \\ COV(\{S_2\}, \{S_1\}) & \sigma^2(\{S_2\}) & \cdots & COV(\{S_2\}, \{S_n\}) \\ \vdots & \vdots & \ddots & \vdots \\ COV(\{S_n\}, \{S_1\}) & COV(\{S_n\}, \{S_2\}) & \cdots & \sigma^2(\{S_n\}) \end{bmatrix} \end{aligned} \tag{4.6}$$

Let $[N]$ be the matrix regrouping the principal components vectors of the data matrix $[X]$. Since principal components are independent, $[N]$ will form an orthonormal reference. Expressing the initial data matrix $[X]$ in this orthonormal reference will result in matrix $[X'] = [N]^T[X]$. Since zero similarity is expected between actions on different dimensions of $[N]$, $COV([X'])$ should be a diagonal matrix ($COV(\{S'_i\},\{S'_j\}) = 0 \; for \; i \neq j$).

$COV([X])$ is made up of $[X][X]^T$ which is a symmetrical matrix and thus has real eigenvalues.

$$[X][X]^T[\emptyset] = [\emptyset][\lambda] \tag{4.7}$$

where $[\emptyset]$ is the eigenvectors matrix and $[\lambda]$ is the diagonal matrix containing the eigenvalues. Eigenvectors are orthonormal vectors and it can be demonstrated that $[\emptyset]$ is the matrix regrouping the principal components vectors of data matrix $[X]$ ($[N] = [\emptyset]$). In fact, for $[X'] = [\emptyset]^T[X]$ we get:

$$COV([X']) = \frac{1}{n-1}[X'][X']^T = \frac{1}{n-1}[\emptyset]^T \underbrace{[X][X]^T[\emptyset]}_{[\emptyset][\lambda]} = [\lambda] \tag{4.8}$$

$COV([X'])$ is a diagonal matrix where $\sigma^2(\{S'_i\}) = \lambda_i$. We notice that the higher λ_i is, the more we have actions on dimension i in the eigenvectors reference. As a conclusion, principal components of the data set $[X]$ are the eigenvectors of $[X][X]^T$ and modes with high eigenvalues are the most influential in representing $[X]$.

Another way of determining the principal components of a data observation matrix $[X]$ is by the Singular Value Decomposition SVD. Any matrix $[X] \in \mathbb{R}^{m\times n}$ can be decomposed to the product of 3 matrices $[U] \in \mathbb{R}^{m\times m}$, $[\Sigma] \in \mathbb{R}^{m\times n}$ and $[V] \in \mathbb{R}^{n\times n}$

$$[X] = [U][\Sigma][V]^T \tag{4.9}$$

$[U]$ and $[V]$ are made up orthonormal vectors, $[\Sigma]$ is a diagonal matrix with positive values placed in the decreasing order. Since $[U]$ and $[V]$ are orthonormal then $[U]^{-1} = [U]^T$ and $[V]^{-1} = [V]^T$.

$$[X][X]^T = [U][\Sigma][V]^T[V][\Sigma]^T[U]^T = [U][\Sigma][\Sigma]^T[U]^T \tag{4.10}$$

and

$$[X][X]^T \underbrace{[U]}_{[\emptyset]} = \underbrace{[U]}_{[\emptyset]} \underbrace{[\Sigma][\Sigma]^T}_{[\lambda]} \tag{4.11}$$

$[U]$ is the eigenvectors matrix of $[X][X]^T$ and $[\Sigma][\Sigma]^T$ is the diagonal matrix containing the eigenvalues. We conclude that the principal components of the data set $[X]$ are found in $[U]$ and $[\Sigma]$ contains the square root of the eigenvalues on its diagonal.

The orthogonal eigenvectors obtained are called POD modes and the corresponding eigenvalues are called Proper Orthogonal Values (POV). The POD modes can be used to reconstruct the initial data matrix $[X]$. The higher the POV is, the more essential its corresponding POD mode is in recreating $[X]$.

By considering the most important s POD modes ($s < m$) and placing them in $[T] \in \mathbb{R}^{m\times s}$, the $\{X_t\}$ snapshot vector previously expressed in m dimensions can now be approximated in the lower s dimensions.

$$\underbrace{\{X_t\}}_{\in\mathbb{R}^{m\times 1}} \cong \underbrace{[T]}_{\in\mathbb{R}^{m\times s}} \underbrace{\{Q_t\}}_{\in\mathbb{R}^{s\times 1}} \tag{4.12}$$

with the following error:

$$error = \sum_{i=1}^{n} \left\| \{X_{t_i}\} - [T]\{Q_{t_i}\} \right\| \tag{4.13}$$

where $\{Q_t\}$ contains the coordinates of the snapshot vector in the new reference $[T]$. Choosing the optimum number s of POD modes to consider in the reduced new reference is a delicate task. In fact, considering a small number of POD modes will increase the efficiency of the reduction process but the approximation errors will be more significant. On the other hand, increasing the number of POD modes will reduce the approximation errors but also the efficiency of the reduction process. For this reason, the optimal number of POD modes to consider is based on an energy criterion. In fact, the POV of a mode gives an indication on the energy carried by this mode. Classically, the first s POD modes carrying at least 99% of the total system energy are considered as optimal choice for the new reduced reference.

$$\frac{\sum_{i=1}^{s} \lambda_i}{\sum_{j=1}^{m} \lambda_j} \geq 99\% \tag{4.14}$$

4.3. Application to nonlinear structural dynamic models

In structural dynamics, the POD Reduced Order Model (POD-ROM) can be applied to the direct integration time history analysis for linear or nonlinear structures. Since observations (snapshot matrix) are required to calculate the POD modes, a classical Full Model (FM) implicit direct integration time history analysis should be carried out initially for the structure subjected to a specific base excitation. Let's consider a nonlinear structural system with m degrees of freedom and n snapshots were taken from the initial FM analysis. We calculate the POD modes and POV of the data matrix $[X]$ and then choose the subspace $[T] \in \mathbb{R}^{m\times s}$ made of the first s POD modes satisfying the truncation criterion. The dynamic equation of the nonlinear system is:

$$[M]\{\ddot{X}(t)\} + [C]\{\dot{X}(t)\} + \{F_{NL}(\{X(t)\})\} = \{F(t)\} \tag{4.15}$$

In this chapter, it should be noted that displacement vectors are indicated by $\{X(t)\}$ instead of $\{U(t)\}$ because U is used in the Singular Value Decomposition (refer to equation (4.9)). By replacing the displacement vector $\{X(t)\}$ and its derivatives by $[T]\{Q(t)\}$ and multiplying both sides of the dynamic equation by $[T]^T$ we get:

$$\underbrace{[M_r]}_{\in\mathbb{R}^{s\times s}}\{\ddot{Q}(t)\} + \underbrace{[C_r]}_{\in\mathbb{R}^{s\times s}}\{\dot{Q}(t)\} + \underbrace{\{F_{NL\ r}([T]\{Q(t)\})\}}_{\in\mathbb{R}^{s\times 1}} = \underbrace{\{F_r(t)\}}_{\in\mathbb{R}^{s\times 1}} \tag{4.16}$$

with

$$\begin{cases} [M_r] = [T]^T[M][T] \\ [C_r] = [T]^T[C][T] \\ \{F_{NL\ r}([T]\{Q(t)\})\} = [T]^T\{F_{NL}([T]\{Q(t)\})\} \\ \{F_r(t)\} = [T]^T\{F(t)\} \end{cases} \tag{4.17}$$

The previously m degrees of freedom dynamic system are reduced to s degrees of freedom. However, the nonlinear restoring force $\{F_{NL}([T]\{Q(t)\})\}$ cannot be reduced and always needs to be calculated in the full coordinate model which makes this step the most time-consuming part of the entire process. Due to this setback and in order to maintain an effective computation time saving, the need for calculating the nonlinear restoring force should be kept minimum during the direct time-integration analysis of the reduced model.

Implicit direct time-integration techniques are usually used in conjunction with the Newton-Raphson approach for solving nonlinear systems. At each time step, multiple iterations are needed to achieve convergence. For every iteration, the calculation of the tangent stiffness matrix and the nonlinear restoring force is required which is time consuming. Using the modified or constant stiffness Newton-Raphson approach will reduce or stop the need for the tangent stiffness calculation. However, the number of iterations required for convergence at each time step will grow, thus increasing the number of calls for nonlinear restoring force calculation.

On the other hand, for explicit direct time-integration techniques, the popular central difference method requires no iterations per time step and no expensive calculation of the tangent stiffness matrix. The expensive nonlinear restoring force is only calculated once per time step. However, the central difference approach is conditionally stable and needs to satisfy the following stability condition:

$$\Delta t < \frac{2}{\omega_{max}} \tag{4.18}$$

where Δt is the time step and ω_{max} is the largest natural pulsation of the system. In the FM analysis, the structure has a relatively large number of degrees of freedom which will result in high natural pulsations. In order to satisfy the stability condition, relatively small-time steps should be adopted for the explicit central difference method thus increasing the computational cost. Therefore, the implicit Newmark-β method will be considered for the full dynamic model analysis in this work. On the other hand, for reduced model analysis, the reduced structure has significantly fewer number of degrees of freedom which will yield relatively smaller natural pulsations thus making it possible to use larger time steps in the explicit central difference method while respecting the stability condition. As a consequence, this explicit central difference method is very effective and will be used in this work for the reduced dynamic systems.

For structural dynamics application, the 99% energy truncation criterion alone is not sufficient. In fact, for a better POD modes truncation, the cumulated modes' energy should be considered and each supplementary mode has to be assessed for the additional energy it brings. Thus, the cumulated POV in function of the mode number $f(s) = \sum_{i=1}^{s} \lambda_i$ is plotted and truncation is made when additional modes stop bringing a remarkable energy. In other words, truncation is made where the curve forms an elbow transition from an increasing part to a relatively stable part (refer to Figure 4.1).

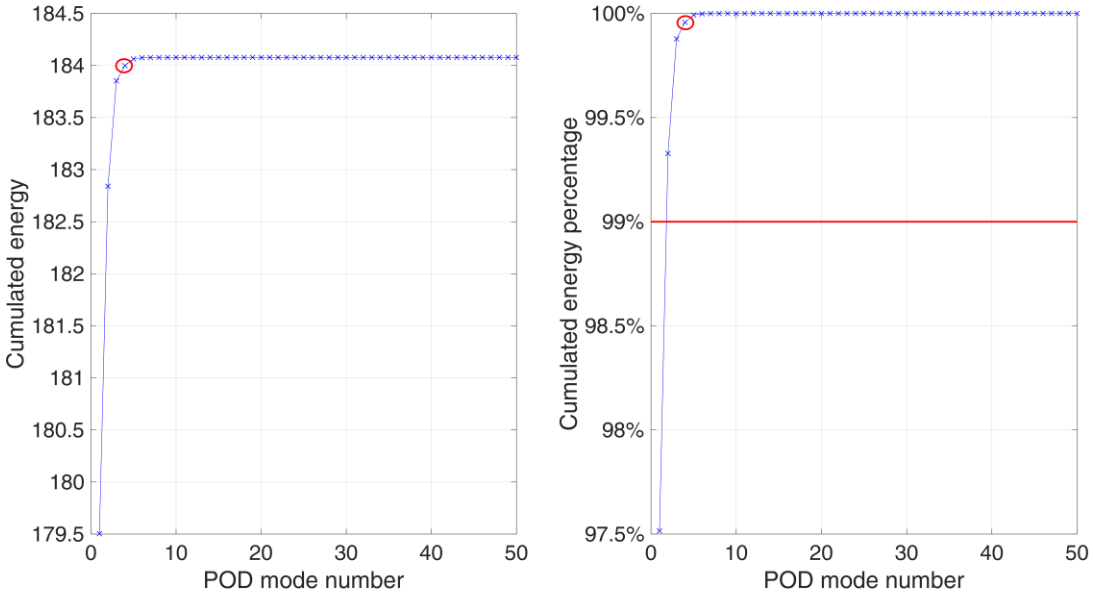

Figure 4.1: Example of POD modal truncation.

As already made clear, the time-consuming FM implicit nonlinear direct time-integration analysis should be carried out initially in order to get the snapshot matrix. Then, POD modes can be calculated, and the structural system reduced. Since there is no escape from this initial time-consuming FM analysis, various techniques have been proposed to benefit from the POD modes after conducting the initial costly analysis. In (Bamer and Bucher, 2012), the dynamic analysis cost of a steel frame structure with nonlinear seismic base isolation is reduced by initially conducting the expensive FM analysis on a portion of the base excitation. Then, snapshots were taken, the POD modes calculated, the dynamic system reduced and the response corresponding to the remaining part of the base excitation was calculated using the time saving reduced model (refer to Figure 4.2).

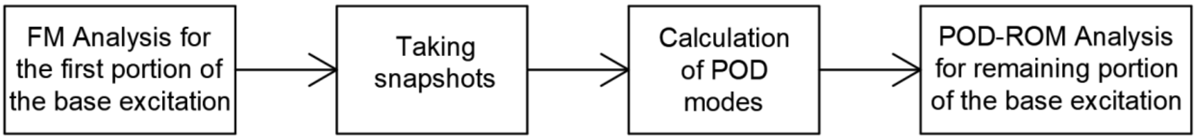

Figure 4.2: POD-ROM process for single base excitation.

Generally, in structural seismic design the structure is studied for a range of possible earthquakes and is analyzed and checked for each excitation (earthquake record) separately. So, (Bamer, Amiri and Bucher, 2017) reduced the analysis cost of a linear reinforced concrete structure with nonlinear seismic base isolation subjected to multiple base excitations. First, they conducted the expensive FM analysis for only one base excitation.

Then they extracted the snapshot matrix, calculated the POD modes and used the time saving reduced dynamic model for the calculation of the remaining base excitations (refer to Figure 4.3).

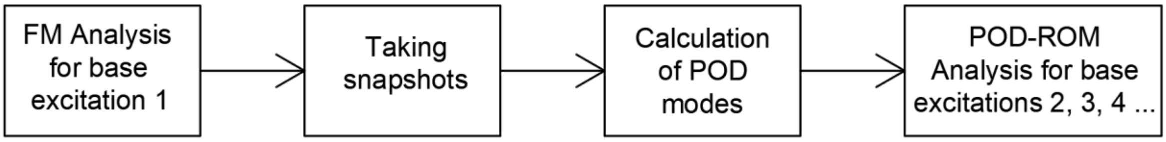

Figure 4.3: POD-ROM process for multiple base excitations.

One original contribution of this thesis is to reduce the dynamic model of a reinforced concrete multistory frame structure or shear wall with material nonlinearities (originating simultaneously from steel reinforcements, confined and unconfined concrete).

4.4. Numerical implementation

To test the accuracy and efficiency in time saving of the POD Reduced Order Model (POD-ROM), comparisons were made between numerical applications for Full Model (FM) and POD-ROM dynamic nonlinear analysis of structures subjected to base excitations. All numerical applications used in this thesis were developed from scratch using MATLAB. The time-consuming FM analysis applications serve as a base reference for comparison purpose and were developed for Reinforced Concrete (RC) multistory frame structure with multifiber elements and also for RC shear wall with layered membrane elements.

The flow chart for computing the response of the full model for RC structures is presented in Algorithm 1. In step 3 of this algorithm, a nonlinear dynamic Newmark direct integration time history analysis is performed as described in 1.6.1 and Appendix A. At each iteration, the nonlinear internal return force and the tangent stiffness matrix are calculated at every nonlinear finite element using respectively the equations (3.34) and (3.35) and for multifiber elements (respectively equations (3.76) and (3.77) for layered membrane elements).

Algorithm 1: FM analysis for RC structures

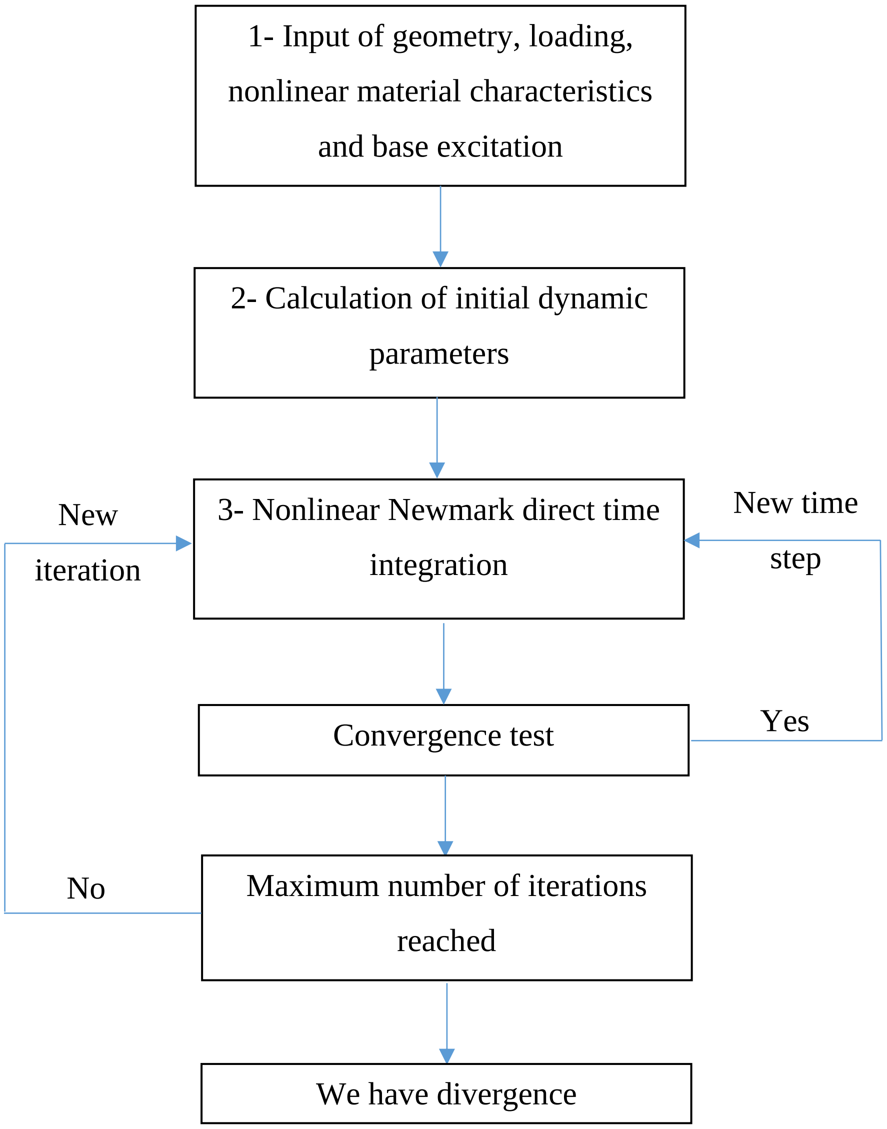

Similarly, POD-ROM analyses were developed for single base excitation (as described in Figure 4.2) and multibase excitation processes (as described in Figure 4.3) The flow chart for computing the response of the POD-ROM for RC structures subjected to single base excitations is given in Algorithm 2.

In step 2 of this algorithm, POD modes are extracted by the Singular Value Decomposition (SVD) and truncated as described in 4.3.

In step 3, the dynamic model is reduced by using equation (4.16).

In step 4, the nonlinear dynamic direct integration time history analysis by central difference is performed as described in 1.6.2. The internal return force used in equation (1.53) is calculated at each finite element level by using equation (3.34) for multifiber elements and equation (3.76) for layered membranes. It should be noted that for particular cases where the central difference approach displays instability problems, a smaller time step can be used or a reduced nonlinear dynamic Newmark direct integration time history analysis can be conducted.

Algorithm 2: POD-ROM for RC structures subjected to single base excitation

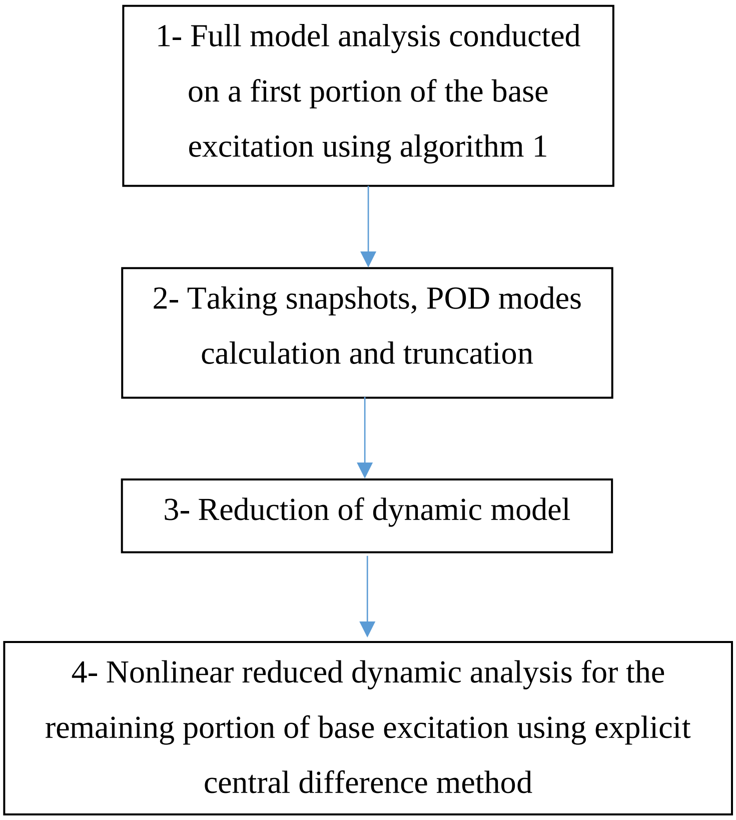

The flow chart for computing the response of the POD-ROM for RC structures subjected to multiple base excitations is given in Algorithm 3.

In step 1 of this algorithm, the FM analysis is not required for the entire time length of the considered base excitation. It is only needed for the interval where snapshots are to be taken.

In step 2, POD modes are extracted by the Singular Value Decomposition (SVD) and truncated as described in 4.3.

In step 3, the dynamic model is reduced by using equation (4.16).

In step 4, the nonlinear dynamic direct integration time history analysis by central difference is performed as described in 1.6.2. The internal return force used in equation (1.53) is calculated at each finite element level by using equation (3.34) for multifiber elements and equation (3.76) for layered membranes. It should be noted that for particular cases where the central difference approach displays instability problems, a smaller time step can be used or a reduced nonlinear dynamic Newmark direct integration time history analysis can be conducted.

Algorithm 3: POD-ROM for RC structures subjected to multiple base excitations

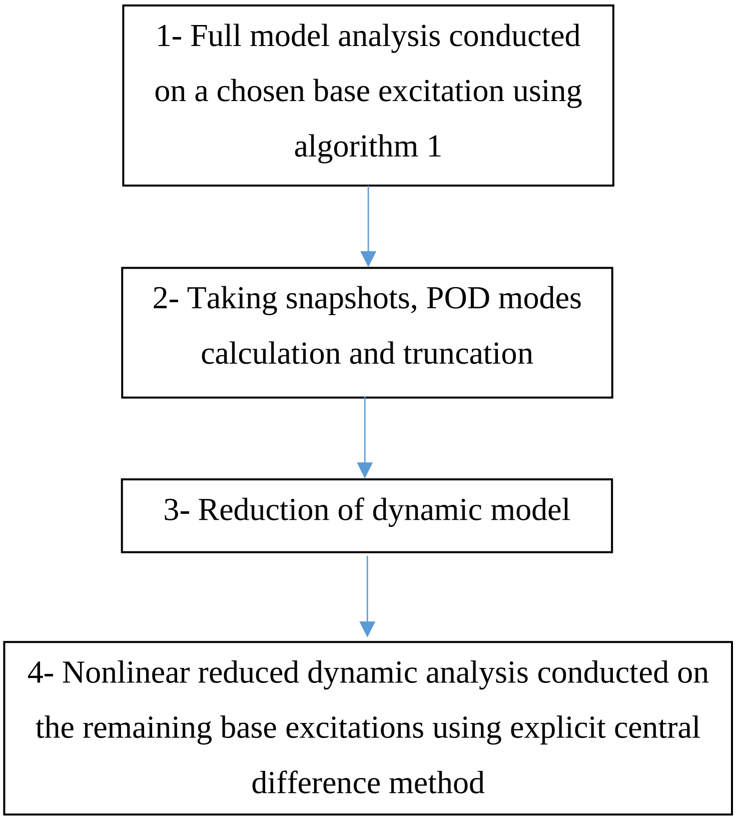

4.5. Conclusions

In this chapter, the concept of the POD method and its application to the model reduction of nonlinear dynamic analysis were detailed. The first issue with the POD-ROM process is its dependency on initial observation data. In other words, a FM time costly analysis is required prior to reducing the dynamic model. This obstacle was softened using propositions made by (Bamer and Bucher, 2012; Bamer, Amiri and Bucher, 2017) respectively for single and multiple base excitations.

One original contribution of this work is by using the propositions of (Bamer and Bucher, 2012; Bamer, Amiri and Bucher, 2017) for the first time on reduced order nonlinear dynamic analysis of a multistory RC frame structure with material nonlinearities modeled via multifiber elements. Also, a first application was made on a POD-ROM of a multistory RC shear wall with material nonlinearities modeled via layered membrane elements. The material nonlinearities originate simultaneously from steel reinforcements, confined and unconfined concrete.

The second problem encountered with the POD-ROM process is that nonlinear return force in the dynamic analysis cannot be calculated in the reduced basis, its calculation had to be done in the time costly full model basis. To minimize the need for this expensive calculation, explicit direct time integration techniques were used when possible.

Numerical algorithms were proposed to compare FM and POD-ROM. Applications of these algorithms are made in the following chapter to test the efficiency and accuracy of the reduction techniques on RC structures with material nonlinearities.

Chapter 5

5. Application to seismic analysis

Abstract: *This chapter presents examples applying Proper Orthogonal Decomposition (POD) reduction techniques for nonlinear dynamic analysis of Reinforced Concrete (RC) multistorey frame structure and RC planar shear wall. The efficiency and accuracy of the proposed reduction techniques are assessed by comparing numerical results from the full and the reduced model.*

Chapter content

5.1. Introduction

In this chapter, a RC multistory frame structure and a shear wall structure were numerically studied using the MATLAB applications developed during this thesis. To assess the accuracy and time saving potential of the POD-ROM techniques proposed in Chapter 4, a comparison in terms of computational time, displacement results, internal forces and stresses was made with full order models. The computer used is equipped with Intel Xeon CPU @ 2.50 GHz with 64 GB RAM.

4 earthquake recordings obtained from the Center of Engineering for Strong Motion Data (*CESMD*, website) were considered (refer to Table 5.1 and Figure 5.1).

Earthquake	Location	Date	Magnitude	Measurement station	Vibration direction	Total duration	Time step
Northridge	Los Angeles, USA	01/17/1994	6.4 ML	Newhall LA county fire station	0°	60s	20ms
Elcentro	California, USA	05/18/1940	6.9 Mw	Elcentro	0°	53.74s	20ms
L’Aquila	L’Aquila, Italy	04/06/2009	6.3 Mw	L'Aquila V.Aterno Centro Valle	90°	60s	20ms
Chile	Off the coast of central Chile	02/27/2010	8.8 Mw	Constitucion city	90°	120s	20ms

Table 5.1: Earthquakes data.

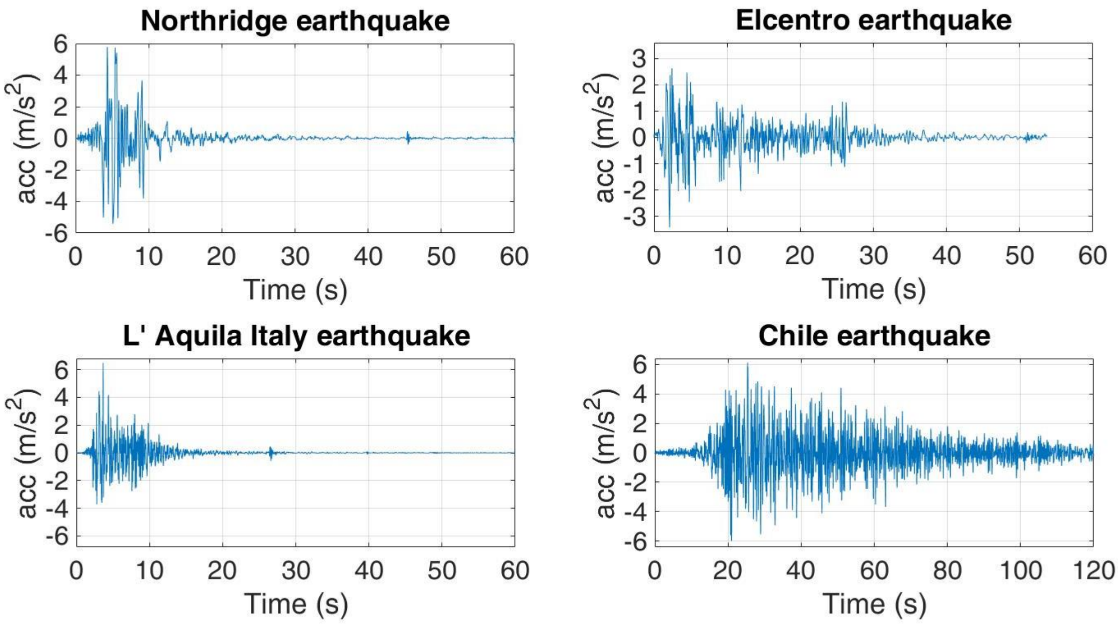

Figure 5.1: Earthquakes accelerograms.

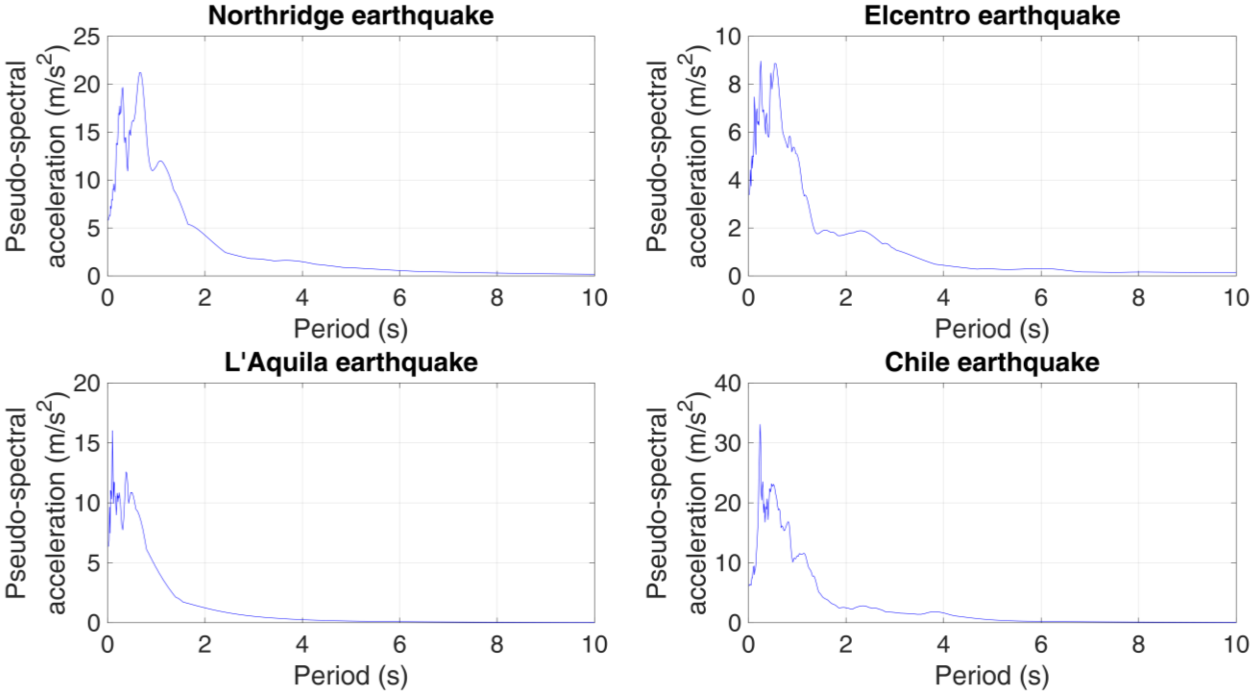

Figure 5.2: Earthquakes linear elastic response spectrums wit 5% viscous damping ratio.

It is obvious in Figure 5.2 that Northridge and Chile earthquakes are of high vibrational amplitudes while L’Aquila and Elcentro are of relatively lower amplitudes.

5.2. RC multistory frame structure

The considered structure is a 2D Reinforced Concrete (RC) multistory frame made up of 10 stories and 5 spans with a 3 m story height, a 5 m span length, a 4 t/m linear load is applied on beams (a diagonal mass matrix with no moment of inertias was considered) and the structural self-weight is neglected (refer to Figure 5.3).

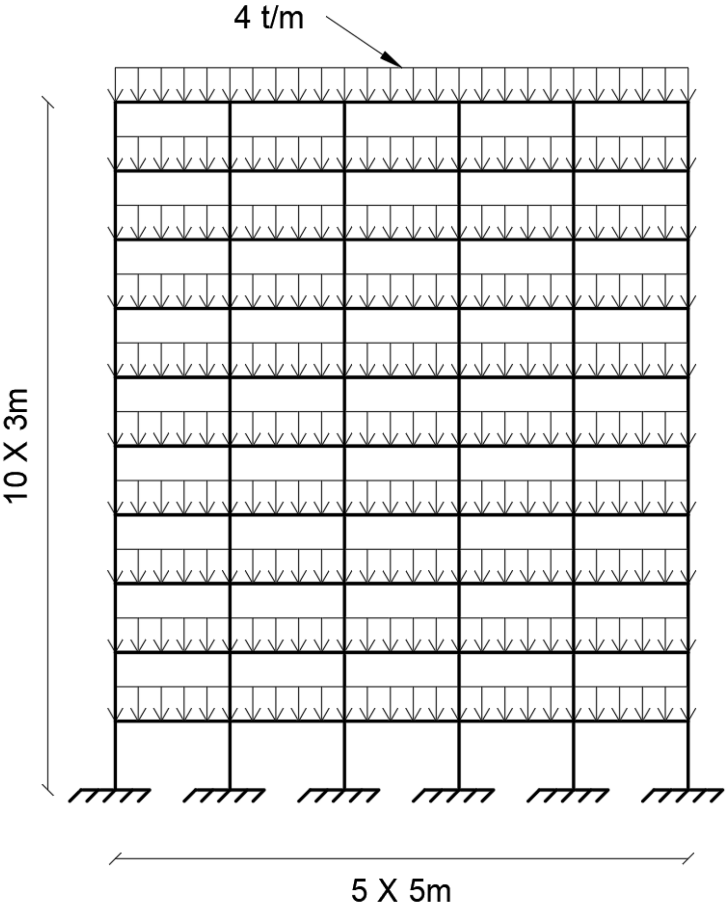

Figure 5.3: Geometry and loading on the 2D RC frame structure.

All concrete columns and beams are divided into 1 m long finite elements of identical cross section 40x40 cm, with four 20 mm High Bond HB reinforcing bars at both top and bottom sides (refer to Figure 5.4). The cross section is composed of 4 concrete fibers and 2 steel fibers.

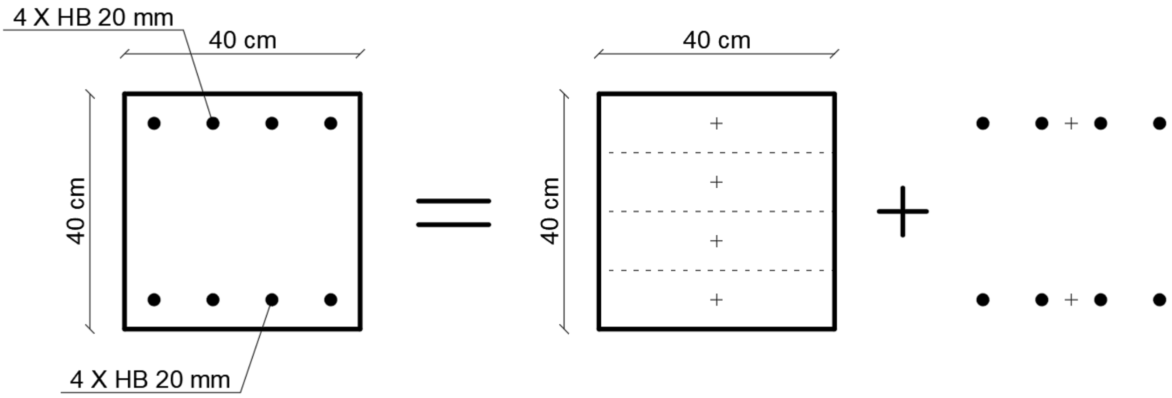

Figure 5.4: Multifiber decomposition of structural beams and columns

Rayleigh damping was used to set a 5% damping ratio for the first two eigenmodes (satisfying the classic linear modes truncation criterion, more than 90% of the total mass is participating in the first two eigenmodes). Material nonlinearity is considered to occur in the elements near the beam column connections at the first 5 stories (refer to Figure 5.5).

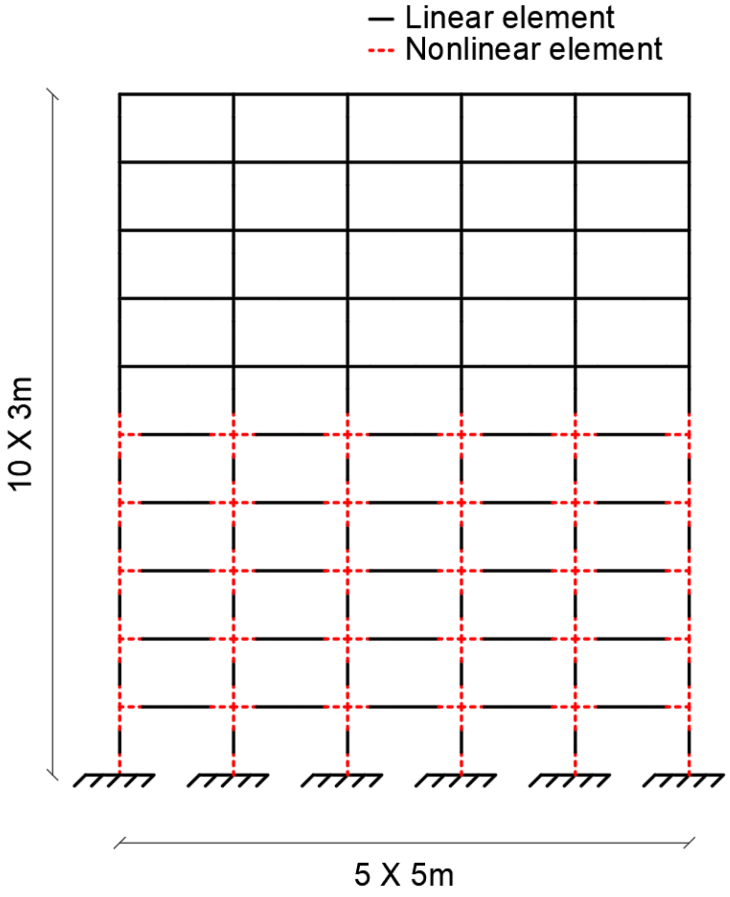

Figure 5.5: Nonlinear elements in the 2D RC frame

As indicated in Chapter 2, the bilinear backbone curve is adopted to model the reinforcing steel bars. Under cyclic loading, if nonlinearity is reached, the steel material will undergo a kinematic hysteresis behavior (for further details refer to Table 5.2 and Figure 5.6).

Material	Elastic Young Modulus	Yield stress	Yield strain	Ultimate stress	Ultimate strain
Rebar	200 GPa	400 MPa	2‰	420 MPa	2.5%

Table 5.2: Steel reinforcement characteristics.

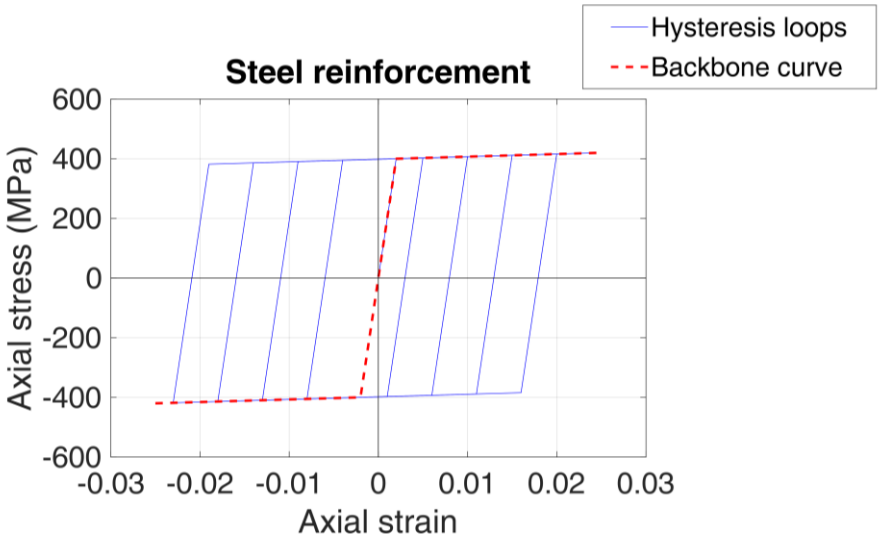

Figure 5.6: Steel reinforcement uniaxial stress-strain curve.

Concrete is unconfined and modeled according to a simplified version of Mander model detailed in Chapter 2 (for further details refer to Table 5.3 and Figure 5.7).

Material	Elastic Young Modulus	Maximum compressive stress	Strain at maximum compressive stress	Ultimate compressive stress	Ultimate compressive strain	Ultimate tensile stress	Ultimate tensile strain
Unconfined Concrete	25 GPa	25 MPa	2‰	20 MPa	4‰	2.5 MPa	0.1‰

Table 5.3: Unconfined concrete characteristics.

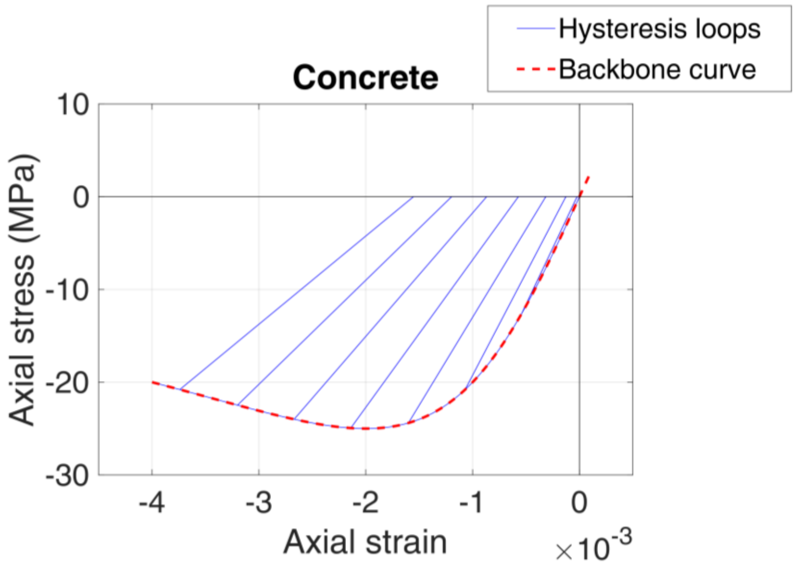

Figure 5.7: Unconfined concrete uniaxial stress-strain curve.

5.2.1. Efficiency of POD modes over classical eigenmodes

Prior to start using POD modes, it should be demonstrated that they are more effective in reducing nonlinear dynamic models than the classical linear eigenmodes. For this reason, a full model implicit nonlinear time-history analysis with a 20 ms time step was conducted for the Northridge earthquake applied at the base of the studied 2D RC frame structure. Then, 50 resulting displacement vectors were taken at equally spaced time intervals during the first 15 seconds of the vibration (where most of the powerful excitation occurs) and gathered in a snapshot matrix. POD modes were extracted from the snapshot matrix and the first 4 POD modes satisfied the truncation criterion (refer to 4.3). For the linear modes of vibration, the two first modes satisfy the classical truncation criterion of 90% effective modal mass participation. However, to make a fair comparison, the first 4 linear modes of vibrations were considered similarly to the POD modes (refer to Figure 5.8). This structure with initially 1140 degrees of freedom is reduced to only 4. Then, explicit nonlinear time-history analyses with a 20 ms time step were conducted using two reduced-order models respectively based on POD modes and linear eigenmodes.

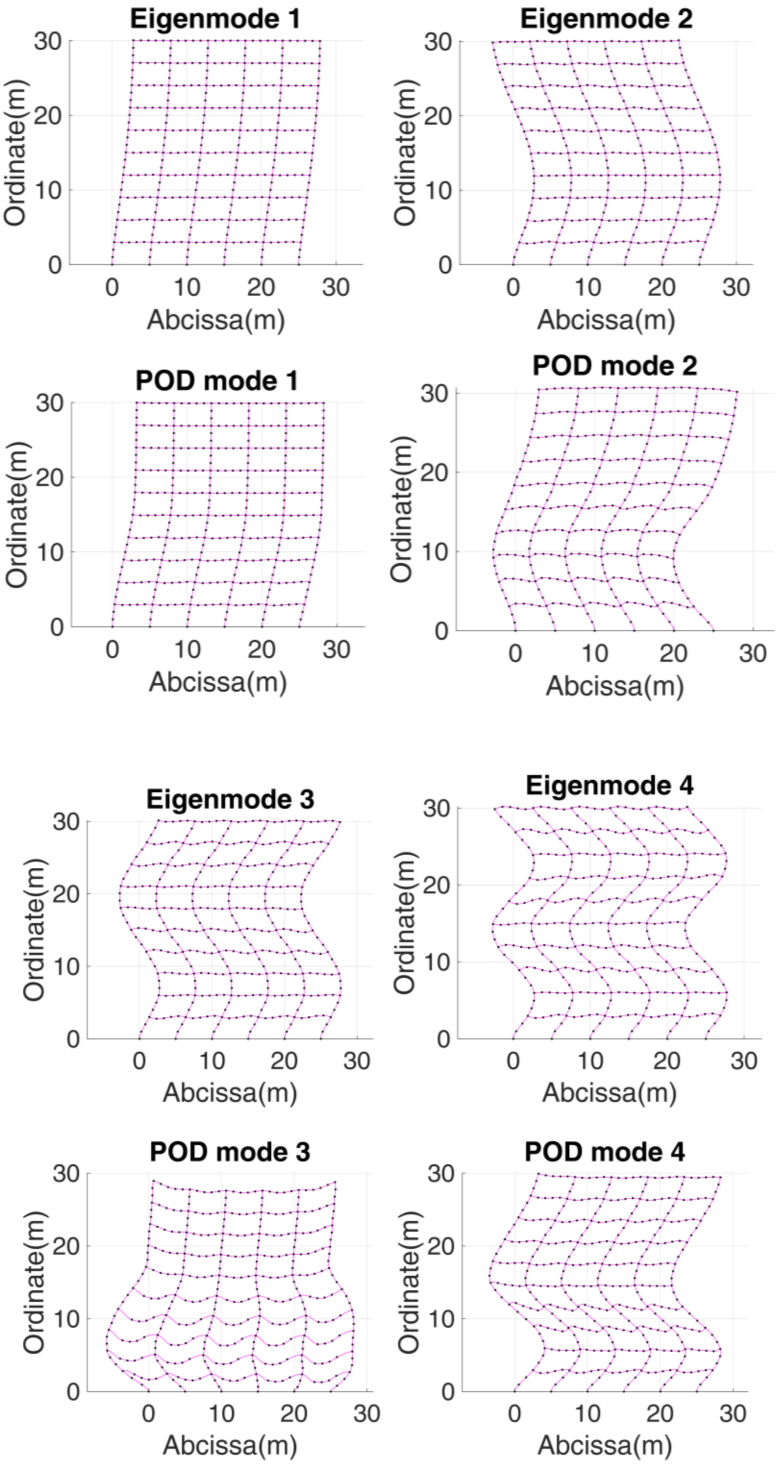

Figure 5.8: Linear structural modes Vs POD modes.

By comparing the POD modes with the classical linear eigenmodes of the structure, we can clearly see the nonlinear behavior of the first 5 stories of the structure in the POD modes, especially for modes 2 and 3.

By studying the top left corner horizontal displacement of the structure subjected to the Northridge earthquake in function of time (refer to Figure 5.9), it is clear that the POD Reduced-Order Model (POD-ROM) is a lot more accurate than the Modal Reduced-Order Model (M-ROM). In fact, the average absolute displacement error for the POD-ROM is 0.28 cm while it is 5.98 cm for the M-ROM.

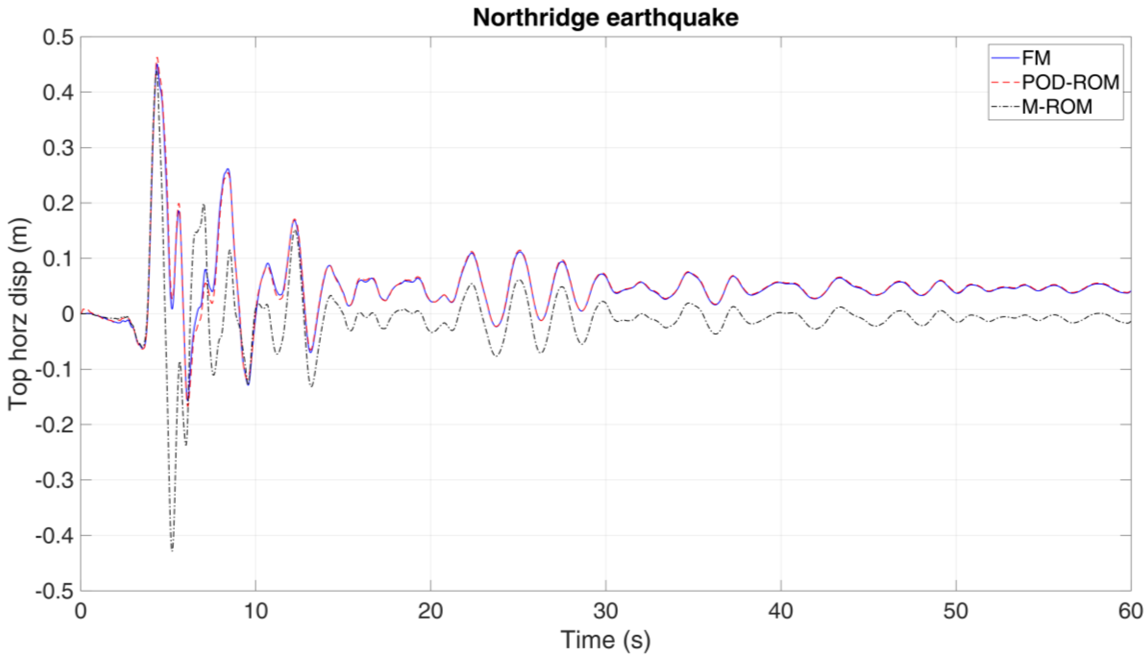

Figure 5.9: Structural top left corner horizontal displacement in function of time for Full Model (FM), POD Reduced-Order Model (POD-ROM) and Modal Reduced-Order Model (M-ROM) analyses.

After demonstrating that linear eigenmodes projection is not suitable for nonlinear models, the efficiency and accuracy of POD reduced dynamic models will be assessed in the following sections.

5.2.2. Application of POD-ROM analysis for single base excitation

Each of the four earthquakes presented in 5.1 was studied separately. A full model implicit nonlinear time-history analysis with a 20 ms time step was conducted solely on the first quarter of the vibration time length. Then, 50 snapshots at equally spaced time intervals were taken from the resulting displacement vector. Next, POD modes were extracted while respecting the truncation criterion in 4.3 and used for a reduced-order model explicit nonlinear time-history analyses with a 20 ms time step carried out on the remaining three quarters of the vibration time length (refer to Figure 5.10).

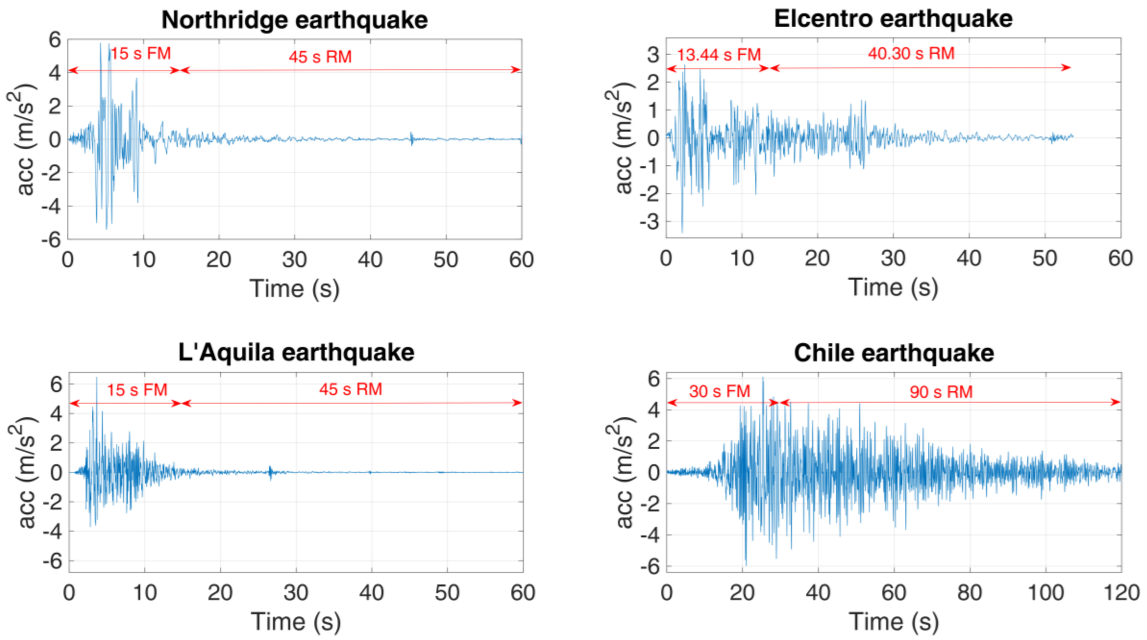

Figure 5.10: Division of each accelerogram between Full Model (FM) and Reduced Model (RM) analyses.

It should be noted that for comparison purpose, a Full Model (FM) implicit nonlinear time-history analysis was conducted for each earthquake over its entire time length in order to have a base reference. In addition, the process of starting with FM analysis for the first quarter and then continuing with a Reduced Model (RM) analysis will be designated as Partially Reduced Model (PRM) analysis. As shown in Figure 5.11, the PRM analyses results are very close to the FM results and at a reduced time cost, for further details refer to Table 5.4.

Earthquake	FM time	PRM time	Time saving	Speedup	Average absolute displacement error	Max horiz displacement
Northridge	795.73 s	239.93 s	69.85%	3.3	0.12 cm	45.06 cm
Elcentro	687.03 s	214.04 s	68.85%	3.2	0.31 cm	23.96 cm
L’Aquila	774.31 s	243.96 s	68.49%	3.2	0.10 cm	15.85 cm
Chile	1661.06 s	426.86 s	74.30%	3.9	1.67 cm	27.24 cm

Table 5.4: Accuracy and time saving of the Partially Reduced Model (PRM) with respect to the Full Model (FM) for 2D RC frame.

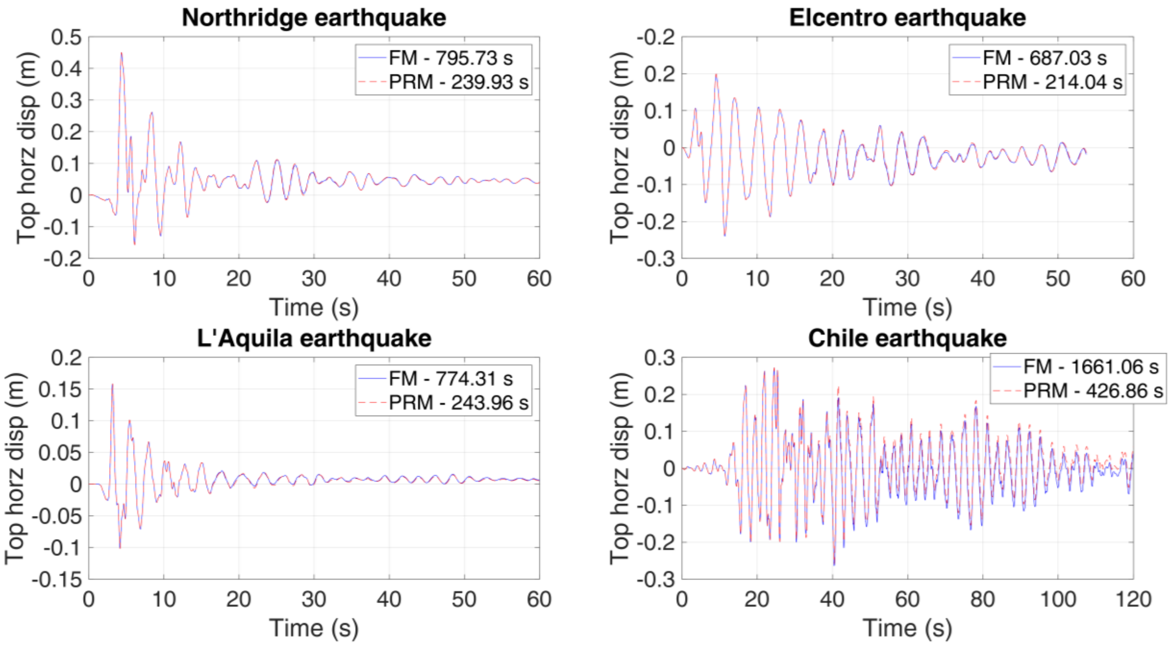

Figure 5.11: Structural top left corner horizontal displacement in function of time for Full Model (FM) and Partially Reduced Model (PRM) analyses of 2D RC frame.

Further comparisons on internal forces and stresses were carried out on a cross section located at the lower Gauss point (it is recalled that a 3-point Gauss integration was used for beams and columns) of the highlighted element in Figure 5.12.

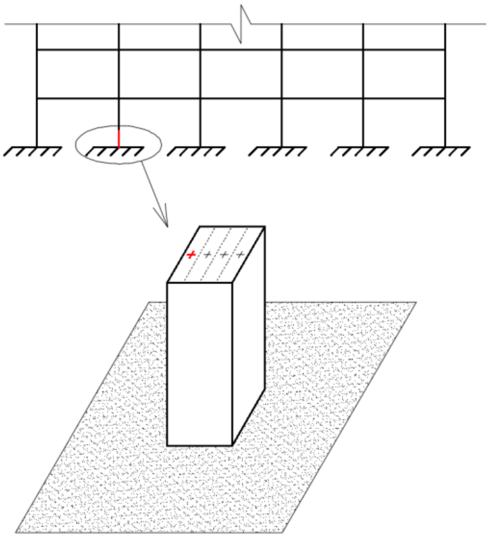

Figure 5.12: Cross section of RC frame studied for internal forces and stresses.

It is clear from Figure 5.13 that the bending moment-curvature relation at the designated cross section is almost identical between the full and partially reduced models for all of the 4 base excitations.

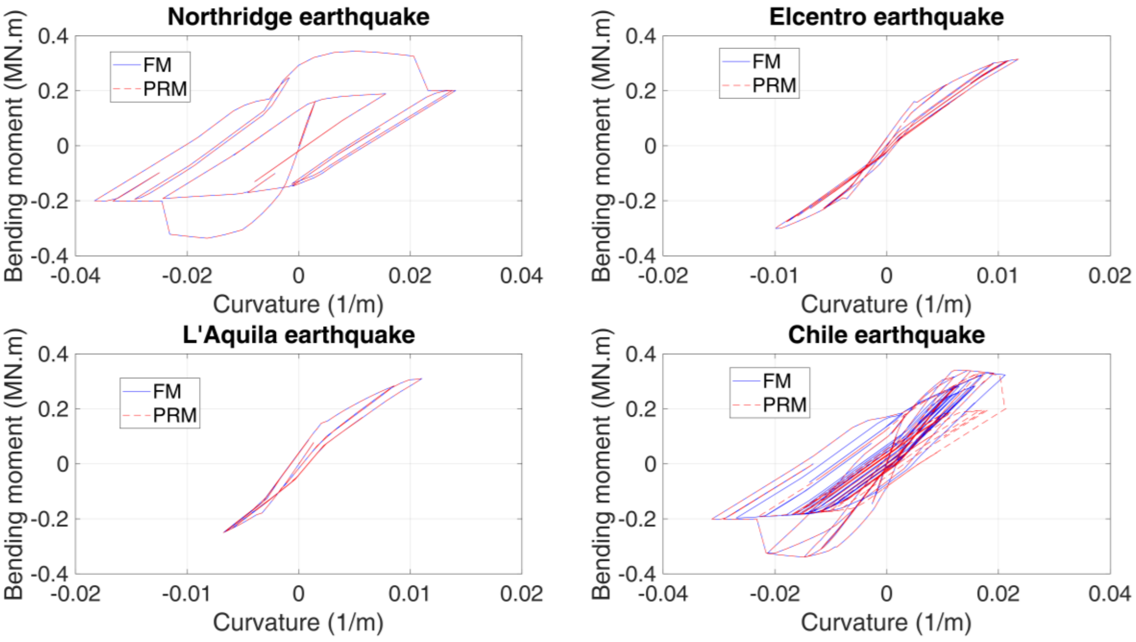

Figure 5.13: Moment-Curvature relation at a designated cross section for Full Model (FM) and Partially Reduced Model (PRM) analyses.

In addition, Figure 5.14 and Figure 5.15 display the stress-strain behavior of respectively a concrete and steel fiber (located at the red dot location in Figure 5.12) in FM and PRM analyses for all 4 base excitations.

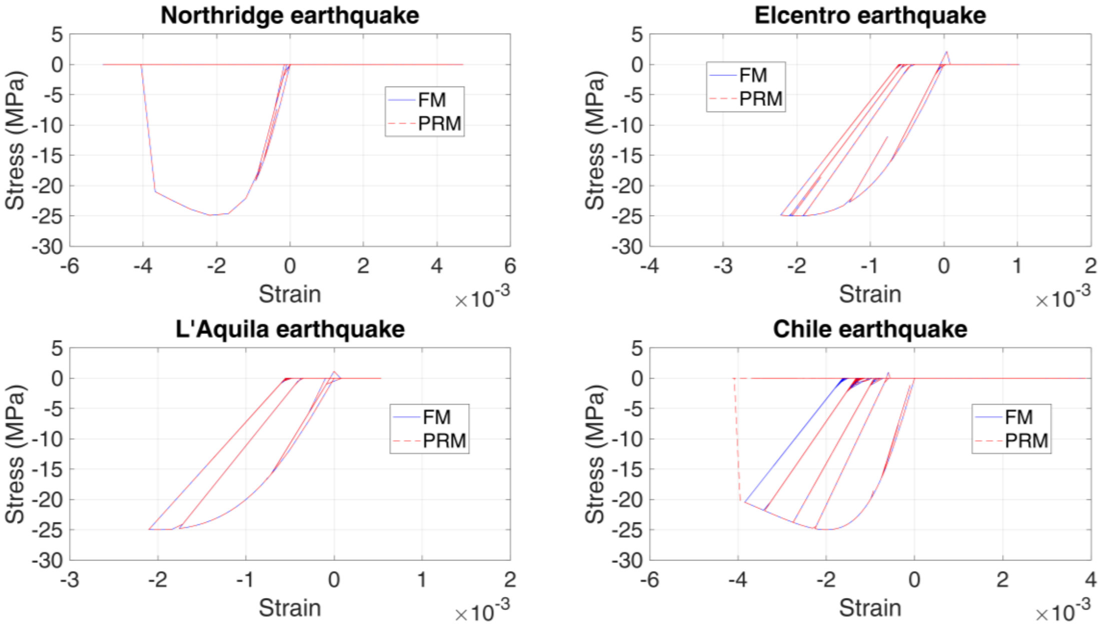

Figure 5.14: Uniaxial stress-strain behavior at a designated concrete fiber for Full Model (FM) and Partially Reduced Model (PRM) analyses.

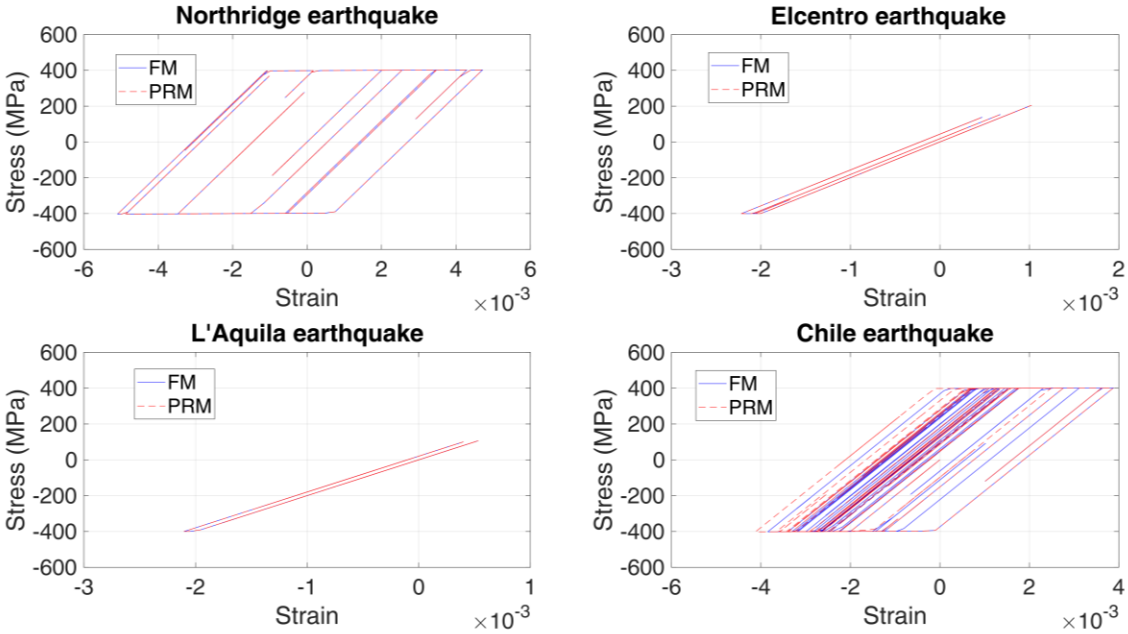

Figure 5.15: Uniaxial stress-strain behavior at a designated steel fiber for Full Model (FM) and Partially Reduced Model (PRM) analyses.

The stress-strain behaviors of concrete and steel fibers are almost the same between the FM and PRM analyses. It can be concluded that using POD-ROM where the POD modes are extracted from an initial FM analysis carried at a portion of the base excitation is an accurate and time saving technique. The speedup obtained was in the order of 3 to 4 times faster which is not very high due to the fact that the analysis for each base excitation should start by an expensive FM analysis prior to continuing with POD-ROM.

5.2.3. Application of POD-ROM analysis for multiple base excitations

The Northridge earthquake is taken as the initial vibration. A dynamic analysis using the Full Model (FM) with a 20 ms time step was carried out for the first 15 seconds of this vibration. Similarly to 5.2.2, 50 snapshots were taken, POD modes were extracted and the dynamic system was reduced. Then, Reduced Model (RM) explicit nonlinear time-history analyses with a 20 ms time step were carried out for the entire time length of all earthquakes (Northridge, Elcentro, L’Aquila and Chile). Figure 5.16 shows that the reduced model results are close to the full models and at a fraction of the time cost, for further details refer to Table 5.5.

Earthquake	FM time	RM time	Time saving	Speedup	Average absolute displacement error	Absolute error at max horiz displacement	Max horiz displacement
Northridge	795.73 s	47.80 s	93.99%	16.6	0.28 cm	1.26 cm	45.06 cm
Elcentro	687.03 s	44.51 s	93.52%	15.4	0.36 cm	0.24 cm	23.96 cm
L’Aquila	774.31 s	47.94 s	93.81%	16.2	0.79 cm	0.52 cm	15.85 cm
Chile	1661.06 s	106.57 s	93.58%	15.6	2.71 cm	0.85 cm	27.24 cm

Table 5.5: Accuracy and time saving of the Reduced Model (RM) with respect to the Full Model (FM).

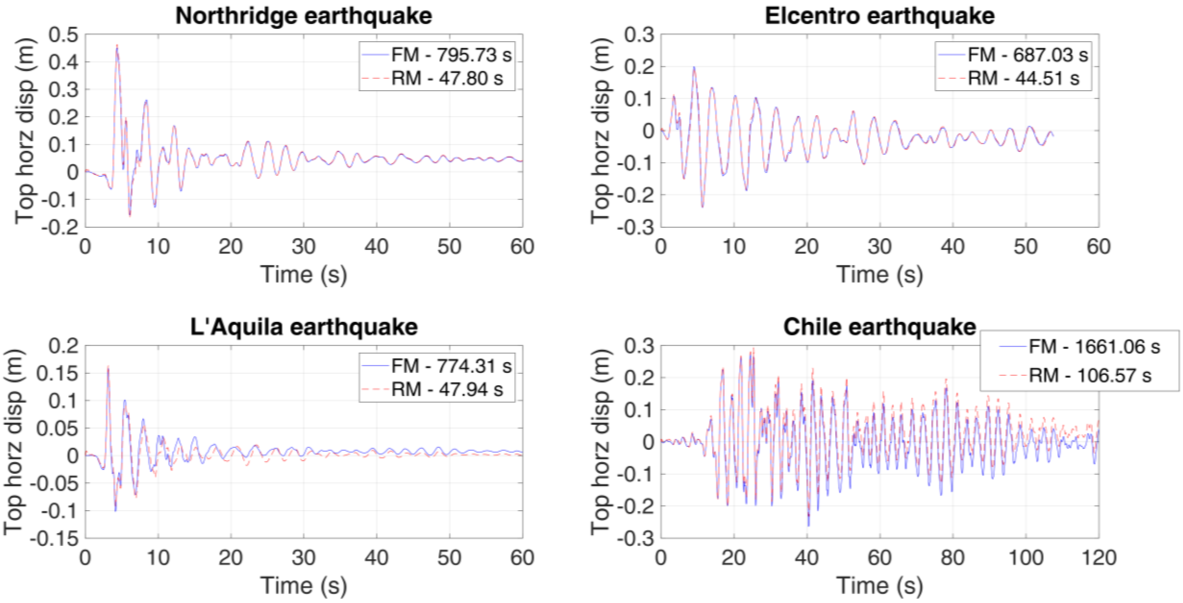

Figure 5.16: Structural top left corner horizontal displacement in function of time for Full Model (FM) and Reduced Model (RM) analyses.

Similarly to 5.2.2, comparisons on internal forces (refer to Figure 5.17) and stresses (refer to Figure 5.18 and Figure 5.19) were carried out on the cross section and fibers indicated in Figure 5.12.

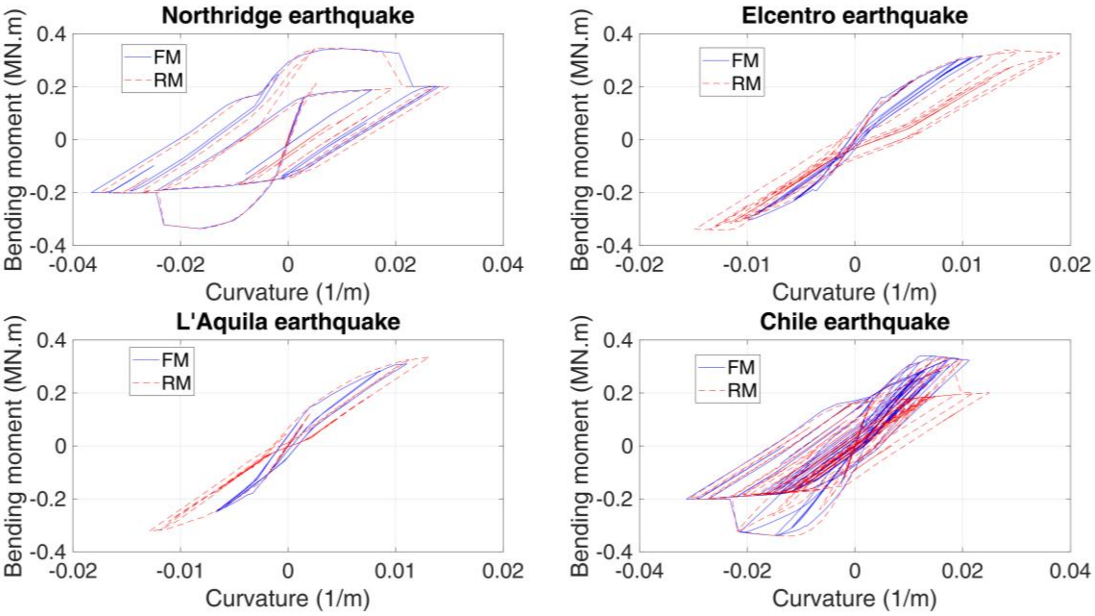

Figure 5.17: Moment-Curvature relation at a designated cross section for Full Model (FM) and Reduced Model (RM) analyses.

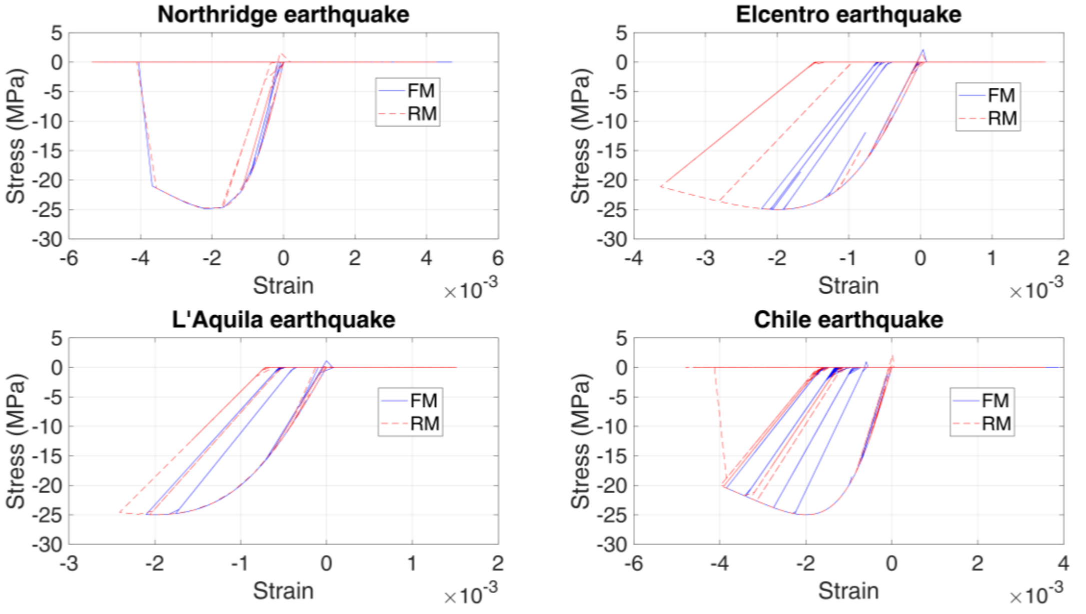

Figure 5.18: Uniaxial stress-strain behavior at a designated concrete fiber for Full Model (FM) and Reduced Model (RM) analyses.

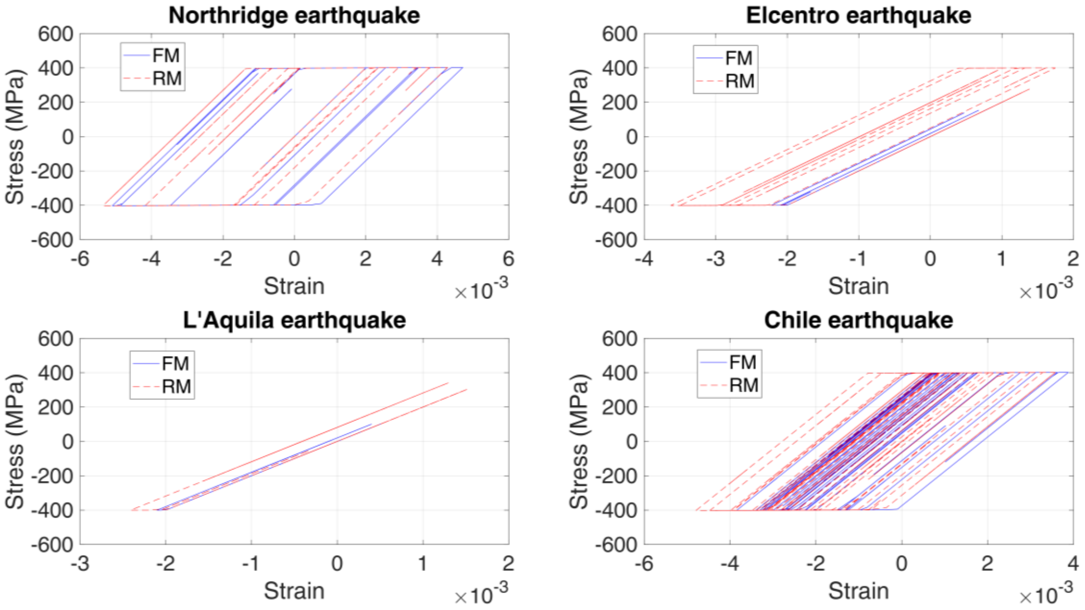

Figure 5.19: Uniaxial stress-strain behavior at a designated steel fiber for Full Model (FM) and Reduced Model (RM) analyses.

The POD-ROM based on POD modes extracted from the FM analysis of Northridge base excitation gave accurate results in terms of bending moment and fiber stresses for Northridge and Chile base vibrations. However, this POD-ROM tends to overestimate the nonlinear behavior from internal moment and stresses point of view for Elcentro and L'Aquila base excitations. To understand this overestimation, we should go back to Figure 5.2 where it is clear that Northridge and Chile earthquakes are stronger than Elcentro and L'Aquila quakes. Since POD modes were extracted from the FM analysis of the strong Northridge base excitation, these obtained POD modes will have more potential to give nonlinear deformations. So, when a dynamic model subjected to a weaker base excitation is projected on these POD modes, the resulting ROM will have a higher tendency for exhibiting additional nonlinear deformations.

It can be concluded that projecting nonlinear dynamic models subjected to different base excitations on a POD modes basis extracted from a FM analysis of a certain quake is accurate and very efficient in time saving (a speedup of 16 times is achieved). However, attention should be made so that the POD-ROM is subjected to base excitations of similar intensity to the one used in extracting the POD modes. Indeed, POD modes are criticized for being load-dependent. Nevertheless, in structural seismic analysis, the dynamic load resulting from a base excitation always has the same pattern (proportional to the product of the mass matrix by the influence vector) regardless of the considered vibration. In addition, placing earthquakes in groups of similar intensity for POD-ROM will reduce this load dependency.

Even more, in the same earthquake intensity group, the accuracy of POD-ROM is influenced by the choice of the base excitation for the initial FM analysis, the number and time instants of taken snapshots. To put this in perspective for our RC frame structure, 4 POD modes basis were extracted respectively from a FM analysis conducted for each of the 4 base excitations. Then POD-ROM analyses based on each of the obtained POD modes basis were conducted for all the 4 base excitations. Then ROM results were compared with FM ones and the values of average absolute displacement errors obtained are presented in Table 5.6

		POD modes base extracted from FM of base excitation			
		Northridge	Elcentro	L’Aquila	Chile
POD-ROM for base excitation	Northridge	0.28 cm	11.2 cm	4.83 cm	4.65 cm
	Elcentro	0.36 cm	1.97 cm	3.89 cm	1.5 cm
	L’Aquila	0.79 cm	0.52 cm	0.44 cm	0.86 cm
	Chile	2.71 cm	3.73 cm	3.44 cm	1.1 cm

Table 5.6: Effects of POD modes base change on the average absolute displacement error computed for the POD-ROM.

As seen in Table 5.6, even in the same seismic intensity group (Northridge and Chile for strong group; Elcentro and L’Aquila for weak group), the choice of the base excitation for the initial FM analysis from which POD modes are extracted has an influence on results accuracy. For this purpose, as a perspective for this thesis, we will propose a synthetic base excitation constructed from the frequency spectrums envelop of earthquakes from the same group in order to eliminate the choice problem and reduce the duration of the base excitation studied with the FM analysis.

5.3. RC multistory shear wall

The considered structure is an isolated 2D Reinforced Concrete (RC) 8 stories shear wall 3 m in width, 30 cm in thickness. The story height is 5 m in length, a 30 t/m linear load is applied on the wall at each story (a diagonal mass matrix was considered) in addition to considering its own self-weight (refer to Figure 5.20).

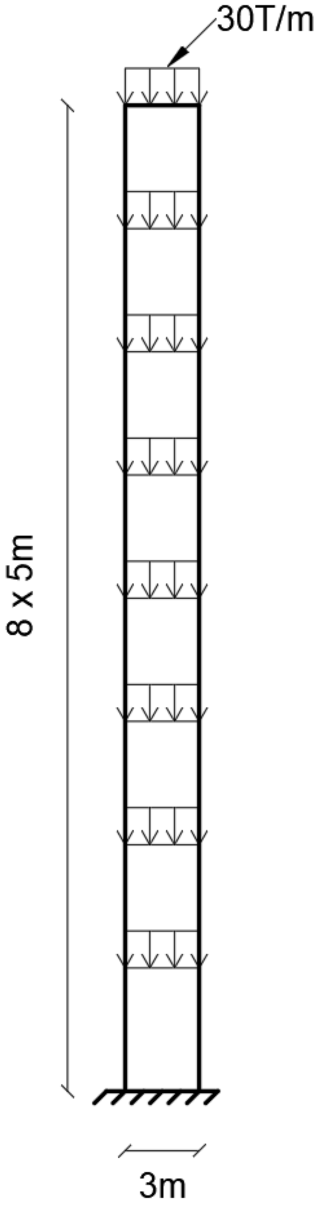

Figure 5.20: Geometry and loading on the 2D RC shear wall.

The wall is meshed into 6 Finite Elements (FE) along its width and 3 per story height (refer to Figure 5.21).

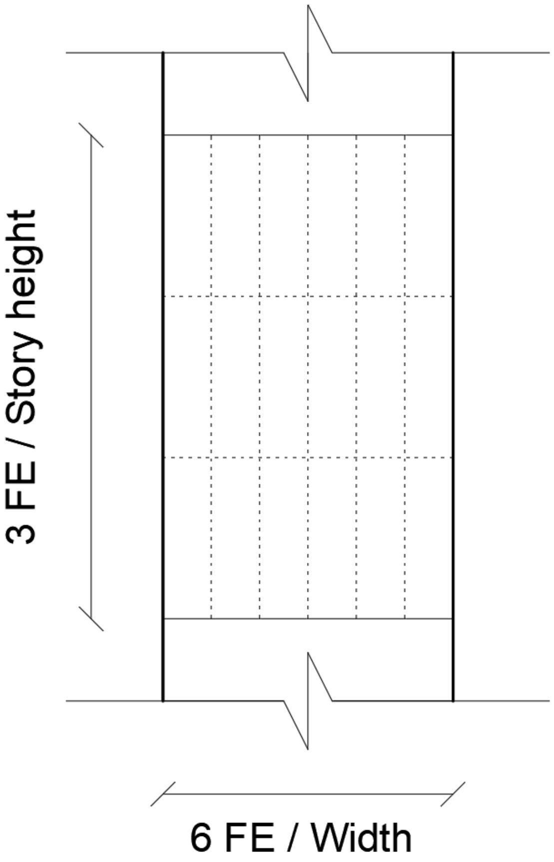

Figure 5.21: Meshing details of the RC shear wall.

The RC shear wall is reinforced at its middle zone by a mesh of 12 mm diameter High Bond HB reinforcing bars spaced at 20 cm in both directions and at both faces. At each edge zone, 8 vertical HB bars of 20 mm in diameter confined by 12 mm HB rectangular ties spaced at 10 cm (for further details refer to Figure 5.22). Since only in plane behavior will be studied, the RC shear wall is considered as a membrane. As a consequence, there is no need to divide the FE thickness into a large number of layers. For each FE, 1 layer of concrete is considered and 1 layer of steel for each vertical and horizontal directions (for further details refer to Figure 5.23 and Figure 5.24). Material nonlinearity is considered to occur only in the elements of the first 4 stories (refer to Figure 5.25). Rayleigh damping was used to set a 5% damping ratio for the first three eigenmodes (satisfying the classic linear modes truncation criterion, more than 90% of the total mass is participating in the first three eigenmodes).

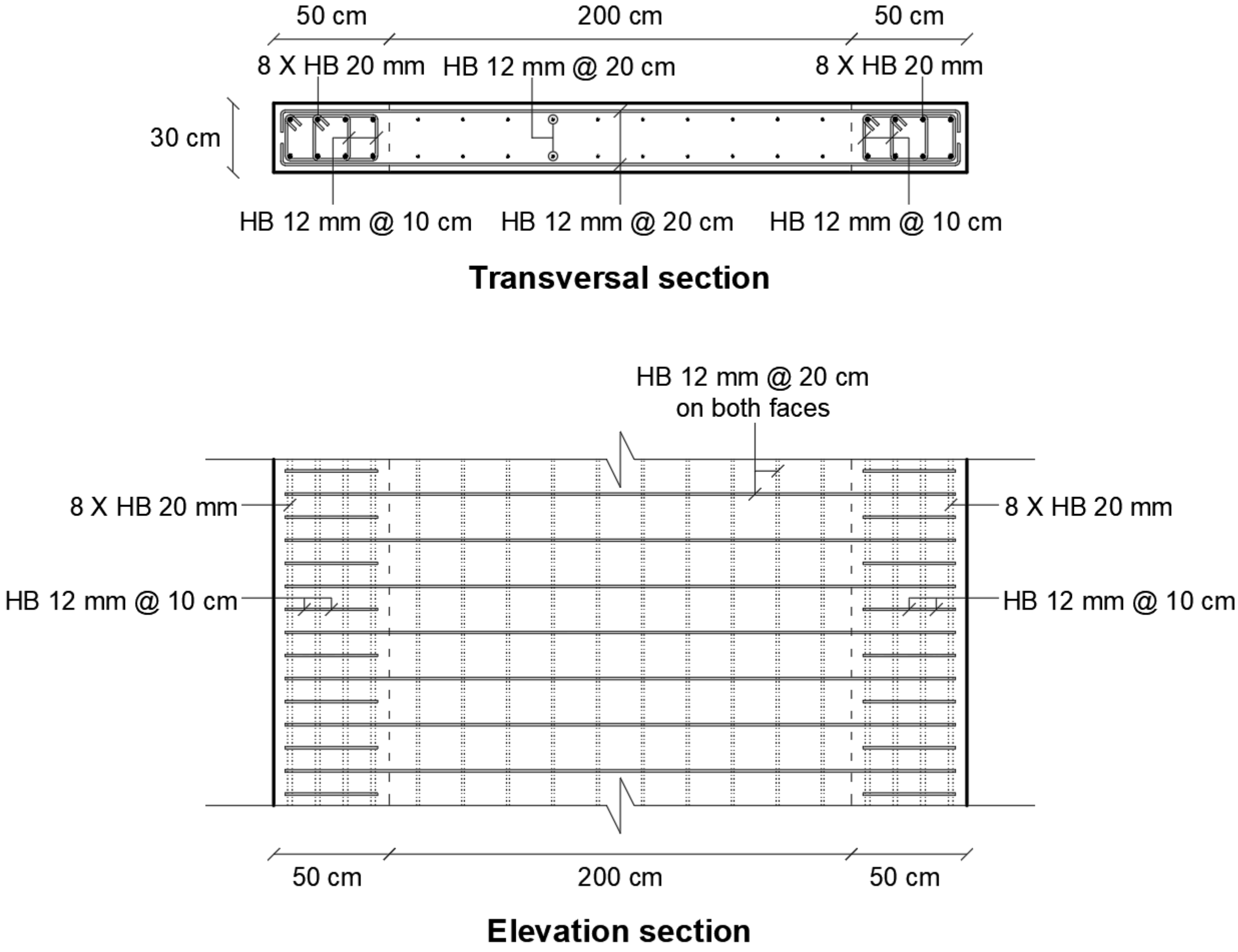

Figure 5.22: RC shear wall reinforcements details.

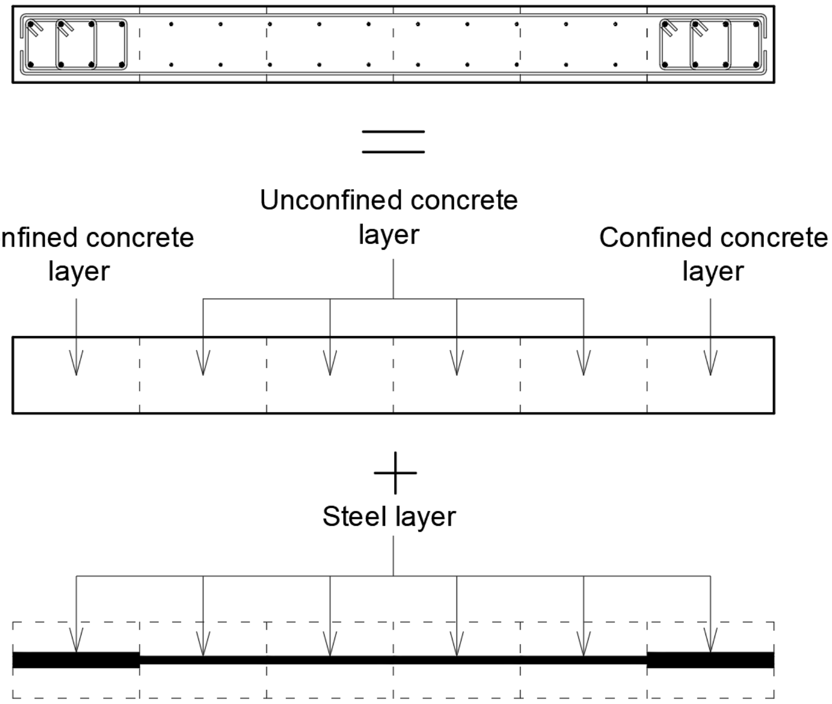

Figure 5.23: Layered membrane elements (cross section view)

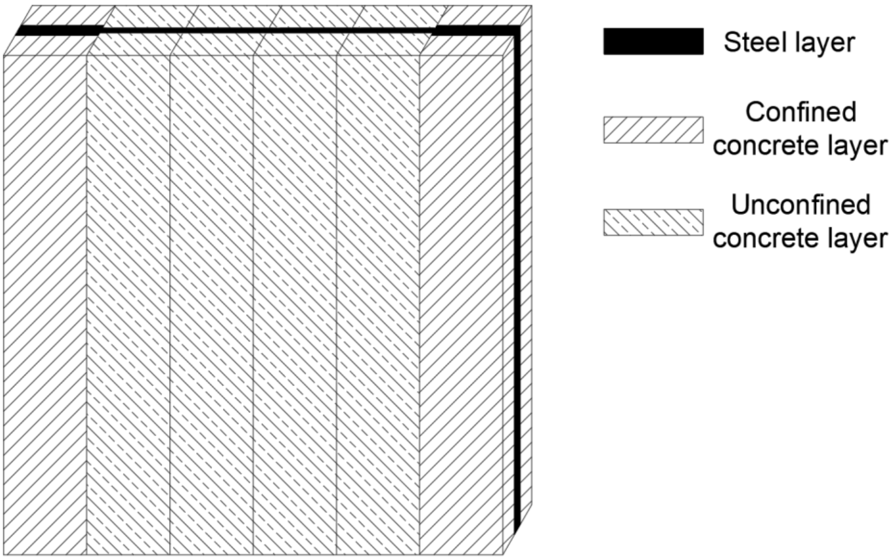

Figure 5.24: Layered membrane elements (3D elevation view)

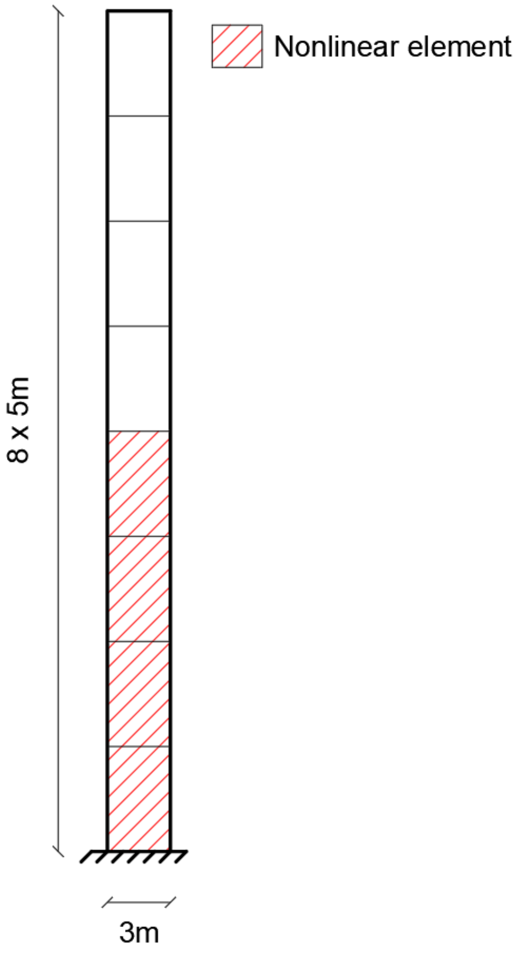

Figure 5.25: Nonlinear elements in the 2D RC frame.

Steel reinforcements and unconfined concrete are identical to the ones used for the 2D frame structure in 5.2 (for further details refer to Table 5.2, Table 5.3, Figure 5.6 and Figure 5.7). Using the Mander confined concrete equations from Chapter 2, the characteristics of confined concrete are calculated (for further details refer to Table 5.7, Figure 5.26 and Figure 5.27).

Material	Elastic Young Modulus	Maximum compressive stress	Strain at maximum compressive stress	Ultimate compressive stress	Ultimate compressive strain	Ultimate tensile stress	Ultimate tensile strain
Confined Concrete	25 GPa	39.5 MPa	7.8‰	39.33 MPa	9.4‰	3.95 MPa	0.158‰

Table 5.7: Confined concrete characteristics.

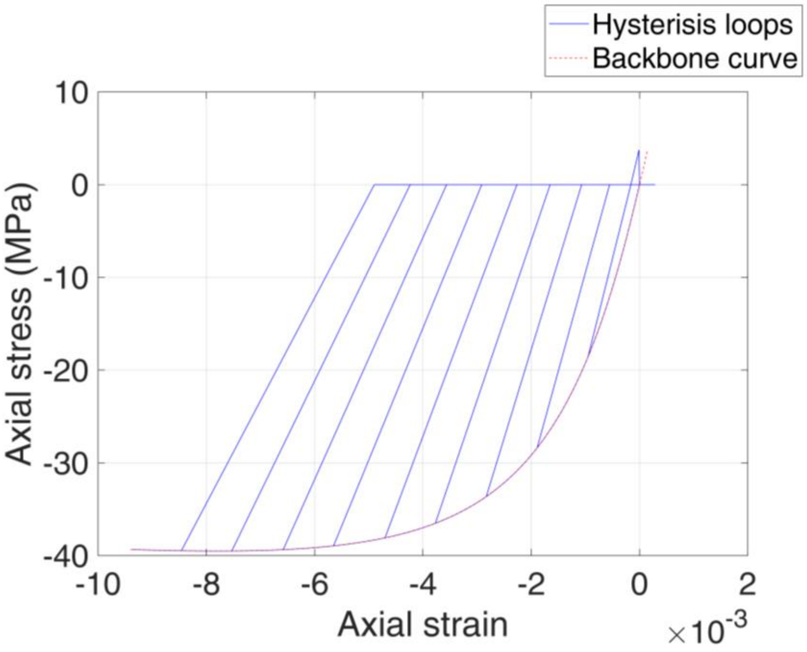

Figure 5.26: Confined concrete uniaxial stress-strain curve.

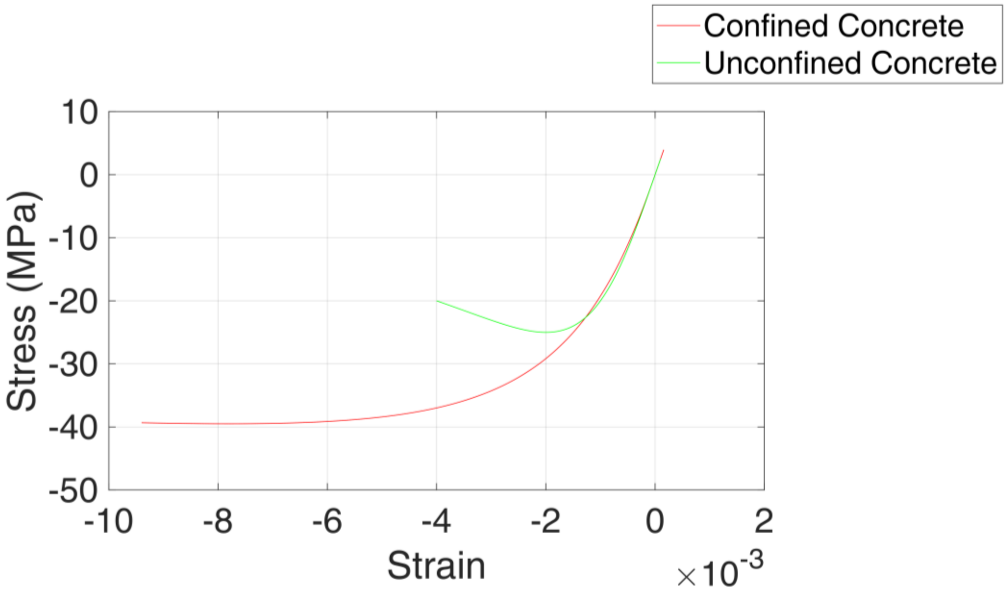

Figure 5.27: Confined Versus unconfined concrete backbone curve.

5.3.1. Application of POD-ROM analysis for single base excitation

A process identical to the one described in 5.2.2 was carried out on for the RC shear wall. As shown in Figure 5.28 the PRM analyses results are very close to the FM results and at a reduced time cost, for further details refer to Table 5.8.

Earthquake	FM time	PRM time	Time saving	Speedup	Average absolute displacement error	Max horiz displacement
Northridge	1117.78 s	405.61 s	63.71%	2.8	0.74 cm	69.09 cm
Elcentro	1007.50 s	404.81 s	59.82%	2.5	0.21 cm	25.48 cm
L’Aquila	1090.28 s	448.13 s	58.90%	2.4	0.45 cm	19.19 cm
Chile	9988.07 s	870.96 s	91.28%	11.5	3.29 cm	69.32 cm

Table 5.8: Accuracy and time saving of the Partially Reduced Model (PRM) with respect to the Full Model (FM) for 2D RC shear wall.

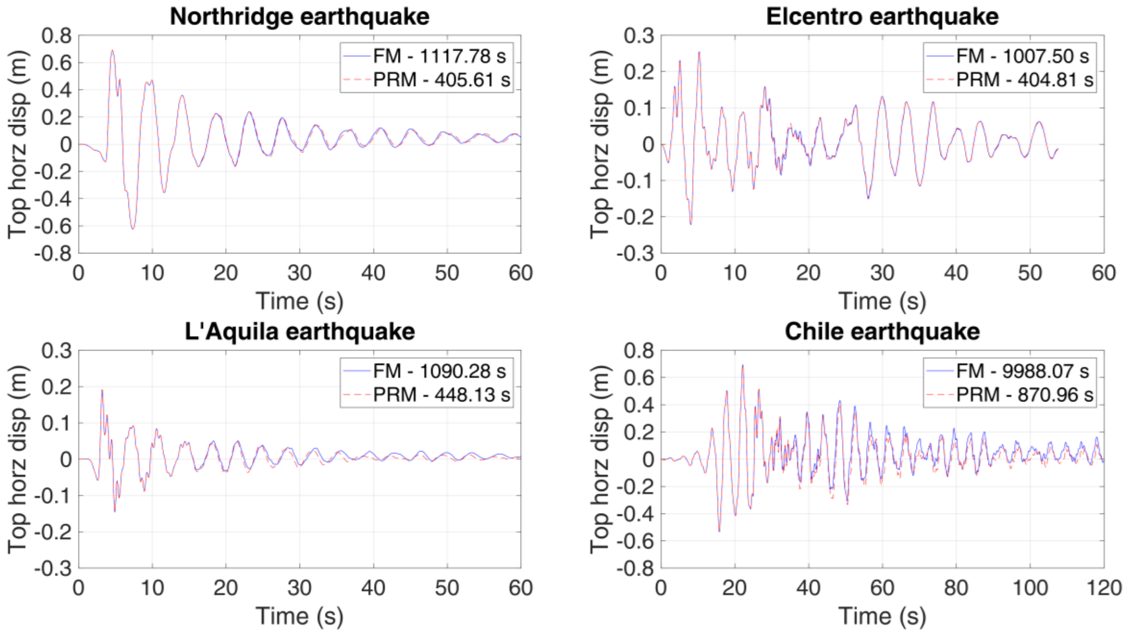

Figure 5.28: Structural top right corner horizontal displacement in function of time for Full Model (FM) and Partially Reduced Model (PRM) analyses of 2D RC shear wall.

The very high FM analysis time for Chile earthquake is remarkable. In fact, the 2D biaxial concrete nonlinear modeling is more computationally demanding. Combining this with the continuous high excitation presented in the Chile accelerogram over an important time interval increased largely the number of iterations needed for convergence at each time step.

Further analyses of stresses and strains were carried out at specific gauss points indicated in Figure 5.29 (a surface integration with 4 Gauss points was used for membrane elements). At point 1, vertical stress-strain behavior of confined concrete and steel reinforcement was studied and at point 2 the vertical stress-strain behavior of unconfined concrete.

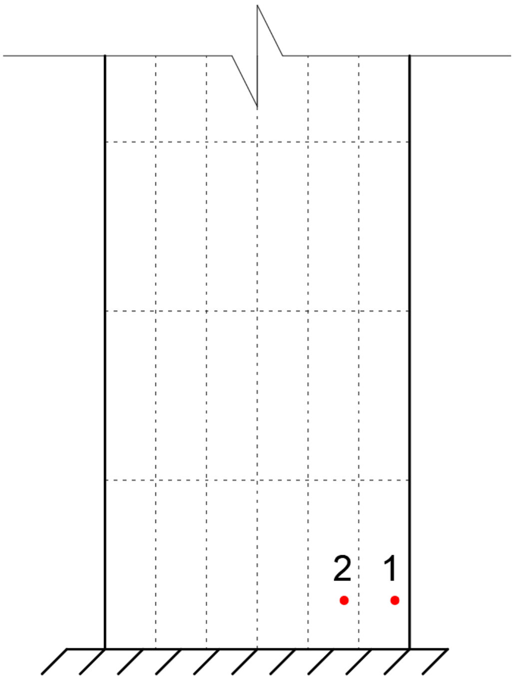

Figure 5.29: Gauss points adopted for stress analysis in the RC shear wall.

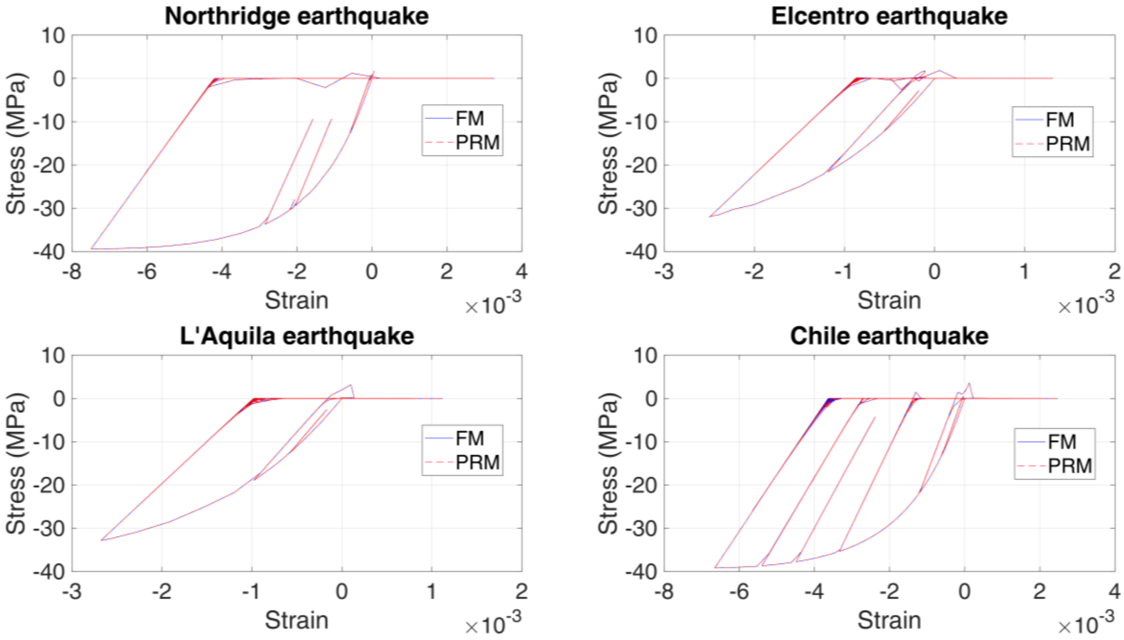

Figure 5.30: Vertical stress-strain behavior of confined concrete at a Gauss point 1 for Full Model (FM) and Partially Reduced Model (PRM) analyses.

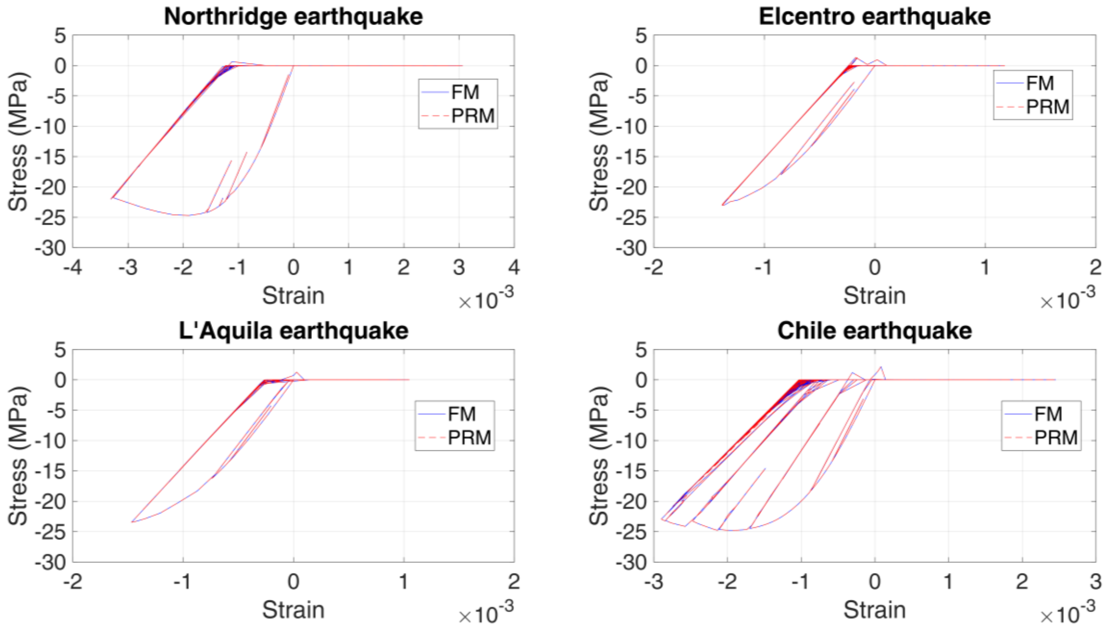

Figure 5.31: Vertical stress-strain behavior of unconfined concrete at a Gauss point 2 for Full Model (FM) and Partially Reduced Model (PRM) analyses.

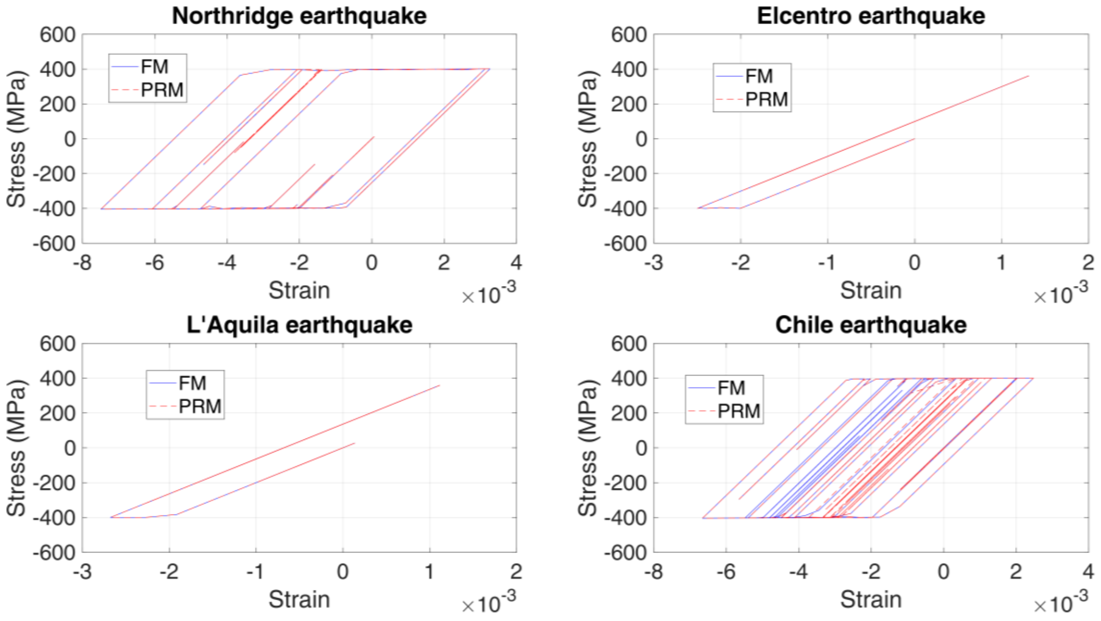

Figure 5.32: Stress-strain behavior of vertical reinforcements at a Gauss point 1 for Full Model (FM) and Partially Reduced Model (PRM) analyses.

The stress-strain behavior of steel reinforcements (refer to Figure 5.32), confined and unconfined concrete (refer to Figure 5.30 and Figure 5.31) are almost the same between the FM and PRM analyses. The speedup achieved with PRM for the RC shear wall is a little bit smaller than the one obtained for the RC frame. This is understandable since the calculation of the nonlinear return force is conducted in the initial full base and for RC walls this nonlinear calculation is more complicated.

5.3.2. Application of POD-ROM analysis for multiple base excitations

A process identical to the one described in 5.2.3 was carried out for the RC shear wall. As shown in Figure 5.33 the RM analyses results are close to the FM results and at a reduced time cost, for further details refer to Table 5.9.

Earthquake	FM time	RM time	Time saving	Speedup	Average absolute displacement error	Absolute error at max horiz displacement	Max horiz displacement
Northridge	1117.78 s	246.18 s	77.98%	4.5	9.88* cm 4.68** cm	2.27 cm	69.09 cm
Elcentro	1007.5 s	222.3 s	77.94%	4.5	3.29 cm	2.23 cm	25.48 cm
L’Aquila	1090.28 s	255.95 s	76.52%	4.3	1.57 cm	0.33 cm	19.19 cm
Chile	9988.07 s	500.25 s	94.99%	20.0	4.87 cm	0.04 cm	69.32 cm
*Average absolute displacement error over the full-time length **Average absolute displacement error over the first 10 seconds							

Table 5.9: Accuracy and time saving of the Reduced Model (RM) with respect to the Full Model (FM) for 2D RC shear wall.

The RM for Northridge excitation is based on POD modes extracted from the first 15 seconds of the FM excited by Northridge accelerogram. Despite that, the average absolute displacement error between FM and RM calculated over the full-time length is important and can be clearly seen in Figure 5.33 after the first quarter of excitation time. Generally, this issue can be solved by taking snapshots for POD over the entire vibration time interval and not only sticking to the first 15 seconds. However, for comparison purposes between the applicability of POD-ROM on shear walls and frames, the same approach in 5.2.3 is applied here with snapshots taken at the first 15 seconds of FM analysis.

For RC shear wall, the POD-ROM based on POD modes extracted from the FM analysis of Northridge base excitation seems to be less accurate and time efficient than the case of RC frame. This is due to the fact that for RC wall we have 3 types of nonlinear materials (instead of 2 for RC frame). In addition, the 2D nonlinear biaxial behavior of concrete is more complicated, computationally demanding and sensitive to approximations made in reduced order models.

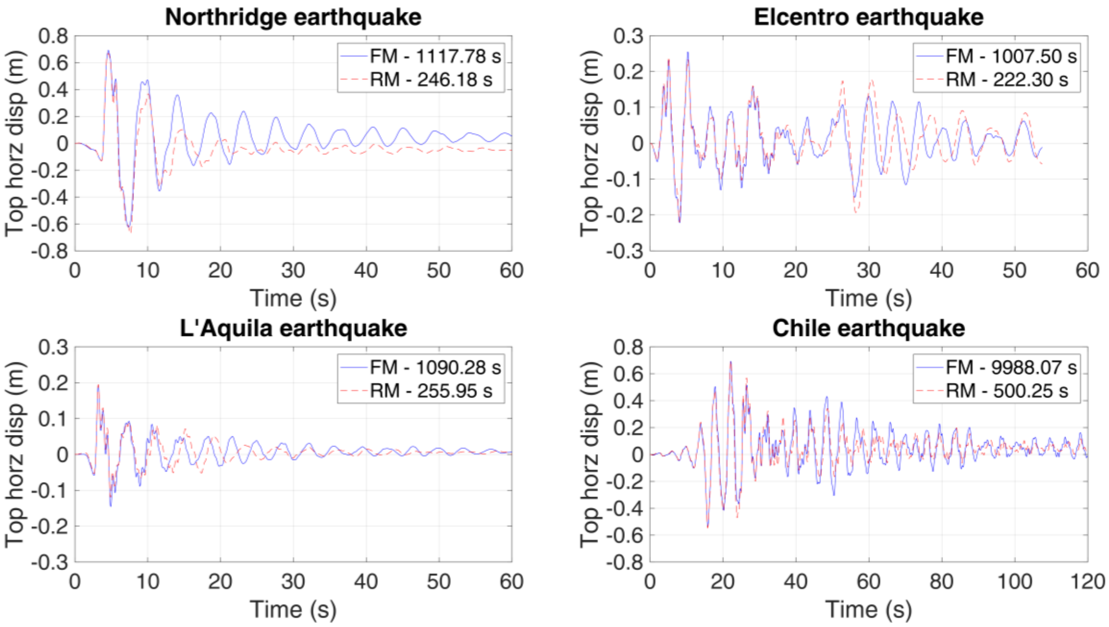

Figure 5.33: Structural top right corner horizontal displacement in function of time for Full Model (FM) and Reduced Model (RM) analyses of 2D RC shear wall.

Similarly to 5.3.1, comparisons on stresses were carried out on the Gauss points indicated in Figure 5.29.

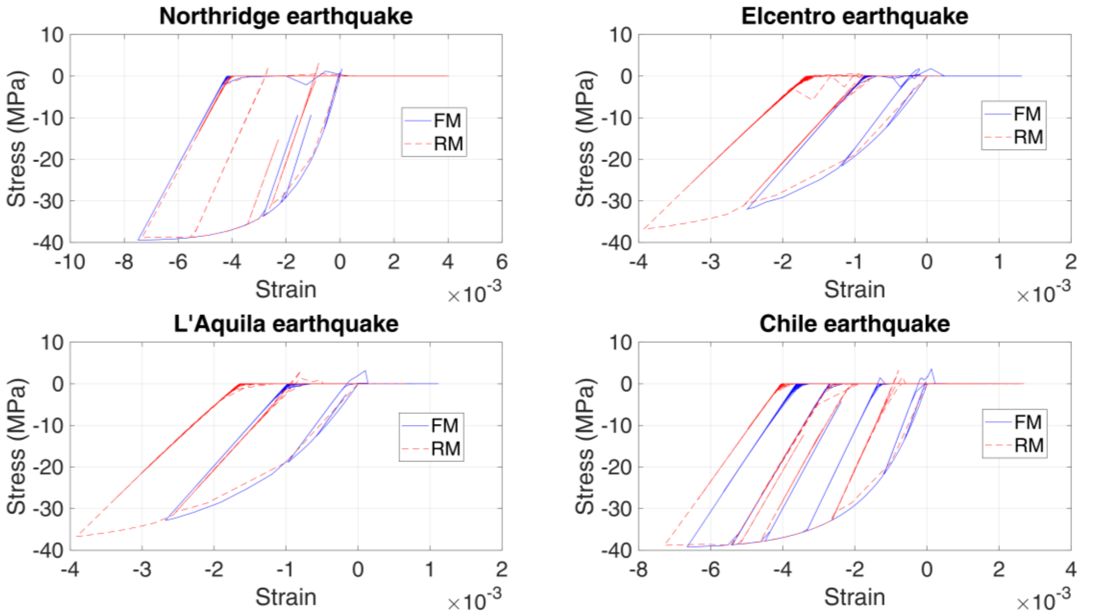

Figure 5.34: Vertical stress-strain behavior of confined concrete at a Gauss point 1 for Full Model (FM) and Reduced Model (RM) analyses.

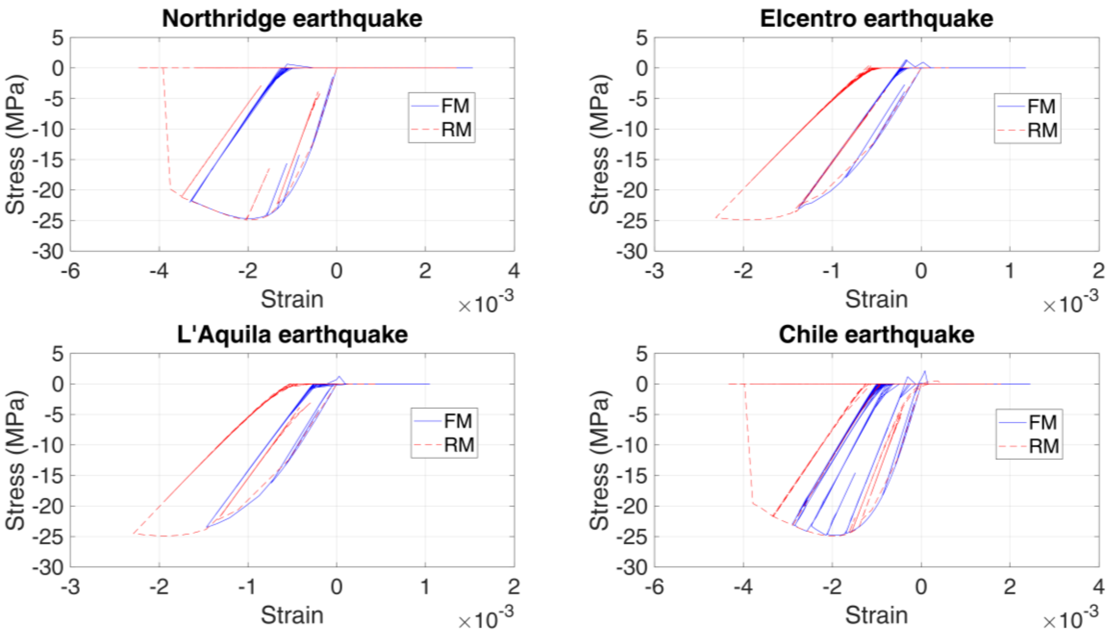

Figure 5.35: Vertical stress-strain behavior of unconfined concrete at a Gauss point 2 for Full Model (FM) and Reduced Model (RM) analyses.

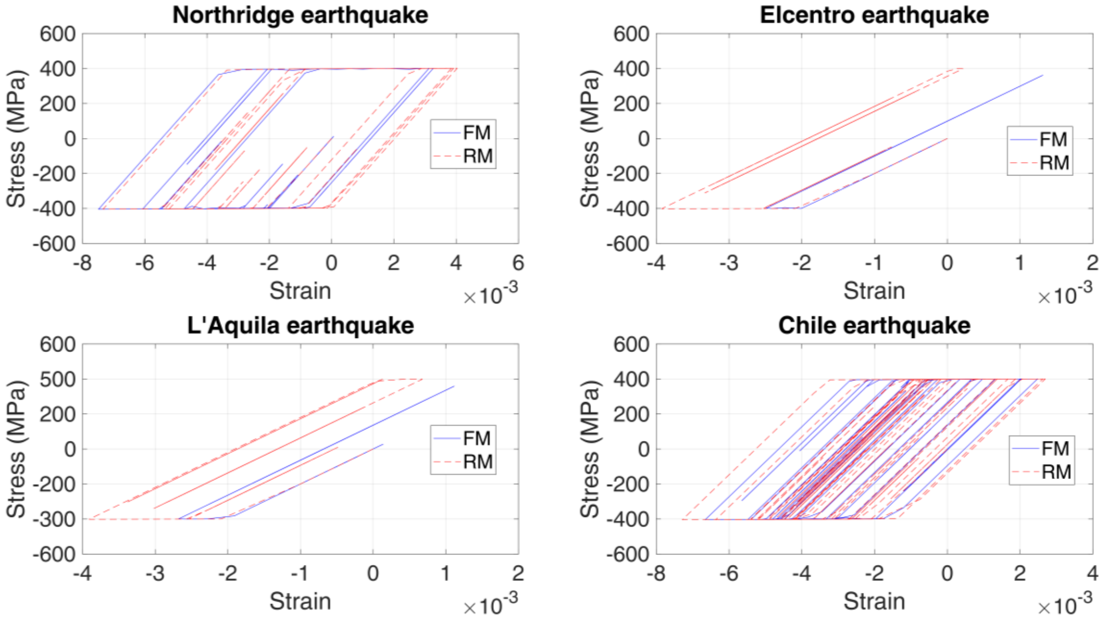

Figure 5.36: Stress-strain behavior of vertical reinforcements at a Gauss point 1 for Full Model (FM) and Reduced Model (RM) analyses.

The POD-ROM based on POD modes extracted from the FM analysis of Northridge base excitation gave good results for stress-strain behavior for Northridge and Chile base vibrations but overestimated the results for Elcentro and L'Aquila accelerograms (refer to Figure 5.34, Figure 5.35 and Figure 5.36). This is similar to what was encountered in 5.2.3

and is due to the fact that Northridge earthquake is relatively strong and POD modes extracted from it are good in representing other strong earthquakes such as Chile but for weaker vibrations (Elcentro and L'Aquila) the POD-ROM tends to give more nonlinear deformations.

5.4. Conclusions

In this chapter, the POD-ROM was tested for a 2D RC frame and a 2D RC shear wall subjected to single and multiple base excitations. It was seen that the POD-ROM works better for frame elements from an accuracy and time efficiency point of view. In addition, the POD-ROM used for the case of multiple base excitations gave better time efficiency than the case of single base excitation study but with a relatively lower accuracy.

Overall, the proposed POD based reduction techniques show very promising results with an important speedup (up to 16 in the tested examples) while maintaining acceptable levels of accuracy.

Conclusions and Perspectives

Conclusions

The purpose of this thesis was to test the accuracy and time efficiency of the POD technique in reducing the dynamic model of a 2D frame structure made of RC multifiber elements and a 2D shear wall consisting of RC layered membranes. Both structures were subjected to base excitations with material nonlinearity taken into account.

For structures studied under a single base excitation, the method proposed by (Bamer and Bucher, 2012) is applied in this thesis, for the first time, on RC structures with material nonlinearities originating simultaneously from steel reinforcements, confined and unconfined concrete. This technique consisted of doing a FM analysis for an initial time portion of the base excitation then POD modes were obtained and used to reduce the dynamic model for the calculation of the remaining time portion.

For structures studied under multiple base excitation scenarios, the method proposed by (Bamer, Amiri and Bucher, 2017) is applied in this thesis, for the first time, on RC structures with material nonlinearities. This technique consisted in performing a FM analysis for a given base excitation, then POD modes were obtained and used to reduce the dynamic model for the calculation of the remaining base excitations.

From numerical testing and comparison between the classical full model dynamic analysis and POD-ROM the following conclusions can be made:

1- For all cases, the POD-ROM succeeded in giving an accurate maximum response of the dynamic system. This is especially beneficial for structures where maximum response is needed but do not satisfy the regularity requirements of the pushover analysis. In this case the POD-ROM is a very appealing cheaper alternative.

2- POD-ROM used for single base excitations were higher in accuracy but lower in time efficiency than the ones used for multiple base excitations. This is logical, seeing the fact that for single base excitation cases, the POD modes are extracted from and used for the same base excitation which gives a better accuracy at the price of requiring an expensive FM analysis for an initial portion of the base excitation.

3- For POD-ROM used for multiple base excitations, the POD modes were influenced by the intensity of the base excitation used for the initial FM analysis. In fact, it was seen that POD modes extracted from an initial FM analysis conducted for Northridge base excitation (relatively strong vibration) had the tendency to overestimate nonlinear stress-strain behavior when the POD-ROM was used for weaker base vibrations. So for better results, POD modes extracted from a FM analysis of an initial base excitation should be applicable only to other base excitations of similar intensity.

4- All POD-ROM techniques presented a lower accuracy with base excitations of continuous strong intensity over a long-time duration such as the Chile accelerogram. This can be explained by the fact that strong excitations call for nonlinear material behavior which in turn present slight differences between the reduced and full model behavior. Having this high nonlinear material behavior for relatively long durations will result in cumulating the differences between full and reduced models and thus giving a lower accuracy.

5- POD-ROM used for RC shear wall were less accurate and time efficient than the ones used for RC frame structure. This is due to the fact that the RC shear wall presented 3 types of nonlinear materials while the RC frame had only 2. Moreover, the concrete in shear wall had a biaxial nonlinear behavior that was modeled using an orthotropic rotating angle smeared crack approach. This makes the structural elements more sensitive to approximations made in model reduction. For all those reasons the calculation of the nonlinear return force became more complicated, which already was the most time-consuming operation in the analysis. Consequently, the accuracy and time efficiency of the POD-ROM were impacted.

6- The central difference explicit direct time integration technique was used to reduce the need for the time costly nonlinear return force calculation. However, it was seen in numerical application that the nonlinear return force calculation still poses a limitation for the time saving efficiency of the POD-ROM especially for shear walls where nonlinear concrete behavior is more complicated and demanding.

Perspectives

In this work, the speedups obtained with the POD-ROM are smaller than those expected from the reduction in model size. For instance, for the 2D frame structure, the full model had initially 1140 Degrees Of Freedom (DOF) and was reduced to only 4 so the scale factor is 285 (285 times smaller) while achieved speedups were up to 16 (16 times faster). It can be seen that despite a large-scale factor of 285, the maximum reached speedup is around 16. This is due to the fact that nonlinear return force has to be always calculated in the original full model basis. Despite minimizing the need for this expensive calculation by using central difference explicit direct time integration technique, it is still a limiting factor for the efficiency of the POD-ROM. As a perspective for this work, we suggest the use of the Proper Orthogonal Decomposition with Discrete Empirical Interpolation Method (POD-DEIM). In the POD-DEIM, snapshots for nonlinear part of return force are taken and corresponding POD modes are obtained and used for reduced order calculation of nonlinear return force. Thus, reducing the time cost and increasing the efficiency of the initial POD-ROM.

Another way to increase efficiency is by optimizing the size of each time step in the analysis of the POD-ROM. Thus, the total number of required time steps is lowered and the POD-ROM becomes more efficient in time saving. Such a technique was proposed by (Reyes *et al.*, 2021) for symmetric-plan buildings.

The POD-ROM for multiple base excitations was influenced by the choice of base vibration used for the initial FM analysis and POD modes extraction. In fact, it was seen that POD modes originating from strong vibrations tended to overestimate the nonlinear behavior of the corresponding POD-ROM when subjected to weaker earthquakes. Furthermore, it was shown in 5.2.3 that even for quakes with close intensity the choice of base excitation for the initial FM analysis had an impact on the POD-ROM accuracy. For this reason, we suggest first to arrange the base excitations in groups according to their intensity. Then, for each group, a synthetic base vibration can be created by taking the frequency spectrum envelop of all present base excitations. By doing so, the synthetic base excitation used for POD modes extraction can have a relative shorter duration and the obtained POD modes will have higher resemblance to all responses resulting from base excitations in the group.

Finally, it would be interesting to extend this work on reinforced concrete structures with material nonlinearities subjected to transient dynamic loadings such as impact and explosion loads. For this type of loadings and due to the high shock on the structural components, special nonlinear material models should be considered such that proposed by (Gatuingt and Pijaudier-Cabot, 2002).

Bibliography

[1] Abd El Fattah, A.M. (2012) *Behavior of concrete columns under various confinement effects*. Departement of Civil Engineering, College of Engineering, Kansas State University.

[2] Argyris, J.H. (1965) ‘Continua and discontinua Matrix methods in structural mechanics’, *1st Conference on Matrix Methods in Structural Mechanics*, pp. 11–189.

[3] ASCE/SEI 7-16 (2017) *Minimum Design Loads and Associated Criteria for Buildings and Other Structures*. 7th edn. Reston, VA: American Society of Civil Engineers. doi:10.1061/9780784414248.

[4] ATC 40 (1996) ‘Seismic evaluation and retrofit of concrete buildings’. Applied Technology Council.

[5] Atik, M., Sadek, M. and Shahrour, I. (2013) ‘Adaptive Pushover Procedure for Seismic assessment of Shear Wall Structures’, *21ème Congrès Français de Mécanique* [Preprint].

[6] Ayoub, A. and Filippou, F.C. (1998) ‘Nonlinear Finite-Element Analysis of RC Shear Panels and Walls’, *Journal of Structural Engineering*, 124(3), pp. 298–308. doi:10.1061/(ASCE)0733-9445(1998)124:3(298).

[7] Ayoub, N. *et al.* (2021) ‘An application of the Proper Orthogonal Decomposition method for nonlinear dynamic analysis of reinforced concrete structures subjected to earthquakes’, *8th International Conference on Computational Methods in Structural Dynamics and Earthquake Engineering* [Preprint].

[8] Babu, R.R., Benipal, G.S. and Singh, A.K. (2005) ‘CONSTITUTIVE MODELLING OF CONCRETE: AN OVERVIEW’, *Asian Journal Of Civil Engineering*, 6(4), pp. 211–246.

[9] Bahn, B.Y. and Hsu, C.-T.T. (1998) ‘Stress-Strain Behavior of Concrete under Cyclic Loading’, *ACI Materials Journal*, 95(2), pp. 178–193. doi:10.14359/363.

[10] Bamer, F., Amiri, A.K. and Bucher, C. (2017) ‘A new model order reduction strategy adapted to nonlinear problems in earthquake engineering’, *Earthquake Engineering & Structural Dynamics*, 46(46), pp. 537–559. doi:10.1002/eqe.2802.

[11] Bamer, F. and Bucher, C. (2012) ‘Application of the proper orthogonal decomposition for linear and nonlinear structures under transient excitations’, *Acta Mechanica*, 223, pp. 2549–2563. doi:10.1007/s00707-012-0726-9.

[12] Banon, H., Irvine, M. and Biggs, J.M. (1981) ‘Seismic Damage in Reinforced Concrete Frames’, *Journal of the Structural Division*, 107(9), pp. 1713–1729.

[13] Barzegar, F. (1988) 'Layering of RC Membrane and Plate Elements in Nonlinear Analysis', *Journal of Structural Engineering*, 114(11), pp. 2474–2492. doi:10.1061/(ASCE)0733-9445(1988)114:11(2474).

[14] Batoz, J.-L. and Dhatt, G. (1979) 'Incremental displacement algorithms for nonlinear problems', *International Journal for Numerical Methods in Engineering*, 14(8), pp. 1262–1267. doi:10.1002/nme.1620140811.

[15] Bauschinger, J. (1886) 'Über die Veränderung der Elasticitätsgrenze und der Festigkeit des Eisens und Stahls durch Strecken und Quetschen, durch Abkühlen und durch oftmals wiederholte Beanspruchung', *Mittheilungen aus dem Mechanisch-Technischem Laboratorium der K. Tech. Hochschule in München*, 15.

[16] Bazant, Z.P. (ed.) (1985) 'Mechanics of fracture and progressive cracking in concrete structures', in *Fracture mechanics of concrete: Structural application and numerical calculation*. Dordrecht, Netherlands: Martinus Nijhoff Publishers. doi:10.1007/978-94-009-6152-4.

[17] Bažant, Z.P. and Oh, B.H. (1983) 'Crack band theory for fracture of concrete', *Matériaux et Constructions*, 16(3), pp. 155–177. doi:10.1007/BF02486267.

[18] Belarbi, A. and Hsu, T.T.C. (1995) 'Constitutive Laws of Softened Concrete in Biaxial Tension Compression', *ACI Structural Journal*, 92(5), pp. 562–573. doi:10.14359/907.

[19] Benakli, S. *et al.* (2020) 'New Approach for Simulating Reinforced Concrete Walls in Quasi-static Loading', *Civil Engineering Journal*, 6(12), pp. 2352–2362. doi:10.28991/cej-2020-03091622.

[20] Besselink, B. *et al.* (2013) 'A comparison of model reduction techniques from structural dynamics, numerical mathematics and systems and control', *Journal of Sound and Vibration*, 332(19), pp. 4403–4422. doi:10.1016/j.jsv.2013.03.025.

[21] Bitar, I. (2017) *Modélisation de la rupture dans les structures en béton armé par des éléments finis poutres généralisées et multifibres*. Institut de Recherche en Génie Civil et Mécanique, École Centrale de Nantes.

[22] Bourahla, N. (2014) 'Equivalent Static Analysis of Structures Subjected to Seismic Actions', in Beer, M. et al. (eds) *Encyclopedia of Earthquake Engineering*. Berlin, Heidelberg: Springer Berlin Heidelberg, pp. 1–13. doi:10.1007/978-3-642-36197-5_169-2.

[23] Bracci, J.M., Kunnath, S.K. and Reinhorn, A.M. (1997) 'Seismic Performance and Retrofit Evaluation of Reinforced Concrete Structures', *Journal of Structural Engineering*, 123(1), pp. 3–10. doi:10.1061/(ASCE)0733-9445(1997)123:1(3).

[24] Breccolotti, M. *et al.* (2015) 'Constitutive modeling of plain concrete subjected to cyclic uniaxial compressive loading', *Construction and Building Materials*, 94, pp. 172–180. doi:10.1016/j.conbuildmat.2015.06.067.

[25] Burnett, D.J. and Schreyer, H.L. (2019) ‘A mesh objective method for modeling crack propagation using the smeared crack approach’, *International Journal for Numerical Methods in Engineering*, 117(5), pp. 574–603. doi:10.1002/nme.5968.

[26] Carpani, B. (2017) ‘Base isolation from a historical perspective’, *16th World conference on Earthquake Engineering*, Paper No. 4934.

[27] Ceresa, P. *et al.* (2009) ‘A fibre flexure-shear model for seismic analysis of RC-framed structures’, *Earthquake Engineering & Structural Dynamics*, 38(5), pp. 565–586. doi:10.1002/eqe.894.

[28] Cerioni, R. *et al.* (2008) ‘Multi-directional modeling of crack pattern in 2D R/C members’, *Engineering Fracture Mechanics*, 75(3–4), pp. 615–628. doi:10.1016/j.engfracmech.2007.04.012.

[29] Cervenka, J. (1994) *Discrete Crack Modelling of Concrete Structures*. CEAE Department, University of Colorado Boulder.

[30] Cervenka, V. (1970) *Inelastic finite element analysis of reinforced concrete panels under in-plane loads*. Departement of Civil Engineering, School of the University of Colorado.

[31] Cervenka, V. and Gerstle, K.H. (1971) ‘Inelastic analysis of reinforced concrete panels: theory’, *IABSE Publications*, 31(2), pp. 31–45. doi:https://doi.org/10.5169/seals-24217.

[32] Cervenka, V. and Gerstle, K.H. (1972) ‘Inelastic analysis of reinforced concrete panels: experimental verification and application’, *IABSE Publications*, 32(2), pp. 25–39. doi:10.5169/SEALS-24951.

[33] Cervera, M. (2008) ‘An orthotropic mesh corrected crack model’, *Computer Methods in Applied Mechanics and Engineering*, 197(17–18), pp. 1603–1619. doi:10.1016/j.cma.2007.12.007.

[34] Cervera, M., Chiumenti, M. and Codina, R. (2011) ‘Mesh objective modeling of cracks using continuous linear strain and displacement interpolations’, *International Journal for Numerical Methods in Engineering*, 87(10), pp. 962–987. doi:10.1002/nme.3148.

[35] *CESMD* (website) *Center for Engineering Strong Motion Data*. Available at: www.strongmotioncenter.org.

[36] Cha, Y.-J. and Buyukozturk, O. (2015) ‘Structural Damage Detection Using Modal Strain Energy and Hybrid Multiobjective Optimization: Damage detection using multiobjective optimization’, *Computer-Aided Civil and Infrastructure Engineering*, 30(5), pp. 347–358. doi:10.1111/mice.12122.

[37] Chang, G.A. and Mander, J.B. (1994) *Seismic Energy Based Fatigue Damage Analysis of Bridge Columns: Part 1 - Evaluation of Seismic Capacity*. Report No. NCEER-94-0006. Buffalo, New york, USA: University at Buffalo, State University of New York.

[38] Chopra, A.K. (2017) *Dynamics of structures: theory and applications to earthquake engineering*. Fifth edition. Hoboken, NJ: Pearson.

[39] Chopra, A.K. (2021) ‘Modal combination rules in response spectrum analysis: Early history’, *Earthquake Engineering & Structural Dynamics*, 50(2), pp. 260–269. doi:10.1002/eqe.3333.

[40] Chopra, A.K. and Goel, R.K. (2002) ‘A modal pushover analysis procedure for estimating seismic demands for buildings’, *Earthquake Engineering & Structural Dynamics*, 31(3), pp. 561–582. doi:10.1002/eqe.144.

[41] Chung, J. and Hulbert, G.M. (1993) ‘A Time Integration Algorithm for Structural Dynamics With Improved Numerical Dissipation: The Generalized-α Method’, *Journal of Applied Mechanics*, 60(2), pp. 371–375. doi:10.1115/1.2900803.

[42] Ciampi, V. and Carlesimo, L. (1986) ‘A nonlinear beam element for seismic analysis of structures’, *8th European Conference on Earthquake Engineering* [Preprint].

[43] Clough, R. and Benuska, K.L. (1967) ‘Nonlinear Earthquake Behavior of Tall Buildings’, *Journal of the Engineering Mechanics Division*, 93(3), pp. 129–146. doi:10.1061/JMCEA3.0000855.

[44] Clough, R.W. (1962) *The Stress Distribution of Norfork Dam*. Series 100, Issue 19. Berkeley, California, USA: Structures and Materials Research, Department of Civil Engineering, University of California.

[45] Clough, R.W. and Johnston, S.B. (1966) ‘Effect of stiffness degradation on earthquake ductility requirements’, *Japan Earthquake Engineering Symposium* [Preprint].

[46] Contrafatto, L., Cuomo, M. and Fazio, F. (2012) ‘An enriched finite element for crack opening and rebar slip in reinforced concrete members’, *International Journal of Fracture*, 178(1–2), pp. 33–50. doi:10.1007/s10704-012-9723-1.

[47] Cope, R.J. *et al.* (1980) ‘Modelling of Reinforced Concrete Behaviour for Finite Element Analysis of Bridge Slabs’, *International Conference In Numerical Methods for Nonlinear Problems*, pp. 457–470.

[48] Craig, R.R. and Bampton, M.C.C. (1968) ‘Coupling of substructures for dynamic analyses.’, *AIAA Journal*, 6(7), pp. 1313–1319. doi:10.2514/3.4741.

[49] Cusson, D. and Paultre, P. (1995) ‘Stress-Strain Model for Confined High-Strength Concrete’, *Journal of Structural Engineering*, 121(3), pp. 468–477. doi:10.1061/(ASCE)0733-9445(1995)121:3(468).

[50] Darwin, D. and Pecknold, D.A. (1974) *Inelastic model for cyclic biaxial loading of reinforced concrete*. Technical report. Urbana, Illinois: University of Illinois.

[51] Darwin, D. and Pecknold, D.A. (1977a) ‘Analysis of cyclic loading of plane R/C structures’, *Computers & Structures*, 7, pp. 137–147.

[52] Darwin, D. and Pecknold, D.A. (1977b) ‘Nonlinear Biaxial Stress-Strain Law for Concrete’, *Journal of the Engineering Mechanics Division*, 103(2), pp. 229–241. doi:10.1061/JMCEA3.0002220.

[53] Dhakal, R.P. and Maekawa, K. (2002) ‘Path-dependent cyclic stress–strain relationship of reinforcing bar including buckling’, *Engineering Structures*, 24(11), pp. 1383–1396. doi:10.1016/S0141-0296(02)00080-9.

[54] Djukic, S. and Saric, A. (2012) ‘Dynamic model reduction: An overview of available techniques with application to power systems’, *Serbian Journal of Electrical Engineering*, 9(2), pp. 131–169. doi:10.2298/SJEE1202131D.

[55] Dolsek, M. (2010) ‘Development of computing environment for the seismic performance assessment of reinforced concrete frames by using simplified nonlinear models’, *Bulletin of Earthquake Engineering*, 8, pp. 1309–1329. doi:10.1007/s10518-010-9184-8.

[56] EC8-1 (2004) ‘Eurocode 8: Design of structures for earthquake resistance - Part 1 : General rules, seismic actions and rules for buildings’. European Committee for Standarization.

[57] EC8-3 (2005) ‘Eurocode 8: Design of structures for earthquake resistance - Part 3: Assessment and retrofitting of buildings’. European Committee for Standarization.

[58] Elnashai, A.S. (2002) ‘A very brief history of earthquake engineering with emphasis on developments in and from the British Isles’, *Chaos, Solitons & Fractals*, 13(5), pp. 967–972. doi:10.1016/S0960-0779(01)00107-2.

[59] Ewins, D.J. (2000) *Modal testing: theory, practice, and application*. 2nd ed. Baldock, Hertfordshire, England ; Philadelphia, PA: Research Studies Press (Mechanical engineering research studies, 10).

[60] Fajfar, P. *et al.* (2006) ‘Pre- and post-test mathematical modelling of a plan-asymmetric reinforced concrete frame building’, *Earthquake Engineering & Structural Dynamics*, 35(11), pp. 1359–1379. doi:10.1002/eqe.583.

[61] Fajfar, P. and Fischinger, M. (1990) ‘Mathematical modeling of reinforced concrete structural walls for nonlinear seismic analysis’, *European Conference on Structural Dynamics*, pp. 471–478.

[62] Fan, T. (2012) *Concrete microstructure homogenization technique with application to model concrete serviceability*. University of New Mexico, Departement of Civil Engineering.

[63] FEMA 356 (2000) ‘Prestandard and Commentary for the Seismic Rehabilitation of Buildings’. Federal Emergency Management Agency.

[64] FEMA 440 (2005) ‘Improvement of Nonlinear Static Seismic Analysis Procedures’. Federal Emergency Management Agency.

[65] FEMA P-750 (2009) ‘NEHRP Recommended Seismic Provisions for New Buildings and Other Structures’. Federal Emergency Management Agency.

[66] Feng, D.-C. *et al.* (2017) ‘A flexure-shear Timoshenko fiber beam element based on softened damage-plasticity model’, *Engineering Structures*, 140, pp. 483–497. doi:10.1016/j.engstruct.2017.02.066.

[67] Filippou, F.C. and Issa, A. (1988) *Nonlinear Analysis of Reinforced Concrete Frames under Cyclic Load Reversals*. Report No. UCB/EERC-88/12. Berkeley, California, USA: Earthquake Engineering Research Center, College of Engineering, University of California.

[68] Fischinger, M., Isakovic, T. and Kante, P. (2004) 'Seismic Vulnerability Evaluation of Lightly Reinforced Walls', *13th World Conference on Earthquake Engineering*, Paper No. 468.

[69] Fischinger, M., Rejec, K. and Isaković, T. (2012) 'Modeling Inelastic Shear Response of RC Walls', *15th World Conference on Earthquake Engineering* [Preprint].

[70] Foster, S.J. and Marti, P. (2003) 'Cracked Membrane Model: Finite Element Implementation', *Journal of Structural Engineering*, 129(9), pp. 1155–1163. doi:10.1061/(ASCE)0733-9445(2003)129:9(1155).

[71] Gatuingt, F. and Pijaudier-Cabot, G. (2002) 'Coupled damage and plasticity modelling in transient dynamic analysis of concrete', *International Journal for Numerical and Analytical Methods in Geomechanics*, 26(1), pp. 1–24. doi:10.1002/nag.188.

[72] Gerstle, W.H. and Xie, M. (1992) 'FEM Modeling of Fictitious Crack Propagation in Concrete', *Journal of Engineering Mechanics*, 118(2), pp. 416–434. doi:10.1061/(ASCE)0733-9399(1992)118:2(416).

[73] Giberson, M.F. (1967) *The response of nonlinear multi-story structures subjected to earthquake excitation*. California Institute of Technology.

[74] Giuffrè, A. and Pinto, P.E. (1970) 'Il comportamento del cemento armato per sollecitazioni cicliche di forte intensità', *Giornale del Genio Civile*, 5, pp. 391–408.

[75] Gomes, A. and Appleton, J. (1997) 'Nonlinear cyclic stress-strain relationship of reinforcing bars including buckling', *Engineering Structures*, 19(10), pp. 822–826. doi:10.1016/S0141-0296(97)00166-1.

[76] Gopinath, S. *et al.* (2012) 'Nonlinear analysis of RC shell structures using multilevel modelling techniques', *Engineering Computations*, 29(2), pp. 104–124. doi:10.1108/02644401211206016.

[77] Gupta, A.K. and Akbar, H. (1984) 'Cracking in Reinforced Concrete Analysis', *Journal of Structural Engineering*, 110(8), pp. 1735–1746. doi:10.1061/(ASCE)0733-9445(1984)110:8(1735).

[78] Guyan, R.J. (1965) 'Reduction of stiffness and mass matrices', *AIAA Journal*, 3(2), pp. 380–380. doi:10.2514/3.2874.

[79] Hajirasouliha, I. and Moghaddam, H. (2009) 'New Lateral Force Distribution for Seismic Design of Structures', *Journal of Structural Engineering*, 135(8), pp. 906–915. doi:10.1061/(ASCE)0733-9445(2009)135:8(906).

[80] Hand, F.R., Pecknold, D.A. and Schnobrich, W.C. (1972) *A layered finite element nonlinear analysis of reinforced concrete plates and shells*. Technical Report No. 389. Urbana, Illinois: University of Illinois.

[81] Harajli, M.H. (2006) ‘Axial stress–strain relationship for FRP confined circular and rectangular concrete columns’, *Cement and Concrete Composites*, 28(10), pp. 938–948. doi:10.1016/j.cemconcomp.2006.07.005.

[82] Hearn, G. and Testa, R.B. (1991) ‘Modal Analysis for Damage Detection in Structures’, *Journal of Structural Engineering*, 117(10), pp. 3042–3063. doi:10.1061/(ASCE)0733-9445(1991)117:10(3042).

[83] Hellesland, J. and Scordelis, A.C. (1981) ‘Analysis of RC bridge columns under imposed deformations’, *IABSE Colloquium on Advanced Mechanics of Reinforced Concrete*, pp. 545–559.

[84] Hilber, H.M., Hughes, T.J.R. and Taylor, R.L. (1977) ‘Improved numerical dissipation for time integration algorithms in structural dynamics’, *Earthquake Engineering & Structural Dynamics*, 5(3), pp. 283–292. doi:10.1002/eqe.4290050306.

[85] Hoehler, M.S. and Stanton, J.F. (2006) ‘Simple Phenomenological Model for Reinforcing Steel under Arbitrary Load’, *Journal of Structural Engineering*, 132(7), pp. 1061–1069. doi:10.1061/(ASCE)0733-9445(2006)132:7(1061).

[86] Hoff, C. and Pahl, P.J. (1988a) ‘Development of an implicit method with numerical dissipation from a generalized single-step algorithm for structural dynamics’, *Computer Methods in Applied Mechanics and Engineering*, 67, pp. 367–385.

[87] Hoff, C. and Pahl, P.J. (1988b) ‘Practical performance of the θ1-method and comparison with other dissipative algorithms in structural dynamics’, *Computer Methods in Applied Mechanics and Engineering*, 67, pp. 87–110.

[88] Hosford, W.F. (2013) *Fundamentals of engineering plasticity*. Cambridge University Press.

[89] Hotelling, H. (1933) ‘Analysis of a complex of statistical variables into principal components’, *Journal of Educational Psychology*, 24(6), pp. 417–441. doi:10.1037/h0071325.

[90] Houbolt, J.C. (1950) ‘A Recurrence Matrix Solution for the Dynamic Response of Elastic Aircraft’, *Journal of the Aeronautical Sciences*, 17(9), pp. 540–550. doi:10.2514/8.1722.

[91] Houlsby, G.T. and Puzrin, A.M. (2006) *Principles of hyperplasticity: an approach to plasticity theory based on thermodynamic principles*. London: Springer.

[92] Hu, H.-T. and Schnobrich, W.C. (1991) ‘Nonlinear finite element analysis of reinforced concrete plates and shells under monotonic loading’, *Computers & Structures*, 38(5–6), pp. 637–651. doi:10.1016/0045-7949(91)90015-E.

[93] Huguet, M. *et al.* (2017) ‘Stress resultant nonlinear constitutive model for cracked reinforced concrete panels’, *Engineering Fracture Mechanics*, 176, pp. 375–405. doi:10.1016/j.engfracmech.2017.02.027.

[94] Ibarra, L.F., Medina, R.A. and Krawinkler, H. (2005) ‘Hysteretic models that incorporate strength and stiffness deterioration’, *Earthquake Engineering & Structural Dynamics*, 34(12), pp. 1489–1511. doi:10.1002/eqe.495.

[95] Ibrahimbegović, A. (1993) ‘Mixed finite element with drilling rotations for plane problems in finite elasticity’, *Computer Methods in Applied Mechanics and Engineering*, 107(1–2), pp. 225–238. doi:10.1016/0045-7825(93)90177-Y.

[96] Ibrahimbegović, A. and Frey, F. (1993) ‘Geometrically non-linear method of incompatible modes in application to finite elasticity with independent rotations’, *International Journal for Numerical Methods in Engineering*, 36(24), pp. 4185–4200. doi:10.1002/nme.1620362406.

[97] Ibrahimbegović, A. and Frey, F. (1995) ‘Variational principles and membrane finite elements with drilling rotations for geometrically non-linear elasticity’, *International Journal for Numerical Methods in Engineering*, 38(11), pp. 1885–1900. doi:10.1002/nme.1620381106.

[98] Ingraffea, A.R. and Saouma, V. (eds) (1985) ‘Numerical modeling of discrete crack propagation in reinforced and plain concrete’, in *Fracture mechanics of concrete: Structural application and numerical calculation*. Dordrecht, Netherlands: Martinus Nijhoff Publishers. doi:10.1007/978-94-009-6152-4.

[99] Izzuddin, B.A. (1990) *Nonlinear dynamic analysis of framed structres*. Civil Engineering Departement, Imperial College of Science and Technology, University of London.

[100] Jiang, H. and Kurama, Y.C. (2010) ‘Analytical Modeling of Medium-Rise Reinforced Concrete Shear Walls’, *ACI Structural Journal*, 107(4), pp. 400–410. doi:10.14359/51663812.

[101] Jirásek, M. and Zimmermann, T. (1998) ‘Analysis of Rotating Crack Model’, *Journal of Engineering Mechanics*, 124(8), pp. 842–851. doi:10.1061/(ASCE)0733-9399(1998)124:8(842).

[102] Kaba, S.A. and Mahin, S.A. (1984) *Refined Modelling of reinforced concrete columns for seismic analysis*. Technical Report No. UCB/EERC-84/3. Berkeley, California: Earthquake Engineering Research Center, College of Engineering, University of California.

[103] Karhunen, K. (1946) ‘Zur Spektraltheorie stochastischer Prozesse’, *Annales Academiæ Scientiarum Fennicæ Series A. I. Mathematica*, 34, pp. 1–7.

[104] Karsan, I.D. and Jirsa, J.O. (1969) ‘Behavior of Concrete Under Compressive Loadings’, *Journal of the Structural Division*, 95(12), pp. 2543–2564.

[105] Kaufmann, W. and Marti, P. (1998) ‘Structural Concrete: Cracked Membrane Model’, *Journal of Structural Engineering*, 124(12), pp. 1467–1475. doi:10.1061/(ASCE)0733-9445(1998)124:12(1467).

[106] Kent, D.C. and Park, R. (1971) ‘Flexural Members with Confined Concrete’, *Journal of the Structural Division*, 97(7), pp. 1969–1990.

[107] Kim, T. and LaFave, J.M. (2017) ‘Proposed new equivalent lateral force design method for low-rise reinforced concrete wall-frame mixed building systems’, *Engineering Structures*, 152, pp. 87–101. doi:10.1016/j.engstruct.2017.09.001.

[108] Kim, T.-H., Lee, K.-M. and Shin, H.M. (2002) ‘Nonlinear Analysis of Reinforced Concrete Shells using Layered Elements with Drilling Degree of Freedom’, *ACI Structural Journal*, 99(4), pp. 418–426. doi:10.14359/12110.

[109] Kolozvari, K., Orakcal, K. and Wallace, J.W. (2015) ‘Modeling of Cyclic Shear-Flexure Interaction in Reinforced Concrete Structural Walls. I: Theory’, *Journal of Structural Engineering*, 141(5). doi:10.1061/(ASCE)ST.1943-541X.0001059.

[110] Kosambi, D.D. (1943) ‘Statistics in function space’, *Journal of the Indian Mathematical Society*, 7, pp. 76–88.

[111] Kotronis, P. and Mazars, J. (2005) ‘Simplified modelling strategies to simulate the dynamic behaviour of R/C walls’, *Journal of Earthquake Engineering*, 9(2), pp. 285–306. doi:10.1080/13632460509350543.

[112] Kunnath, S.K., Heo, Y. and Mohle, J.F. (2009) ‘Nonlinear Uniaxial Material Model for Reinforcing Steel Bars’, *Journal of Structural Engineering*, 135(4), pp. 335–343. doi:10.1061/(ASCE)0733-9445(2009)135:4(335).

[113] Lam, L. and Teng, J.G. (2009) ‘Stress–strain model for FRP-confined concrete under cyclic axial compression’, *Engineering Structures*, 31(2), pp. 308–321. doi:10.1016/j.engstruct.2008.08.014.

[114] Li, P. *et al.* (2018) ‘Cyclic stress-strain model for FRP-confined concrete considering post-peak softening’, *Composite Structures*, 201, pp. 902–915. doi:10.1016/j.compstruct.2018.06.088.

[115] Loève, M. (1948) ‘Fonctions aléatoires du second ordre’, in *Processus Stochastique et Mouvement Brownien*.

[116] Mahdiabadi, M.K. (2019) *Nonlinear Model Order Reduction and Substructuring for Structural Dynamics Analysis*. Faculty of Mechanical Engineering at the Technical University of Munich.

[117] Mander, J.B. (1983) *Seismic design of bridge piers*. Departement of Civil Engineering, University of Canterbury.

[118] Mander, J.B., Priestley, M.J.N. and Park, R. (1988) ‘Theoretical Stress-Strain Model for Confined Concrete’, *Journal of Structural Engineering*, 114(8), pp. 1804–1826. doi:10.1061/(ASCE)0733-9445(1988)114:8(1804).

[119] Mark, K.M.S. and Roesset, J.M. (1976) *Nonlinear dynamic response of reinforced concrete frames*. Technical Report No. R76-38. Cambridge, Massachusetts: School of Engineering, Massachusetts Institute of Technology.

[120] Massicotte, B., MacGregor, J.G. and Elwi, A.E. (1990) 'Behavior of Concrete Panels Subjected to Axial and Lateral Loads', *Journal of Structural Engineering*, 116(9), pp. 2324–2343. doi:10.1061/(ASCE)0733-9445(1990)116:9(2324).

[121] Mazars, J. *et al.* (2006) 'Using multifiber beams to account for shear and torsion Applications to concrete structural elements', *Computer Methods in Applied Mechanics and Engineering*, 195(52), pp. 7264–7281. doi:10.1016/j.cma.2005.05.053.

[122] Mendes, L.A.M. and Castro, L.M.S.S. (2014) 'A simplified reinforcing steel model suitable for cyclic loading including ultra-low-cycle fatigue effects', *Engineering Structures*, 68, pp. 155–164. doi:10.1016/j.engstruct.2014.02.031.

[123] Mendis, P., Pendyala, R. and Setunge, S. (2000) 'Stress–strain model to predict the full-range moment curvature behaviour of high-strength concrete sections', *Magazine of Concrete Research*, 52(4), pp. 227–234. doi:10.1680/macr.2000.52.4.227.

[124] Menegotto, M. and Pinto, P.E. (1973) 'Method of analysis for cyclically loaded R.C. plane frames including changes in geometry and non-elastic behaviour of elements under combined normal force and bending', *Proceedings of IABSE Symposium on Resistance and Ultimate Deformability of Structures Acted On by Well Defined Repeated Loads*, pp. 15–22. doi:10.5169/SEALS-13741.

[125] Mitchell, D. *et al.* (2010) 'Evolution of seismic design provisions in the National building code of Canada', *Canadian Journal of Civil Engineering*, 37(9), pp. 1157–1170. doi:10.1139/L10-054.

[126] Mohammadi, R.K. and EL Naggar, M.H. (2004) 'Modifications on equivalent lateral force method', *13th World conference on Earthquake Engineering*, Paper No. 928.

[127] Monti, G. and Spacone, E. (2000) 'Reinforced Concrete Fiber Beam Element with Bond-Slip', *Journal of Structural Engineering*, 126(6), pp. 654–661. doi:10.1061/(ASCE)0733-9445(2000)126:6(654).

[128] Muto, K. *et al.* (1960) 'Non-linear response analyzers and application to earthquake resistant design', *2nd World Conference on Earthquake Engineering*, 2, pp. 649–668.

[129] Neuenhofer, A. and Filippou, F.C. (1997) 'Evaluation of Nonlinear Frame Finite-Element Models', *Journal of Structural Engineering*, 123(7), pp. 958–966. doi:10.1061/(ASCE)0733-9445(1997)123:7(958).

[130] Newmark, N.M. (1959) 'A Method of Computation for Structural Dynamics', *Journal of the Engineering Mechanics Division*, 85(3), pp. 67–94.

[131] Ngo, D. and Scordelis, A.C. (1967) 'Finite Element Analysis of Reinforced Concrete Beams', *ACI Journal Proceedings*, 64(3), pp. 152–163. doi:10.14359/7551.

[132] Nilson, A.H. (1968) 'Nonlinear Analysis of Reinforced Concrete by the Finite Element Method', *ACI Journal Proceedings*, 65(9), pp. 757–766. doi:10.14359/7510.

[133] Obukhov, A.M. (1954) 'Statistical description of continuous fields', *Tr. Geophys. Int. Akad. Nauk. SSSR*, 24, pp. 3–42.

[134] Orakcal, K. and Wallace, J.W. (2006) ‘Flexural Modeling of Reinforced Concrete Walls - Experimental Verification’, *ACI Structural Journal*, 103(2), pp. 196–206. doi:10.14359/15177.

[135] Otani, S. (1974) ‘Inelastic Analysis of R/C Frame Structures’, *Journal of the Structural Division*, 100(7), pp. 1433–1449.

[136] Owen, D.R.J. and Hinton, E. (1980) *Finite elements in plasticity: theory and practice*. Swansea, U.K.: Pineridge Press.

[137] Papaioannou, I., Fragiadakis, M. and Papadrakakis, M. (2005) ‘Inelastic Analysis of Framed Structures Using the Fiber Approach’, *5th GRACM International Congress on Computational Mechanics* [Preprint].

[138] Park, R., Priestley, M.J.N. and Gill, W.D. (1982) ‘Ductility of Square-Confined Concrete Columns’, *Journal of the Structural Division*, 108(4), pp. 929–950.

[139] Patel, R. *et al.* (2021) ‘Simulating 3D crack propagation with XFEM to investigate failure mechanism in high strength concrete’, *Proceedings in Applied Mathematics and Mechanics*, 20(1). doi:10.1002/pamm.202000296.

[140] Petrangeli, M., Pinto, P.E. and Ciampi, V. (1999) ‘Fiber Element for Cyclic Bending and Shear of RC Structures. I: Theory’, *Journal of Engineering Mechanics*, 125(9), pp. 994–1001. doi:10.1061/(ASCE)0733-9399(1999)125:9(994).

[141] Polak, M.A. (1998) ‘Modeling Punching Shear of Reinforced Concrete Slabs Using Layered Finite Elements’, *ACI Structural Journal*, 95(1), pp. 71–80. doi:10.14359/528.

[142] Polak, M.A. and Vecchio, F.J. (1993) ‘Nonlinear Analysis of Reinforced-Concrete Shells’, *Journal of Structural Engineering*, 119(12), pp. 3439–3462. doi:10.1061/(ASCE)0733-9445(1993)119:12(3439).

[143] Popovics, S. (1973) ‘A numerical approach to the complete stress-strain curve of concrete’, *Cement and Concrete Research*, 3(5), pp. 583–599. doi:10.1016/0008-8846(73)90096-3.

[144] Powell, G.H. and Chen, P.F. (1986) ‘3D Beam-Column Element with Generalized Plastic Hinges’, *Journal of Engineering Mechanics*, 112(7), pp. 627–641. doi:10.1061/(ASCE)0733-9399(1986)112:7(627).

[145] Prasad, M.V.K.V. and Krishnamoorthy, C.S. (2002) ‘Computational model for discrete crack growth in plain and reinforced concrete’, *Computer Methods in Applied Mechanics and Engineering*, 191(25–26), pp. 2699–2725. doi:10.1016/S0045-7825(02)00210-4.

[146] Pugachev, V.S. (1953) ‘The general theory of correlation of random functions’, *Izvestiya Rossiiskoi Akademii Nauk, Seriya Matematicheskaya*, 17(5), pp. 401–420.

[147] Qi, H. and Li, Y.-G. (2014) ‘The Uniaxial Constitutive Models of Reinforcement and Concrete for Nonlinear Dynamic Analysis’:, *International Conference on Mechanics and Civil Engineering* [Preprint]. doi:10.2991/icmce-14.2014.29.

[148] Rainieri, C. and Fabbrocino, G. (2014) *Operational Modal Analysis of Civil Engineering Structures*. New York, NY: Springer New York. doi:10.1007/978-1-4939-0767-0.

[149] Rao, S.S. (2007) *Vibration of continuous systems*. Hoboken, N.J: Wiley.

[150] Rashid, Y.R. (1968) 'Ultimate strength analysis of prestressed concrete pressure vessels', *Nuclear Engineering and Design,* 7(4), pp. 334–344. doi:10.1016/0029-5493(68)90066-6.

[151] Razvi, S. and Saatcioglu, M. (1999) 'Confinement Model for High-Strength Concrete', *Journal of Structural Engineering,* 125(3), pp. 281–289. doi:10.1061/(ASCE)0733-9445(1999)125:3(281).

[152] Rebiai, C. and Belounar, L. (2013) 'A new strain based rectangular finite element with drilling rotation for linear and nonlinear analysis', *Archives of Civil and Mechanical Engineering,* 13(1), pp. 72–81. doi:10.1016/j.acme.2012.10.001.

[153] Reitherman, R. (2006) 'Earthquakes that have initiated the development of earthquake engineering', *Bulletin of the New Zealand Society for Earthquake Engineering,* 39(3), pp. 145–157. doi:10.5459/bnzsee.39.3.145-157.

[154] Reyes, J.C. *et al.* (2021) 'Reducing Processing Time of Nonlinear Analysis of Symmetric-Plan Buildings', *Journal of Structural Engineering,* 147(6), p. 04021073. doi:10.1061/(ASCE)ST.1943-541X.0003000.

[155] Richart, F.E., Brandtzaeg, A. and Brown, R.L. (1928) 'A study of the failure of concrete under combined compressive stresses', *University of Illinois Bulletin,* 16(12).

[156] Richart, F.E., Brandtzaeg, A. and Brown, R.L. (1929) 'Failure of plain and spirally reinforced concrete in compression', *University of Illinois Bulletin,* 16(31).

[157] Rojas, F. (2012) *Development of a nonlinear quadrilateral layered membrane element with drilling degrees of freedom and a nonlinear quadrilateral thin flat layered shell element for the modeling of reinforced concrete walls*. Faculty of the USC Graduate School, University of Southern California.

[158] Rojas, F., Anderson, J.C. and Massone, L.M. (2016) 'A nonlinear quadrilateral layered membrane element with drilling degrees of freedom for the modeling of reinforced concrete walls', *Engineering Structures,* 124, pp. 521–538. doi:10.1016/j.engstruct.2016.06.024.

[159] Rojas, F., Anderson, J.C. and Massone, L.M. (2019) 'A nonlinear quadrilateral thin flat layered shell element for the modeling of reinforced concrete wall structures', *Bulletin of Earthquake Engineering,* 17(12), pp. 6491–6513. doi:10.1007/s10518-019-00566-8.

[160] Roy, H.E.H. and Sozen, M.A. (1965) 'Ductility of Concrete', *ACI Symposium Publication,* 12, pp. 213–235. doi:10.14359/16718.

[161] Roy, R. and Mahato, S. (2013) 'Equivalent lateral force method for buildings with setback: adequacy in elastic range', *Earthquakes and Structures,* 4(6), pp. 685–710. doi:10.12989/EAS.2013.4.6.685.

[162] Sampaio, R.P.C., Maia, N.M.M. and Silva, J.M.M. (1999) ‘Damage detection using the frequency-response-function curvature method’, *Journal of Sound and Vibration*, 226(5), pp. 1029–1042. doi:10.1006/jsvi.1999.2340.

[163] Sargin, M. (1971) *Stress-Strain Relationship for Concrete and the Analysis of Structural Concrete Sections*. Report No. 4. Waterloo, Canada: Solid Mechanics Division, University of Waterloo.

[164] Sato, Y. and Fujii, S. (2002) ‘Local Stresses and Crack Displacements in Reinforced Concrete Elements’, *Journal of Structural Engineering*, 128(10), pp. 1263–1271. doi:10.1061/(ASCE)0733-9445(2002)128:10(1263).

[165] Schnobrich, W.C. (1977) ‘Behavior of reinforced concrete structures predicted by the finite element method’, *Computers & Structures*, 7(3), pp. 365–376. doi:10.1016/0045-7949(77)90074-8.

[166] Scordelis, A.C. and Chan, E.C. (1987) ‘Nonlinear analysis of reinforced concrete shells’, *ACI Symposium Publication*, 98, pp. 25–28. doi:10.14359/2819.

[167] Scott, B.D., Park, R. and Priestley, M.J.N. (1982) ‘Stress-Strain Behavior of Concrete Confined by Overlapping Hoops at Low and High Strain Rates’, *ACI Journal Proceedings*, 79(1), pp. 13–27. doi:10.14359/10875.

[168] Scott, M.H. and Fenves, G.L. (2006) ‘Plastic Hinge Integration Methods for Force-Based Beam–Column Elements’, *Journal of Structural Engineering*, 132(2), pp. 244–252. doi:10.1061/(ASCE)0733-9445(2006)132:2(244).

[169] Shen, Y. *et al.* (2021) ‘Comparison of Reduction Methods for Finite Element Geometrically Nonlinear Beam Structures’, *Vibration*, 4(1), pp. 175–204. doi:10.3390/vibration4010014.

[170] Sima, J.F., Roca, P. and Molins, C. (2008) ‘Cyclic constitutive model for concrete’, *Engineering Structures*, 30(3), pp. 695–706. doi:10.1016/j.engstruct.2007.05.005.

[171] Sinha, B.P., Gerstle, K.H. and Tulin, L.G. (1964) ‘Stress-Strain Relations for Concrete Under Cyclic Loading’, *ACI Journal Proceedings*, 61(2), pp. 195–212. doi:10.14359/7775.

[172] Spacone, E., Filippou, F.C. and Taucer, F.F. (1996) ‘Fibre beam–column model for non-linear analysis of R/C frames: Part I. Formulation’, *Earthquake Engineering & Structural Dynamics*, 25, pp. 711–725.

[173] Strutt, J.W. and Rayleigh, B. (1877) *The theory of sound*. London, UK: Macmillan and Co.

[174] Suidan, M. and Schnobrich, W.C. (1973) ‘Finite Element Analysis of Reinforced Concrete’, *Journal of the Structural Division*, 99(10), pp. 2109–2122.

[175] Takeda, T., Sozen, M.A. and Nielsen, N.N. (1970) ‘Reinforced Concrete Response to Simulated Earthquakes’, *Journal of the Structural Division*, 96(12), pp. 2557–2573.

[176] Taucer, F.F., Spacone, E. and Filippou, F.C. (1991) *A Fiber beam-column element for seismic response analysis of reinforced concrete structures*. Technical Report No. UCB/EERC-91/17. Berkeley, California: Earthquake Engineering Research Center, College of Engineering, University of California.

[177] Thomsen, J.H. and Wallace, J.W. (2004) 'Displacement-Based Design of Slender Reinforced Concrete Structural Walls—Experimental Verification', *Journal of Structural Engineering*, 130(4), pp. 618–630. doi:10.1061/(ASCE)0733-9445(2004)130:4(618).

[178] Torre-Casanova, A. *et al.* (2013) 'Confinement effects on the steel–concrete bond strength and pull-out failure', *Engineering Fracture Mechanics*, 97, pp. 92–104. doi:10.1016/j.engfracmech.2012.10.013.

[179] UBC (1997) '1997 Uniform Building Code'. International Conference of Building Officials.

[180] Vallejos, R.C. (2018) *Characterization of Large Diameter Reinforcement Under Large Strain Cyclic Reversals*. University of California San Diego.

[181] Valliappan, S. and Doolan, T.F. (1972) 'Nonlinear Stress Analysis of Reinforced Concrete', *Journal of the Structural Division*, 98(4), pp. 885–898. doi:10.1061/JSDEAG.0003204.

[182] Valoroso, N., Marmo, F. and Sessa, S. (2014) 'Limit state analysis of reinforced shear walls', *Engineering Structures*, 61, pp. 127–139. doi:10.1016/j.engstruct.2013.12.032.

[183] Vecchio, F.J. (1989) 'Nonlinear Finite Element Analysis of Reinforced Concrete Membranes', *ACI Structural Journal*, 86(1), pp. 26–35.

[184] Vecchio, F.J. and Collins, M.P. (1986) 'The Modified Compression-Field Theory for Reinforced Concrete Elements Subjected to Shear', *ACI Journal Proceedings*, 83(2), pp. 219–231. doi:10.14359/10416.

[185] Veletsos, A.S. and Newmark, N.M. (1960) 'Effect of inelastic behavior on the response of simple systems to earthquake motions', *2nd World Conference on Earthquake Engineering*, 2, pp. 895–912.

[186] Vulcano, A., Bertero, V. and Colotti, V. (1988) 'Analytical Modeling of R/C structural walls', *9th World Conference on Earthquake Engineering* [Preprint].

[187] Wilson, E.L. (1968) *A Computer Program for the Dynamic Stress Analysis of Underground Structures*. Report No. 68-1. Berkeley, California, USA: Division of Structural Engineering and Structural Mechanics, University of California.

[188] Wood, W.L., Bossak, M. and Zienkiewicz, O.C. (1980) 'An alpha modification of Newmark's method', *International Journal for Numerical Methods in Engineering*, 15(10), pp. 1562–1566. doi:10.1002/nme.1620151011.

[189] Yang, Z.J. and Chen, J. (2005) 'Finite element modelling of multiple cohesive discrete crack propagation in reinforced concrete beams', *Engineering Fracture Mechanics*, 72(14), pp. 2280–2297. doi:10.1016/j.engfracmech.2005.02.004.

[190] Yankelevsky, D.Z. and Reinhardt, H.W. (1987) ‘Model for Cyclic Compressive Behavior of Concrete’, *Journal of Structural Engineering*, 113(2), pp. 228–240. doi:10.1061/(ASCE)0733-9445(1987)113:2(228).

[191] Yuzugullu, O. and Schnobrich, W.C. (1973) ‘A Numerical Procedure for the Determination of the Behavior of a Shear Wall Frame System’, *ACI Journal Proceedings*, 70(7), pp. 474–479. doi:10.14359/11225.

[192] Zeris, C.A. and Mahin, S.A. (1988) ‘Analysis of Reinforced Concrete Beam-Columns under Uniaxial Excitation’, *Journal of Structural Engineering*, 114(4), pp. 804–820. doi:10.1061/(ASCE)0733-9445(1988)114:4(804).

[193] Zhang, Y.X., Bradford, M.A. and Gilbert, R.I. (2007) ‘A layered cylindrical quadrilateral shell element for nonlinear analysis of RC plate structures’, *Advances in Engineering Software*, 38(7), pp. 488–500. doi:10.1016/j.advengsoft.2006.09.017.

[194] Zouari, W., Hammadi, F. and Ayad, R. (2016) ‘Quadrilateral membrane finite elements with rotational DOFs for the analysis of geometrically linear and nonlinear plane problems’, *Computers & Structures*, 173, pp. 139–149. doi:10.1016/j.compstruc.2016.06.004.

Appendix A : Nonlinear calculation

Determining the load deflection path of a nonlinear structural system is not a straightforward calculation like the one used for linear structures. In fact, a large variety of numerical methods and tools exist. Generally, all these methods are incremental and work in iterations. The controlling parameter is applied in increments. Nonlinear methods can be controlled by force increments (force control methods such as Newton-Raphson), by displacement increments (displacement control method) or by a mixture of force and displacement increments (such as arc-length method).

At each increment step, multiple iterations are conducted to minimize the unbalance of the system until force, displacement and energy convergences are achieved. In fact within each iteration, linear relations are used. This creates an offset in the results since the actual behavior is nonlinear.

So, in general the nonlinear calculation methods consist of dividing the problem into relatively small steps, linear relations are assumed within each step. This linear assumption produces an offset that is corrected by considering the system's unbalance.

In this appendix, a subscript on the right side of a parameter denotes the step (increment) number and A superscript on the right side of a parameter denotes the iteration number. For example, $\{V\}_i^j$ is vector $\{V\}$ for step i at iteration j.

A.1. Force control Newton-Raphson

The Full Newton-Raphson method is one of the most used nonlinear calculation methods. It consists of applying the load on the system by increments (steps). Within each increment, multiple iterations are conducted in order to minimize the system's unbalance.

For a structure with nonlinear behavior on which we want to apply a loading vector $\{F_{ext}\}$. This loading is divided into increments $\{\Delta F_{ext}\}$.

$$\{F_{ext}\}_{i+1} = \{F_{ext}\}_i + \{\Delta F_{ext}\}_{i+1} \tag{A.1}$$

where $\{F_{ext}\}_{i+1}$ is the external force applied on the system during increment (step) $i+1$ and for the case of the Newton Raphson method this external force is constant for all iterations within step $i+1$. $\{\Delta F_{ext}\}_{i+1}$ is the increment in external forces applied on the system while passing from load step i to $i+1$.

Let's consider that for a certain step i the system has converged at iteration l (last iteration). Load step $i+1$ starts from the last iteration of step i. So, we get the following equalities:

$$\{F_{int}\}_{i+1}^{0} = \{F_{int}\}_{i}^{l} \tag{A.2}$$

$$[K_T]_{i+1}^{0} = [K_T]_{i}^{l} \tag{A.3}$$

$$\{U\}_{i+1}^{0} = \{U\}_{i}^{l} \tag{A.4}$$

The phase prior to conducting the first iteration is called iteration 0, the unbalance $\{R\}_{i+1}^{0}$ is defined as:

$$\{R\}_{i+1}^{0} = \{F_{ext}\}_{i+1} - \{F_{int}\}_{i+1}^{0} \tag{A.5}$$

Using the stiffness matrix $[K_T]_{i+1}^{0}$ in a linear approximation, this unbalance will produce an increment in the displacements $\{\Delta U\}_{i+1}^{1}$.

$$\{\Delta U\}_{i+1}^{1} = {[K_T]_{i+1}^{0}}^{-1}\{R\}_{i+1}^{0} \tag{A.6}$$

The new displacement vector $\{U\}_{i+1}^{1}$ is:

$$\{U\}_{i+1}^{1} = \{U\}_{i+1}^{0} + \{\Delta U\}_{i+1}^{1} \tag{A.7}$$

Since the internal forces and tangent stiffness matrix are in function of displacement, this new displacement will cause new internal forces $\{F_{int}\}_{i+1}^{1}$ and a new stiffness matrix $[K_T]_{i+1}^{1}$.

$$\{F_{int}\}_{i+1}^{1} = f(\{U\}_{i+1}^{1}) \tag{A.8}$$

$$[K_T]_{i+1}^{1} = g(\{U\}_{i+1}^{1}) \tag{A.9}$$

Now we recalculate the new unbalance:

$$\{R\}_{i+1}^{1} = \{F_{ext}\}_{i+1} - \{F_{int}\}_{i+1}^{1} \tag{A.10}$$

We keep redoing equations (A.6) to (A.10) until the force, displacement and energy unbalance is within acceptable limits. Once calculation has converged for step $i+1$ we move on to calculate step $i+2$ in the same way and so on (refer to Figure A.1).

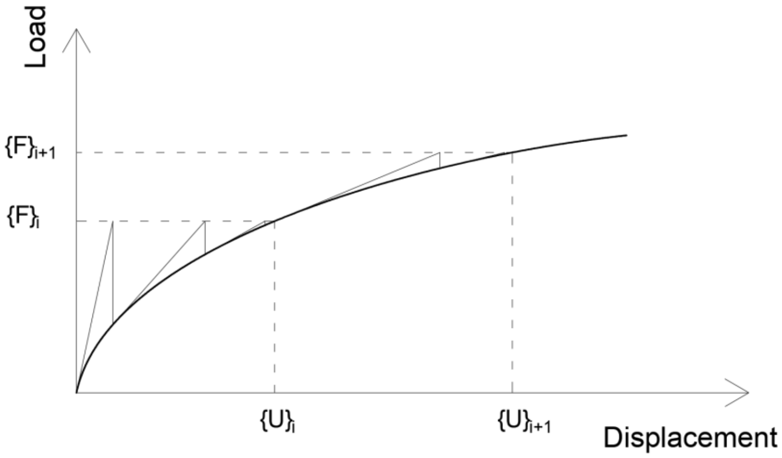

Figure A.1: Full Newton-Raphson method.

A.1. Force control Newton-Raphson

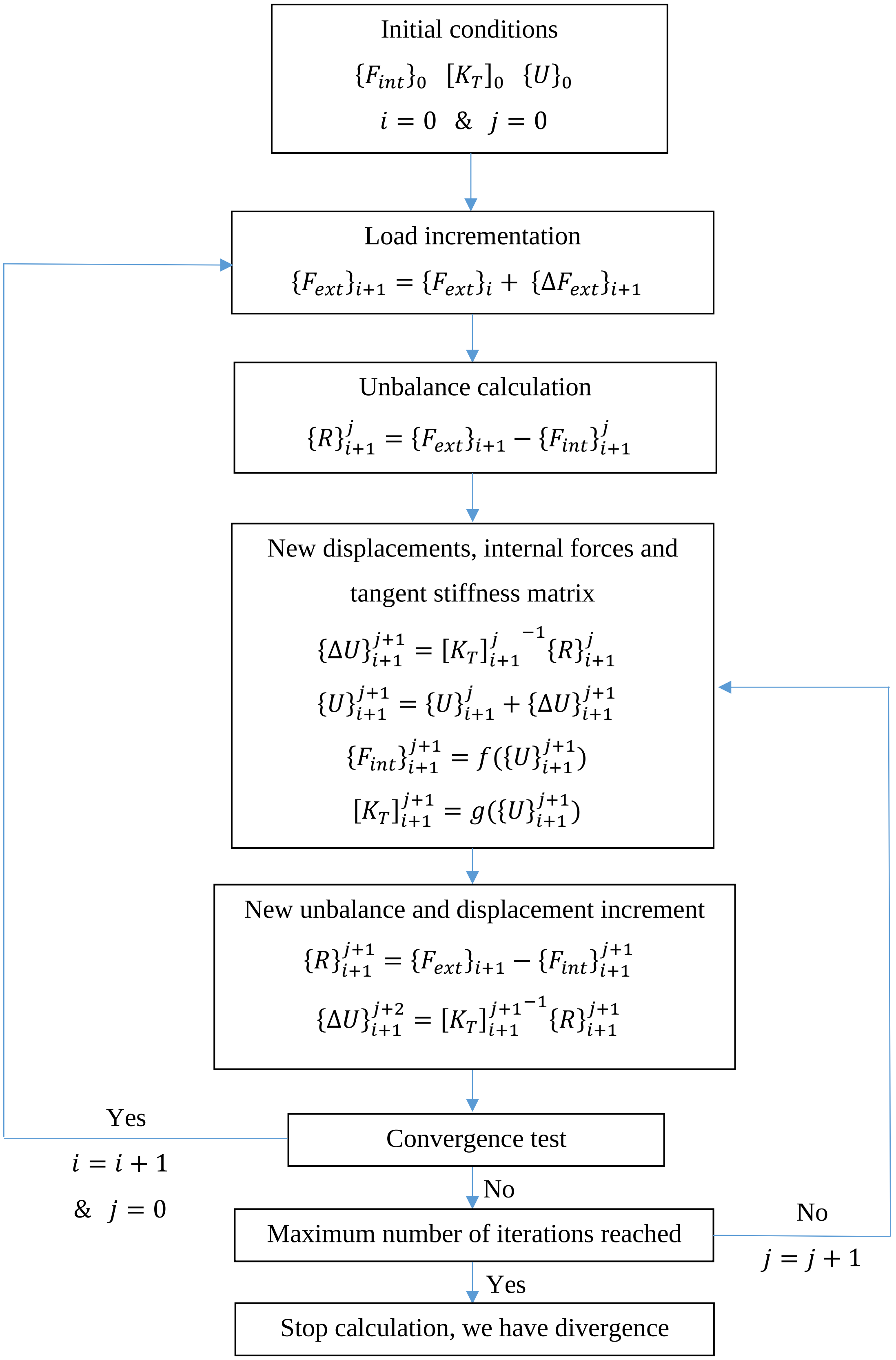

The modified Newton-Raphson method is the same as the full one except for one difference, the tangent stiffness matrix is updated only once at the beginning of a load step and remains constant while iterating (refer to Figure A.2). In other words, for any iteration j at a load step i we have the following constant stiffness matrix:

$$[K_T]_i^j = [K_T]_i^0 = g(\{U\}_i^0) \tag{A.11}$$

Since the updating of the search direction (tangent stiffness matrix) is conducted only once for the whole load step, the run time of each iteration is lower than the full method. However, each load step requires more iterations to reach convergence. Generally, the modified Newton-Raphson method is efficient for the cases of large structural systems where the update of the stiffness matrix is very time costly.

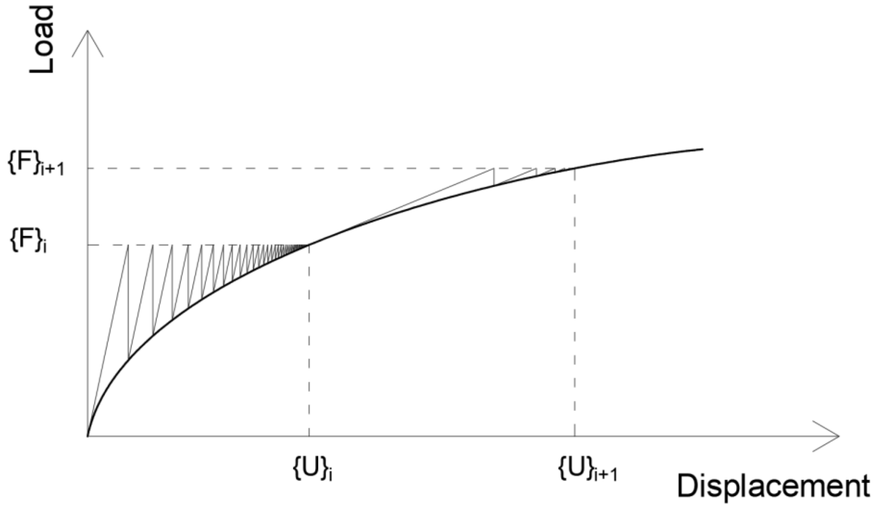

Figure A.2: Modified Newton-Raphson method.

For the constant stiffness Newton Raphson method, the stiffness matrices used in all iterations and for all load increments are considered constant and equal to the initial linear stiffness matrix (refer to Figure A.3). In other words, for any iteration j at any load step i we have:

$$[K_T]_i^j = [K_T]_0 \tag{A.12}$$

Since no tangent stiffness matrix is calculated throughout the whole process, this method has by far the fastest iterations. However, the convergence speed of each step is the lowest since the search direction is never updated. This approach is recommended only for structural systems where the calculation of the tangent stiffness matrix is very problematic and time consuming.

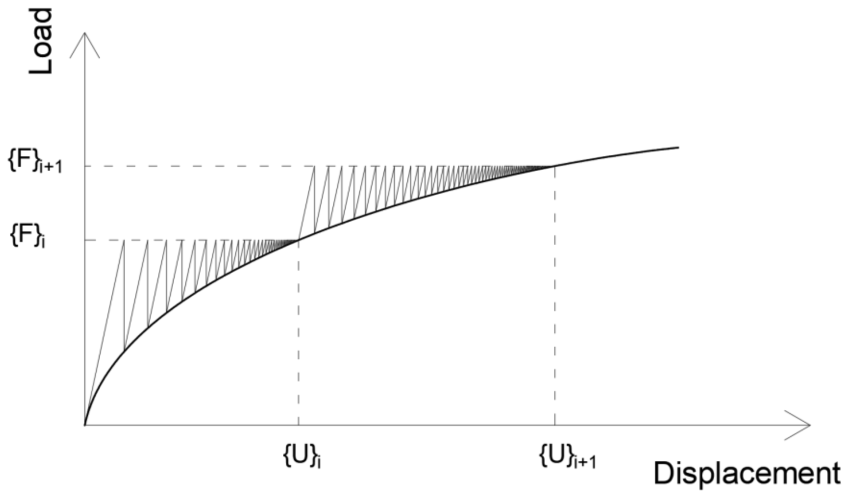

Figure A.3: Constant stiffness Newton-Raphson method.

One major limitation of the force control methods is the incapacity of catching post peak behavior. In fact, let's consider a structural system with deflection curve presenting a post peak strength loss. Piloting the nonlinear calculation with force increments will allow us to reach the peak point. After that state, if we keep adding load increments on the system we will not get any result (refer to Figure A.4).

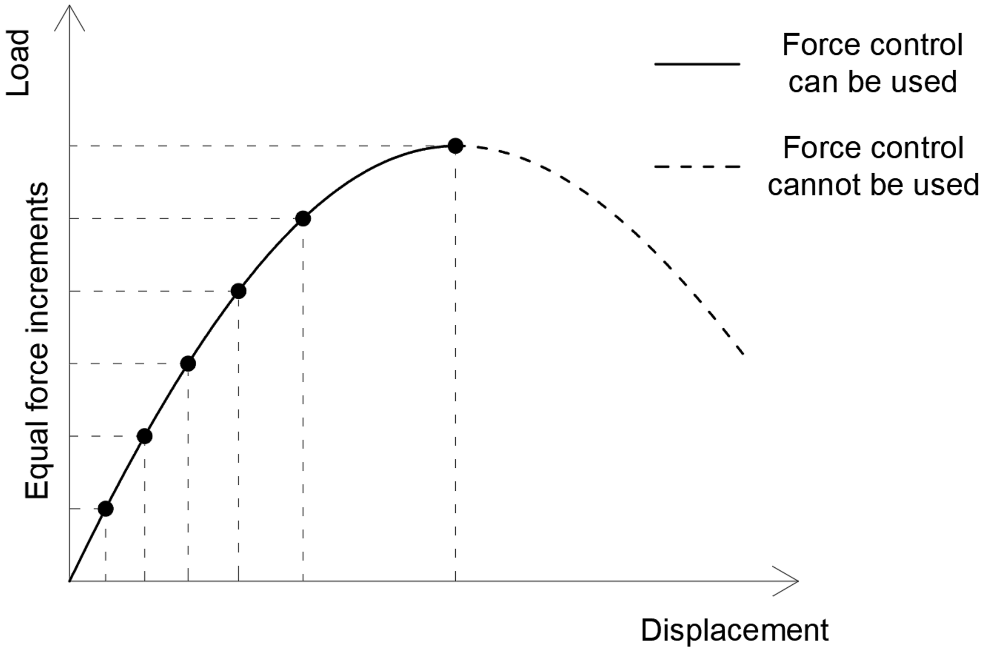

Figure A.4: Force control method limitation.

A.2. Displacement control method

Unlike force control methods, the displacement control method can identify the system’s post peak behavior. It was firstly introduced by (Argyris, 1965) and to get a better understanding of this method we need to have a look first at (Batoz and Dhatt, 1979) decomposition of the displacement vector.

Let’s consider that for a load step i, we are applying a force increment $\{\Delta F_{ext}\}_i^j$ while passing from iteration $j-1$ to j.

$$\{F_{ext}\}_i^j = \{F_{ext}\}_i^{j-1} + \{\Delta F_{ext}\}_i^j \tag{A.13}$$

where $\{F_{ext}\}_i^j$ is the external force applied on the system at iteration j in step i.

Let’s consider a reference load pattern $\{F\}$ according to which the load increment on the structure $\{\Delta F_{ext}\}_i^j$ is applied.

$$\{\Delta F_{ext}\}_i^j = \Delta\lambda_i^j\{F\} \tag{A.14}$$

where $\Delta\lambda_i^j$ is the load increment scale parameter. Inserting equation (A.14) in (A.13) gives:

$$\{F_{ext}\}_i^j = \{F_{ext}\}_i^{j-1} + \Delta\lambda_i^j\{F\} \tag{A.15}$$

at every iteration we have the following relation:

$$[K_T]_i^{j-1}\{\Delta U\}_i^j = \{F_{ext}\}_i^j - \{F_{int}\}_i^{j-1} \tag{A.16}$$

the unbalance at iteration $j-1$ is defined as:

$$\{R\}_i^{j-1} = \{F_{ext}\}_i^{j-1} - \{F_{int}\}_i^{j-1} \tag{A.17}$$

replacing $\{F_{ext}\}_i^{j-1}$ in equation (A.17) by the one in (A.15) we get:

$$\{R\}_i^{j-1} = \{F_{ext}\}_i^j - \Delta\lambda_i^j\{F\} - \{F_{int}\}_i^{j-1} \tag{A.18}$$

inserting equation (A.16) in (A.18) gives:

$$\{R\}_i^{j-1} = [K_T]_i^{j-1}\{\Delta U\}_i^j - \Delta\lambda_i^j\{F\} \tag{A.19}$$

so

$$[K_T]_i^{j-1}\{\Delta U\}_i^j = \Delta\lambda_i^j\{F\} + \{R\}_i^{j-1} \tag{A.20}$$

let's consider:

$$\{F\} = [K_T]_i^{j-1}\{\Delta\widehat{U}\}_i^j \tag{A.21}$$

where $\{\Delta\widehat{U}\}_i^j$ is the tangent displacement increment corresponding to the force reference load pattern $\{F\}$ at iteration j in step i and let's pose:

$$\{R\}_i^{j-1} = [K_T]_i^{j-1}\{\Delta\overline{U}\}_i^j \tag{A.22}$$

Where $\{\Delta\overline{U}\}_i^j$ is the residual displacement increment corresponding to the residual force (unbalance) $\{R\}_i^{j-1}$. Inserting equations (A.21) and (A.22) in equation (A.20) and multiplying both sides by the inverse of $[K_T]_i^{j-1}$ we get the (Batoz and Dhatt, 1979) displacement decomposition:

$$\{\Delta U\}_i^j = \Delta\lambda_i^j\{\Delta\widehat{U}\}_i^j + \{\Delta\overline{U}\}_i^j \tag{A.23}$$

The displacement control method is piloted by displacement increments at a particular degree of freedom of a control node. Let's consider that a point q in the structure is the control node. Using equation (A.23) we get:

$$\Delta u_{i\,q}^j = \Delta\lambda_i^j \Delta\hat{u}_{i\,q}^j + \Delta\bar{u}_{i\,q}^j \tag{A.24}$$

Where $\Delta u_{i\,q}^j$ is the displacement increment of control node q at iteration j in step i. We should pay attention that even though the displacement control method is piloted by the control node displacement, however this is never a case of imposed displacements on structure. In fact, the loading is applied on the structure following a reference pattern $\{F\}$ and is adjusted to get the desired displacements at the control node.

Let's consider that for a certain step i the system is well defined and calculation has converged. Step $i+1$ begins from the last iteration l of step i. So, we get the following equalities:

$$\{F_{int}\}_{i+1}^0 = \{F_{int}\}_i^l \tag{A.25}$$

$$[K_T]_{i+1}^0 = [K_T]_i^l \tag{A.26}$$

$$\{U\}_{i+1}^0 = \{U\}_i^l \tag{A.27}$$

The displacement increment of the control node at first iteration in step $i+1$ $\Delta u_{i+1\,q}^1$ is defined (since it is a displacement control method, we specify the displacement increment).

$$\Delta u_{i+1\,q}^{1} = \Delta\lambda_{i+1}^{1}\Delta\hat{u}_{i+1\,q}^{1} + \Delta\bar{u}_{i+1\,q}^{1} \tag{A.28}$$

The unbalance before running the first iteration $\{R\}_{i+1}^{0}$is considered zero since no load incrementation was made prior to the iterative calculation. The tangent and residual displacement increments are calculated as follows:

$$\{R\}_{i+1}^{0} = \{0\} \rightarrow \{\Delta\bar{U}\}_{i+1}^{1} = [K_T]_{i+1}^{0}{}^{-1}\{R\}_{i+1}^{0} = \{0\} \tag{A.29}$$

$$\left\{\Delta\widehat{U}\right\}_{i+1}^{1} = [K_T]_{i+1}^{0}{}^{-1}\{F\} \tag{A.30}$$

The displacement increment becomes:

$$\{\Delta U\}_{i+1}^{1} = \Delta\lambda_{i+1}^{1}\left\{\Delta\widehat{U}\right\}_{i+1}^{1} + \underbrace{\{\Delta\bar{U}\}_{i+1}^{1}}_{\{0\}} \tag{A.31}$$

Since the residual displacement increment is zero, from equation (A.28) we get:

$$\Delta\lambda_{i+1}^{1} = \frac{\Delta u_{i+1\,q}^{1}}{\Delta\hat{u}_{i+1\,q}^{1}} \tag{A.32}$$

The load increment applied on the system while at iteration 1 in step $i+1$ is:

$$\{\Delta F_{ext}\}_{i+1}^{1} = \Delta\lambda_{i+1}^{1}\{F\} \tag{A.33}$$

We calculate the displacement vector at iteration 1 $\{U\}_{i+1}^{1}$

$$\{U\}_{i+1}^{1} = \{U\}_{i+1}^{0} + \{\Delta U\}_{i+1}^{1} \tag{A.34}$$

The internal nodal forces and tangent stiffness matrix are then calculated

$$\{F_{int}\}_{i+1}^{1} = f(\{U\}_{i+1}^{1}) \tag{A.35}$$

$$[K_T]_{i+1}^{1} = g(\{U\}_{i+1}^{1}) \tag{A.36}$$

Now the displacement of the control node has reached the required value, however we have unbalance in the system

$$\{F_{ext}\}_{i+1}^{1} = \{F_{ext}\}_{i+1}^{0} + \Delta\lambda_{i+1}^{1}\{F\} \tag{A.37}$$

and

$$\{R\}_{i+1}^{1} = \{F_{ext}\}_{i+1}^{1} - \{F_{int}\}_{i+1}^{1} \tag{A.38}$$

In the next iterations, we need to minimize the system's unbalance while keeping the displacement value at the control node fixed. So we have:

$$\Delta u_{i+1\,q}^{2}=\Delta\lambda_{i+1}^{2}\Delta\hat{u}_{i+1\,q}^{2}+\Delta\bar{u}_{i+1\,q}^{2}=0 \tag{A.39}$$

So from equation (A.39) we get:

$$\Delta\lambda_{i+1}^{2}=-\frac{\Delta\bar{u}_{i+1\,q}^{2}}{\Delta\hat{u}_{i+1\,q}^{2}} \tag{A.40}$$

The new tangent and residual displacement increments are calculated as follows:

$$\{R\}_{i+1}^{1}=[K_T]_{i+1}^{1}\{\Delta\bar{U}\}_{i+1}^{2}\rightarrow\{\Delta\bar{U}\}_{i+1}^{2}=[K_T]_{i+1}^{1}{}^{-1}\{R\}_{i+1}^{1} \tag{A.41}$$

$$\{F\}=[K_T]_{i+1}^{1}\left\{\Delta\hat{U}\right\}_{i+1}^{2}\rightarrow\left\{\Delta\hat{U}\right\}_{i+1}^{2}=[K_T]_{i+1}^{1}{}^{-1}\{F\} \tag{A.42}$$

and the displacement increment is:

$$\{\Delta U\}_{i+1}^{2}=\Delta\lambda_{i+1}^{2}\left\{\Delta\hat{U}\right\}_{i+1}^{2}+\{\Delta\bar{U}\}_{i+1}^{2} \tag{A.43}$$

We keep redoing iterations from equation (A.34) to (A.43) until the unbalance is minimized (refer to Figure A.5).

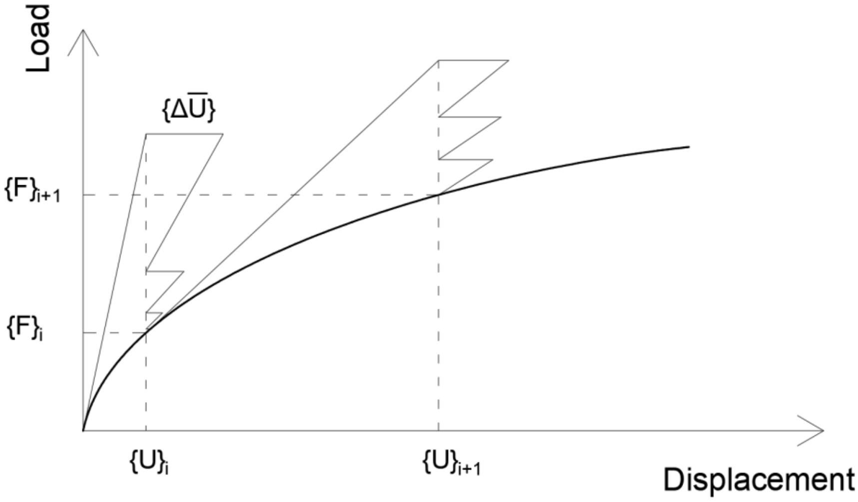

Figure A.5: Displacement control method.

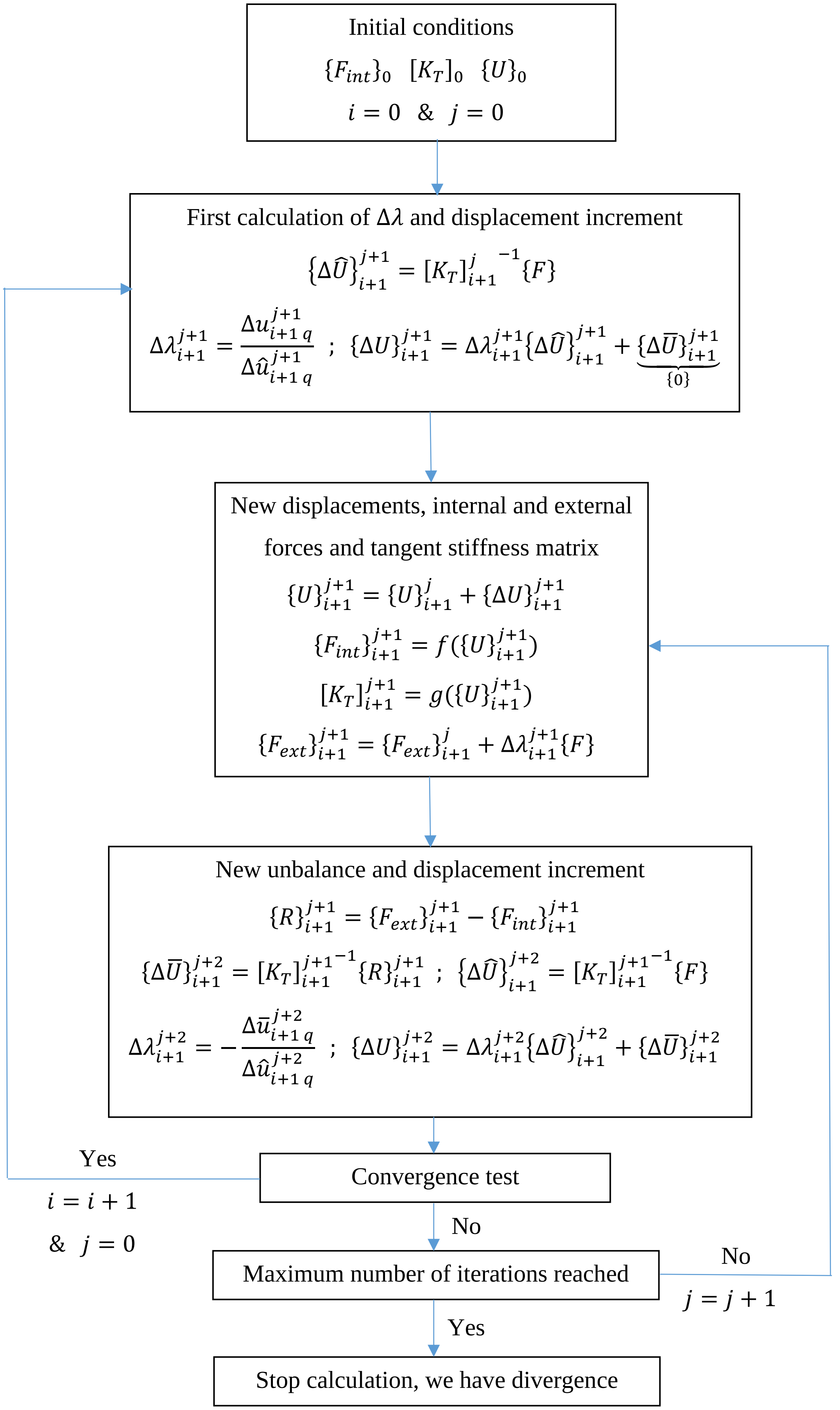
Initial conditions
$\{F_{int}\}_0 \quad [K_T]_0 \quad \{U\}_0$
$i = 0 \ \ \& \ \ j = 0$
First calculation of $\Delta\lambda$ and displacement increment
$\{\Delta\widehat{U}\}_{i+1}^{j+1} = {[K_T]_{i+1}^{j}}^{-1}\{F\}$
$\Delta\lambda_{i+1}^{j+1} = \dfrac{\Delta u_{i+1\,q}^{j+1}}{\Delta\hat{u}_{i+1\,q}^{j+1}} \ ; \ \{\Delta U\}_{i+1}^{j+1} = \Delta\lambda_{i+1}^{j+1}\{\Delta\widehat{U}\}_{i+1}^{j+1} + \underbrace{\{\Delta\overline{U}\}_{i+1}^{j+1}}_{\{0\}}$
New displacements, internal and external forces and tangent stiffness matrix
$\{U\}_{i+1}^{j+1} = \{U\}_{i+1}^{j} + \{\Delta U\}_{i+1}^{j+1}$
$\{F_{int}\}_{i+1}^{j+1} = f(\{U\}_{i+1}^{j+1})$
$[K_T]_{i+1}^{j+1} = g(\{U\}_{i+1}^{j+1})$
$\{F_{ext}\}_{i+1}^{j+1} = \{F_{ext}\}_{i+1}^{j} + \Delta\lambda_{i+1}^{j+1}\{F\}$
New unbalance and displacement increment
$\{R\}_{i+1}^{j+1} = \{F_{ext}\}_{i+1}^{j+1} - \{F_{int}\}_{i+1}^{j+1}$
$\{\Delta\overline{U}\}_{i+1}^{j+2} = {[K_T]_{i+1}^{j+1}}^{-1}\{R\}_{i+1}^{j+1} \ ; \ \{\Delta\widehat{U}\}_{i+1}^{j+2} = {[K_T]_{i+1}^{j+1}}^{-1}\{F\}$
$\Delta\lambda_{i+1}^{j+2} = -\dfrac{\Delta\bar{u}_{i+1\,q}^{j+2}}{\Delta\hat{u}_{i+1\,q}^{j+2}} \ ; \ \{\Delta U\}_{i+1}^{j+2} = \Delta\lambda_{i+1}^{j+2}\{\Delta\widehat{U}\}_{i+1}^{j+2} + \{\Delta\overline{U}\}_{i+1}^{j+2}$
Yes
$i = i + 1$
$\& \ \ j = 0$
Convergence test
No
Maximum number of iterations reached
No
$j = j + 1$
Yes
Stop calculation, we have divergence

The displacement control method is beneficial for catching post peak behaviors; however it cannot handle a snap back in the control node (snap back behavior is indicated in figure). The good choice of control node is essential for a displacement control method. In fact, the control node should not present any snap back behavior in order for the method to converge (refer to Figure A.6).

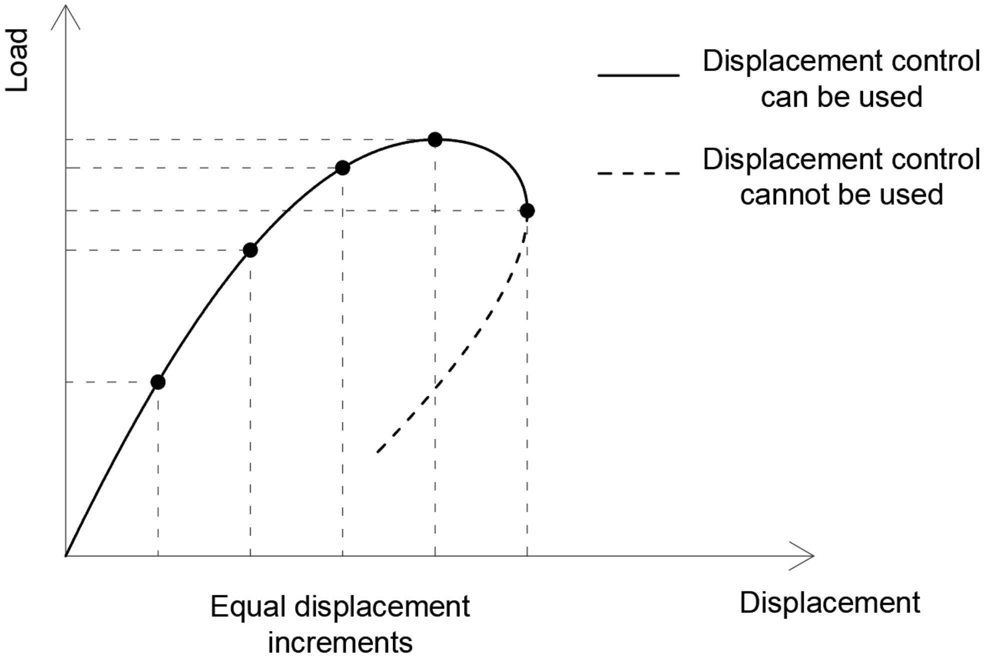

Figure A.6: Displacement control element.

A.3. Newmark nonlinear dynamic calculation via Newton-Raphson solver

In the following formulation, a subscript on the right side of a parameter denotes the time step (instant) and a superscript on the right side of a parameter denotes the iteration number. For example, $\{U\}_{i+1}^{j}$ is the displacement at the j^{th} iteration in the Newton-Raphson procedure at time t_{i+1}.

For continuity purpose, time step $i+1$ starts from the last iteration l of time step i. Thus the initial vectors and matrices for step $i+1$ are:

$$\{U\}_{i+1}^{0} = \{U\}_{i}^{l} = \{U\}_{i} \tag{A.44}$$

$$\{\dot{U}\}_{i+1}^{0} = \{\dot{U}\}_{i}^{l} = \{\dot{U}\}_{i} \tag{A.45}$$

$$\{\ddot{U}\}_{i+1}^{0} = \{\ddot{U}\}_{i}^{l} = \{\ddot{U}\}_{i} \tag{A.46}$$

$$\{F_{NL}\}_{i+1}^{0} = \{F_r\}_{i}^{l} = \{F_{NL}\}_{i} \tag{A.47}$$

$$[K_T]_{i+1}^{0} = [K_T]_{i}^{l} = [K_T]_{i} \tag{A.48}$$

$$\begin{aligned}\{\hat{F}\}_{i+1} = \{F\}_{i+1} &+ \left(\frac{1}{\beta\Delta t^2}[M] + \frac{\gamma}{\beta\Delta t}[C]\right)\{U\}_i \\ &+ \left(\frac{1}{\beta\Delta t}[M] + \left(\frac{\gamma}{\beta} - 1\right)[C]\right)\{\dot{U}\}_i \\ &+ \left(\left(\frac{1}{2\beta} - 1\right)[M] + \left(\frac{\gamma}{2\beta} - 1\right)\Delta t[C]\right)\{\ddot{U}\}_i\end{aligned} \tag{A.49}$$

The Newton Raphson procedure can be described by the following steps and starting with $j = 0$

Algorithm

1. Calculation of the force unbalance

$$\{\hat{R}\}_{i+1}^{j+1} = \{\hat{F}\}_{i+1} - \{F_{NL}\}_{i+1}^{j} - \left(\frac{1}{\beta\Delta t^2}[M] + \frac{\gamma}{\beta\Delta t}[C]\right)\{U\}_{i+1}^{j} \tag{A.50}$$

2. Calculation of displacement increment

$$\{\Delta U\}_{i+1}^{j+1} = \left([K_T]_{i+1}^{j}\right)^{-1}\{\hat{R}\}_{i+1}^{j+1} \tag{A.51}$$

3. Calculation of tangent stiffness and return force

$$\{U\}_{i+1}^{j+1} = \{U\}_{i+1}^{j} + \{\Delta U\}_{i+1}^{j+1} \tag{A.52}$$

$$[K_T]_{i+1}^{j+1} = f\left(\{U\}_{i+1}^{j+1}\right) \tag{A.53}$$

$$\{F_{NL}\}_{i+1}^{j+1} = g\left(\{U\}_{i+1}^{j+1}\right) \tag{A.54}$$

$$[\hat{K}_T]_{i+1}^{j+1} = [K_T]_{i+1}^{j+1} + \frac{\gamma}{\beta\Delta t}[C] + \frac{1}{\beta\Delta t^2}[M] \tag{A.55}$$

4. Calculation of new unbalance

$$\{\hat{R}\}_{i+1}^{j+2} = \{\hat{F}\}_{i+1} - \{F_{NL}\}_{i+1}^{j+1} - \left(\frac{1}{\beta\Delta t^2}[M] + \frac{\gamma}{\beta\Delta t}[C]\right)\{U\}_{i+1}^{j+1} \tag{A.56}$$

5. Calculation of new displacement increment

$$\{\Delta U\}_{i+1}^{j+2} = \left(\left[\hat{K}_T\right]_{i+1}^{j+1}\right)^{-1} \left\{\hat{R}\right\}_{i+1}^{j+2} \tag{A.57}$$

6. Convergence check

- If we do not have convergence: j is incremented by 1 $(j = j + 1)$ and steps 3 to 6 are repeated
- If we have convergence: $j + 1$ is considered as the last iteration at time step t_{i+1} $\left(\{U\}_{i+1}^{j+1} = \{U\}_{i+1}\right)$ and we proceed to time step t_{i+2}. The final velocity and acceleration vectors at time t_{i+1} are given by

$$\left\{\ddot{U}\right\}_{i+1} = \frac{1}{\beta \Delta t^2}\left(\{U\}_{i+1} - \{U\}_i\right) - \frac{1}{\beta \Delta t}\left\{\dot{U}\right\}_i - \left(\frac{1}{2\beta} - 1\right)\left\{\ddot{U}\right\}_i \tag{A.58}$$

$$\left\{\dot{U}\right\}_{i+1} = \frac{\gamma}{\beta \Delta t}\left(\{U\}_{i+1} - \{U\}_i\right) + \left(1 - \frac{\gamma}{\beta}\right)\left\{\dot{U}\right\}_i + \left(1 - \frac{\gamma}{2\beta}\right)\Delta t\left\{\ddot{U}\right\}_i \tag{A.59}$$

Appendix B : Finite elements formulation

B.1. Shape functions

For beam and column elements, the following linear interpolation shape functions are adopted for longitudinal translation:

$$N_1^t(x) = 1 - \frac{x}{L} \tag{B.1}$$

$$N_2^t(x) = \frac{x}{L} \tag{B.2}$$

and the following Hermitian shape functions are considered for bending:

$$N_1^b(x) = 1 - \frac{3}{L^2}x^2 + \frac{2}{L^3}x^3 \tag{B.3}$$

$$N_2^b(x) = x - \frac{2}{L}x^2 + \frac{1}{L^2}x^3 \tag{B.4}$$

$$N_3^b(x) = \frac{3}{L^2}x^2 - \frac{2}{L^3}x^3 \tag{B.5}$$

$$N_4^b(x) = -\frac{1}{L}x^2 + \frac{1}{L^2}x^3 \tag{B.6}$$

For membrane elements, the shape functions for the Q8 finite element model are adopted and can be expressed as follows:

$$N_1(\xi,\eta) = -\frac{1}{4}(1-\xi)(1-\eta)(1+\xi+\eta) \tag{B.7}$$

$$N_2(\xi,\eta) = -\frac{1}{4}(1+\xi)(1-\eta)(1-\xi+\eta) \tag{B.8}$$

$$N_3(\xi,\eta) = -\frac{1}{4}(1+\xi)(1+\eta)(1-\xi-\eta) \tag{B.9}$$

$$N_4(\xi,\eta) = -\frac{1}{4}(1-\xi)(1+\eta)(1+\xi-\eta) \tag{B.10}$$

$$N_5(\xi,\eta) = \frac{1}{2}(1-\xi^2)(1-\eta) \tag{B.11}$$

$$N_6(\xi,\eta) = \frac{1}{2}(1+\xi)(1-\eta^2) \tag{B.12}$$

$$N_7(\xi,\eta) = \frac{1}{2}(1-\xi^2)(1+\eta) \tag{B.13}$$

$$N_8(\xi,\eta) = \frac{1}{2}(1-\xi)(1-\eta^2) \tag{B.14}$$

B.2. Gauss points integration

For 1D integration via 3 points Gauss quadrature, the following weight W_p and abscissa ξ_p of points are considered:

ξ_p	W_p	Location of points
$-\sqrt{3/5}$	$5/9$	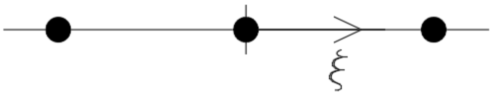
0	$8/9$	
$\sqrt{3/5}$	$5/9$	

Table B.1: Gauss points for 1D integration.

For 2D integration via 4 points Gauss quadrature, the following weight W_p and coordinates (ξ_p, η_p) of points are considered:

ξ_p	η_p	W_p	Location of points
$-1/\sqrt{3}$	$-1/\sqrt{3}$	1	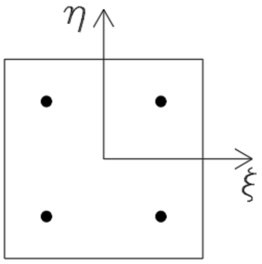
$1/\sqrt{3}$	$-1/\sqrt{3}$	1	
$-1/\sqrt{3}$	$1/\sqrt{3}$	1	
$1/\sqrt{3}$	$1/\sqrt{3}$	1	

Table B.2: Gauss points for 2D integration.

Résumé étendu en Français

I. Introduction

Cette thèse concerne la construction de modèles éléments finis d’ordre réduit pour l’analyse dynamique non-linéaire des structures en béton armé sous excitations sismiques. En général, les structures soumises à des sollicitations sismiques présentent un comportement matériau non-linéaire. Cependant le calcul classique en ingénierie est linéaire. En effet, des techniques d’analyse sismique linéaire dans lesquelles la non-linéarité matérielle est prise en compte via un facteur global de comportement, sont classiquement utilisées. Ces approches linéaires sont très critiquées car le comportement non-linéaire de toute la structure est décrit par un simple coefficient global grossièrement estimé.

Ainsi, il est clair que les analyses sismiques linéaires sont insuffisantes et que des approches plus complexes intégrant directement la non-linéarité seront nécessaires. Parmi ces techniques non-linéaires, la méthode de "poussée progressive" (ou méthode de pushover) et les approches d’intégration temporelle non-linéaire sont les plus connues. La poussée progressive permet de calculer la réponse sismique maximale pour des structures régulières uniquement. Par contre, l’intégration temporelle non-linéaire fournit une réponse sismique temporelle pour n’importe quelle structure mais avec un coût de calcul très élevé.

Face au dilemme entre les limitations de la poussée progressive et le coût numérique important de l’intégration temporelle non-linéaire, cette thèse propose de développer une méthode de réduction de modèle dynamique en étendant, pour la première fois, l’application de la technique de décomposition orthogonale aux valeurs propres (POD) aux structures en Béton Armé avec des non-linéarités matérielles provenant simultanément du béton et des armatures en acier. Le Modèle d’Ordre Réduit (MOR) est ensuite utilisé dans l’intégration temporelle non-linéaire afin de réduire le coût de calcul tout en maintenant un niveau de précision acceptable.

Dans ce résumé des travaux, on commence par une bibliographie sur les analyses sismiques structurelles. Ensuite, on s’intéresse aux modèles des éléments structuraux capables d’incorporer la non-linéarité matérielle tout en discutant les modèles constitutifs du béton armé. On explique ensuite l'implémentation éléments finis des modèles structuraux puis la technique de réduction de modèle par projection sur modes POD est présentée. Enfin, une application est faite sur des structures de type portique et mur de contreventement en béton armé sous excitations sismiques suivie par les conclusions et perspectives de ce travail.

II. Bibliographie sur les analyses sismiques structurelles

Les techniques d'analyse sismique sont divisées en deux grandes familles : analyses linéaires et non-linéaires. En plus, dans chaque catégorie, certaines approches fournissent uniquement la réponse sismique maximale des structures tandis que d'autres permettent d'obtenir la réponse sismique temporelle (cf. Figure 1).

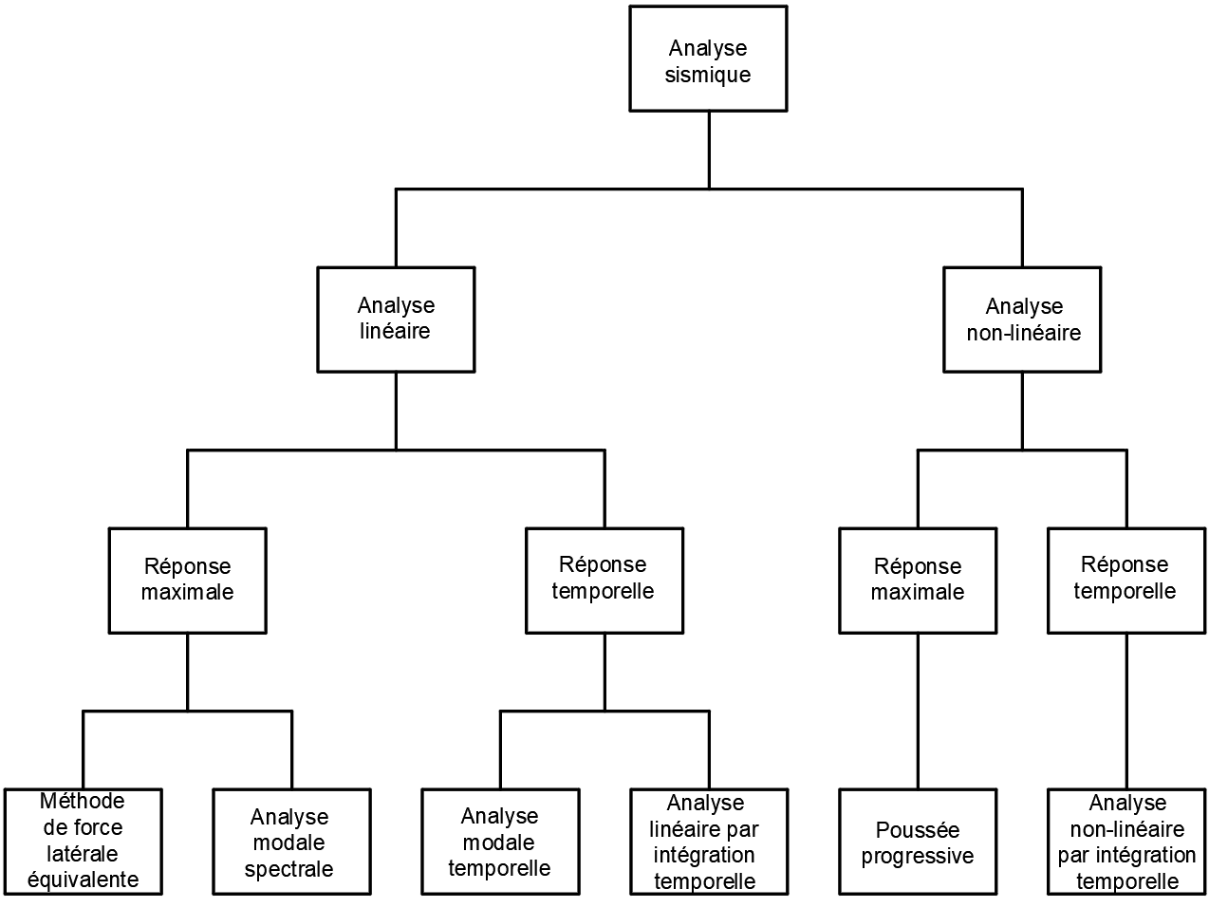

Figure 1 : Techniques d'analyse sismique.

Pour les analyses linéaires, la méthode de force latérale équivalente est la plus simple à utiliser mais ne s'applique qu'aux structures régulières et est limitée à la réponse sismique maximale. L'approche modale spectrale fournit la réponse structurale maximale pour tout type de structure. Les analyses modale et intégration temporelle sont capables de calculer la réponse sismique temporelle des structures mais à un coût de calcul plus élevé. Il est évident que les analyses linéaires (en particulier pour les techniques ne fournissant que des réponses maximales) prennent beaucoup moins de temps que les analyses non linéaires (cf. Figure 2).

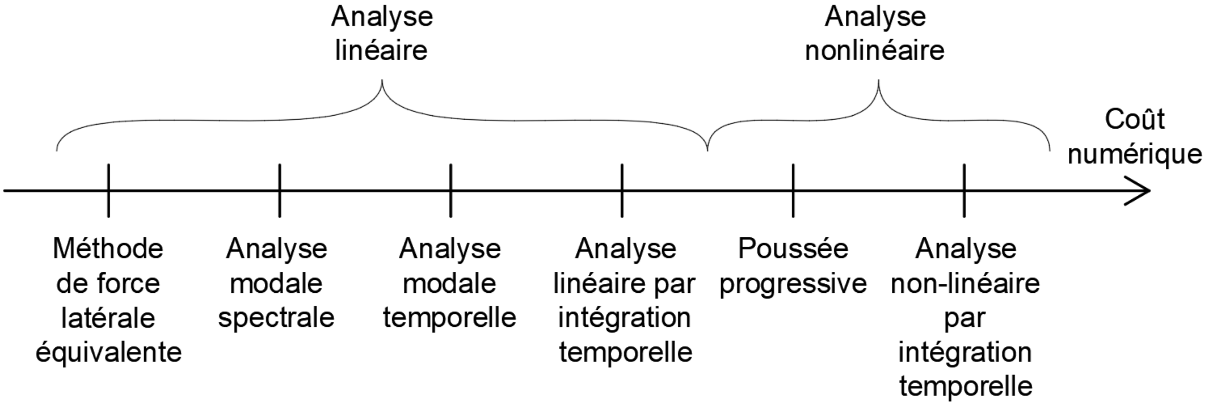

Figure 2 : Coût numérique des techniques d'analyse sismique.

III. Modèles structuraux avec non-linéarités matérielles

En général, les éléments structuraux les plus courants (poteaux, poutres, dalles, murs…) sont discrétisés en éléments finis 1D et 2D. Dans cette thèse, on s'intéresse aux éléments structuraux 1D capables d'incorporer une non-linéarité matérielle unidimensionnelle afin de pouvoir modéliser les poutres et poteaux en béton armé. De la même manière, pour les éléments structuraux surfacique, on s'intéresse aux modèles 2D avec une non-linéarité matérielle biaxiale.

III.1. Modèles structuraux

Pour les éléments structuraux 1D, les modèles les plus utilisées en analyse sismique pour modéliser la non-linéarité matérielle sont la rotule plastique et la section multifibres (cf. Figure 3).

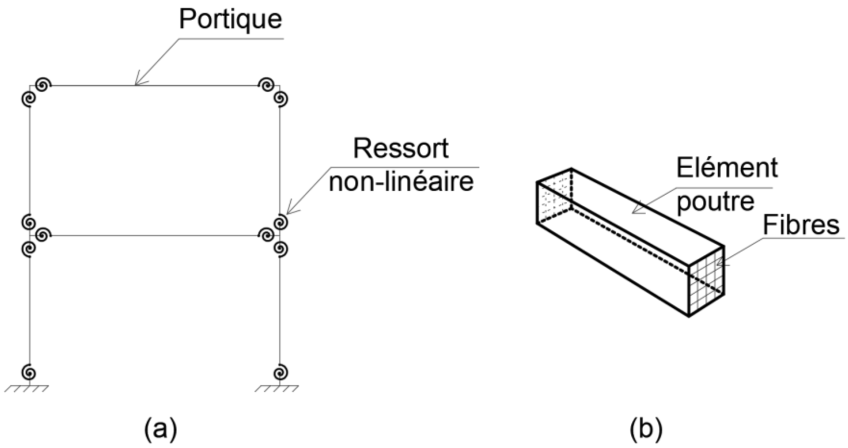

Figure 3 : (a) Rotule plastique dans structure en portique ; (b) Elément multifibres.

L'approche de la rotule plastique, introduite initialement par (Clough & Johnston, 1966), consiste à représenter la non-linéarité matérielle de l'élément structurel par des ressorts non-linéaire. La loi constitutive de ces ressorts est exprimée sous forme de courbes moment-rotation pour les rotules de flexion et force-déplacement pour les rotules axiales. Le modèle des rotules plastiques est adopté dans la plupart des codes sismiques tels que (FEMA 356, 2000; EC8-3, 2005) où la courbe caractéristique de ces rotules est définie en fonction de la section des éléments structuraux, du ferraillage, des conditions de confinement du béton et des efforts internes.

L'approche de la section multifibres, introduite initialement par (Mark & Roesset, 1976; Owen & Hinton, 1980; Hellesland & Scordelis, 1981), consiste à diviser la section de l'élément structurel en un ensemble de fibres longitudinales. Chaque fibre est constituée d'un seul matériau et peut subir une déformation longitudinale inélastique non-linéaire selon la courbe caractéristique contrainte-déformation uniaxiale de son matériau.

Dans cette thèse, l'approche multifibres est utilisée pour modéliser la non-linéarité matérielle des poutres et poteaux en béton armé. En effet, cette technique est plus précise que les rotules plastiques, possède un large domaine d'application et a un coût de calcul acceptable.

Pour les éléments structuraux 2D, les modèles les plus utilisées en analyse sismique pour modéliser la non-linéarité matérielle sont la membrane et la coque multicouches (cf. Figure 4).

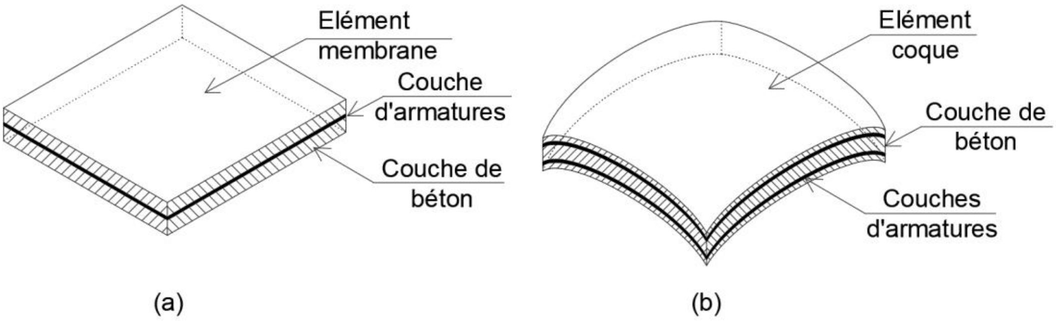

Figure 4 : (a) Membrane multicouches ; (b) Coque multicouches.

L’approche multicouches, introduite initialement par (Cervenka, 1970; Cervenka & Gerstle, 1971, 1972) pour les membranes et par (Hand, Pecknold & Schnobrich, 1972; Schnobrich, 1977) pour les coques, consiste à diviser l’élément structurel en couches tout au long de son épaisseur. Chaque couche est composée d’un seul matériau avec un comportement non-linéaire biaxial.

Dans cette thèse, on étudie des murs de contreventement planaires en béton armé. Généralement en analyses sismiques, le comportement de tels murs est considéré uniquement dans leur propre plan. Ainsi, les membranes multicouches sont considérées pour la modélisation des murs dans ce travail.

III.2. Modèles constitutifs du béton armé

L’étude des éléments en béton armé nécessite une connaissance approfondie du comportement de leurs matériaux constitutifs. Le béton est un matériau fragile. Sous déformation non-linéaire, il dissipe l’énergie par formation et propagation des fissures. Par contre, les armatures d’acier sont un matériau ductile. Sous déformation non-linéaire, elles dissipent l’énergie par plasticité.

La modélisation du comportement du béton seul n’est pas suffisante. En fait, le béton est un matériau hétérogène (mélange de ciment, sable, gravier …) et non-symétrique (comportement diffèrent en traction et compression). De plus, le comportement du béton dépend de ses conditions du confinement. La présence des armatures transversales de confinement autour du béton lui procure un caractère ductile tout en augmentant sa résistance (cf. Figure 5).

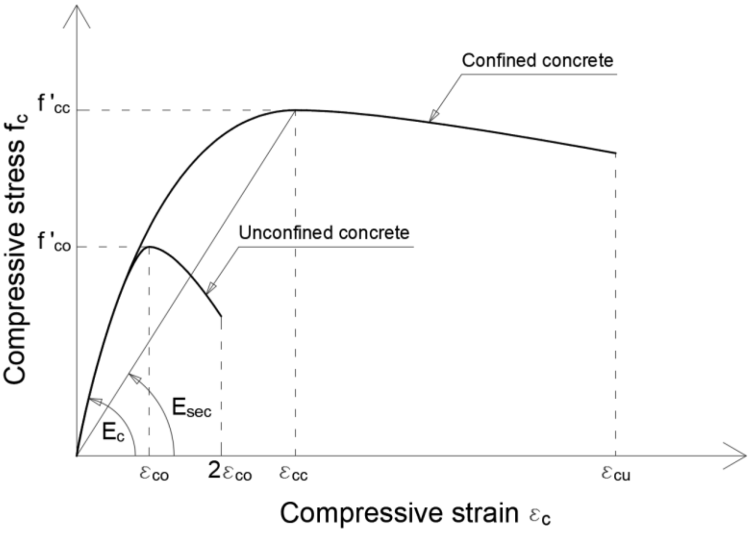

Figure 5 : Courbe contrainte-déformation uniaxiale du béton confiné et non-confiné.

Avoir des modèles avancés de comportement non-linéaire des matériaux est important. Cependant, l’objectif essentiel de cette thèse est de développer des modèles réduits pertinents. Ainsi, des simplifications sur le comportement non-linéaire des matériaux sont faites tout en gardant un bon niveau de fiabilité. Pour les bétons confinés et non confinés, un modèle simplifié de (Mander, Priestley & Park, 1988) est adopté pour le comportement unidimensionnel (cf. Figure 6) et un modèle modifié de (Darwin & Pecknold, 1974) en bidimensionnel.

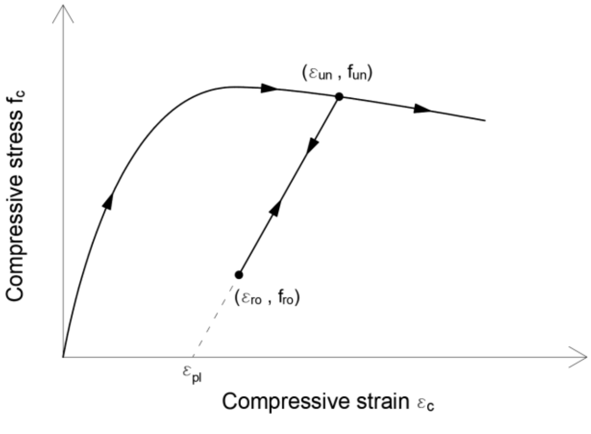

Figure 6 : Chargement et déchargement du modèle béton de Mander.

Pour les armatures en acier, un modèle unidimensionnel bilinéaire simplifié est utilisée avec un écrouissage cinématique tout en négligeant l’effet (Bauschinger, 1886) (cf. Figure 7)

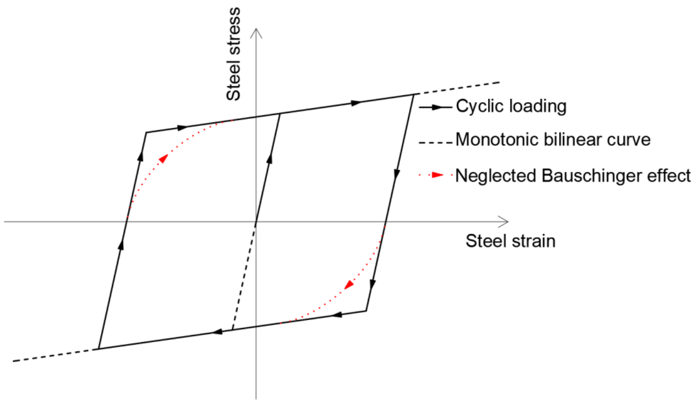

Figure 7 : Comportement hystérétique simplifié adopté pour les armatures en acier.

IV. Implémentation et validation en éléments finis

IV.1. Modèles structuraux

La section multifibres est adoptée pour la modélisation de la non-linéarité matérielle des poutres et poteaux en béton armé. Cette approche est basée sur 3 niveaux d'analyses : fibre, section et élément fini.

Les fibres sont les éléments constitutifs de base. Chaque fibre est composée d'un seul matériau et se comporte longitudinalement selon la relation contrainte-déformation unidimensionnelle de son matériau constitutif. Pour les structures en béton armé, les fibres peuvent être en acier, béton confiné ou non-confiné. Au niveau de la section, on applique l'hypothèse d'Euler-Bernoulli. Par conséquence, une adhésion parfaite est considérée entre les fibres.

Au niveau de l'élément fini, une analyse structurelle bidimensionnelle est considérée. Les poutres et poteaux sont modélisées par des éléments filaires 1D à 2 nœuds (chacun avec 3 degrés de liberté, cf. Figure 8). Les fonctions de forme de degré 3 (polynômes d'Hermite) sont considérées en flexion et une interpolation linéaire est adoptée en traction.

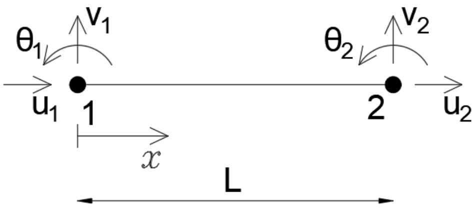

Figure 8 : Elément fini poutre/poteau.

En appliquant le principe du travail virtuel sur l'élément multifibres, la matrice de rigidité tangentielle de l'élément $[K_T]$ et le vecteur de force nodale $\{F_{nodes}\}$ sont obtenus par les équations suivantes :

$$[K_T] = \int_0^L [B(x)]^T \left(\int_s \begin{Bmatrix} 1 \\ -y \end{Bmatrix} E_T(x,y) \{1 \quad -y\} ds \right) [B(x)] dx \tag{1}$$

$$\{F_{nodes}\} = \int_0^L [B(x)]^T \left(\int_s \begin{Bmatrix} 1 \\ -y \end{Bmatrix} \sigma(x,y) ds \right) dx \tag{2}$$

où $[B(x)]^T$ contient les dérivés des fonctions de forme, $E_T(x,y)$ et $\sigma(x,y)$ sont respectivement le module du Young tangentiel et la contrainte axiale des fibres. Pour les équations (1) et (2), l'intégral surfacique est effectué par discrétisation de la section en fibres et l'intégral longitudinal par points de Gauss.

De façon similaire, la modélisation de la membrane multicouches est menée à 3 niveaux : couches, épaisseur et élément fini. Chaque couche est formée d'un seul matériau avec un comportement non-linéaire bidimensionnel. Les couches sont regroupées au niveau de l'épaisseur de l'élément tout en considérant l'hypothèse d'adhésion parfaite entre les couches.

Pour la modélisation élément fini, les éléments de membrane utilisés dans cette thèse sont des éléments planaires 2D. Ainsi, un élément quadrilatéral à 8 nœuds (Q8) est adopté avec 2 degrés de liberté de translation par nœud (cf. Figure 9).

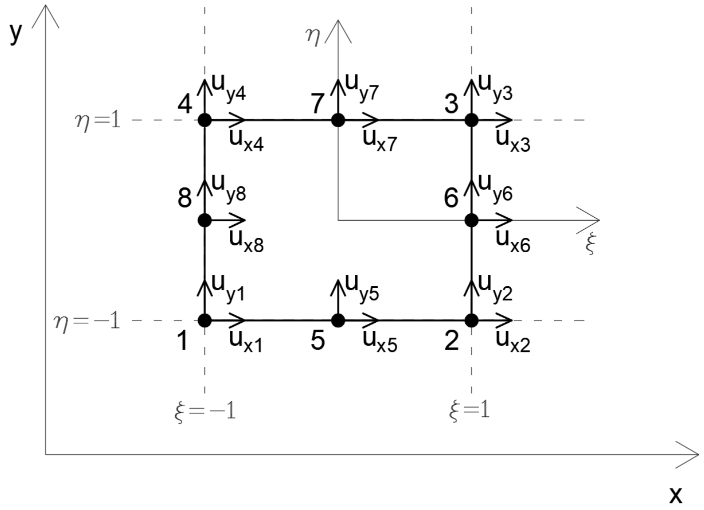

Figure 9 : Elément fini de membrane Q8.

En appliquant le principe du travail virtuel sur la membrane multicouche, la matrice de rigidité tangentielle de l'élément $[K_T]$ et le vecteur de force nodale $\{F_{nodes}\}$ sont obtenus par les équations suivantes :

$$[K_T] = \int_{s} [B(x,y)]^T \left(\int_{-\frac{h}{2}}^{\frac{h}{2}} [D_T(x,y,z)]\, dz \right) [B(x,y)]\, ds \tag{3}$$

$$\{F_{nodes}\} = \int_{s} [B(x,y)]^T \left(\int_{-\frac{h}{2}}^{\frac{h}{2}} \{\sigma(x,y,z)\} dz \right) ds \tag{4}$$

Pour les équations (3) et (4), l'intégral au niveau de l'épaisseur est effectué par discrétisation en couches et l'intégral surfacique par points de Gauss.

IV.2. Validation expérimentale en statique

Afin de valider les modèles d'éléments finis proposés, une comparaison entre des résultats expérimentaux de la littérature et la simulation numérique est effectuée. L'expérience considérée est bien détaillée dans (Thomsen & Wallace, 2004; Orakcal & Wallace, 2006). Elle s'agit d'un mur en béton armé soumis à des déplacements latéraux cycliques quasi-statiques imposés sur son sommet.

La simulation numérique de cette expérience, en utilisant les modèles éléments finis proposés, montre que les résultats numériques sont très proches de ceux obtenus expérimentalement. Ainsi, les modèles éléments finis sont validés.

V. Modèle d'ordre réduit par POD

L'un des objectifs de cette thèse est de réduire le coût numérique de l'analyse dynamique des structures en béton armées soumises à des excitations sismiques tout en prenant en compte la non-linéarité matérielle.

Diverses techniques existent pour la réduction de modèles en dynamique linéaire. La troncature modale est l'approche la plus courante pour ces systèmes. Par contre, les techniques de réduction deviennent plus difficiles lorsque des forces de retour non-linéaires sont présentes dans le système dynamique. Dans cette thèse, la décomposition orthogonale aux valeurs propres (POD) est adoptée pour la réduction des modèles dynamiques non-linéaires.

V.1. Généralité sur l’approche POD

L’analyse modale ne peut s’appliquer qu’aux systèmes dynamiques linéaires. Elle consiste à exprimer la réponse dynamique de la structure en fonction des composantes principales de vibration (modes propres). Toutefois, si la structure est non-linéaire et qu’on connait sa réponse dynamique temporelle à une excitation sismique, les composantes principales de vibration peuvent être déterminées par une décomposition orthogonale aux valeurs propres (POD).

La méthode POD, introduite initialement par (Hotelling, 1933), est une approche statistique qui cherche les composante principales dans une base de données. Aujourd’hui, cette technique est appliquée dans diverse domaines : mécanique des fluides, dynamique des structures, électromécanique …

Considérons une matrice de données $[X]$ contenant n vecteurs d’observation :

$$[X] = [\{X_1\} \quad \cdots \quad \{X_n\}] = \begin{bmatrix} x_{11} & \cdots & x_{1n} \\ \vdots & \ddots & \vdots \\ x_{m1} & \cdots & x_{mn} \end{bmatrix} \tag{5}$$

Les composantes principales de la matrice $[X]$ sont déterminées par décomposition en valeurs singulières (SVD). Chaque matrix $[X] \in \mathbb{R}^{m\times n}$ peut-être décomposée en un produit de 3 matrices $[U] \in \mathbb{R}^{m\times m}$, $[\Sigma] \in \mathbb{R}^{m\times n}$ et $[V] \in \mathbb{R}^{n\times n}$:

$$[X] = [U][\Sigma][V]^T \tag{6}$$

où $[U]$ et $[V]^T$ sont des matrices orthonormales et $[\Sigma]$ est une matrice diagonale avec des valeurs positives placées par ordre décroissant. Les vecteurs orthonormaux verticaux (colonnes) de $[U]$ sont les composantes principales (modes POD) recherchées de la matrice $[X]$ et leur importance est proportionnelle aux valeurs correspondantes de la matrice carrée diagonale $[\Sigma][\Sigma]^T$.

V.2. Application du POD sur des modèles structuraux en dynamique non-linéaire

En dynamique des structures, les modèles d'ordre réduit par POD (POD-ROM) sont applicables en analyses linéaires et non-linéaires par intégration temporelle. Puisque cette technique de réduction nécessite une base de données (snapshot matrix) pour déterminer les modes POD, une analyse par intégration temporelle du modèle structural complet devra être initialement effectuée.

Considérons un système structurel non-linéaire avec m degrés de liberté. n snapshots (capture de vecteur déplacement) sont extraits de l'analyse temporelle initiale effectuée sur le modèle complet. Ensuite, les modes POD sont calculés à partir de la matrice des snapshots $[X]$. Puis, un sous-espace $[T] \in \mathbb{R}^{m\times s}$, constitué par les premiers s modes POD satisfaisant un critère de troncature énergétique, est considéré pour la réduction du système dynamique.

$$\underbrace{\{X(t)\}}_{\in\mathbb{R}^{m\times 1}} \cong \underbrace{[T]}_{\in\mathbb{R}^{m\times s}} \underbrace{\{Q(t)\}}_{\in\mathbb{R}^{s\times 1}} \tag{7}$$

où $\{X(t)\}$ et $\{Q(t)\}$ sont respectivement les vecteurs déplacements en base complète et réduite. En remplaçant $\{X(t)\}$ par $[T]\{Q(t)\}$ dans l'équation dynamique initiale on aboutit au système dynamique réduit :

$$[T]^T[M][T]\{\ddot{Q}(t)\} + [T]^T[C][T]\{\dot{Q}(t)\} + [T]^T\{F_{NL}([T]\{Q(t)\})\} = [T]^T\{F(t)\} \tag{8}$$

Il faut noter ici que la force de retour non-linéaire $\{F_{NL}([T]\{Q(t)\})\}$ n'est pas réduite et devra toujours être calculée dans la base complète. Ainsi, cette tâche est l'opération numérique la plus coûteuse dans le calcul réduit. Afin de limiter son impact sur l'efficacité globale de la technique de réduction, une intégration temporelle explicite (méthode des différences centrées) est adoptée puisqu'elle minimise le besoin de calculer la force de retour non-linéaire.

V.3. Implémentation numérique

Pour les modèles d'ordre réduit par POD, on ne peut pas échapper au calcul par intégration temporelle du modèle structurel complet effectuer initialement afin de déterminer les modes POD. Pour pouvoir bénéficier de la réduction par POD après ce calcul initial couteux, plusieurs techniques sont proposées.

Dans (Bamer & Bucher, 2012), une structure en portique métallique ayant un système d’isolation sismique non-linéaire en sa base est sollicitée par une vibration sismique. Le coût numérique de l’analyse dynamique est réduit en effectuant initialement l’analyse temporelle du modèle complet sur une portion de la durée de l’excitation sismique. Ensuite, les snapshots sont extraits et les modes POD sont calculés de façon à construire le système dynamique réduit. La réponse temporelle correspondante à la partie restante de l’excitation sismique est alors calculée avec le modèle dynamique réduit qui est moins coûteux numériquement (cf. Figure 10). Dans tout ce qui suit, cette technique sera nommée approche 1.

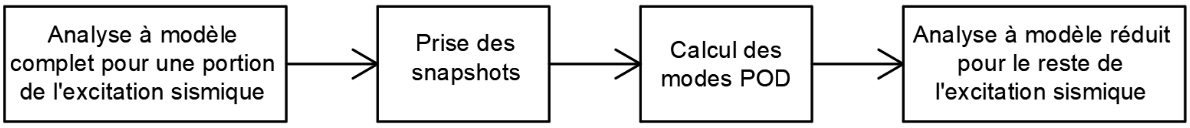

Figure 10 : Diagramme de l’approche 1.

Généralement, en génie parasismique, la tenue de la structure doit être vérifiée pour une gamme de séismes potentiels afin de couvrir divers scénarios possibles. (Bamer, Amiri & Bucher, 2017) ont considéré une structure linéaire en béton armé ayant un système d’isolation sismique non-linéaire en sa base. Cette structure est étudiée séparément pour plusieurs excitations sismiques. L’économie de temps de calcul est réalisée en effectuant l’analyse temporelle obligatoire du modèle complet uniquement pour une seule excitation. Ensuite, les snapshots sont extraits et les modes POD sont calculés de façon à construire le système dynamique réduit. Les réponses temporelles correspondantes aux autres excitations sont ensuite calculées avec le modèle dynamique réduit (cf. Figure 11). Dans tout ce qui suit, cette technique sera nommée approche 2.

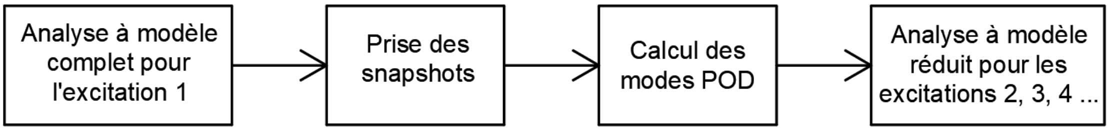

Figure 11 : Diagramme de l’approche 2.

Une originalité de cette thèse est d’appliquer pour la première fois les approches 1 et 2 sur des modèles d’ordre réduit en analyse dynamique d’une structure multiétages en béton armé avec de la non-linéarité matérielle modélisée via les éléments multifibres. De plus, les approches 1 et 2 sont appliquées à un mur de contreventement multiétages en béton armé avec de la non-linéarité matérielle modélisée via les membranes multicouches.

VI. Application en analyse sismique

Pour tester la précision et l'efficacité des approches 1 et 2 sur des structures non-linéaires en béton armé, des comparaisons au niveau des applications numériques sur MATLAB sont faites entre les résultats des modèles dynamiques complets et réduits par POD pour des structures en béton armé non-linéaire soumises à des excitations sismiques. Il faut noter que toutes les applications numériques utilisées dans cette thèse sont développées sur MATLAB. L'ordinateur utilisé est équipé d'un processeur Intel Xeon CPU @ 2.50 GHz avec 64 GB RAM.

4 enregistrements sismiques (accélérogrammes) obtenus du "Center of Engineering for Strong Motion Data" (*CESMD*, website) sont considérés (cf. Figure 12).

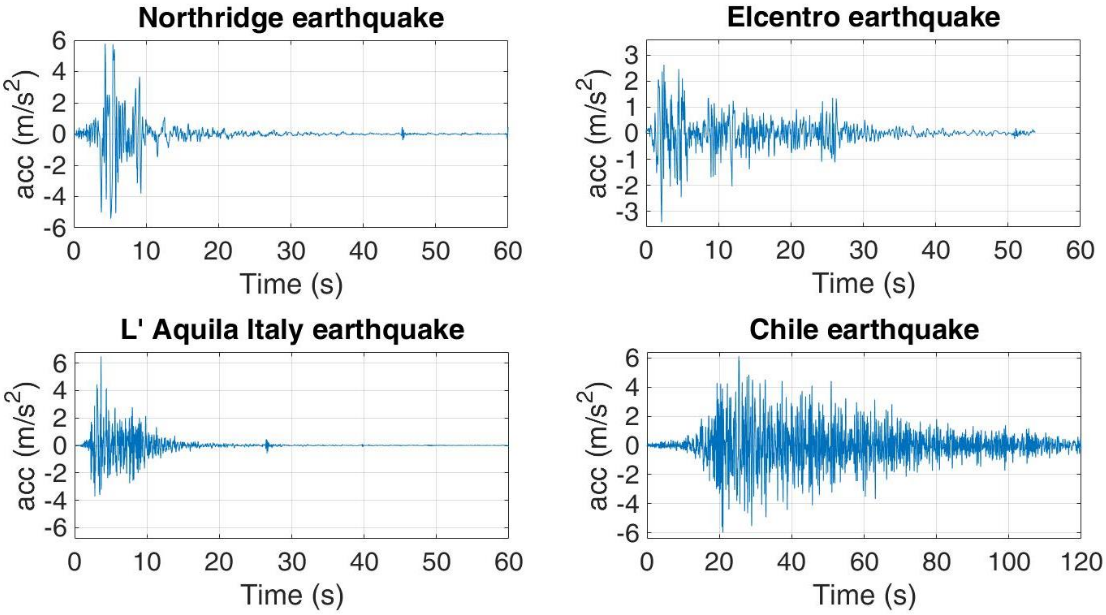

Figure 12 : Accélérogrammes des séismes.

VI.1. Structure multiétages en béton armé

La structure considérée est un portique 2D en béton armé de 10 étages et 5 travées par niveau. La hauteur d'étage est 3m et la longueur de travée 5m. Une charge linéaire de 4 t/m est appliquée à toutes les travées de chaque niveau. Tous les éléments structuraux ont une section identique de 40x40 cm avec 4 barres d'armatures de 20 mm en lit supérieur et inférieur. Chaque section est divisée en 4 fibres de béton et 2 d'aciers. La non-linéarité matérielle est supposée se produire aux extrémités des poutres et poteaux de 5 premiers étages.

Pour chaque accélérogramme considéré, une analyse par intégration temporelle du modèle complet est réalisée pour toute la durée du signal sismique. Ces analyses serviront de références pour évaluer les résultats et l'efficacité des modèles réduits.

L'application de l'approche 1 est effectuée séparément pour les 4 enregistrements sismiques adoptés. Pour chaque accélérogramme, une analyse par intégration temporelle du modèle complet est effectuée sur le premier quart de la durée du signal sismique. Ensuite 50 snapshots également espacés sont extraits et les modes POD sont calculés afin de construire le système dynamique réduit. Une analyse par intégration temporelle du modèle réduit est effectuée sur le trois quart restant du signal sismique. L'économie de temps et l'erreur du déplacement au sommet de la structure obtenues par l'approche 1 sont présentées dans le Tableau 1.

Séisme	Temps de calcul modèle complet	Temps de calcul approche 1	Economie du temps	Speedup	Erreur absolue moyenne en déplacement	Déplacement horizontal maximal
Northridge	795.73 s	239.93 s	69.85%	3.3	0.12 cm	45.06 cm
Elcentro	687.03 s	214.04 s	68.85%	3.2	0.31 cm	23.96 cm
L'Aquila	774.31 s	243.96 s	68.49%	3.2	0.10 cm	15.85 cm
Chile	1661.06 s	426.86 s	74.30%	3.9	1.67 cm	27.24 cm

Tableau 1 : Efficacité et précision de l'approche 1 sur la structure portique en béton armé.

Dans l'application de l'approche 2, une analyse par intégration temporelle du modèle complet est effectuée pour les premières 15 secondes du séisme Northridge. Ensuite 50 snapshots également espacés sont extraits et les modes POD sont calculés afin de construire le système dynamique réduit. Une analyse par intégration temporelle du modèle réduit est effectuée pour la durée entière des 4 séismes (Northridge, Elcentro, L'Aquila et Chile). L'économie de temps et l'erreur du déplacement au sommet de la structure obtenues par l'approche 2 sont présentées dans le Tableau 2.

Séisme	Temps de calcul modèle complet	Temps de calcul approche 2	Economie du temps	Speedup	Erreur absolue moyenne en déplacement	Erreur absolue au déplacement horizontal maximal	Déplacement horizontal maximal
Northridge	795.73 s	47.80 s	93.99%	16.6	0.28 cm	1.26 cm	45.06 cm
Elcentro	687.03 s	44.51 s	93.52%	15.4	0.36 cm	0.24 cm	23.96 cm
L’Aquila	774.31 s	47.94 s	93.81%	16.2	0.79 cm	0.52 cm	15.85 cm
Chile	1661.06 s	106.57 s	93.58%	15.6	2.71 cm	0.85 cm	27.24 cm

Tableau 2 : Efficacité et précision de l’approche 2 sur la structure portique en béton armé.

Il est clair que les deux approches contribuent à une économie importante des temps de calcul, surtout avec l’approche 2 (16 fois plus rapide que le calcul classique). De plus, en termes de précision des résultats, ces techniques donnent des résultats satisfaisants, surtout avec l’approche 1.

Il faut noter qu’en testant la précision de l’approche 2, on remarque que les modes POD issues d’un modèle complet soumis à un séisme fort (Northridge) avaient une tendance à surestimer les contraintes et efforts internes lorsque le modèle réduit était sollicité par un séisme plus faible (Elcentro, L’Aquila). Le choix du séisme à prendre en compte pour extraire les modes POD influe donc sur la précision des résultats.

VI.2. Mur de contreventement multiétages en béton armé

La structure considérée est un mur de contreventement planaire en béton armé de 8 étages avec 3 m de largeur, 30 cm d’épaisseur et 5 m de hauteur par étage. Une charge linéaire de 30 t/m est appliquée sur le mur à chaque niveau. La non-linéarité matérielle est considérée au niveau de 4 premiers étages. Pour plus de détails sur les dimensions et ferraillage de la structure, le lecteur peut se référer à la Figure 13.

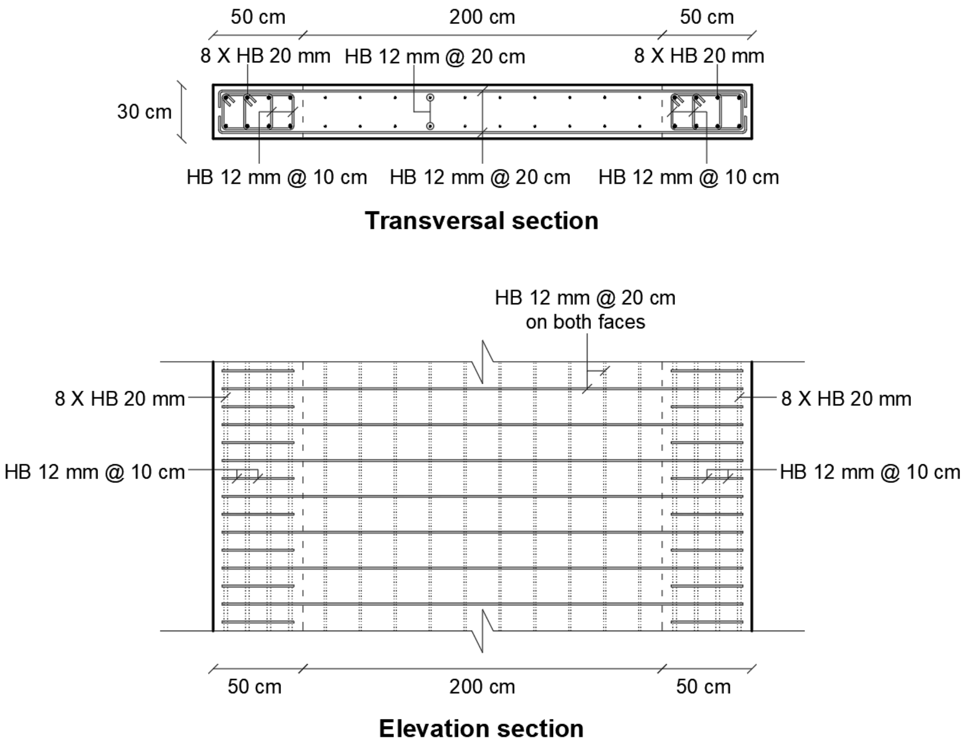

Figure 13 : Ferraillage du mur de contreventement en béton armé.

Des tests similaires à ceux réalisés sur le portique multiétages sont effectués ici pour le mur de contreventement avec les approches 1 et 2. Des résultats similaires (de qualité inferieur mais acceptable) sont observés en termes de précision et de réduction de coûts de calcul des modèles réduits.

VII. Conclusions et perspectives

L'objectif de cette thèse était de tester la précision et l'efficacité de la réduction du modèle dynamique par POD des structures en béton armé soumises à des excitations sismiques tout en tenant compte de la non-linéarité des matériaux. A partir d'applications numériques sur MALAB et en comparant l'analyse dynamique du modèle complet avec le modèle réduit par POD, on peut tirer les conclusions suivantes :

1- Pour tous les cas, les modèles réduits ont permis d'obtenir avec précision la réponse maximale des structures solliciter par un séisme.

2- En termes d'efficacité, l'approche 2 présente une économie de temps supérieur à celle de 1. Cependant, l'approche 1 est plus fiable en résultats.

3- Dans l'approche 2, les modes POD issus d'un modèle complet soumis à un fort séisme ont la tendance à surestimer les efforts internes et contraintes dans les modèles réduits solliciter par des séismes relativement faibles.

4- Les modèles réduits sollicités par des séismes ayant des pics de courte durée sont plus fiable que les modèles soumis à des seimes de forte intensité continue sur un grand intervalle de temps.

5- Les modèles réduits de mur de contreventement apparaissent moins fiables et efficaces que ceux des structures en portique.

6- Malgré les efforts pour minimiser son impact, le calcul de la force de retour non-linéaire en base complète continue à limiter l'efficacité des modèles réduits.

Comme futures perspectives pour ce travail, on propose les axes de recherche suivants :

1- Réduire le coût de calcul de la force de retour non-linéaire en utilisant la méthode POD avec une interpolation empirique discrète (POD-DEIM).

2- Augmenter l'efficacité des modèles dynamiques réduits par POD en optimisant la taille de chaque pas de temps dans l'analyse par intégration temporelle.

3- Dans l'approche 2, vue l'influence du choix de séisme initial dans l'extraction des modes POD, on propose de créer un signal synthétique basé sur l'enveloppe du spectre fréquentiel de tous les séismes en considération et d'utiliser ensuite ce signal synthétique pour extraire les modes POD.

4- Etendre l'application de ce travail sur d'autres types de chargement dynamique comme des chocs ou des explosions.

Naim AYOUB

Reduced order finite element models for the nonlinear dynamic analysis of reinforced concrete structures under seismic excitations

Résumé : Cette thèse concerne le développement de modèles d'ordre réduit pour l'analyse dynamique des structures en béton armé avec des non-linéarités matérielles et soumises à des excitations sismiques. La réduction du modèle est réalisée en étendant l'application de la décomposition orthogonale aux valeurs propres (POD) aux modèles dynamiques de structures en béton armé avec des non-linéarités matérielles dues à la plasticité des armatures en acier et à l'endommagement du béton. Cette technique de réduction est d'abord testée sur une structure de type portique à plusieurs étages où la non-linéarité des matériaux est modélisée par l'approche de la section multifibre. Ensuite, des essais similaires sont effectués sur un voile de contreventement à plusieurs étages en béton armé avec des non-linéarités matérielles introduites par une approche de membrane multicouche.

Mots clés : Structures en béton armé, Non-linéarités matérielles, Modèle dynamique d'ordre réduit, Décomposition orthogonale aux valeurs propres, Poutre multifibre, Membrane multicouche, Excitations sismiques.

Abstract: This thesis concerns the development of reduced order models for dynamic analysis of reinforced concrete structures with material nonlinearities and subjected to seismic excitations. Model reduction is achieved by extending the application of the Proper Orthogonal Decomposition (POD) to dynamic models of reinforced concrete structures with material nonlinearities originating from steel reinforcement plasticity and concrete damaging. This reduction technique is tested first on a reinforced concrete multistory frame structure where material nonlinearity is modeled by the multifiber section approach. Then, similar testing is made on a multistory planar reinforced concrete shear wall with material nonlinearities introduced via the layered membrane approach.

Keywords: Reinforced concrete structures, Material nonlinearities, Reduced order dynamic model, Proper orthogonal decomposition, Multifiber beam, Layered membrane, Seismic excitations.